

## 5. SITE 1258<sup>1</sup>

Shipboard Scientific Party<sup>2</sup>

### BACKGROUND AND OBJECTIVES

Site 1258 is located in a water depth of 3192.2 meters below sea level (mbsl) on the gently dipping western slope (~2°) of Demerara Rise, which is ~380 km north of Suriname (see Fig. F1, p. 5, in Shipboard Scientific Party ["Site Survey and Underway Geophysics"], this volume). The site is located on a ridge of Paleogene sediments outcropping on the seafloor. Site 1258 is the deepest member of the paleoceanographic depth transect across Demerara Rise. The major objectives were the following:

1. Core and log a Paleogene–Albian section to evaluate paleoceanographic and paleoclimatic changes, with emphasis on major and abrupt events during this interval (e.g., the Eocene/Oligocene [E/O] and Paleocene/Eocene [P/E] boundaries and Cretaceous oceanic anoxic events [OAEs]).
2. Reconstruct the history of the opening of the Equatorial Atlantic Gateway by obtaining benthic foraminifer proxy data. These data will help improve understanding of changes in bottom water circulation over the Demerara Rise during the gradual opening of the seaway.
3. Recover continuous and expanded sediment records of the Paleogene and Cretaceous periods in order to reconstruct short- and long-term changes in greenhouse forcing.

### Seismic Stratigraphy

Site 1258 is on the northwest-facing slope of a small promontory of Demerara Rise, with a local seafloor gradient of 1.5° toward the northwest. The seafloor falls away more steeply ~1 km from the site. To the southeast (upslope), the sedimentary sequence thickens above Reflector

<sup>1</sup>Examples of how to reference the whole or part of this volume.

<sup>2</sup>Shipboard Scientific Party addresses.

“C” (post-Albian). The seismic stratigraphy for the site is described by line GeoB221, which transects northeast–southwest, and line 207-L1S, which crosses orthogonally to line GeoB221 (Figs. F1, F2). A nearby industry multichannel seismic line (line C2211) passes nearly parallel with line 207-L1S, which is ~5.5 km to the southwest (Fig. F3).

Reflector “A,” representing the top of a presumably early Miocene erosional unconformity, crops out at the seafloor at the site (within the resolution of the survey data). Between the Reflector A (the seafloor in this case) and Reflector “B” is seismic Unit 2 (seismic Unit 1 is missing from this site). Unit 2 is 300 ms thick (two-way traveltime) at this location, calculated to be 265 meters below seafloor (mbsf) using downhole logging velocity data from the site. The unit shows an echo character of reasonably coherent but slightly folded reflections with offsets, which probably describes a sediment sequence that has undergone mass failure and rotational displacement. A relatively coherent package of higher-amplitude reflections of short lateral duration is present at 220 ms subbottom (189 mbsf).

Reflector B at 300 ms subbottom (265 mbsf) marks the top of seismic Unit 3, and Reflector C at 480 ms subbottom (~459 mbsf) is its base. It is a flat-lying sequence at this site that dips gently to the north-northwest at an angle of 1.5°. The sequence thins and pinches out in the downslope direction from the drill site. Reflector B is not well defined at Site 1258 because the reflections are incoherent. Coherency improves laterally, especially in the upslope (southwest) direction. Seismic Unit 3a, defined at the interval between Reflectors B and “B’” (300–450 ms subbottom [265–417 mbsf]), is relatively transparent and incoherent in profile, with low-amplitude coherent parallel reflections that become apparent only toward its base. Subunit 3b underlies Subunit 3a and is the sequence between Reflectors B’ and C (450–515 ms subbottom [417–480 mbsf]). It is defined on the basis of a series of strong parallel coherent reflections that are laterally contiguous.

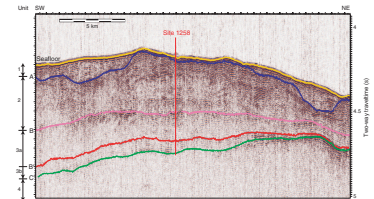
On industry profile line C2211, the entire section from Reflector A to B’ appears relatively incoherent with contorted reflections (Fig. F3). More than 16 km upslope (southwest), the same interval comprises a coherent parallel set of reflections that terminates in a listric fashion against this incoherent unit. The character and upslope truncation suggests most of the interval of seismic Unit 2 and Subunit 3a at the drill site has slumped as a rotational mass failure. The package of reflectors composing seismic Subunit 3b, however, appears contiguous and may be undeformed. Reflectors below Horizon C appear folded into a possible small anticline below the drill site and contact Reflector C as an angular unconformity. There are numerous listric-normal faults and folds in this section (Fig. F3).

## **OPERATIONS**

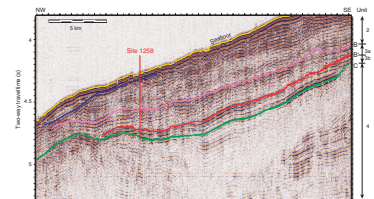
### **Transit from Site 1257 to Site 1258**

The 23.5-nmi transit to Site 1258 was made in 2.5 hr at an average speed of 9.4 kt. As the ship settled on the site’s coordinates, a positioning beacon was launched, initiating operations at 1815 hr on 22 January 2003.

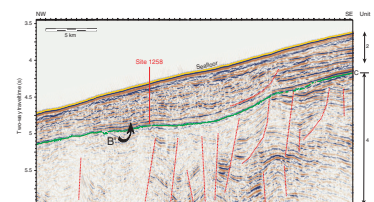
**F1.** Seismic line GeoB221, p. 42.



**F2.** Seismic line 207-L1S, p. 43.



**F3.** Industry multichannel seismic reflection line, p. 44.



### Hole 1258A

The same rotary core barrel (RCB) bottom-hole assembly (BHA) used at Site 1257 was deployed, tagging the seafloor at 3203.2 meters below rig floor (mbrf) (3192.2 mbsl). Hole 1258A was spudded at 0015 hr on 23 January, coring from 0 to 322.4 mbsf and recovering 34 cores. While recovering Core 34R, the aft wireline parted from the core barrel at 405 mbrf. Fishing the wireline and core barrel required 3 hr. After cutting 1100 m of damaged wireline, the core barrel was reheaded and placed back in service.

Coring in Hole 1258A resumed from 322.4 to 447.5 mbsf, recovering an additional 16 cores for an average recovery of 83.9% (Table T1). With the depth objective achieved, the hole was filled with sepiolite mud for abandonment and the drill string was retracted. We concluded operations in Hole 1258A when the bit cleared the seafloor at 1010 hr on 25 January.

---

T1. Coring summary, p. 86.

---

### Hole 1258B

The ship was offset 30 m east of Hole 1258A, and Hole 1258B was spudded at 1245 hr on 25 January. An RCB core (Core 1R) was recovered (0–7.1 mbsf), and the hole was drilled ahead 7 m to 14.1 mbsf in an attempt to provide better stratigraphic overlap with Hole 1258A. RCB coring resumed from 14.1 to 349.3 mbsf. Poor recovery in Core 37R (1.1%) and high pump pressures suggested the bit was obstructed, so the bit deplugger was deployed. Cores 38R through 41R were taken to 383.8 mbsf, but no recovery in Core 41R and the return of elevated pump pressures indicated the bit was obstructed again. Two separate deployments of the bit deplugger were conducted. After a return to normal pressures, RCB coring resumed from 383.3 to 460.9 mbsf. We collected a total of 57 cores from Hole 1258B (average recovery = 76.3%) (Table T1). With the depth objective achieved, coring was terminated and the hole displaced with 143 bbl of sepiolite mud. The drill string was pulled back, and the bit cleared the seafloor at 1010 hr on 28 January, ending Hole 1258B.

### Hole 1258C

The ship was offset 30 m east of Hole 1258B, and Hole 1258C was spudded at 1145 hr on 28 January and drilled ahead to 120 mbsf. RCB coring commenced at 120 mbsf and advanced to 206.1 mbsf, collecting nine cores. We drilled ahead to 245.3 mbsf, where we resumed coring. After low recovery in Cores 10R and 11R, we suspected the bit was obstructed and the deplugger was deployed. After clearing the bit, coring deepened the hole to 274.2 mbsf. Subsequent drilling ahead to 384.8 mbsf was followed by coring to the depth objective of 485.0 mbsf. A total of 34 cores were taken in Hole 1258C (recovery = 74.9%) (Table T1).

In preparation for logging, the hole was swept with 30 bbl of sepiolite mud, which was followed by a wiper trip. Twenty-five meters of fill was noted on the bottom, prompting a second mud sweep. The bit was released, the hole was displaced with 150 bbl of mud, and the drill string was pulled to 100 mbsf for logging.

The first logging run was made with the triple combination (triple combo) tool string, which was deployed to ~485 mbsf and logged to the base of the drill pipe in two passes. Two more passes were made with just the Multi-Sensor Spectral Gamma Ray Tool (MGT) activated. The

second logging run included two passes with the Formation MicroScanner (FMS)-sonic tool string from 485 mbsf to the base of the drill string. After completion of the logging operations, the drill string was retrieved, clearing the rig floor at 0750 hr on 1 February, ending operations at Site 1258. After recovery of the beacon and retraction of the thrusters and hydrophones, the ship began the transit to Site 1259.

## LITHOSTRATIGRAPHY

Site 1258 is located in the greatest water depth (3192 mbsl) of the Leg 207 Demerara Rise depth transect. From the three holes at Site 1258, we recovered 79% of the ~1120 m cored (Fig. F4).

Five lithostratigraphic units were recognized at Site 1258 (Table T2). The oldest unit recovered (Unit V) is dominated by phosphoritic calcareous claystone. The superjacent unit (Unit IV) is composed dominantly of laminated calcareous organic-rich black shale and laminated chalk/limestone. The youngest three units (Units I–III) recognized are pelagic and composed dominantly of calcareous microfossils, siliceous microfossils, and clay. These pelagic sediments are pervasively bioturbated; pyrite and other iron sulfides are found throughout the pelagic interval but are most abundant in Unit III. Clay and zeolite are also relatively abundant in Unit III, whereas Subunit IIA contains a relatively high abundance of either siliceous microfossils or zeolite. The carbonate content for the pelagic Units I–III varies from 30 to 80 wt%. Sediments and sedimentary rocks recovered at Site 1258 range in age from Albian to Miocene (see “Biostratigraphy,” p. 10), but the record is interrupted by at least two major and several minor hiatuses and/or gravity flow deposits.

Lithostratigraphic units recognized at Site 1258 generally parallel those reported for the other Leg 207 sites and Site 144 (Hayes, Pimm, et al., 1972). Differences among the lithologic divisions represent differences in the level at which unit boundaries were placed and can be attributed to uncertainty related to coring gaps at Site 144 and to differences in the definition of the Unit II/III boundary between Sites 1257 and 1258.

### Lithostratigraphic Units

#### Unit I

Intervals: 207-1258A-1R-1, 0 cm, through 2R-3, 42 cm; and 207-1258B-1R-1, 0 cm, through 1R-4, 111 cm

Depths: Hole 1258A: 0.00–8.52 mbsf and Hole 1258B: 0.00–5.61 mbsf

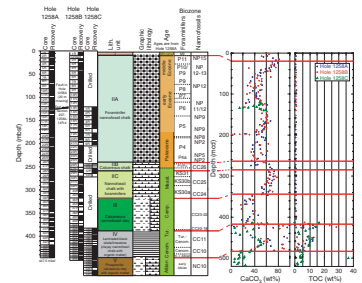
Thickness: 8.52 m (Hole 1258A)

Age: middle Miocene–early Oligocene

Lithology: nannofossil ooze with foraminifers

Unit I is predominantly a nannofossil ooze that exhibits a gradual color change downhole from pale yellow to light greenish gray. The unit was cored only in Holes 1258A and 1258B. It contains abundant black mottles, but other indications of bioturbation are rarely visible throughout. There is a sharp color change observed only in Hole 1258A from pale yellow/pale brown to greenish gray at 3.47 mbsf. However, neither sediment composition nor sediment fabric changes noticeably at this

F4. Lithostratigraphic units, carbonate content, and TOC, p. 45.



T2. Lithostratigraphic unit boundaries, p. 89.

boundary, and it is interpreted as a diagenetic redox boundary that propagated down from the seafloor. Below this color change, the sediments are light greenish gray, with only subtle variations. The base of Unit I is placed at a distinct lithologic change from nannofossil ooze to nannofossil chalk and corresponds to a major stratigraphic hiatus from the early Oligocene to middle Eocene.

## Unit II

Intervals: 207-1258A-2R-3, 42 cm, through 34R-4, 128 cm; 207-1258B-1R-4, 111 cm, though 36R-1, 55 cm; and 207-1258C-1R-1, 0 cm, through 12R-CC, 22 cm (boundaries are not cored in Hole 1258C)

Depths: Hole 1258A: 8.52–318.58 mbsf; Hole 1258B: 5.61–330.65 mbsf; and Hole 1258C: 120.00–264.85 mbsf

Thickness: 325.04 m (Hole 1258B)

Age: middle Eocene–Maastrichtian

Lithology: nannofossil chalk with foraminifers and calcareous chalk with foraminifers

Unit II consists of light greenish gray to greenish gray nannofossil chalk containing 30–80 wt% carbonate content in dominant lithologies (Fig. F4). *Zoophycos* and *Chondrites* trace fossils are found throughout. The unit is divided into three subunits. Subunit IIA contains 10%–25% foraminifers and 10%–25% clay and zeolites. Subunit IIB is defined by a marked increase in abundance of diagenetic calcite and carbonate debris (values of up to 70% of material identified in smear slides). Subunit IIC is dominated by nannofossils and foraminifers, but clay content is as high as 45%. The upper contact of Unit II is placed at a distinct lithologic change from nannofossil ooze to nannofossil chalk, whereas the bottom contact corresponds to an equally prominent downhole increase in clay content.

### Subunit IIA

Intervals: 207-1258A-2R-3, 42 cm, through 26R-4, 15 cm; 207-1258B-1R-4, 111 cm, though 25R-6, 12 cm; and 207-1258C-1R-1, 0 cm, though 9R-CC, 8 cm

Depths: Hole 1258A: 8.52–240.15 mbsf; Hole 1258B: 5.61–241.32 mbsf; and Hole 1258C: 120.00–203.57 mbsf (boundaries are not cored in Hole 1258C)

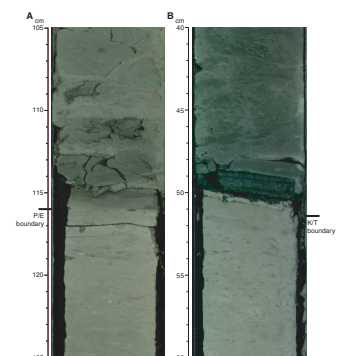
Thickness: 235.71 m (Hole 1258B)

Age: middle Eocene–late Paleocene

Lithology: nannofossil chalk with foraminifers

Subunit IIA (Fig. F5A) is composed of carbonate-rich (nannofossils and foraminifers) pelagic sediment with minor amounts of clay and either zeolite or radiolarians and diatoms. The latter two were observed only in the upper and middle parts (base of lower Eocene) of the subunit. The top of this subunit is placed at a distinct lithologic change from nannofossil ooze to nannofossil chalk at 8.52 mbsf (Hole 1258A). The lithologic change coincides with the beginning of a steady decrease in carbonate content from 70–80 wt% to values stabilizing at ~30–50 wt%. There are also color changes associated with the top of Subunit IIA. In Hole 1258A, this ooze to chalk transition is associated with a change from greenish gray to light greenish gray at 8.52 mbsf, contrasting with the top of Subunit IIA in Hole 1258B, which is characterized by a change

F5. Representative lithologies from Unit II, p. 46.



from pale yellow to darker pale yellow. This contrast in color between the two holes at the top of Subunit IIA indicates that this depth horizon in Hole 1258B is still above the speculated diagenetic redox boundary found in Unit I in Hole 1258A (3.47 mbsf); this boundary does not occur in Hole 1258B until slightly deeper in Subunit IIA at 7.02 mbsf. Below this redox color change, the sediments are characterized by lighter–darker color cycles, which persist throughout Subunit IIA at varying intensities. Black mottles and streaks are found throughout and are often concentrated in burrows. Sediments range from homogeneous to burrow mottled, and the number of discrete traces increases downhole. The base of Subunit IIA is placed at a marked increase in abundance of diagenetic calcite and carbonate debris (values of up to 70% of material identified in smear slides), which also coincides with a color change to a predominance of reddish brown.

The Paleocene/Eocene Thermal Maximum (PETM) is present in this subunit. In Section 207-1258A-19R-5, the sediment changes gradually from greenish gray chalk to brownish clayey chalk followed by dark greenish, faintly laminated, carbonate-free clay. The contact with the underlying chalk (Section 207-1258A-19R-5, 116 cm) is sharp. The onset of the PETM is marked by the last occurrence of bioturbation 2 cm into the chalk.

#### ***Subunit IIB***

Intervals: 207-1258A-26R-4, 15 cm, through 28R-3, 20 cm; 207-1258B-25R-6, 12 cm, through 28R-CC, base; and 207-1258C-12R-1, 0 cm, through 12R-7, 45 cm.

Depths: Hole 1258A: 240.20–258.10 mbsf; Hole 1258B: 241.32–260.12 mbsf; and Hole 1258C: 254.90–263.58 mbsf

Thickness: 19.80 m

Age: early Paleocene–latest Maastrichtian

Lithology: calcareous chalk with foraminifers

Subunit IIB consists of calcareous chalk with foraminifers (upper part of Fig. F5B), with a distinct yellowish red and yellowish brown color in parts. The color is more intense downcore. Typically, light greenish gray to olive-gray burrows and mottles are observed, which seem to represent reducing environments around the burrowed sediment. The subunit is mottled throughout and is pervasively bioturbated except for short intervals marked by basal layers of opaque minerals. Discrete trace fossils include *Zoophycos*, *Chondrites*, and *Planolites*. Traces of pyrite are present.

This subunit is marked by a significant increase in abundance of diagenetic calcite and carbonate debris. The sediment also contains abundant foraminifers (20%–40%), and clay content increases downhole. In contrast to the overlying and underlying lithologic Subunits IIA and IIC, nannofossils are rare and poorly preserved in this particular interval. Carbonate content varies between 40 and 65 wt%.

The Cretaceous/Tertiary (K/T) boundary is located in this subunit. Interval 207-1258B-27R-1, 49–51 cm, contains a well-preserved 1.5-cm-thick impact ejecta layer of green microspherules (Fig. F5B). The spherules appear to be arranged in layers and grade from 2–3 mm diameter at the bottom of the layer to 1.5 mm at the top; some laminations are lighter than others. Pyrite is also present at the base of this ejecta layer. Beneath the ejecta layer is a very thin interval of white sediment (3–5 mm thick), and below this is another single layer of green spherules. The lower contact is sharp and represents an abrupt lithologic and color

change from the dark green ejecta layer above to the mottled light green-gray calcareous chalk below.

### Subunit IIC

Intervals: 207-1258A-28R-3, 20 cm, through 34R-4, 128 cm; 207-1258B-28R-CC, base, through 36R-1, 55 cm; and 207-1258C-12R-7, 45 cm, through 12R-CC, base.

Depths: Hole 1258A: 258.10–318.60 mbsf; Hole 1258B: 260.12–330.65 mbsf; and Hole 1258C: 263.58–264.85 mbsf

Thickness: 70.53 m (Hole 1258B)

Age: Maastrichtian (not latest Maastrichtian)

Lithology: nannofossil chalk with foraminifers

Subunit IIC consists of a greenish gray nannofossil chalk with foraminifers and clay, which is moderately burrowed with black and white mottles (Fig. F5C). Distinct *Zoophycos* burrows (black) are common to abundant throughout the entire subunit. *Chondrites* burrows appear downcore and are abundant. Barite and pyrite concretions up to several centimeters in diameter are common in the lower part of Subunit IIC. A pronounced cyclic color banding (decimeter scale) in various shades of light greenish gray and greenish gray is observed throughout this subunit (Fig. F5C). Smear slide analysis showed abundant diagenetic (blocky) calcite, foraminifer fragments, and carbonate debris. Carbonate content varies between 50 and 80 wt%.

### Unit III

Intervals: 207-1258A-34R-4, 128 cm, through 42R-1, 0 cm; 207-1258B-36R-1, 55 cm, through 44R-2, 51 cm; and 207-1258C-14R-1, 0 cm, through 15R-3, 96 cm.

Depths: Hole 1258A: 318.60–389.80 mbsf; Hole 1258B: 330.65–394.67 mbsf; and Hole 1258C: 384.80–393.73 mbsf

Thickness: 71.2 m (Hole 1258A)

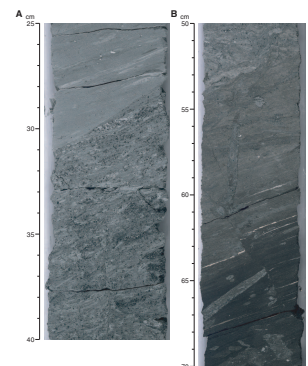
Age: Campanian

Lithology: calcareous nannofossil clay

Unit III consists of calcareous nannofossil clay displaying cyclic color banding between light greenish gray and greenish gray on a decimeter scale (Fig. F6A). Barite and pyrite crystals are abundant throughout this unit. The boundary between Subunit IIC and Unit III is defined by a sharp change in the composition, texture, and bioturbation of the sediment, although the color (greenish gray) remains the same. The primary constituents of Unit III are clay and calcite. Nannofossil, foraminifer, and coccolith contents increase downhole. Trace amounts of pyrite, quartz, and zeolites are present in smear slides. The contact is also characterized by a drop in carbonate content from ~65 wt% in Subunit IIC to ~35 wt% in Unit III. Bioturbation increases from moderate in Subunit IIC to pervasive throughout Unit III. Bioturbation slightly obscures the color cycles. *Planolites*, *Chondrites*, and *Zoophycos* burrows are abundant and occasionally have black halos of monosulfide. The lower contact of Unit III is placed at the transition to laminated lithologies.

Two different boundary contacts were captured for the lower contact of Unit III. In Hole 1258B, a gradual boundary between Units III and IV is observed in Section 207-1258B-44R-2, covering ~40 cm, and is expressed in both lithologic and color changes (Fig. F6A, F6B, F6C). The transition is gradual from the major lithology of Unit III, greenish gray

F6. Transition from calcareous nannofossil clay to black shale, p. 48.



calcareous nannofossil clay, to a greenish gray quartzose nannofossil chalk with abundant glauconite and fish remains, to a black calcareous claystone with organic matter in Unit IV. The minor lithology in Unit III, quartzose nannofossil chalk, is composed mainly of glauconite, quartz, some feldspar, and nannofossils (Fig. F7A). The base of Unit III in Hole 1258C displays a sharp lithologic and color contact between Units III and IV in Section 207-1258C-15R-3, 96 cm (Fig. F6D). Above the contact, pyrite nodules with glauconite were observed. The color changes from greenish gray to black. The top 15 cm of Unit IV is massive, suggesting that this interval is slumped. The Unit III/IV contact was not recovered in Hole 1258A but the core catcher of Core 207-1258A-41R contains abundant glauconite followed by black shale from Unit IV at the top of Core 42R.

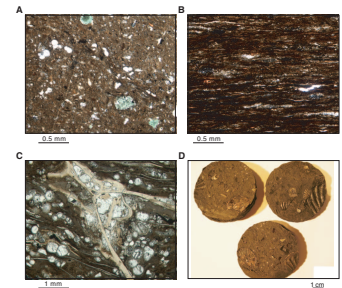
### Unit IV

Intervals: 207-1258A-42R-1, 0 cm, through 50R-2, 30 cm; 207-1258B-44R-2, 51 cm, through 56R-CC, base; and 207-1258C-15R-3, 96 cm, through 27R-2, 65 cm  
 Depths: Hole 1258A: 389.80–444.06 mbsf; Hole 1258B: 394.67–454.05 mbsf; and Hole 1258C: 393.73–449.56 mbsf  
 Thickness: 59.38 m (Hole 1258B)  
 Age: Turonian–middle late Albian  
 Lithology: laminated black shale/chalk/limestone (clayey nannofossil chalk/limestone with organic matter)

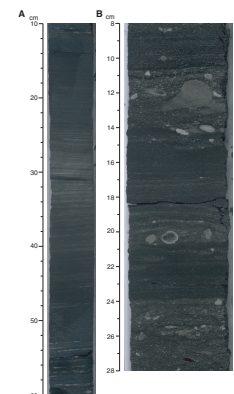
Lithostratigraphic Unit IV primarily consists of dark olive-gray to black finely laminated calcareous claystone with organic matter (black shale) and clayey chalk and limestone containing organic matter (Figs. F7B, F8A). The unit shows well-developed submillimeter-scale laminations and has a strong petroliferous odor. Rhythmic color variations between dark olive gray and black are visible on a decimeter scale throughout (Fig. F8A). The lighter colors reflect higher carbonate content in general and strong diagenetic calcite growth in particular. Thus, carbonate contents are highly variable and range from as high as ~95 wt% in individual carbonate-rich layers to as low as ~5 wt% in black claystones (Fig. F4). Carbonate constituents include nannofossils (concentrated in fecal pellets), foraminifers, and shell fragments (e.g., inoceramids). Total organic carbon (TOC) values range from ~5 to 28 wt% in the black shale. Rock-Eval pyrolysis analyses indicate Type II kerogen, which is consistent with a marine origin of the organic matter. The organic matter is clearly visible in thin sections (Fig. F7B) (Sample 207-1258B-45R-4, 114–117 cm; TOC = 28 wt%). Fish scales and bone fragments (*Francolite*) (Fig. F7C) and amorphous to cryptocrystalline phosphatic nodules (*Collophane*, up to 2 cm diameter with soft and hard consistency) are common throughout. They are present either parallel to bedding or concentrated in thin gravity deposits and appear as white to light brown blebs and streaks on core surfaces (Figs. F8B, F9B).

The black shales in the uppermost part of the unit show clear signs of mass movement; the sediment is distorted, contacts dip steeply, and laminae are not visible. Shell material, clasts of laminated claystone, and phosphoric clasts are scattered throughout the sediment and show a distinct matrix-supported fabric (Fig. F6C). In Section 207-1258C-15R-3, 96 cm, the topmost part of the black shales is distorted (Fig. F6D). This deformation is seen in thin sections as distinct kinks in the laminated fabric.

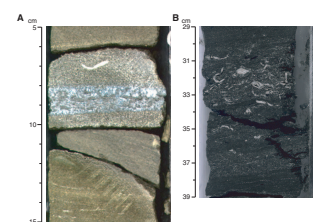
F7. Typical lithologies, p. 50.



F8. Representative lithologies of black shale from Unit IV, p. 51.



F9. Minor lithologies of black shale from Unit IV, p. 53.



In the lower part of the unit, the rhythmic chalk lithology is replaced by well-cemented limestones with sharp basal contacts, grading, and gradual laminated transition into black shale (Fig. F8C). Oyster and other pelecypod fragments are present, especially toward the base, and can form discrete lags (Fig. F9C). The limestones are rich in planktonic foraminifers, which are concentrated in layers. Diagenetic calcite formation is common. Occasional layers of diagenetic calcite with a distinct bluish tint are present (Fig. F9A). The calcite may grow perpendicular to the bedding, forming several-millimeter-high pinnacles. The graded units are interpreted as tempestites and/or turbidites.

### **Unit V**

Intervals: 207-1258A-50R-2, 30 cm, through 50R-3, 103 cm; 207-1258B-56R-CC, base, through 56R-CC, base; and 207-1258C-27R-2, 65 cm, through 34R-3, 117 cm

Depths: Hole 1258A: 444.06–446.22 mbsf; Hole 1258B: 454.05–458.90 mbsf; and Hole 1258C: 449.56–484.87 mbsf

Thickness: >35.31 m (Hole 1258C)

Age: early Albian

Lithology: phosphatic calcareous claystone with organic matter

Lithostratigraphic Unit V primarily consists of dark olive-gray to black phosphoritic calcareous claystone with organic matter (black shale). The cores show strong drilling disturbance in parts. Unit V sediments resemble the black shale lithology of Unit IV. Differences are the lack of obvious lamination, the paucity of “tempestites/turbidites,” the distinct drop in carbonate content, and the regular presence of phosphoritic layers and ammonites/bivalves on bedding planes (Fig. F7D). Rare and thin bioclastic limestone intervals are intercalated; they may represent occasional small-scale tempestites or turbidites. The carbonate content drops to values between 5 and 25 wt%, whereas the organic carbon content is relatively high, with up to 5 wt% TOC of marine origin.

### **Summary**

The oldest interval recovered at Site 1258 is a unit dominated by TOC-rich phosphoritic layers (Unit V) of early–late Albian age. These rocks lie below or in Reflector C (see [Shipboard Scientific Party](#) [“Site Survey and Underway Geophysics”], this volume), which represents the trace of an angular unconformity on Demerara Rise and thus may represent synrift deposition. The lithology is quite homogeneous overall but shows distinct bedding and faint lamination. Macrofossils are frequent (fish ammonite fragments), but trace fossils are absent. The lack of bioturbation and benthic organisms, the relatively high TOC content (up to 5 wt% marine organic matter), and the common occurrence of phosphoritic layers suggest a sheltered, probably shallow but fully marine (common ammonites) environment. Rare and thin bioclastic limestone intercalated with the TOC-rich claystones may be tempestites (storm deposits), limiting the water depths to storm wave base or less.

During the middle Albian–Coniacian, high productivity and low bottom water oxygen levels resulting in the preservation of large volumes of organic and phosphoritic matter prevailed at Site 1258. This phase is recorded by sediment dominated by dark laminated calcareous claystones and laminated chalks/limestones of Unit IV. TOC concentrations in Unit IV approach 30 wt%, and the organic matter is of marine origin.

Zeolites (clinoptilolite) and rare radiolarians suggest siliceous microfossils were a common component of the sediment. Carbonate values are highly variable (5–95 wt%) and reflect diagenetic dissolution and precipitation of calcite.

Open marine conditions and oxic bottom waters were established in the early Campanian, as indicated by the bioturbated pelagic marls of Unit III. The sharp contact between the bioturbated marls of Unit III and the laminated shales and limestones of Unit IV in Hole 1258C reflects a hiatus, but an expanded glauconite-rich interval in Hole 1258B is consistent with the transition being recorded by a highly condensed interval. Furthermore, the trace fossils and abundance of pyrite may indicate that bottom waters were relatively dysoxic in the late Campanian and early Maastrichtian. Variations in sedimentary fabric and minor sedimentary components, however, suggest that conditions at the seafloor and/or overlying water column fluctuated on geologically short timescales.

The K/T boundary interval seems to be complete in Hole 1258B with the uppermost Maastrichtian of Subunit IIC below, followed by a discrete ejecta interval showing a graded spherule layer, and basal Paleocene calcareous claystone above. The spherules are up to 2.5 mm in diameter, an exceptional size considering the distance to the proposed impact crater.

The P/E boundary record also seems to be relatively complete at Site 1258. A 3-cm-thick clay layer in Hole 1258C falls within an interval that contains the P/E boundary (see “[Biostratigraphy](#),” p. 10). The lack of carbonate in this layer is consistent with sedimentary changes expected at the PETM.

Gravity flow deposits and temporal gaps are common in the pelagic record at Site 1258. The most prominent one occurs in Hole 1258A, where ~20 m of sediment appears to be missing relative to Holes 1258B and 1258C. This difference is possibly due to faulting or mass-failure displacement.

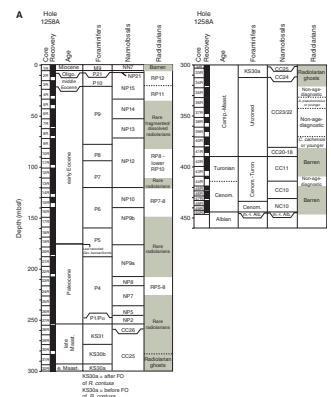
## BIOSTRATIGRAPHY

The three holes at Site 1258 yielded primarily middle Eocene–early Albian marine sediments that contain planktonic foraminifers, calcareous nannofossils, and radiolarians in abundances and states of preservation that vary widely with lithology and sediment induration. Shipboard examination of these microfossil groups in core catcher samples, supplemented as necessary by additional samples from the cores, permitted zonal or stage assignments to be made for the entire sequence. Datum levels are summarized in Figure F10 and in Tables T3, T4, T5, T6, T7, and T8.

A veneer of middle Miocene ooze at the top of the section overlies a sliver of lower Oligocene calcareous ooze rich in diatoms and radiolarians. All microfossil groups are abundant and well preserved.

About 25 m of middle Eocene biosiliceous chalk disconformably overlies a 143-m lower Eocene chalk as measured in the nonfaulted portion of Hole 1258B. The P/E boundary is present in Cores 207-1258A-19R, 207-1258B-21R, and 207-1258C-8R. Radiolarians cannot be identified to species in the Paleocene section, where the conspicuous presence of zeolites and locally abundant opal-CT lepispheres evident in nannofossil smear slides (see also “[Lithostratigraphy](#),” p. 4) indicate that these and other siliceous microfossils, formerly present, have been

F10. Foraminifer, nannofossil, and radiolarian biozonation, p. 55.



T3. Calcareous nannofossils, p. 90.

T4. Planktonic foraminifers, Hole 1258A, p. 91.

T5. Planktonic foraminifer datums, p. 92.

T6. Core catcher ages, p. 93.

T7. Planktonic foraminifers, Hole 1258B, p. 95.

T8. Planktonic foraminifers, Hole 1258C, p. 96.

largely destroyed by sediment diagenesis. The secondary silica was sufficiently disseminated in the expanded chalk section, however, that porcellanites did not form to the extent that they impeded good core recovery.

The K/T boundary ejecta layer is present in Core 207-1258B-27R. The uppermost Maastrichtian nannofossil *Micula prinsii* was identified immediately below the ejecta horizon, and overlying strata contain the lowermost Danian planktonic foraminifers in Zone P $\alpha$ . Site 1258 captured an especially thick (~20 m) uppermost Maastrichtian section (planktonic foraminiferal Zone KS31 [nannofossil Zones CC25C–CC26]).

The entire Maastrichtian–lower Campanian zeolitic chalk section at the present site is considerably expanded. The virtual absence of holococcoliths, however, indicates that this chalk represents relatively deep-water deposition with consequent dissolution of nonresistant calcareous nannofossils. Nannolith preservation does improve somewhat in the lower Campanian. Radiolarians in this Campanian interval show moderate–good preservation.

A condensed glauconite-rich horizon visible in Core 207-1258B-44R separates the Campanian chalk from the ~56 m of black shales below (lithostratigraphic Unit IV) that compose or represent the lower part of OAEs 3 and 2. The contact between the glauconite-rich layer and black shale is best displayed in Section 207-1158B-44R-1, where the heavily bored top of the black shale is a light tan color. Laminated strata in Section 207-1158B-44R-2 have been dated by sparse calcareous nannofossils as Coniacian (Zone CC14). A debris flow in Section 207-1158B-44R-3 contains a mixture of Turonian and Coniacian nannofossils that includes an unusually high abundance of the normally rare but dissolution-resistant *Martasterites furcatus*.

Calcareous microfossils are generally present throughout the black shales, although foraminifers are often poorly preserved and of low diversity. Both upper Turonian and middle–lower Turonian microfossil assemblages were distinguished. In the latter interval the distinctive evolutionary radiation that occurs among the eproolithids, a calcareous nannofossil group, appears to be well represented by exceptionally well preserved (i.e., long rayed) specimens.

The bulk of the black shale sequence is Cenomanian in age. The preservation and abundance of the Cenomanian calcareous microfossils is better than at the other Leg 207 sites, although these remain spotty in distribution, particularly for the planktonic foraminifers. Fish scales are common, and a fish vertebra ~1 cm in diameter was recovered in Sample 207-1258B-45R-4, 75 cm (Fig. F9) (see “Lithostratigraphy,” p. 4).

A disconformity may be present in Cores 207-1258B-55R and 207-1258C-27R that separates the lower Cenomanian from underlying middle Albian black shales. Clay-rich beds of early Albian age below these shales yielded some of the best-preserved microfossils at the site, including nannofossils pristine in appearance and “glassy” planktonic foraminifers that compare well visually with Holocene assemblages. In addition, ammonites as small as 1 cm in diameter are abundant in some laminae.

The calcareous microfossil groups in combination allowed the base of Hole 1258C to be dated as early Albian (foraminiferal and nannofossil Zone KS13 and Subzone NC8a–NCb, respectively; the latter as correlated to substage by Bown et al., 1998 [figs. 5.2, 5.4]).

## Calcareous Nannofossils

Three holes at Site 1258 recovered primarily Paleogene–mid-Cretaceous sediments that generally contain common to abundant calcareous nannofossils of moderate to good preservation. These allowed for zonal or stage assignments that are summarized in Figure F10 and Tables T3 and T6. Core catcher samples were examined for all holes and supplemented as necessary by samples from the cores to further refine the zonal assignments. Major unconformities are observed separating the following sedimentary packages:

1. A thin veneer of middle Miocene ooze at the top of the hole or site above an expanded middle Eocene–lowermost Eocene calcareous sequence.
2. An expanded upper Paleocene chalk, on top of which the PETM was recorded, followed by an expanded lower and lowermost Paleocene chalky sequence.
3. An upper Maastrichtian chalk underlain by a thick chalky Maastrichtian–Campanian unit.
4. A Coniacian–Cenomanian black shale sequence, grading into a clay sequence of Albian age at the base.

From the above, hiatuses, unconformities, and/or condensed sequences may be derived for the following:

Miocene/Pleistocene contact (gap = 9 m.y.);  
Middle Eocene/Miocene contact (gap = 31.6 m.y.);  
Maastrichtian/Paleocene contact (gap = 0.2 m.y.);  
Turonian/Campanian contact (gap = 11 m.y.); and  
Albian/Cenomanian contact (gap = ~3 m.y.).

In the more detailed descriptions that follow, the assemblages and ages pertain to Hole 1258A unless noted otherwise.

Sample 207-1258A-1R-CC recovered a nannofossil assemblage of middle Miocene age (Zone NN7 of the Martini, 1971 scheme), including *Discoaster exilis*, *Discoaster variabilis*, *Discoaster challengerii*, and *Discoaster kugleri*. Samples 207-1258A-2R-CC to 4R-CC are of middle Eocene age (Zone NP15) as indicated by the presence of *Nannotetrina fulgens*, *Chiasmolithus grandis*, *Chiasmolithus gigas*, *Dictiococcites bisecta*, and *Ericsonia formosa*. The presence of *C. gigas* here and in Sample 207-1258B-2R-CC denotes Okada and Bukry (1980) Subzone CP13b (middle NP15); a specimen of *Chiphragmalithus calathus* in Sample 207-1258B-4R-CC is considered reworked.

Sections 207-1258A-5R-CC to 6R-CC contain a middle Eocene assemblage (Zone NP14) that includes *Sphenolithus radians*, *Zygrhablithus bijugatus*, *Discoaster barbadiensis*, *Discoaster sublodoensis*, and *Discoaster lodoensis*. The subjacent Sections 207-1258A-7R-CC to 8R-CC have an early Eocene age (Zone NP13), yielding *D. lodoensis*, *E. formosa*, and *S. radians*. Specimens of overgrown *Orthorhabdus tribrachiatus* at this level in Hole 1258B (Cores 207-1258B-7R and 8R) are considered reworked, as they lie well above the foraminiferal *Planorotalites palmerae* datum for the base of Zone P9 (see “**Planktonic Foraminifers**,” p. 14).

Based on the presence of *Discoaster tani nodifer*, *Discoaster saipanensis*, *S. radians*, *D. lodoensis*, and *Tribrachiatus orthostylus*, Sections 207-1258A-9R-CC to 13R-CC have been assigned an early Eocene age (Zone NP12). The underlying Samples 207-1258A-14R-CC to 15R-CC are of

earliest Eocene age (Zone NP10) based on the presence of *Discoaster multiradiatus*, *Toweius eminens*, *Campylosphaera eodela*, *Discoaster diastypus*, and *Rhomboaster* spp.

Relative to Hole 1258A, downhole offsets in Holes 1258B and 1258C of the boundaries of Zone NP10 are attributed to the fault that cut both holes. Faulting apparently reduced the stratigraphic section in Hole 1258A by ~20 m relative to Hole 1258B (see “[Composite Depths](#),” p. 21).

Samples 207-1258A-16R-CC to 22R-CC contain *D. multiradiatus*, *Discoaster mohleri*, *Neochiastozygus junctus*, and *Fasciculithus tympaniformis* and are thus of earliest Eocene to latest Paleocene age (Zone NP9). In that zone but above the P/E boundary in Cores 207-1258A-19R, 207-1258B-21R, and 207-1258C-8R, *N. junctus* and *Z. bijugatus* are abundant, whereas fasciculiths replace the latter as dominant taxa below the P/E boundary (see Bralower, 2002).

A nannofossil assemblage consisting of *D. mohleri*, *Heliolithus riedelii*, and *F. tympaniformis* in the absence of *D. multiradiatus* characterizes Sample 207-1258A-23R-CC as late Paleocene age (Zone NP8). A late Paleocene age (Zone NP7) is also assigned to Samples 207-1258A-24R-CC and 25R-CC based on the presence of *Chiasmolithus consuetus*, *Heliolithus kleinpellii* (Sample 24R-CC only), *Ellipsolithus macellus*, and *Discoaster splendidus*, along with common to abundant *D. mohleri*. *Discoaster mohleri*, however, is absent in Sample 207-1258A-26R-CC but *Fasciculithus involutus* (few), small *E. macellus*, and abundant large *Cruciplacolithus tenuis* (up to 10 µm long) denote Zone NP5.

Sample 207-1258A-27R-CC contains primarily *C. tenuis* but no fasciculiths and thus has an earliest Paleocene age (Zone NP2). This sample also yielded a rich reworked nannoflora of Maastrichtian age.

Samples 207-1258A-28R-CC to 32-CC yield nannofossil assemblages of late Maastrichtian age (Zone CC25 of the Sissingh, 1977, scheme) including *Micula murus* and *Arkhangelskiella cymbiformis*. In the expanded uppermost Maastrichtian section of Hole 1258B (Cores 207-1258B-30R and 32R), *Ceratholithoides kamptneri* is present in the absence of *M. murus* (i.e., in an order of first appearances opposite that given for “Tethyan-intermediate” province zones by Burnett [1998], figs. 6.6 and 6.7).

Sample 207-1258A-33R-CC is of early Maastrichtian age (Zone CC24) as indicated by the presence of *Reinhardtites levis*. Samples 207-1257A-34R-CC to 40R-CC contain an early Maastrichtian to late Campanian assemblage (Zones CC23 and CC22), including *Uniplanarius trifidum*, *R. levis*, *A. cymbiformis*, and *Uniplanarius sissinghi*. The subjacent Sample 207-1258A-41R-CC yielded *Reinhardtites anthoporus*, *Aspidolithus parvus constrictus*, *Micula concavata*, *Micula decussata*, and *Eiffellithus eximius* but no *Eprolithus floralis*, allowing an early Campanian age assignment (Zones CC20 to upper CC18).

The black shales of Hole 1258A underlie a sharp erosional contact with the overlying Campanian chalk. An impoverished flora of Turoonian age with *Radiolithus planus* and *Stoverius achylosus* is present in Samples 207-1257A-42R-CC to 44R-CC.

In Hole 1258B, the top of the black shales was encountered at a greater subbottom depth than in either Holes 1258A or 1258C. It is also the only one of the three that preserves the top of the sequence, which appears to be younger than in the other two holes. The upper strata in Hole 1258B are light tan and heavily burrowed (Sample 207-1258B-44R-2, 58 cm). A black-colored sample below that (Sample 207-1258B-44R-2, 64 cm) contains *Eiffellithus turriseiffelii* and *E. floralis* and is therefore no

younger than late Coniacian. A debris flow at Sample 207-1258B-44R-3, 96 cm, yielded abundant *M. furcatus*, a dissolution-resistant form normally rare in chalks but here possibly concentrated by dissolution. Other taxa include abundant *E. turriseiffelii*, *E. eximius*, *Gartnergo* cf. *costatum*, common to few *M. decussata*, a possible specimen of *Lithastrinus moratus*, and rare but well-preserved *Eprolithus eptapetalus*. Assuming the latter specimen is reworked, this somewhat mixed assemblage is considered to be Coniacian in age. Sample 207-1258B-44R-4, 19 cm, contains common *E. floralis*, *E. turriseiffelii*, and rare *E. eptapetalus* and is assigned to the Turonian. In Hole 1258C, the upper Turonian is well represented in Sample 207-1258C-15R-CC, which contains *E. eximius* and several specimens of *Quadrum gartneri*.

In all holes, a definite Cenomanian age (Zone CC10) is assigned to Samples 207-1257A-45R-CC to 49R-CC, based on the combined presence of *Corolithion kennedyi* and *Axopodorhabdus albianus*. Sample 207-1257A-50R-CC has a late middle–early late Albian age based on the absence of *E. turriseiffelii* and the presence of *Tranolithus orionatus* and *A. albianus*.

The Albian section was drilled deepest in Hole 1258C. Eiffelithids are absent in Sample 207-1258C-27R-CC, but *A. albianus* is present; therefore, the sample is referred to middle Albian Subzone NC9a. *Axopodorhabdus albianus*, in turn accompanied by *Prediscosphaera columnata*, *Rhagodiscus angustus*, *Microstaurus chiastus*, *E. floralis*, *Eprolithus apertior*, *R. planus*, and occasional *Watznaueria britannica* and *Heliolithus trabeculatus* range downhole to Sample 207-1258C-32R-CC and denote middle Albian Subzone NC9a.

*Prediscosphaera columnata*, few in number but found amidst rich and well-preserved Albian nannoflora, continue to the bottom of the hole in Sample 207-1258C-34R-CC. It is accompanied by *Rhagodiscus achlyostarius*, *R. angustus*, common *L. floralis*, and rare *Nannoconus truitti* and *Lapediocassis coronuta*. These date the assemblage and the bottom of the hole as early Albian (Subzone NC8a–NC8b).

### Planktonic Foraminifers

Planktonic foraminifer biostratigraphy at Site 1258 was based on a combination of core catchers from all three holes and samples taken from every section in Hole 1258A. Zonal assignments are summarized in Figure F10 and Tables T4, T7, and T8. Planktonic foraminifer Zone M9 through Albian Zone KS13 were identified in Hole 1258A along with significant breaks in the biozonation in the middle Oligocene–middle Miocene, middle Eocene–middle Oligocene, upper Danian, Santonian–lower Campanian, and upper Albian–lower Cenomanian. Planktonic foraminifers were present in nearly all samples but varied widely in preservation and abundance. Preservation was best in clay-rich parts of the Cenomanian–Turonian sequence and middle Albian, although foraminifers were difficult to extract and completely clean in the organic marls. Foraminifers in the light-colored bands in the organic marls were frequently filled with calcite spar. Good preservation was found in the Miocene, Oligocene, middle Eocene, and lower Danian, whereas preservation was moderate or poor in the chalk of the lower Eocene and Maastrichtian–Campanian sequences.

Sample 207-1258A-1R-1, 0–2 cm, contains a mixture of modern diatoms with Pleistocene planktonic foraminifers such as *Globorotalia tumida*. Pleistocene sediments are only a few centimeters thick and were nearly entirely washed off the core top in Hole 1258B, where surficial

foraminiferal sands are of middle Miocene age. Yellow calcareous ooze in Section 207-1258A-1R-1 contains a diverse middle Miocene assemblage that includes *Fohsella fohsi*, *Fohsella robusta*, *Menardella praemenardii*, *Globoconella miozea*, and *Dentoglobigerina altispira* and indicates middle Miocene Zone M9.

The top of Section 207-1258A-2R-1 contains an Oligocene assemblage assigned to the Subzone P21a/P21b boundary. Subzone P21b is represented in Section 207-1258A-2R-1 and Sample 2R-2, 50–53 cm, by a diverse assemblage containing *Globigerina angulisuturalis*, *Globigerina ouachitensis*, *Globoquadrina euapertura*, and *Globigerina ciperoensis* without *Chiloguembelina cubensis*. A similar assemblage is present in Sample 207-1258A-2R-3, 50–55 cm, but with abundant *C. cubensis*, indicating Subzone P21a.

Sample 207-1258A-2R-3, 50–55 cm, also contains abundant middle Eocene foraminifers belonging to Zone P12, including *Turborotalia pomeroli*, *Morozovella lehneri*, and *Acarinina bullbrooki*. In contrast, the next sample below this (Sample 207-1258A-2R-4, 50–55 cm) contains *Morozovella aragonensis* and *Guembelitrioides nuttali* without *Globigerinatheka kugleri*, which suggests Zone P10 of early middle Eocene age. Although the sample does not contain *Hantkenina*, it does contain *Clavigerinella eocanica*, which makes its first appearance just below the base of Zone P10. The presence of *A. bullbrooki* also suggests the sample cannot be older than latest Zone P9.

*Guembelitrioides nuttali* associated with *Clavigerinella akersi* and *C. eocanica* are present together as low as Sample 207-1258A-3R-5, 50–55 cm, which we suggest approximates the P9/P10 zonal boundary. Sample 207-1258A-3R-6, 50–54 cm, contains small specimens that may record the evolutionary origin of *G. nuttali* along with a typical lower middle Eocene assemblage that includes *M. aragonensis*, *Acarinina praetopilensis*, *Igorina broedermanni*, *Acarinina pentacamerata*, and *Subbotina inaequispira*.

Zone P9 occurs between Samples 207-1258A-3R-5, 50–55 cm, and 9R-2, 49–51 cm. *Globigerina lozanoi*, a species ancestral to the globigerinathekids, makes its last occurrence (LO) in Sample 207-1258A-5R-CC. Sample 207-1258A-6R-CC contains specimens of *M. aragonensis*, strikingly similar to modern *Globorotalia truncatulinoides*, as well as examples of *Pseudohastigerina micra* that are notably evolute and have more chambers in the final whorl than is typical for this species. Otherwise, the Zone P9 planktonic foraminifers are typical of tropical assemblages and include *A. pentacamerata*, *Acarinina aspenis*, *Planorotalites renzi*, and *G. lozanoi*. *Planorotalites palmerae* ranges between Samples 207-1258A-7R-CC and 9R-2, 49–51 cm, suggesting that these samples represent the lower part of Zone P9. Sample 207-1258A-9R-3, 45–47 cm, contains transitional forms between *P. renzi* and *P. palmerae* that have deeply lobate chambers without terminal spines. Transitional forms between *S. inaequispira* and clavigerinellids are present over an extended interval in Zone P9 between Samples 207-1258A-7R-CC and 8R-CC.

Zone P8 occurs in the interval from the extinction of *Morozovella formosa* between Samples 207-1258A-11R-2, 50–53 cm, and 11R-3, 50–53 cm, and the first appearance of *P. palmerae* between Samples 207-1258A-9R-3, 45–47 cm, and 9R-2, 49–51 cm. In Zone P8, there are a number of last appearances, including that of *Morozovella subbotinae* between Samples 207-1258A-10R-5, 48–50 cm, and 10R-4, 50–52 cm, and that of *Acarinina quetra* between Samples 207-1258A-9R-5, 50–53 cm, and 9R-6, 50–53 cm, just below the top of Zone P8. The first appearance of *A. pentacamerata* occurs between Samples 207-1258A-10R-1, 50–54

cm, and 10R-2, 51–56 cm. Typical species in Zone P8 include *A. quetra*, *M. aragonensis*, *Globigerina praecentralis*, and *M. subbotinae*.

The first occurrence (FO) of *M. aragonensis* between Samples 207-1258A-13R-7, 49–53 cm, and 13R-CC marks the base of Zone P7. A well-developed transition occurs in the base of Core 207-1258A-13R with the overlap of large five-chambered *Morozovella lensiformis* and even larger six- or seven-chambered *M. aragonensis*. Assemblages in Zone P7 include few to common *A. quetra*, *Morozovella gracilis*, *M. formosa*, *M. subbotinae*, *Acarinina wilcoxensis*, and *Acarinina coalingensis* with subordinate *M. lensiformis* and *Morozovella aequa*. Poor preservation in Zone P6 made it difficult to subdivide this zone with confidence using the FO of *M. formosa*. However the base of Zone P6 could be established between Samples 207-1258A-17R-CC and 18R-CC using the LO of *Morozovella velascoensis*, *Morozovella acuta*, and *Morozovella occlusa*. The P/E boundary is believed to be located in Core 207-1258A-19R in an interval of green claystone. Sample 207-1258A-19R-CC contains rare specimens of *Gavelinella beccariiiformis*, a benthic foraminifer that became extinct at the P/E boundary, suggesting that this sample is of late Paleocene age.

A thick Paleocene succession is found between Samples 207-1257A-19R-CC and 27R-CC. The Zone P4/P5 boundary can be located between Samples 207-1258A-20R-CC and 21R-CC based on the LO of *Globanomalina pseudomenardii*. We were not able to reliably subdivide Zone P4 owing to the near absence of *Acarinina subspherica* and *Parasubbotina variospira*. Assemblages characteristic of Zone P4 contain *M. acuta*, *M. velascoensis*, *Subbotina triangularis*, *Subbotina triloculinoides*, and *Igorina albeari*. *Parasubbotina varianta*, *Acarinina nitida*, *Morozovella passionensis*, and *M. aequa* are rare constituents in most samples. Core 207-1258A-26R contains a mixture of Zone P4 and Subzone P3a assemblages. *Praemurica uncinata* and *Morozovella praeangulata* are present, suggesting Zone P2 or Subzone P3a, but most samples also contain *G. pseudomenardii*, *M. velascoensis*, and acarininids, all of which are more typical of Zone P4 or younger assemblages.

Core 207-1258A-27R contains a lower Danian foraminifer assemblage between the core catcher and Sample 207-1258A-27R-3, 0–2 cm. A sample from the top of Core 207-1258A-27R yielded a mixed fauna of *Morozovella angulata*, *Eoglobigerina edita*, *Igorina pusilla*, and *G. pseudomenardii*. This last species is indicative of Zone P4, whereas the others are found in Zone P1 or P3. Hence, the top of Core 207-1258A-27R appears to contain an extensive collection of reworked species as seen in the overlying core. In contrast, Sample 207-1258A-27R-3, 0–2 cm, contains *Praemurica pseudoinconstans*, *Eoglobigerina eobulloides*, *S. triloculinoides*, and *Praemurica taurica* that together suggest Subzone P1c. The next sample below this, Sample 207-1258A-27R-4, 0–2 cm, includes *Woodringina claytonensis*, *E. eobulloides*, *Parvulorugoglobigerina eugubina*, and *P. taurica* in the absence of *S. triloculinoides*, suggesting a P $\alpha$  zonal assignment. Samples 207-1258A-27R-5, 112–114 cm, and 27R-CC have only a dwarfed fauna with *Guembelitra cretacea*, *P. eugubina*, *Parvulorugoglobigerina extensia*, and *P. taurica*, indicating Zone P $\alpha$ . The >150- $\mu$ m fraction in both samples contains only reworked Cretaceous species and benthics. Hence, Core 207-1258A-27R appears to contain a relatively complete sequence of biozones between the K/T boundary and Danian Subzone P1c. The apparently complete K/T section in Core 207-1258B-27R was not sampled in detail for foraminifers other than to confirm the Maastrichtian age of the core catcher, but lithostratigraphy suggests this core forms part of a spliced section between Cores 27R and 28R.

Maastrichtian foraminifer assemblages were identified between the top of Core 207-1258A-28R and 33R-CC. Tan and white chalk clasts at the top of Core 207-1258A-28R were sampled and found to contain only upper Maastrichtian species (Zone KS31) based on the occurrence of *Abathomphalus mayaroensis* in the >250- $\mu$ m fraction and the absence of Danian species from the <150- $\mu$ m fraction. Zone KS31 extends to Sample 207-1258A-29R-CC given the continued rare occurrence of *A. mayaroensis*. Typical species in the upper Maastrichtian include *Globotruncanita stuarti*, *Rugoglobigerina rugosa*, *Rugoglobigerina rotundata*, *Abathomphalus intermedius*, and *Pseudoguembelina palpebra*. Zone KS30 was identified in Samples 207-1258A-30R-CC to 33R-CC. Samples 207-1258A-30R-CC to 32R-CC all contain *Contusotruncana contusa*, suggesting that they belong to the *Racemiguembelina fructicosa*–*C. contusa* Subzone of Zone KS30. Assemblages in Zone KS30 are composed in part of *C. contusa*, *R. rugosa*, *Gansserina gansseri*, and *Rugoglobigerina hexacamerata* with subordinate *Rugotruncana subcircumnodifer*, *Pseudoguembelina costillifera*, and *Heterohelix globulosa*. Below the FO of *C. contusa*, assemblages change to include few to common *G. stuarti*, *Globotruncana arca*, *Globotruncanella pschadae*, and *Rosita fornicata*. Planktonic foraminifers were absent from Samples 207-1258A-34R-4, 0–2 cm, to 41R-CC.

Cenomanian and Turonian foraminifers are present between Samples 207-1258A-42R-CC and 49R-CC. These samples have mostly low species diversity, with few taxa diagnostic of particular zones. An assemblage of *Whiteinella baltica*, *Whiteinella inornata*, *Heterohelix moremani*, *Hedbergella delrioensis*, and *Hedbergella planispira* is present in Samples 207-1258A-42R-CC to 43R-CC and between Samples 45R-CC and 49R-CC. *Globigerinelloides caseyi* tends to become more common downhole, whereas biserial foraminifers tend to become less so. An interval with extremely small foraminifers is present in Sample 207-1258A-44R-CC, an interval that was also noted at similar depths in Holes 1258B and 1258C, which probably corresponds to the K/T boundary. The first distinctive foraminifer datum occurs in Sample 207-1258A-47R-CC with the occurrence of both *Rotalipora globotruncanoides* and *Praeglobotruncana delrioensis*, both suggesting a Cenomanian age.

A distinct change in the composition of the fauna occurs between Samples 207-1258A-49R-CC and 50R-CC. The presence of *Ticinella primula* and *Biticinella breggiensis* in Sample 207-1258A-50R-CC provides a date in the *B. breggiensis* Zone of the late middle Albian (Zone KS14) and suggests that much if not all of the upper Albian and possibly part of the lower Cenomanian is missing at Site 1258. Albian sediments are also present between Cores 207-1258C-27R and 34R. The contact between the *B. breggiensis* Zone and the underlying *T. primula* Zone occurs between Samples 207-1258C-27R-1, 85–89 cm, and 27R-2, 89–92 cm, which includes the first appearance of *B. breggiensis*. Species present in the *B. breggiensis* Zone include *Globigerinelloides bentonensis*, *T. primula*, *Ticinella roberti*, and *Hedbergella simplex*. Four-chambered hedbergellids are also present, some of which show a pattern of aligned pustules reminiscent of the lower Cenomanian species *Costellagerina lybica*. These costellate species continue into the underlying *T. primula* Zone and are joined by *Clavihedbergella subcretacea*, *Clavihedbergella moremani*, *Ticinella madecassiana*, and *Ticinella raynaudi*, which represent Zone KS13. The assemblage dominated by various species of *Ticinella* sp. continues to the bottom of Hole 1258C in Sample 207-1258C-34R-CC.

## Radiolarians

Radiolarians were found in most of the Tertiary and Cretaceous sediments at Site 1258, but were abundant and adequately preserved for identification and age assignment only in particular stratigraphic intervals (i.e., middle Eocene, Campanian, and Albian). Core catcher samples were examined systematically from Hole 1258A. A limited number of samples were also taken from Holes 1258B and 1258C, mainly to examine the presence or absence of radiolarians in the Cretaceous sediments. Occurrences are summarized in Figure F10.

Radiolarians appear to be absent in the veneer of Miocene sediments at the top of the site. On the other hand, they are abundant and well preserved in Eocene sediments, which also contain some diatoms and occasionally siliceous sponge spicules. Cores 207-1258A-2R to 4R yielded middle Eocene radiolarian assemblages. They are assigned to Zones RP11 and RP12 based on the presence of *Theocotyle conica* and *Thyrsocyrtis triacantha* in Sample 207-1258A-2R-CC and *Dictyoprora mongolfieri* and *Thyrsocyrtis tensa* in Sample 207-1258A-4R-CC. Both *T. tensa* and *T. triacantha* were observed in Sample 207-1258A-2R-CC, but the former species outnumbers the latter. As the evolutionary transition of *T. tensa* to *T. triacantha* is approximately synchronous with the lower limit of Zone RP12, the boundary between Zones RP11 and RP12 is placed in Sample 207-1258A-3R-CC.

Radiolarians are rare and poorly preserved (often transformed into zeolites) farther below. The presence of *Buryella clinata* in Samples 207-1258A-10R-CC and 12R-CC suggests an assignment to Zones RP8–RP10 (lower part). Samples 207-1258A-14R-CC and 16R-CC are assigned to Zones RP7–RP8 based on the presence of *Pterocodon ampla*, *Podocyrtis papalis*, and *Thyrsocyrtis tarsipes*. Farther downhole, radiolarians are rare and poorly preserved in general. However, *Buryella tetradica* was observed in Samples 207-1258A-23R-CC and 24R-CC and allows assignment to Zones RP5–RP8.

Age-diagnostic Cretaceous radiolarians were observed in Cores 207-1258A-36R and 40R and 207-1257C-10R. Preliminary identifications were made on board on the basis of observations with a stereoscopic microscope, but they will need to be confirmed with the use of the scanning electron microscope. The assemblage in Sample 207-1258A-36R-CC is characterized by the presence of the Campanian species *Amphipyndax pseudoconulus* (Sanfilippo and Riedel, 1985), whereas the presence of the marker species *Crucella cachensis* in Sample 207-1258A-40R-CC allows an assignment to the lower Turonian Zones *C. cachensis* (Erbacher and Thurow, 1998) or *Alievum superbum* (O'Dogherty, 1994) or to a higher interval.

Pyritized Cretaceous radiolarians are present in the lowermost cores of Hole 1258C. As *Thanarla broweri* was observed in both Samples 207-1258C-32R-CC and 34R-CC and *Triactoma paronai* in the latter sample, they are assigned to the *Mallanites romanus* Subzone of O'Dogherty (1994).

## PALEOMAGNETISM

Shipboard and shore-based paleomagnetic measurements from Holes 1258A, 1258B, and 1258C potentially resolved Chrons C33r–C29r of Campanian–Maastrichtian age and Chrons C26r–C20r of late Paleocene–middle Eocene age.

## Shipboard and Shore-Based Procedures and Data Filters

Details are given in “Paleomagnetism,” p. 16, in the “Explanatory Notes” chapter of the standard shipboard analysis using the pass-through cryogenic magnetometer, the filtering and polarity interpretation procedures of this shipboard data, and the shore-based progressive demagnetization of discrete minicores. Shipboard measurements of each section were at natural remanent magnetization (NRM), 10- and 15-mT alternating-field (AF) demagnetization steps, with an additional 20-mT step applied if core flow permitted (Table T9). As at the other sites drilled during Leg 207, the 10-mT step appeared to be effective in removing extraneous overprints induced during the drilling process. In general, the additional 20-mT demagnetization step did not significantly alter the magnetic directions obtained at the prior 15-mT step for the majority of the sediment types. The black shale intervals of the Cenomanian–Santonian displayed magnetizations near the background noise level of the shipboard cryogenic magnetometer, are commonly highly fractured or biscuited, and are within the Long Cretaceous Normal Polarity Superchron C34n. We decided to leave the majority of the black shale cores intact rather than partially demagnetize the sediments without the prospect of obtaining useful shipboard information.

Oriented paleomagnetic cylinders were drill-pressed from all Campanian–middle Eocene sediments from Hole 1258B for combined progressive AF and thermal demagnetization at the magnetic-shielded room facility at the University of Munich, Germany. Additional postcruise sampling of sediments from Holes 1258A and 1258B enabled 1-m resolution of most polarity zone boundaries and replicated the majority of the polarity succession in the adjacent hole. The magnetic polarity of each minicore was interpreted from an examination of the movement of its magnetic vector during progressive demagnetization (see “Paleomagnetism,” p. 16, in the “Explanatory Notes” chapter) (Table T10). These shore-based measurements enabled resolution of removed and characteristic components of magnetization and significantly modified the tentative shipboard polarity interpretations from all facies.

One or two faults cause a relative displacement of strata as much as 20 m among the holes of Site 1258; therefore, adjustments of mbsf depth to meters composite depth (mcd) is important to compare stratigraphy and paleomagnetic results (left columns of Figs. F11, F12). The biostratigraphy for this composite stratigraphy is an average of the zonations for Holes 1258A and the combined zonations Holes 1258B and 1258C, but the relative placements of zonal boundaries were not always consistent on this composite depth scale. Another problem for exact biostratigraphic calibration of the polarity zones was that the foraminifer and calcareous nannofossil zones in the holes did not always correspond to their proposed correspondence (and associated calibration to the magnetic polarity timescale) on the reference timescale used during Leg 207 (Fig. F5, p. 59, in the “Explanatory Notes” chapter). These uncertainties in biostratigraphic constraints imply that some assignments of polarity chrons to the observed polarity zones might undergo future modification.

---

T9. Shipboard cryogenic magnetometer analyses, p. 98.

---



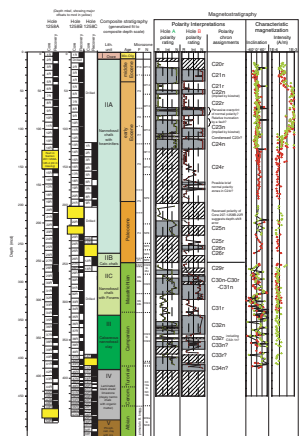
---

T10. Polarity interpretations and characteristic directions, p. 99.

---

F11. Shipboard paleomagnetic data, p. 57.

F12. Shore-based magnetostratigraphy, p. 58.



## Paleomagnetic Behavior and Interpretations of Magnetostratigraphy

### Lower and Middle Eocene

A reddish brown carbonate chalk predominates from ~40 to 100 mcd in the composite stratigraphy of Site 1258. Compared to other Paleocene–Eocene intervals, this reddish zone displays a relatively high magnetic intensity and susceptibility (Fig. F11). Applying 5- to 10-mT AF demagnetization removed a steep positive inclination that probably represents a drilling-induced overprint. After this initial change, the magnetization of the reddish sediments displayed no significant difference in the intensity and inclination upon 15- or 20-mT AF demagnetization steps during shipboard analyses (Fig. F11). However, shore-based thermal demagnetization of the extensive minicore suite above 150°C was very effective in removing a normal polarity overprint, and samples with reversed polarity displayed an increasing magnetic intensity through 200°C followed by a univectorial decay. Characteristic directions were computed for each sample from the 250°–400°C or 450°C thermal demagnetization steps, and the polarity pattern was duplicated in detail in Holes 1258A and 1258B (Fig. F12).

Other than this zone of reddish brown chalk spanning the lower (Ypresian)–middle (Lutetian) Eocene transition, the Eocene is primarily greenish white foraminifer nannofossil chalk. Magnetic intensity of these sediments after 15-mT AF demagnetization was generally in the range of  $10^{-5}$ – $10^{-3}$  A/m, but a large number of shipboard measurements were filtered out by the lower limit of significant background noise at  $3 \times 10^{-5}$  A/m (Fig. F11). These chinks yielded a relatively well defined suite of polarity zones during shore-based thermal demagnetization of minicores (Fig. F12).

Polarity chron assignments to each polarity zone are based on average paleontological ages. The uppermost zone of reversed polarity in nannofossil Zone NP15 is constrained to be Chron C21r, and the reversed polarity zone at the Paleocene/Eocene boundary is constrained to be Chron C24r. Between these two zones, the polarity pattern in each hole closely matches Chrons C24r–21n, including resolution of the brief reversed polarity subchrons within Chrons C24n and C23n. The only discrepancy is the apparent width of the reversed polarity zone that is interpreted to correspond to Chron C23r is significantly thinner in Hole 1258A relative to Hole 1258B, whereas C24n is thicker. The same offset is observed in the shipboard assignment of the boundary between foraminifer Zones P8 and P7, which suggests the possibility of another fault in Hole 1258A at this level that may have displaced a significant portion of the Chron C23r–C24n interval.

The extensive minicore suite indicates that Site 1258 was slightly south of the paleoequator throughout the early Eocene. Zones of normal polarity are characterized by a predominance of low-angle negative inclinations, and reversed polarity zones are associated with positive characteristic inclinations. This southern paleolatitude during early Eocene was also documented at other Leg 207 sites.

### Paleocene

The greenish white foraminifer nannofossil chalk of the Paleocene is generally characterized by relatively weak intensity and susceptibility. Magnetic intensity of the greenish white chalk after 15-mT AF demag-

netization was generally in the range of  $10^{-5}$ – $10^{-3}$  A/m, with a large number of measurements below the noise limit of the long-core cryogenic magnetometer (Fig. F11). The composite polarity zone pattern obtained from the analyses of postcruise minicores is consistent with Chrons C26r–C25n, although a reliable assignment is inhibited by the discrepancy with foraminifer and nannofossil zonal ages in the lower portion (Fig. F12).

### **Campanian–Maastrichtian**

The uppermost Maastrichtian contains reddish brown chalk layers that are similar to the Eocene reddish chalk interval in their high intensity and susceptibility and in their persistent normal overprints during AF demagnetization. Thermal demagnetization of minicores yielded reversed polarity in the uppermost Maastrichtian in both Holes 1258A and 1258B, which is constrained by nannofossil Zone CC26 to be Chron C29r (Fig. F12).

The underlying chalk to calcareous nannofossil clay of the Maastrichtian–Campanian is characterized by weak magnetic intensity and susceptibility (Fig. F11). The magnetic intensity of many minicores approached the noise level of the cryogenic magnetometer at the Munich laboratory upon heating beyond 200°C. The weak magnetizations added uncertainty to several polarity interpretations but clustering of normal and reversed polarity samples in both holes allowed a generalized identification of the main polarity zones (Fig. F12). However, a reliable assignment of polarity chronos to these zones is inhibited by lack of detailed biostratigraphic constraints. The general pattern and age assignments are consistent with the top of Chron C34n to C30n, but these tentative interpretations may be modified after further paleontological studies.

In summary, Site 1258 yielded preliminary magnetostratigraphic patterns that, when combined with the shipboard paleontological constraints, can be unambiguously correlated to the biomagnetic polarity timescale for the majority of the late Paleocene–earliest middle Eocene. The polarity chron assignments in the Upper Cretaceous sediments are more ambiguous. The high-resolution magnetostratigraphy of the relatively expanded lower Eocene and its continuous extension into the lowermost middle Eocene section provides an important reference section for future cycle and isotope stratigraphy studies.

## **COMPOSITE DEPTHS**

Coring at Site 1258 extended to a total depth of 485 mbsf, and a composite section was established for much of the cored interval. Magnetic susceptibility, gamma ray attenuation (GRA) bulk density, and noncontact resistivity (NCR) data were collected with the multisensor track (MST) at 2.5-cm intervals on all whole-core sections. Natural gamma ray (NGR) data were collected at 7.5-cm intervals on all whole cores at Site 1258. In addition, color spectral reflectance data were collected at 2.5-cm intervals on all split cores. The magnetic susceptibility data provided the primary data set used to correlate between holes above the Cretaceous black shale sequences. In the black shales, NGR data provided better core-to-core comparisons.

## Composite Section

The depth offsets that define the composite section for Holes 1258A, 1258B, and 1258C are given in Table T11. Excellent RCB recovery in the upper portions of Holes 1258A and 1258B provided continuous core overlap from 35 mcd (top of Core 207-1258A-4R) to ~210 mcd (Section 207-1258A-20R-5, 122 cm), ~10 m below the P/E boundary. Data used to construct the composite section over this interval are presented in Figures F13 and F14. Faulting and/or slumping in Hole 1258A in the lower Eocene sequence resulted in 22 m not recovered in Hole 1258A (~130–150 mcd) that was recovered in Holes 1258B (Cores 207-1258B-14R, 15R, and top of 16R) and 1258C (from the lower part of Core 207-1258C-1R to the middle of Core 4R). Similar faulting/slumping resulted in ~11 m of missing section in Hole 1258B (between Cores 207-1258B-21R and 22R or possibly in Core 22R) (~205–215 mcd) that were recovered in Cores 207-1258A-20R and/or 21R from Hole 1258A.

Moderate core recovery and further faulting/slumping below the P/E boundary made it impossible to construct a continuous composite depth scale for the remainder of Site 1258. In some intervals below the P/E boundary, reliable correlations were still possible among the holes at Site 1258 (i.e., features on the MST profiles could be matched between holes) (Fig. F15). In other intervals, distinct core-to-core tie points across the holes were not obvious and correlations were based on similarities in overall trends rather than by matching unique structures in the MST profiles. Furthermore, below the P/E boundary, many coring gaps were not spanned and the absolute depth of the cores in this interval cannot be accurately determined (e.g., see alignment of the Cretaceous black shales in Fig. F16). Rather, the cores “hang” in the composite depth scale linked to correlative cores in other holes but not to those above or below. Improvements in the biostratigraphic and magnetostratigraphic record postcruise should result in refinements to the composite depth scale in many intervals, including the Cretaceous black shales.

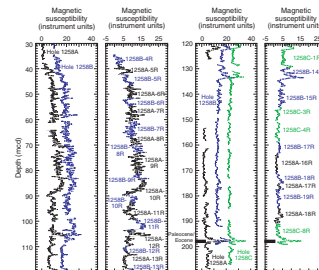
The periodic variability in the Eocene magnetic susceptibility data at Site 1258 will provide a good basis for postcruise cyclostratigraphic studies. Age control is excellent, with well-defined paleomagnetic datums in the section (e.g., the top of Chron C21n and the base of Chron C22r) (see “Paleomagnetism,” p. 18). Preliminary investigation suggests the dominant periodicities of the magnetic susceptibility data are Milankovitch in nature.

## Splice Record

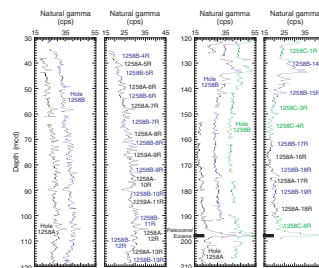
Following construction of the composite depth section at Site 1258, a single spliced record was assembled for the aligned cores in the interval from 35 to 210 mcd. Intervals having significant disturbance or distortion were avoided where possible when making the splice. As explained above, moderate to poor recovery below the P/E boundary prevented us from continuing the splice record below ~210 mcd. When utilizing this splice as a sampling guide, it is advisable to overlap a few decimeters from different holes during sampling to accommodate anticipated ongoing development of the depth scale. The reason for this approach is that distortion of the cored sequence can lead to stretching or compression of sedimentary features. However, at crossover points along the splice (Table T12), care was taken to align highly identifiable features from cores in each hole. Postcruise work will establish a detailed corre-

T11. Composite depth offsets, p. 100.

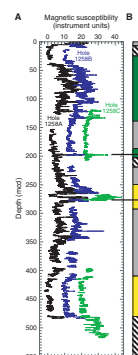
F13. Composite and spliced magnetic susceptibility, p. 60.



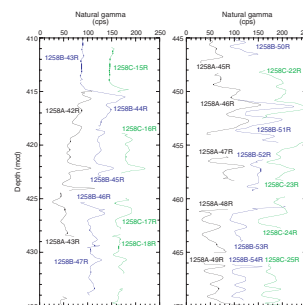
F14. Composite and spliced NGR data, p. 61.



F15. Magnetic susceptibility data, p. 62.



F16. NGR data, p. 63.



lation between holes by establishing a revised meters composite depth (rmcd) scale that allows differential stretching and squeezing in cores.

## SEDIMENTATION RATES

### Age-Depth Model

An age-depth model was established for Site 1258 by combining all available biostratigraphic and magnetostratigraphic datums of Hole 1258A (Fig. F17). The diagram was constructed by plotting highest and lowest possible ages for selected paleontological samples examined shipboard against the depth of those samples (Table T13). In addition, the age and depth of magnetic reversals recognized shipboard (Table T14) are also plotted.

Moderate to poor preservation and even absence of the microfossils limit the biostratigraphic age estimates in parts of the succession investigated. In particular, the Turonian interval was difficult to date using shipboard samples. Reliable magnetostratigraphic datums are restricted to the middle Eocene–early Paleocene (Table T14).

### Sedimentation Rates

Linear sedimentation rates (LSRs) in Hole 1258A varied between 10 and 15 m/m.y (Table T15). These rates are typical for pelagic chalks and oozes, lithologies that characterize the Eocene–Campanian interval (lithostratigraphic Units II and III) (see “**Lithostratigraphy**,” p. 4). Hiatuses separate the sequences into four segments with approximately constant sedimentation rates (Fig. F17). The Neogene (0–5 mbsf), with few biostratigraphic datums, is not included in the subsequent discussion:

1. middle Eocene–late Paleocene (5–245.32 mbsf): LSR = ~15 m/m.y.
2. early Paleocene (245.32–249.8 mbsf): lower rates but little age control, precluding more precise calculations.
3. Maastrichtian–late Campanian (249.8–385.45 mbsf): LSR = ~10 m/m.y.
4. Turonian–Albian (385.45–446.22 mbsf [base of Hole 1258A]): LSR = 3 m/m.y.

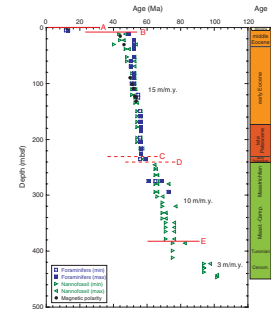
Mass accumulation rates (MARs) were calculated from LSRs and averaged dry bulk density data of the four intervals discussed above (see “**Physical Properties**,” p. 30) (Table T15). These MAR calculations may allow for better assessment of the sedimentation processes because the influence of sediment compaction has been taken into account. Eocene–late Paleocene MAR values are 1.7 g/cm<sup>2</sup>/k.y., the highest values calculated at this site. Paleocene values are 1.5 g/cm<sup>2</sup>/k.y., whereas values of 1.6 g/cm<sup>2</sup>/k.y. were calculated for the Late Cretaceous interval excluding the black shale facies (Unit IV [249–442 mbsf]).

### Hiatuses

The succession is characterized by intervals of approximately constant sedimentation rates separated by apparent breaks. These breaks suggest five distinct hiatuses, periods of slow deposition, erosion

T12. Splice tie points, p. 101.

T17. Age-depth plot, p. 64.



T13. Nannofossil and foraminifer datums, p. 102.

T14. Magnetostratigraphic datums, p. 104.

T15. LSRs and MARs, p. 105.

events, or a combination of these (see letters A–E in Fig. F17). Each of these hiatuses spans at least 1 m.y., based on biostratigraphic dating (see “[Biostratigraphy](#),” p. 10). Hiatus A covers ~10 m.y. (Pleistocene–late Miocene), Hiatus B spans ~32 m.y. (middle Miocene–late Eocene), Hiatus C covers ~1 m.y. (early Paleocene; nannofossil Zone NP 3), Hiatus D spans 1 m.y. (earliest Paleocene), and Hiatus E spans 15 m.y. (early Campanian–Turonian).

## ORGANIC GEOCHEMISTRY

Concentrations of inorganic carbon (IC) and TOC were determined on sediments from Holes 1258A, 1258B, and 1258C. Organic matter atomic carbon/nitrogen (C/N) ratios and Rock-Eval pyrolysis analyses were employed to assess the type of organic matter contained in the sediments. Routine monitoring of interstitial gas contents of the three holes was performed for drilling safety and pollution prevention, and possible microbial activity was investigated from headspace gas contents of Hole 1258A.

### Inorganic and Organic Carbon Concentrations

Concentrations of inorganic carbon vary from 0.7 to 11.5 wt% at Site 1258 (Table T16). These concentrations are equivalent to 6–96 wt% sedimentary CaCO<sub>3</sub>, assuming that all of the carbonate is present as calcite or aragonite. All five lithostratigraphic units at this site (see “[Lithostratigraphy](#),” p. 4) contain CaCO<sub>3</sub> but show differences in average concentrations related to their facies. Units I and II are strongly carbonate-dominated fine-grained sediments having concentrations in the range of 40–80 wt%. The average carbonate content declines in Unit III to 20–40 wt%. The black shales in Unit IV average ~50 wt% but have a marked layer-by-layer scale variation between 4 and 96 wt%. This variability relates to lithologic changes, mainly the alternating presence of abundant calcite-enriched laminae between more clay-dominated black shale intervals. In Unit V, carbonate content averages 15.5 wt% and ranges between 6 and 24 wt%.

TOC concentrations of the five lithostratigraphic units at Site 1258 have a wide range. The sediments of Units I–III contain <0.7 wt% TOC (average = 0.1 wt% TOC) (Table T16). The sediments of Unit IV have an average TOC concentration of 7.9 wt% but vary widely between 0.1 and 28.3 wt%. In strong contrast to the age-equivalent unit at Site 1257, the calcareous mudstones that compose Unit V at Site 1258 have much higher TOC values, ranging from 2.2 to 5.4 wt% (average = 4.2 wt%). An unusually high TOC of 36.6 wt% was measured in Sample 207-1258C-31R-2, 74–75 cm, in Unit V, which is a piece of charcoal embedded in surrounding shale (see Table T16).

### Organic Matter Source Characterization

Atomic C/N ratios were employed to help identify the origins of organic matter in sediments at Site 1258. Most of the C/N values in organic-lean Units I–III are low (Table T16) and are below the range typical of fresh algal organic matter (4–10) (Meyers, 1997). These values are probably an artifact of low TOC concentrations combined with the tendency of clay minerals to sorb ammonium ions generated during degradation of organic matter (Müller, 1977). Some values are artificially ele-

---

T16. Carbon and nitrogen, p. 106.

vated because the low concentrations of C and N are near the limits of detection of the elemental analyzer.

The C/N ratios of the black shales in Unit IV average 31.2, which is a value typical of land-plant organic matter but is also common to Cretaceous black shales (Meyers, 1997). A van Krevelen-type plot of hydrogen index (HI) and oxygen index (OI) values (Fig. F18) indicates that the black shales in Unit IV contain Type II (algal) organic matter. High HI and low  $T_{\max}$  values ( $\sim 400^{\circ}\text{C}$ ) like those found in the black shales (Table T17) are characteristic of thermally immature, relatively well preserved marine organic matter (Espitalié et al., 1977; Peters, 1986). Consequently, the elevated C/N values that mimic those of land-derived organic matter are likely to be the result of partial alteration of marine organic matter. A probable scenario is that nitrogen-rich components are preferentially degraded during sinking of organic matter to the seafloor, thereby elevating the C/N ratio of the surviving organic matter (Twichell et al., 2002).

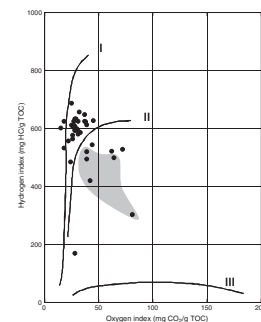
Organic matter in Unit V yields slightly lower HI values than those found in Unit IV, whereas the OI values remain similar. The C/N values of Unit V vary from 18.2 to 30.1 (average = 25.8), which is too high for unaltered marine organic matter. This unit seems to contain mostly marine but also some terrestrial organic matter that represents a mixture of Types II and III. This mixture can be inferred from the lower HI values and their cluster in Figure F18 as well as from the observation of charcoal and wood particles (see “Lithostratigraphy,” p. 4). The average  $T_{\max}$  value of  $418^{\circ}\text{C}$  for Unit V is higher than that in Unit IV, which can be explained by the mixed organic matter type in Unit V (i.e., namely by the minor contribution of terrestrial organic matter). On the other hand, it cannot be ruled out that the observed difference in  $T_{\max}$  values might also indicate overall poorer conditions of organic matter preservation in Unit V as discussed previously for the age-equivalent sediments of Unit V at Site 1257 (see “Organic Matter Source Characterization,” p. 23, in “Organic Geochemistry” in the “Site 1257” chapter).

### Interstitial Gas Contents

Concentrations of interstitial gases in lithostratigraphic Units I–III at Site 1258 were low but increased in Units IV and V. Gas voids were not observed, but some cores from Unit IV showed minor amounts of degassing when brought on deck. Small gas bubbles were visible through the core liner for a short time until the cores adjusted to the surrounding warm temperature and low pressure conditions. A faint odor of hydrogen sulfide was noticeable in cores from organic matter-rich Units IV and V but to a lesser extent than described at Site 1257 (see “Interstitial Gas Contents,” p. 23, in “Organic Geochemistry” in the “Site 1257” chapter).

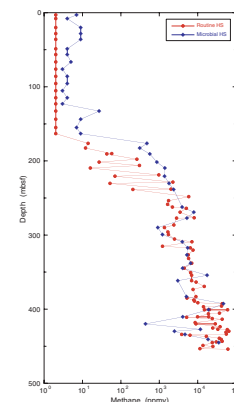
Headspace gas results from routine safety monitoring and the special microbial gas study are very similar (Fig. F19). Methane was at background levels ( $<5$  ppmv) in the upper part of the sequence and slowly but continuously increased until  $\sim 220$  mbsf, where concentrations exceeded 1000 ppmv for the first time. Methane concentrations thereafter continued to increase slowly in a more or less linear manner until the top of the black shales of Unit IV was penetrated at  $\sim 390$  mbsf. Here, the methane yield increased from  $\sim 10,000$  to 43,300 ppmv and ethane was recorded for the first time in concentrations  $>100$  ppmv (Table T18). Methane concentrations continued to increase with depth and

F18. Rock-Eval van Krevelen-type diagram, p. 65.



T17. Rock-Eval pyrolysis, p. 111.

F19. Headspace gas and microbial methane concentrations, p. 66.



T18. Headspace analyses of interstitial and microbial gases, p. 112.

reached a maximum of 65,000 ppmv at 430 mbsf and then slowly declined to ~30,000 ppmv at 482 mbsf in the last core taken. The absolute values of ethane and propane were relatively low compared to the yields of methane, but they also seemed to show a depth-related increase. The natural gas analyzer (NGA) was employed to monitor higher molecular weight volatile compounds like butane, pentane, and hexane, which were present in traces below 425 mbsf (Table T19). The latter compounds are usually not considered to be associated with microbial activity (Claypool and Kvenvolden, 1983). At Site 1257, high methane/ethane ratios and the absence of measurable amounts of higher molecular weight volatile hydrocarbons indicated that the methane was biogenic, rather than thermogenic, in origin. For Site 1258, the situation is more complicated, as it seems that both microbial and thermogenic gases were present. Another difference between the two sites is that the ratio of methane to ethane continued to stay relatively low throughout Unit V at Site 1258. The lower ratio could be explained by the higher amounts of organic carbon in Unit V, which potentially provided a better substrate for microbial activity than in Unit V at Site 1257, or it could indicate migration of gases into this unit from deeper in the section. Because of the possible presence of thermogenic gases, gas monitoring was performed on all three holes drilled at Site 1258.

A point for further consideration would be the potential at Site 1258 for gas hydrate formation or preservation, as it is located at a water depth of 3192 m. The ~450-mbsf drilling depth places the organic-rich Units IV and V in the gas hydrate stability zone (Claypool and Kaplan, 1974) over a rather wide temperature range. Interstitial chlorinity decreases in Units IV and V (see “**Inorganic Geochemistry**,” p. 26), which is often an indicator of hydrate decomposition. In contrast, results from downhole logging (see “**Downhole Logging**,” p. 33) do not provide any supporting evidence for the presence of gas hydrates either in Unit IV or V. Resistivity logs also strongly contradict the observation of lowered interstitial chlorinity for Unit V. Nevertheless, it cannot be completely ruled out that gas hydrates may have been present in Units IV and V during the past and have recently dissociated so that only a relict signal (i.e., in the pore water) has remained. It would be potentially useful to analyze the oxygen isotopic composition of pore water or of newly overgrown carbonate cements in the critical intervals, as gas hydrate formation is known to increase the  $\delta^{18}\text{O}$  value of pore water (e.g., Matsumoto and Borowski, 2000).

## INORGANIC GEOCHEMISTRY

We collected interstitial water from 38 samples at Site 1258: 24 from Hole 1258A (1.45–361.53 mbsf), 12 from Hole 1258B (133.80–448.27 mbsf), and 2 from Hole 1258C (462.52–483.55 mbsf). The samples from all three holes were taken to constitute a single depth profile. However, slight differences in lithology may cause minor breaks in concentration-depth gradients of some chemical parameters. An incomplete data set exists for Sample 207-1258A-37R-2, 110–120 cm, and no data exist for Sample 207-1258B-43R-2, 110–120 cm, because of low and zero interstitial water yields, respectively (Table T20).

Alkalinity, chloride, ammonium, and silica were determined by standard shipboard procedures (see “**Inorganic Geochemistry**,” p. 31, in the “Explanatory Notes” chapter). The major ions Na, K, Mg, and Ca

---

T19. NGA analyses of interstitial and microbial gases, p. 114.

---

---

T20. Interstitial water analyses, p. 115.

---

were analyzed by inductively coupled plasma–atomic emission spectroscopy (ICP-AES) after 50-fold sample dilution with deionized water. The minor components Li, B, Si, Fe, Mn, and Sr were determined by ICP-AES from 10-fold diluted interstitial water samples. From the minor component dilution, we determined sulfate from total sulfur by ICP-AES. Calibration and quality control were performed using appropriate calibration solutions and spiked International Association for the Physical Sciences of the Ocean (IAPSO) seawater standards. Details of the methods, including the emission lines used for analysis, are given in “*Inorganic Geochemistry*,” p. 31, in the “Explanatory Notes” chapter. Results of the chemical analyses are presented in Table T20 and Figure F20.

### Black Shales as a Diagenesis Bioreactor

Interstitial water chemistry at Site 1258 is dominated by the presence of black shales and associated organic matter–rich sediments. These sediments are of Turonian–Albian age (lithostratigraphic Unit IV [~390–450 mbsf]). Sulfate concentrations approach zero at the top of lithostratigraphic Unit IV (see Fig. F20F), and the gradient from the top of Unit IV to the sediment/water interface is almost linear. These observations suggest the following:

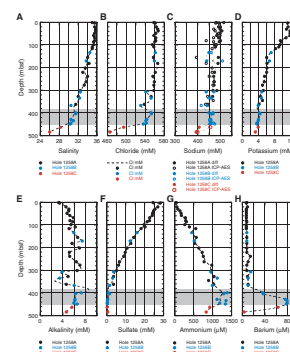
1. Almost 100 m.y. after Unit IV was deposited, the organic matter–rich sediments continue to provide a suitable substrate for ongoing microbial activity.
2. Sulfate reduction is of minor importance at shallower depth intervals.
3. The resulting downhole profile is controlled by the existence of one major stratigraphic sink (Unit IV) and simple compensatory downward diffusion from the sediment/seawater interface.

We interpret this situation to reflect minimal accumulation of sediments younger than middle Eocene at Site 1258 (Fig. F10). Unfortunately, the two samples that we collected from the Albian phosphatic calcareous claystones at the base of Hole 1258C (lithostratigraphic Unit V) do not lie far enough below Unit IV to determine whether the black shale sequence is also supplied by the diffusion of sulfate from below (Fig. F20F) as is the case at Site 1257.

At Site 1258, we detected no smell of hydrogen sulfide during core-splitting procedures on the catwalk. Occasionally, however, an H<sub>2</sub>S smell was detected from interstitial water whole rounds taken from lithostratigraphic Unit III during the routine scraping undertaken to remove contaminated material prior to squeezing. It is possible that pyrite formation in the Unit III sediments is triggered by hydrogen sulfide diffusion upward from the Unit IV sediments, which are most likely iron limited. Shore-based sulfur isotopic studies will help to test this hypothesis.

The reducing character of the sedimentary column also is seen in remarkably well-constrained profiles showing elevated manganese and iron concentrations (Fig. F20O, F20P). Peak concentrations of ~8 μM manganese and 50 μM iron are attained at ~60–80 and 110 mbsf, respectively. These results represent a somewhat expanded version of the classic interstitial water chemically reductive sequence of Froelich et al. (1979) and are consistent with the dominant role played by the existence of an old deep-seated bioreactor (Unit IV). In fact, the interstitial

F20. Interstitial water analyses, p. 67.



water iron profile shows a second, smaller peak ( $\sim 15 \mu\text{M}$ ) at  $\sim 300$  mbsf. We note the broad association between the two interstitial water iron peaks and the two stratigraphic intervals at the site with sediments having a distinct red coloration (see “**Lithostratigraphy**,” p. 4).

In contrast to lithostratigraphic Units II and III, only very low interstitial water concentrations of the redox-sensitive metals are attained in lithostratigraphic Unit IV ( $\text{Mn} = <1 \mu\text{M}$  and  $\text{Fe} = 5 \mu\text{M}$ ) with the exception of one questionable data point in our iron profile (Fig. F200). The same is true of Unit V. A similar association between organic matter-rich sediments and low interstitial water concentrations of manganese and iron was observed at Site 1257. Our favored working hypothesis for this observation is that these redox-sensitive metals were completely remobilized during or shortly after the host organic matter-rich units were deposited, implying conditions of severe syndimentary oxygen depletion. Alternatively, the low interstitial water manganese concentrations observed in Units IV and V reflect the formation of manganese-rich carbonate phases (e.g., ankerite/rhodochrosite). Shore-based chemical analysis of the interstitial water “squeeze cakes” will provide a definitive test of these two competing hypotheses.

As expected, sulfate depletion in interstitial water samples is accompanied by increases in ammonium (Fig. F20G), consistent with organic matter consumption. As at Site 1257, ammonium concentrations peak in lithostratigraphic Unit IV and decrease almost linearly toward the sediment/seawater interface. Significantly, ammonium concentrations in Unit V are slightly lower than those in the overlying black shale sequence, supporting our interpretation that Unit IV is the main “microbial bioreactor” influencing interstitial water chemistry at the site.

The complete absence of sulfate in Unit IV at Site 1258 most probably promotes the same two phenomena inferred at other Leg 207 sites: (1) mobilization of barium and (2) formation of dolomite.

Increases in barium concentration (Fig. F20H) are governed by barite solubility (Church and Wolgemuth, 1972) and are prone to even slight contamination by seawater sulfate. All cores at Site 1258 were taken using RCB drilling technology, so minor seawater contamination cannot be excluded. However, the convincing form of the downhole interstitial water barium profile, together with extensive sedimentological evidence, indicates intense barium mobilization from near the base of the black shale sequence at Site 1258. Authigenic barite crystals of millimeter to centimeter scale are frequently observed in the overlying Upper Cretaceous chinks (lithostratigraphic Unit III) (see “**Lithostratigraphy**,” p. 4). Similar sedimentological and mineralogical relationships are reported elsewhere (Brumsack, 1986; Torres et al., 1996).

The downhole interstitial water magnesium profile is nearly linear from the sediment/water interface to the basal sediments at Site 1258. In contrast, the downhole interstitial water calcium profile is nonlinear. Calcium concentrations peak at  $\sim 2$  times seawater values at  $\sim 275$ – $300$  mbsf and, despite decreasing to lower values deeper in the section, remain comparatively high ( $\sim 1.5$  times seawater) downhole to the basal sediments at the site (Fig. F20I). These observations indicate the existence of a significant sink for magnesium and a source for calcium in the sulfate-depleted black shale interval, most probably dolomite formation.

The nonlinearity of the calcium profile from the top of Unit IV to the sediment/water interface indicates carbonate diagenesis in sediments of Late Cretaceous and Paleogene age, as deduced from associated trends in alkalinity (Fig. F20E). The alkalinity and calcium concentration

depth profiles show particularly pronounced structure in lithostratigraphic Subunits IIB and IIC and Unit III, where two pronounced maxima are seen in both calcium and alkalinity. The first maxima is between ~260 and 310 mbsf and the second at ~400 mbsf, corresponding to the lower Paleocene and Maastrichtian chalks (Subunits IIB and IIC) and the top of the black shale sequence (Unit IV), respectively. Interstitial water calcium and alkalinity concentrations are significantly lower in the intervening claystones of Unit III. This general covariation between these two parameters and sediment  $\text{CaCO}_3$  content (see Fig. F4) implies that these interstitial water gradients are locally controlled by ongoing carbonate dissolution and reprecipitation reactions or recrystallization. Our interpretation of these nonlinear depth gradients in terms of carbonate diagenetic reactions is consistent with reports of particularly poor preservation of calcareous microfossils in strata of Maastrichtian age (see “**Lithostratigraphy**,” p. 4, and “**Biostratigraphy**,” p. 10). On the other hand, the downhole interstitial water strontium and ammonium profiles, which are widely thought to be sensitive proxies for recrystallization of biogenic carbonate and organogenic bicarbonate (e.g., Baker et al., 1982), respectively, show minimal local control. Instead, we see a near-linear downhole increase in both parameters, indicating sources at depth and simple diffusion to the sediment/water interface (Fig. F20J). One interpretation of the decoupled behavior between these parameters (calcium and alkalinity vs. strontium and ammonium) is that carbonate diagenesis in the Upper Cretaceous chalks (Unit III) is dominated by calcite precipitation fed by chemical diffusion from below rather than dissolution or in situ recrystallization. In fact, the form of the strontium interstitial water depth profile (Fig. F20J) suggests that the main locus of carbonate recrystallization most likely lies below the strata that we drilled at Site 1258. We interpret the simple diffusion-dominated strontium and ammonium profiles to reflect minimal accumulation of sediments younger than middle Eocene age at Site 1258 (see Fig. F10). Similar findings have been reported from Blake Nose, where Eocene-age sediments crop out at the seafloor (Rudnicki et al., 2001). Maximum interstitial water strontium concentrations and average linear depth gradients are noticeably lower at Site 1258 than at Site 1257 (~5 times vs. ~10 times seawater and ~1  $\mu\text{M}/\text{m}$  vs. ~5  $\mu\text{M}/\text{m}$ , respectively) and modest relative to many Deep Sea Drilling Project/ODP sites (Rudnicki et al., 2001). These observations suggest that Site 1258 pore fluids are not in communication with a once aragonite-rich source as hypothesized at Site 1257 (see “**Inorganic Geochemistry**,” p. 24, in the “Site 1257” chapter).

Dissolved silica concentrations at Site 1258 are significantly higher in sediments of Eocene age (~600–800  $\mu\text{M}$  [~20–200 mbsf]) than in those of Paleocene–Cenomanian age (~400–600  $\mu\text{M}$  [~200–450 mbsf]) and decrease sharply to even lower values from the middle of the black shale sequence into the basal Albian claystones (~200  $\mu\text{M}$ ) (Fig. F20N). These patterns undoubtedly track the abundance of biogenic silica and its transformation to opal-CT and possibly chert, but alteration of volcanic ash may also play a role (see “**Lithostratigraphy**,” p. 4, and “**Biostratigraphy**,” p. 10). As is the case at Site 1257, the clay-rich Albian sediments below the black shale sequence appear to serve as a sink for potassium (Fig. F20D).

## Low Salinity/Chlorinity Anomalies

Arguably the most remarkable feature of the interstitial water chemistry at Site 1258 is the presence of low salinity and chloride concentration anomalies between ~300 mbsf and the base of the site (Fig. F20A–F20C). These anomalies are in contrast to our findings at Sites 1257, 1259, and 1261, where significant increases in salinity and chloride concentration indicate the presence of a brine in the black shale sequence of lithostratigraphic Unit IV. The most pronounced of the low chloride concentration anomalies at Site 1258 are paralleled by sodium, and the average Na/Cl ratio at the Site 1258 is 0.85, which is very close to the IAPSO seawater value of 0.86. Minima in salinity and Cl concentration (26 psu and 465 mM, respectively) are attained in the deepest sample analyzed (interval 207-1258C-34R-2, 135–150 cm [483.55 mbsf]), and from the latter we calculate a 17% freshening relative to the sample taken from the shallowest depth at the site. Low-chlorinity anomalies such as those seen in Figure F20 are not easy to interpret with confidence on the basis of shipboard data alone. The presence of significant concentrations of methane in headspace gas analyses (>50,000 ppmv) (see “Interstitial Gas Contents,” p. 25, in “Organic Geochemistry”) are consistent with the anomalies that were caused by dissociation of gas hydrates. Unfortunately, estimates of the geothermal gradient for the outer Demerara Rise are not available to us. If we use the value estimated for Ceara Rise (47°C/km) (Curry, Shackleton, Richter, et al., 1995) and make the assumptions that all of any hydrate-stored gas is methane and the salinity is 35 psu, then using the hydrate program CSMHYD (Sloan, 1998), we estimate that Cretaceous strata at Site 1258 are near the base of the gas hydrate stability zone.

Alternative explanations for the salinity and chloride anomalies are clay dehydration reactions and dilution by meteoric water. The former possibility seems unlikely given the lithology at Site 1258, but the latter possibility cannot be excluded even though the nearest landmass is located nearly 400 km away. Lithium interstitial water concentrations show significant elevation at Site 1258 (Fig. F20L), suggesting that the association between high lithium concentrations and the brines of the black shale sequence at Site 1257 may be coincidental, but the cause of these significant lithium anomalies remains enigmatic.

In summary, the interstitial water chemistry profiles from Site 1258 primarily reflect ongoing organic matter diagenesis in the black shales, carbonate diagenesis, and the dissolution of biogenic silica. In sharp contrast to our findings at Sites 1257, 1259, and 1261, where lithostratigraphic Unit IV appears to act as an aquifer for fluids of relatively high salinity, we observe pronounced low salinity and chlorinity anomalies at Site 1258. We hypothesize these anomalies to be caused by either gas hydrate dissociation or dilution by meteoric water.

## PHYSICAL PROPERTIES

Physical property measurements at Site 1258 were conducted on whole cores, split cores, and discrete samples. Whole-core measurements conducted with the MST included GRA bulk density, magnetic susceptibility, resistivity, and NGR. Compressional (*P*)-wave velocity was measured in the transverse direction on split cores at intervals of 50 cm and along both transverse and longitudinal directions on cube samples taken at a frequency of one per core in Hole 1258B. Moisture and

density (MAD) were determined on discrete samples at a frequency of one per section from Hole 1258A. Intervals not recovered in Hole 1258A were sampled from Hole 1258B. A full description of the various measurement techniques can be found in “Physical Properties,” p. 33, in the “Explanatory Notes” chapter. Physical property sampling was minimal through the black shale sequence and across critical boundaries.

### Density and Porosity

The MAD (index) properties determined at Site 1258 include bulk density, porosity, grain density, water content, and void ratio (Table T21). Bulk density was determined on whole-core sections using the MST (GRA density) and on discrete samples. The GRA method tends to underestimate the bulk density in RCB cores because the core does not completely fill the liner. At this site, the average difference between GRA and discrete sample density is 0.13 g/cm<sup>3</sup> and is approximately constant with depth. Despite the offset, the bulk density trend with depth derived by the two methods is essentially the same (Fig. F21).

Downhole trends of index properties reflect lithologic boundaries and compositional variations in sediments in the defined lithostratigraphic units (Fig. F22). Bulk density increases with depth at a relatively constant rate in Unit I and Subunit IIA (0–280 mcd), ranging from 1.55 g/cm<sup>3</sup> at the surface to 1.9 g/cm<sup>3</sup> at the base of Subunit IIA. Correspondingly, porosity gradually decreases from 69% to 54%.

Between ~125 and 170 mcd, the general trend of MAD properties is interrupted by a drop in bulk density and increase in porosity, followed by an increase in bulk density and decrease in porosity between 170 and 190 mcd, just above the P/E boundary (Fig. F22).

In the interval between ~280 and ~343 mcd (Subunits IIB and IIC), bulk density and porosity are relatively constant with depth, with average values of 2 g/cm<sup>3</sup> and 40%, respectively (Fig. F22). This interval, however, is characterized by a higher degree of variability in the data that corresponds to cyclic variations in color and hardness of the sediment (see “Lithostratigraphy,” p. 4). The boundary between Subunits IIC and Unit III (343 mcd) coincides with a drop in bulk density from ~2 to 1.8 g/cm<sup>3</sup> and in grain density from ~2.7 to 2.4 g/cm<sup>3</sup>, whereas porosity remains constant. The few data collected from the laminated black shale sequence (Unit IV) are not sufficiently representative to characterize this interval.

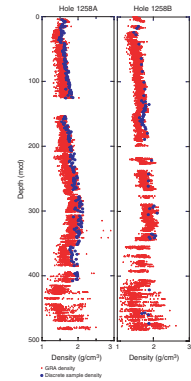
The grain density generally decreases between 0 and ~70 mcd, with values ranging from 2.75 to ~2.5 g/cm<sup>3</sup>. From 70 to ~343 mcd, grain density gradually increases from 2.5 to 2.7 g/cm<sup>3</sup>, with offsets corresponding to lithostratigraphic unit boundaries (Fig. F22). At the boundary between Subunit IIC and Unit III, the grain density rapidly decreases to ~2.4 g/cm<sup>3</sup>. Grain density data from Unit III are lower in magnitude but higher in variability than the overlying units.

### Acoustic Velocity

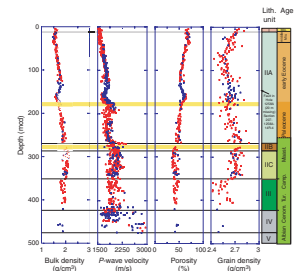
P-wave velocity was measured on split cores using the modified Hamilton Frame apparatus. In addition, measurements of transverse (x- and y-direction) and longitudinal (z-direction) P-wave velocity were conducted on cube samples from Hole 1258B (Table T22).

T21. MAD from discrete samples, p. 116.

F21. MAD bulk density vs. GRA bulk density, p. 69.



F22. Wet bulk density,  $V_p$ , grain density, and porosity, p. 70.



T22. Velocity measurements, p. 117.

Acoustic velocities increase downhole, with peaks in over-consolidated or lithified intervals (Figs. F22, F23). The depth profile correlates directly with bulk density and inversely with porosity. Velocity increases with depth in Unit I and Subunit IIA. Similar to bulk density, velocity decreases below 125 mcd and then increases rapidly at ~190 mcd. Beginning at the P/E boundary (192 mcd), variability in velocity increases significantly, with fluctuations as high as 200 m/s over short (2 m) depth intervals. This high variability continues throughout Subunit IIC and Unit III and reflects large compositional and diagenetic variations. In Unit IV, acoustic velocity varies even more than in units above because of the large density differences in the alternating black shale and limestone.

Velocity is isotropic from 0 to ~280 mcd (Unit I and Subunits IIA and IIB), with <1% difference between longitudinal and transverse directions (Fig. F23). Below 280 mcd, in Subunit IIC and Unit III, the sediment develops a small degree of *P*-wave velocity anisotropy with higher velocities in the transverse direction, possibly corresponding to higher clay content.

### Whole-Core Multisensor Track

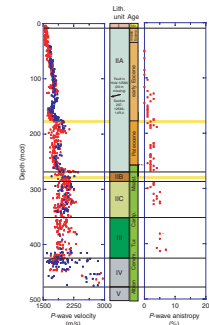
MST data from the three holes at Site 1258 have similar trends throughout the defined lithostratigraphic units once mbsf depths have been translated into mcd (see “Composite Depths,” p. 21). The Miocene ooze of Unit I is characterized by moderately high NGR emissions (~10 cps) and a strong magnetic susceptibility signature (~15–20). (Magnetic susceptibility is reported as dimensionless instrument units throughout. See “Multisensor Track Measurements,” p. 33, in “Physical Properties” in the “Explanatory Notes” chapter for conversion factors to SI) (Fig. F24). A sharp decline in both NGR emissions (to <5 cps) and magnetic susceptibility reflects the change from the ooze of Unit I to the foraminifer nannofossil chalk of Unit II.

First-order changes in MST data in Unit II generally track trends in the carbonate content of the sediment (Fig. F24). High carbonate content is associated with low NGR emissions and low magnetic susceptibility, whereas a drop in carbonate content, potentially reflecting a more substantial contribution of sediments from terrigenous sources, is accompanied by a rise in both NGR emissions and magnetic susceptibility.

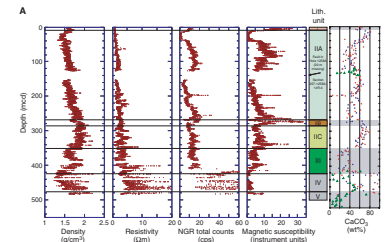
In the middle of Subunit IIA, an unconformity is present, which is expressed in Hole 1258A as a 20-m gap in the sediment record (~125–145 mcd) and in Hole 1258B as a decrease in the bulk density at 145 mcd. The P/E boundary is recorded in all the holes as a spike in both NGR emissions and magnetic susceptibility measurements at ~200 mcd and with a reduction in the carbonate content (Fig. F24). Between the P/E and the K/T boundaries, magnetic susceptibility and NGR emissions gradually increase. The K/T boundary, found in Subunit IIB, is characterized by large and variable changes in magnetic susceptibility, with values reaching a maximum of 35 in Hole 1258A and 30 in Hole 1258C. The same general trend is observed in Hole 1258B but with gaps in recovery at intervals comparable to those where peak readings were observed in other holes.

NGR emissions remain relatively constant through much of Subunit IIC and Unit III, whereas a peak in magnetic susceptibility appears at the bottom of Subunit IIC (~340 mcd) in Holes 1258A and 1258B (Fig. F24). A drop in the GRA density and magnetic susceptibility defines the

F23.  $V_p$  measurements and *P*-wave anisotropy, p. 71.



F24. MST data vs. lithostratigraphic units, p. 72.



transition from Subunit IIC to Unit III. At 400 mcd (Hole 1258A), a broad peak in the GRA density is also reflected in the magnetic susceptibility data; however, gaps in recovery prevent correlation with either Hole 1258B or 1258C.

The laminated shales of Unit IV show a high degree of variation in GRA density, resistivity, and NGR emissions, reflecting the alternations of organic-rich layers and highly lithified and cemented sections. Magnetic susceptibility remains low and constant through the laminated shales relative to the overlying sequence, increasing in variability and magnitude below the transition into Unit V (Fig. F24). Density generally increases with depth in all holes through Unit IV. The largest variability in the shale sequence is seen in NGR emissions, probably due to uranium enrichment in the organic-rich intervals (see “Downhole Logging,” p. 33) (Fig. F25).

Hole 1258C penetrated deepest into Unit V, where density and NGR emissions, although variable, tend to be relatively high (1.7 g/cm<sup>3</sup> and 30 cps, respectively). Magnetic susceptibility gradually increases from <5 at the base of Unit IV to ~12 at the bottom of the hole.

Resistivity measurements proved difficult to correlate between holes. The NCR sensor is highly sensitive to changes in core diameter, which was exacerbated by RCB drilling during Leg 207. Where core disturbance is minimal, there is a strong correspondence between resistivity and GRA density. Marked changes in resistivity delineate major lithologic boundaries, as do other physical property data. The absolute value of the individual resistivity data points, however, is suspect because of the large variability in core diameter.

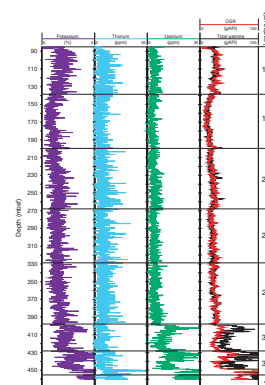
## DOWNHOLE LOGGING

Following completion of RCB coring operations in Hole 1258C, the hole was conditioned with a wiper trip and pumped with sepiolite mud. The drill pipe was initially set at 96 mbsf and pulled for all logging passes to 86 mbsf. The following two tool strings were run:

1. The triple combo tool string with the Lamont-Doherty Earth Observatory (LDEO) Temperature/Acceleration/Pressure (TAP) tool and MGT tool and
2. The FMS-sonic tool string (see “Downhole Logging,” p. 39, in the “Explanatory Notes” chapter for further tool specifications).

The wireline heave compensator (WHC) was used on all passes, with heave varying between 1.4 and 2.0 m throughout the operation. The first tool string run was the triple combo, which was lowered to the bottom of the hole at 488 mbsf logging depth (drillers depth = 485 mbsf). Two full logging-upward passes were made with the triple combo tool string. Following this run, control of the wireline passed to the downhole measurements laboratory (DHML) and the MGT was powered up and stabilized. Two full passes (the bottom of the hole was reached on both) were made with the MGT. The second tool string (FMS-sonic) was also successfully run to the bottom of the hole. Two full passes were made with the FMS-sonic tool string. Due to the reduced telemetry requirements of the Long Spacing Sonic (LSS) tool, it was possible to run this tool string at 548.6 m/hr (normal logging speed when running the FMS-sonic tool string with the Dipole Sonic Imager [DSI] = 274 m/hr). To check data quality, the first pass of the tool string was at 274 m/hr

F25. High-resolution MGT gamma ray logs, p. 75.



and the second at 548.6 m/hr. In summary, two tool strings were run during the logging operation, with six separate logging passes. All passes were from total depth into the pipe, providing a logged section of 402 m (Fig. F26). The wireline depth to seafloor was set at 3195 mbrf, determined from the step increase in gamma ray counts found at the sediment/seafloor interface, and recorded on the first pass of the triple combo tool string. The drillers depth to seafloor was 3203 mbrf. This discrepancy accounts for some of the differential between the drillers pipe and total depths (80 and 485 mbsf, respectively) and the wireline depths (86 and 488 mbsf, respectively).

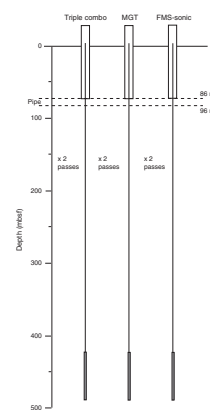
### Data Quality

Borehole diameter can affect the response of some tools, for example the Hostile Environment Litho-Density Tool (HLDT) and Accelerator Porosity Sonde (APS), and so the size and shape of the borehole is important for interpreting the quality of logging data. The caliper logs from the triple combo (one per pass) and the FMS-sonic (two per pass) tool strings provide information on the borehole size (Fig. F27). From the base of the pipe (86 mbsf) to 455 mbsf, the hole diameter is for the most part just beyond bit size, varying only in a few places (e.g., ~260 mbsf) but always less than the maximum extension of the FMS-sonic calipers (15.5 in; 39.4 cm). From 455 mbsf to total depth, the hole diameter varies significantly, sometimes extending beyond the FMS-sonic caliper maximum extension. Thus, FMS-sonic data in a few short sections of the borehole below 455 mbsf are unusable because of loss of wall contact. Caliper data from both the FMS-sonic (C1) and triple combo tool strings indicate hole enlargements at ~9.5-m spacings from 103 to 196 mbsf (Fig. F27). These data indicate borehole enlargement due to incomplete active heave compensation of the drill pipe, which is exacerbated during drill pipe addition and core barrel recovery and re-load. Any time-series analysis on logging data through this interval that shows cycles corresponding to 9- to 10-m wavelengths should be treated with caution. The borehole conditions as indicated by the caliper logs were excellent.

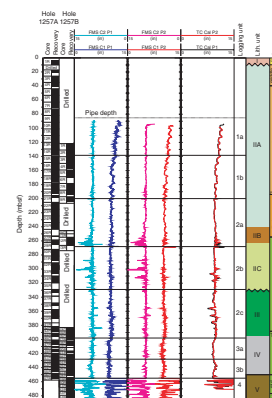
Data from the triple combo tool string are good, with excellent repeatability and only minor depth mismatches between passes. Gamma ray data from the Hostile Environment Gamma Ray Sonde (HNGS), MGT, and Scintillation Gamma Ray Tool (SGT) are also well matched in depth and magnitude, providing easy depth shifting for the MGT and FMS-sonic logging runs. FMS-sonic data have been processed, and almost all of the 400-m logged section is good on both passes. This result indicates that when the tool string configuration allows (i.e., the FMS-sonic tool string is not running with the DSI), the FMS-sonic may be run at 548.6 m/hr without loss of data quality. Indeed, the image quality may be marginally better at the higher logging speed.

Core physical property data provide a rapid method for visualization of the core-log correlation (Fig. F28). Because of drilling ahead with selective coring, the lack of core data from Hole 1258C was supplemented by using core data from Hole 1258B. The core density values from the MST (see “Physical Properties,” p. 33, in the “Explanatory Notes” chapter) are lower than the in situ recorded logging values. Density and porosity data from the few index property measurements available for Hole 1258B are close to the logging values. Core resistivity data are suspect because of the RCB coring. However, core velocities (measured directly on the core with the modified Hamilton Frame) are close to the

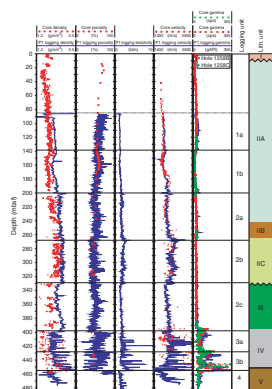
F26. Logging runs, p. 76.



F27. Borehole caliper logs, p. 77.



F28. Geophysical logs and equivalent core physical properties, p. 78.



logging values. NGR values measured on the MST underestimate the logging natural gamma values. The depth match between logging mbsf and coring (drillers) mbsf is offset in Hole 1258C because of the 8-m depth difference in the estimated seafloor depths. Overall, the patterns observed in the core physical properties are matched to the logging data, although core-log depth matching will require some depth shifting of the core data.

## Logging Stratigraphy

Four logging units have been defined for Hole 1258C.

### Unit 1 (base of pipe [86 mbsf]–200 mbsf)

Logging Unit 1 is characterized by downhole increases in resistivity, density (covarying with porosity), and velocity logs (Fig. F29). The porosity and gamma ray logs display high-amplitude cyclicality. This logging unit is further divided into two subunits.

#### Subunit 1a (86–138.5 mbsf)

Resistivity, density, and velocity increase steadily downhole through this subunit (Fig. F29) and show only small-scale fluctuations. Porosity decreases downhole, as expected, but displays high-amplitude cyclicality. The high-resolution MGT gamma ray log also displays cyclicality through this subunit (Fig. F25). The increase in density is matched by an increase in carbonate content downhole (see “Organic Geochemistry,” p. 24).

#### Subunit 1b (138.5–200 mbsf)

Gamma ray, resistivity, density, and velocity decrease downhole to ~160 mbsf, where they begin to gradually increase again to the base of the subunit at 200 mbsf (Figs. F25, F29). Porosity covaries with density and displays high-amplitude cyclicality, also seen in the MGT log (Fig. F25). The change in density appears to relate to the change in clay content as revealed by the potassium contribution in the gamma ray spectrum (Fig. F25).

### Unit 2 (200–398 mbsf)

The top of the unit is best seen as a peak in the gamma ray log and a step change in density. This change is closely related to the P/E boundary (see “Biostratigraphy,” p. 10) seen in cores from Holes 1258B and 1258C. Resistivity, density, and velocity all show increased amplitude fluctuations throughout this unit (Fig. F29), clearly distinguishing it from Unit 1 above. Porosity and gamma ray logs have well-developed cyclicality. This logging unit is further subdivided into three subunits.

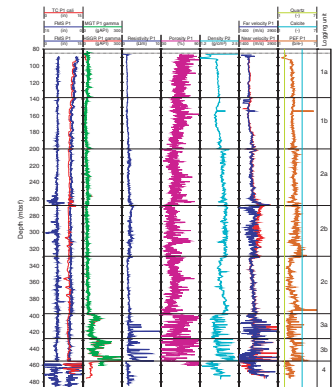
#### Subunit 2a (200–268 mbsf)

Gamma ray counts increase downhole, as does the resistivity, density, and velocity (Figs. F25, F29). Porosity and gamma ray logs display well-developed cyclicality, which is matched in the FMS-sonic dynamic images (Fig. F30). The base of the subunit is marked by a spike and/or step shift seen in all the logs.

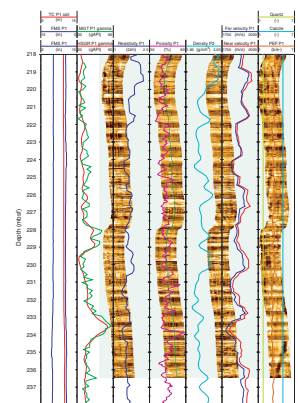
#### Subunit 2b (268–329 mbsf)

Density and velocity increase at the Subunit 2a/2b boundary, with a concomitant decrease in porosity. Gamma ray counts decrease across

F29. Geophysical logs, caliper data, and logging units, p. 79.



F30. Wireline physical property variations, p. 80.



the boundary and then increase downhole. Between 317 mbsf and the base of the subunit, the photoelectric effect (PEF) log increases significantly, approaching and sometimes exceeding the calcite line (Fig. F29). The increase in the PEF log is not the result of increasing carbonate content (see “Organic Geochemistry,” p. 24) but is likely caused by the barite and pyrite concretions (see “Lithostratigraphy,” p. 4). Even in relatively small amounts, these minerals will produce a significant deflection of the PEF log because of their high photoelectric absorption cross-section index ( $Pe$ ) values. The  $Pe$  value for barite is 266.8 b/e<sup>-</sup> and for pyrite is 16.97 b/e<sup>-</sup> (Rider, 1996).

#### **Subunit 2c (329–398 mbsf)**

The top of this unit is defined by a sharp decrease in density and velocity with a covarying increase in porosity (Fig. F29). Density values continue to fall to ~344 mbsf and then rise back to levels seen at the top of the subunit, with porosities covarying. Gamma ray and velocity values increase gradually downhole throughout the subunit (Figs. F25, F29). In the middle and lower portions of the subunit, the gamma ray logs have a prominent cyclicity at a periodicity of ~10 m (Fig. F25). The Subunit 2b/2c boundary correlates with the lithostratigraphic Unit II/III boundary (see “Lithostratigraphy,” p. 4).

### **Unit 3 (398–455 mbsf)**

Logging Unit 3 is characterized by a large step increase in the gamma ray and porosity logs, with a concomitant decrease in the density and velocity logs (Fig. F29). The gamma ray spectrum (Fig. F25) reveals the source of increased gamma ray emission to be from potassium (clay) and uranium (organic matter). The high organic matter content indicated by the uranium contribution to the gamma ray spectrum is corroborated by correlation of logging Unit 3 with lithostratigraphic Unit IV (laminated black shale) (see “Lithostratigraphy,” p. 4, and “Organic Geochemistry,” p. 24). Large-amplitude fluctuations are observed in all the logs and are interpreted to result from the periodic occurrence of cemented layers giving peaks in density (troughs in porosity), resistivity, and velocity and are highlighted in Figure F31. The PEF log indicates that the layers are calcite cemented (calcite  $Pe = 5.08$  b/e<sup>-</sup>) (Fig. F31). Unit 3 is further subdivided into two subunits (Figs. F25, F29, F30).

#### **Subunit 3a (398–428 mbsf)**

Subunit 3a is characterized by lower total counts and lower-amplitude fluctuations in the gamma ray logs (Figs. F25, F31). A similar situation is observed in the porosity, density, and velocity logs (Figs. F29, F31).

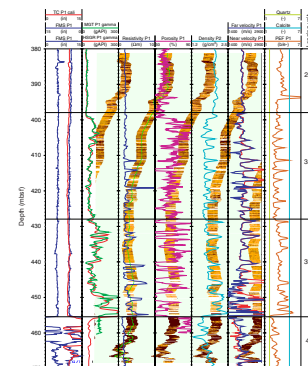
#### **Subunit 3b (428–455 mbsf)**

Cyclic variations in gamma ray and density have markedly higher amplitude and average gamma ray, density, and PEF values than in Subunit 3a above (Figs. F25, F29, F30). The base of the unit is defined by a sharp decrease in all of the logs with porosity covarying (Figs. F29, F31).

### **Unit 4 (455–total depth [488 mbsf])**

Logging Unit 4 is characterized by low resistivity (the lowest for the whole formation) and low gamma ray values (Fig. F25). Both density and velocity increase downhole from the pronounced drop that marks

F31. Stratigraphy of the black shale interval, p. 81.



the top boundary of the unit (Fig. F24). This unit correlates with lithostratigraphic Unit V (see “**Lithostratigraphy**,” p. 4). The borehole is widened beyond the HLDT caliper maximum in three locations (455.5–460, 461.5–463.5, and 471–472 mbsf). Density and porosity measurements are adversely affected by this hole enlargement, but the resistivity (especially intermediate and deep), velocity, and gamma ray logs should still be of good quality.

### Discussion

Excellent hole conditions (mostly just beyond bit size) combined with good heave compensation led to the acquisition of high-quality logging data at Site 1258. For the most part, the logging units described above correlate well with the designated lithostratigraphic units (see “**Lithostratigraphy**,” p. 4); however, a few further points of interest shall now be addressed.

### Black Shale

The continuous data derived from the logs through the black shale interval (logging Unit 3) provide the opportunity for estimation of the TOC content in this unit. The result is only approximate because the shale porosity is assumed to equate that of the sediments above, and values for some densities (e.g., organic matter) that are not well constrained are also assumed. Following Rider (1996), the following three equations are used to calculate the TOC:

$$\phi_{fi} = (\rho_{bk} - \rho_{ma}) / (\rho_{fi} - \rho_{ma}),$$

$$\phi_{om} = (\rho_{bs} - \rho_{bk}) / (\rho_{om} - \rho_{ma}), \text{ and}$$

$$\text{TOC (wt\%)} = ([0.85 \times \rho_{om} \times \phi_{om}] / [(\rho_{om} \times \phi_{om}) + \rho_{ma}(1 - \phi_{om} - \phi_{fi})]) \times 100\%,$$

where

$\rho_{bk}$  = density of the background sediment from the density log (2.045 g/cm<sup>3</sup>).

$\rho_{bs}$  = density of the black shale interval, taken from the density log.

$\rho_{om}$  = density of the organic matter (assumed) (1.15 g/cm<sup>3</sup>).

$\rho_{ma}$  = density of the matrix (grain density) averaged from five MAD measurements (2.44 g/cm<sup>3</sup>).

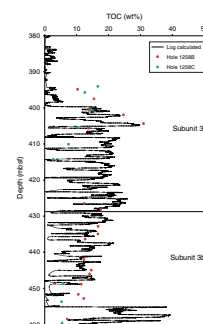
$\rho_{fi}$  = density of seawater (1.05 g/cm<sup>3</sup>).

$\phi_{fi}$  = water-filled porosity.

$\phi_{om}$  = volume fraction of organic matter.

The results are plotted along with values measured on core samples from Holes 1258B and 1258C (see “**Organic Geochemistry**,” p. 24) and are shown in Figure F32. Despite the fact that the measured values are from Holes 1258B and 1258C and are not depth matched to the logging mbsf depths, the results are very good. Logging Subunit 3a displays a ~2- to 3-m cyclicity pattern, which breaks down with the transition into Subunit 3b.

F32. Core-measured vs. log-calculated TOC, p. 82.



## Photoelectric Effect

The PEF log can be used qualitatively to indicate lithology and changes in mineral composition. The calcite  $Pe$  (5.08 b/e<sup>-</sup>) was used to indicate the presence of carbonate-cemented layers in parts of the formation (e.g., Figs. F29, F31). In the PEF log, a shift toward the calcite  $Pe$  in the carbonate-dominated sediments encountered during Leg 207 can be taken as an indication of increasing carbonate content. To demonstrate the accuracy of this approach, the PEF log from the first triple combo pass is plotted against depth along with measured CaCO<sub>3</sub> percentages (see “Organic Geochemistry,” p. 24) from Holes 1258B and 1258C (Fig. F33), with the PEF log tracking the measured trends in CaCO<sub>3</sub>.

## Gas Hydrates

Pore water chemistry indicated a freshening of the formation below 425 mbsf, which could be explained by the presence of gas hydrate (see “Inorganic Geochemistry,” p. 26). The APS neutron porosity tool is essentially blind to gas hydrate and will record true formation porosities. If gas hydrate is present in pore spaces, the HLDT may record increased densities. Thus, if porosities derived from the density log are lower than neutron-measured porosities this difference may indicate the presence of gas hydrate. A porosity measurement can be obtained from the density log using the following equation:

$$\phi = (\rho_{ma} - \rho_b) / (\rho_{ma} - \rho_{fl}),$$

where

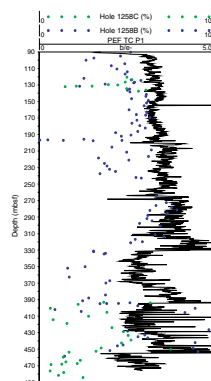
$\phi$  = porosity and  
 $\rho_b$  = bulk density.

The density-derived porosity is lower than the APS neutron porosity. However, this difference appears to be the case for the whole formation not just the zone of pore water freshening.

Gas hydrate-bearing sediments will exhibit high electrical resistivities compared to water-saturated units. Resistivity data from below 425 mbsf do not support the suggestion of a gas hydrate-bearing formation. There is no distinct change in the character of the resistivity logs downhole through logging Subunit 3b that cannot be explained by carbonate cementation. Logging Unit 4 shows a step decrease in formation resistivity, observed in both logging data (Fig. F29) and FMS imagery (Fig. F31).

Sonic velocities drop in logging Unit 4, except for a number of high-velocity peaks associated with cemented layers. If this unit was hydrate-saturated, higher average velocities would be expected. It is possible that there are small quantities of disseminated hydrate in the lower portions of the formation, perhaps concentrated in the higher-porosity layers in Unit 4. Following drilling disturbance, they would rapidly dissociate close to the borehole. However, the intermediate and deep resistivity logs would then show higher values than the shallow measurement. This response is not observed, so based on the downhole logging data it appears that there are no gas hydrates present in the formation.

F33. PEF and CaCO<sub>3</sub> percentages, p. 83.

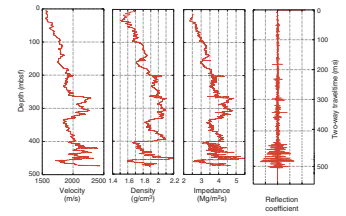


## Synthetic Seismograms

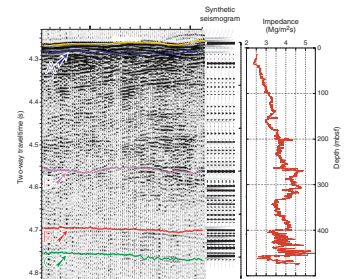
To compute a synthetic seismogram, formation density and velocity profiles are needed. Wireline logging provided high-quality density and velocity logs from the bottom of the hole up to pipe depth (86 mbsf). Density and velocity data for the remainder of the formation (above the pipe) were obtained from MAD (bulk density) and the Hamilton Frame (PWS3 velocity) measurements (see “Physical Properties,” p. 30). Downhole impedance was calculated from velocity  $\times$  density, and the impedance contrast between successive layers gave the reflection coefficient series (Fig. F34). An Ormsby wavelet was convolved with the reflection coefficient series to generate a synthetic seismogram (Fig. F35).

The synthetic seismogram matches the seismic data well, which allowed regional Reflectors B, B', and C to be correctly identified in the time domain (Fig. F35). Reflector C represents the base of the black shales. Reflector B' is the top of the black shales, and Reflector B is the density and velocity step across the logging Subunit 2a/2b boundary and the lithostratigraphic Subunit IIB/IIC boundary (see “Lithostratigraphy,” p. 4).

F34. Density, velocity, impedance, and reflection profiles, p. 84.



F35. Line Geob221, synthetic seismogram, and impedance, p. 85.



## REFERENCES

- Baker, P.A., Gieskes, J.M., and Elderfield, H., 1982. Diagenesis of carbonates in deep-sea sediments—evidence from  $\text{Sr}^{2+}/\text{Ca}^{2+}$  ratios and interstitial dissolved  $\text{Sr}^{2+}$  data. *J. Sediment. Petrol.*, 52:71–82.
- Bown, P.R., Rutledge, D.C., Crux, J.A., and Gallagher, L.T., 1998. In Bown, P.R. (Ed.), *Calcareous Nannofossil Biostratigraphy*: London (Chapman and Hall), 86–131.
- Bralower, T.J. 2002. Evidence for surface water oligotrophy during the Late Paleocene–Eocene Thermal Maximum: nannofossil assemblages data from Ocean Drilling Program Site 690, Maud Rise, Weddell Sea. *Paleoceanography*, 17:1–12.
- Brumsack, H.-J., 1986. The inorganic geochemistry of Cretaceous black shales (DSDP Leg 41) in comparison to modern upwelling sediments from the Gulf of California. In Summerhayes, C.P., and Shackleton, N.J. (Eds.), *North Atlantic Palaeoceanography*. Geol. Soc. Spec. Publ., 21:447–462.
- Burnett, J.A., 1998. Upper Cretaceous. In Bown, P.R. (Ed.), *Calcareous Nannofossil Biostratigraphy*: London (Chapman and Hall), 132–199.
- Church, T.M., and Wolgemuth, K., 1972. Marine barite saturation. *Earth Planet. Sci. Lett.*, 15:35–44.
- Claypool, G.E., and Kaplan, I.R., 1974. The origin and distribution of methane in marine sediments. In Kaplan, I.R. (Ed.), *Natural Gases in Marine Sediments*: New York (Plenum), 99–139.
- Claypool, G.E., and Kvenvolden, K.A., 1983. Methane and other hydrocarbon gases in marine sediment. *Annu. Rev. Earth Planet. Sci.*, 11:299–327.
- Curry, W.B., Shackleton, N.J., Richter, C., et al., 1995. *Proc. ODP, Init. Repts.*, 154: College Station, TX (Ocean Drilling Program).
- Erbacher, J., and Thurow, J., 1998. Mid-Cretaceous radiolarian zonation for the North Atlantic: an example of oceanographically controlled evolutionary processes in the marine biosphere? In Cramp, A., MacLeod, C.J., Lee, S.V., and Jones, E.J.W. (Eds.), *Geological Evolution of Ocean Basins: Results from the Ocean Drilling Program*. Geol. Soc. Spec. Publ., 131:71–82.
- Espitalié, J., Laporte, J.L., Madec, M., Marquis, F., Leplat, P., Paulet, J., and Boutefeu, A., 1977. Méthode rapide de caractérisation des roches mères, de leur potentiel pétrolier et de leur degré d'évolution. *Rev. Inst. Fr. Pet.*, 32:23–42.
- Froelich, P.N., Klinkhammer, G.P., Bender, M.L., Luedtke, N.A., Heath, G.R., Cullen, D., Dauphin, P., Hammond, D., Hartman, B., and Maynard, V., 1979. Early oxidation of organic matter in pelagic sediments of the eastern equatorial Atlantic: suboxic diagenesis. *Geochim. Cosmochim. Acta*, 43:1075–1090.
- Hayes, D.E., Pimm, A.C., et al., 1972. *Init. Repts. DSDP*, 14: Washington (U.S. Govt. Printing Office).
- Martini, E., 1971. Standard Tertiary and Quaternary calcareous nannoplankton zonation. In Farinacci, A. (Ed.), *Proc. 2nd Int. Conf. Planktonic Microfossils Roma*: Rome (Ed. Tecnosci.), 2:739–785.
- Matsumoto, R., and Borowski, W.S., 2000. Gas hydrate estimates from newly determined oxygen isotopic fractionation ( $\delta^{18}\text{O}$ -IW) and  $\delta^{18}\text{O}$  anomalies of the interstitial waters: Leg 164, Blake Ridge. In Paull, C.K., Matsumoto, R., Wallace, P.J., and Dillon, W.P. (Eds.), *Proc. ODP, Sci. Results*, 164: College Station, TX (Ocean Drilling Program), 59–66.
- Meyers, P.A., 1997. Organic geochemical proxies of paleoceanographic, paleolimnologic, and paleoclimatic processes. *Org. Geochem.*, 27:213–250.
- Müller, P.J., 1977. C/N ratios in Pacific deep sea sediments: effect of inorganic ammonium and organic nitrogen compounds sorbed by clays. *Geochim. Cosmochim. Acta*, 41:765–776.
- O'Dogherty, L., 1994. Biochronology and paleontology of middle Cretaceous radiolarians from Umbria–Marche Appennines (Italy) and Betic Cordillera (Spain). *Mem. Geol. Lausanne*, 21:1–351.

- Okada, H., and Bukry, D., 1980. Supplementary modification and introduction of code numbers to the low-latitude coccolith biostratigraphic zonation (Bukry, 1973; 1975). *Mar. Micropaleontol.*, 5:321–325.
- Peters, K.E., 1986. Guidelines for evaluating petroleum source rock using programmed pyrolysis. *AAPG Bull.*, 70:318–329.
- Rider, M.H., 1996. *The Geological Interpretation of Well Logs* (2nd ed.): Caithness (Whittles Publishing).
- Rudnicki, M.D., Wilson, P.A., and Anderson, W.T., 2001. Numerical models of diagenesis, sediment properties and pore fluid chemistry on a paleoceanographic transect: Blake Nose, Ocean Drilling Program Leg 171B. *Paleoceanography*, 16:561–573.
- Sanfilippo, A., and Riedel, W.R., 1985. Cretaceous radiolaria. In Bolli, H.M., Saunders, J.B., and Perch-Nielsen, K. (Eds.), *Plankton Stratigraphy*: Cambridge (Cambridge Univ. Press), 573–630.
- Sissingh, W., 1977. Biostratigraphy of Cretaceous calcareous nannoplankton. *Geol. Mijnbouw*, 56:37–65.
- Sloan, D., 1998. *Clathrate Hydrates of Natural Gases* (2nd Ed.): New York (Marcel Dekker).
- Torres, M.E., Brumsack, H.-J., Bohrmann, G., and Emeis, K.C., 1996. Barite fronts in continental margin sediments: a new look at barium remobilization in the zone of sulfate reduction and formation of heavy barites in diagenetic fronts. *Chem. Geol.*, 127:125–139.
- Twichell, S.C., Meyers, P.A., and Diester-Haass, L., 2002. Significance of high C/N ratios in organic-carbon-rich Neogene sediments under the Benguela Current upwelling system. *Org. Geochem.*, 33:715–722.

Figure F1. Seismic line GeoB221 at Site 1258. See Figure F1, p. 5, in Shipboard Scientific Party ("Site Survey and Underway Geophysics"), this volume, for a location map for this line.

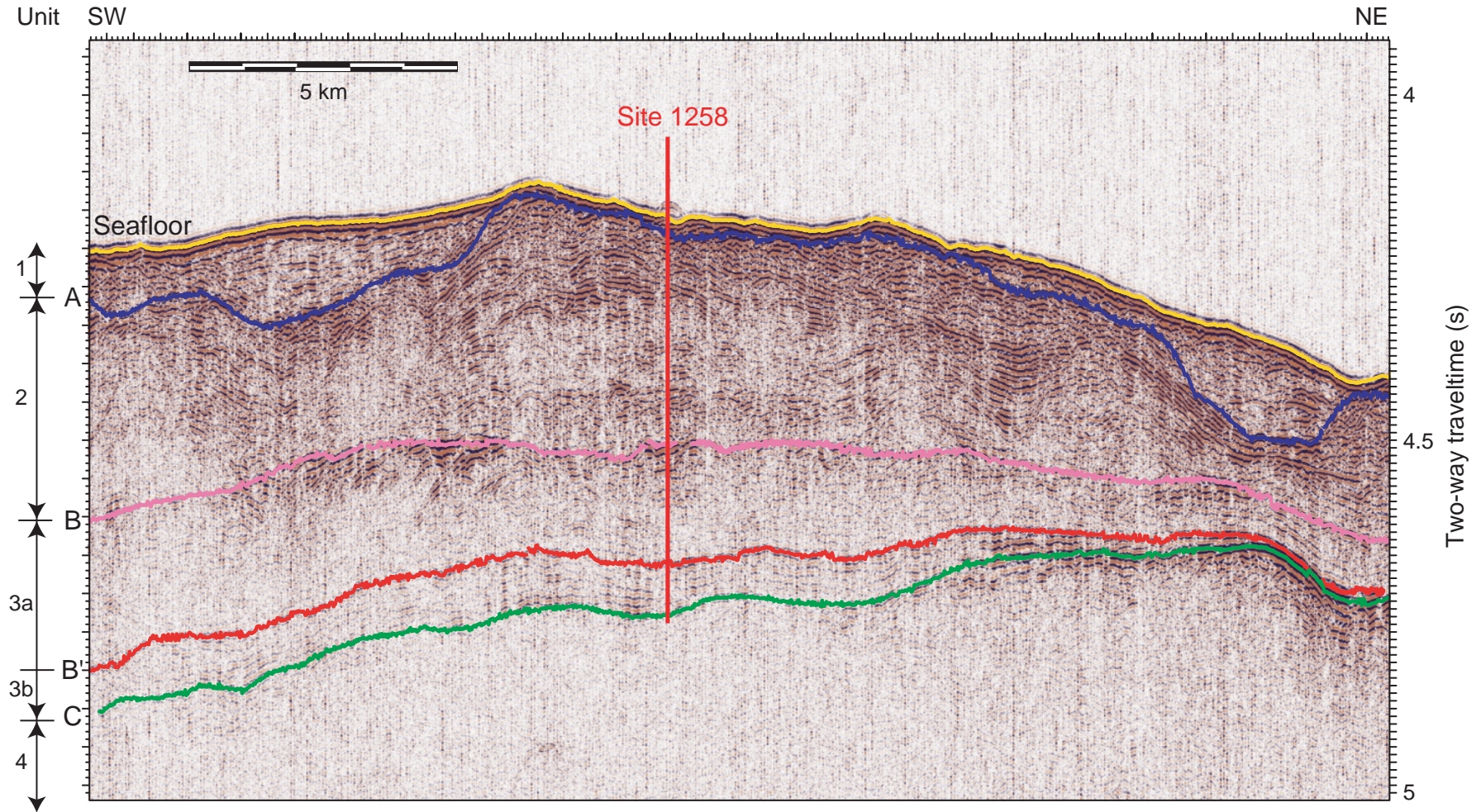
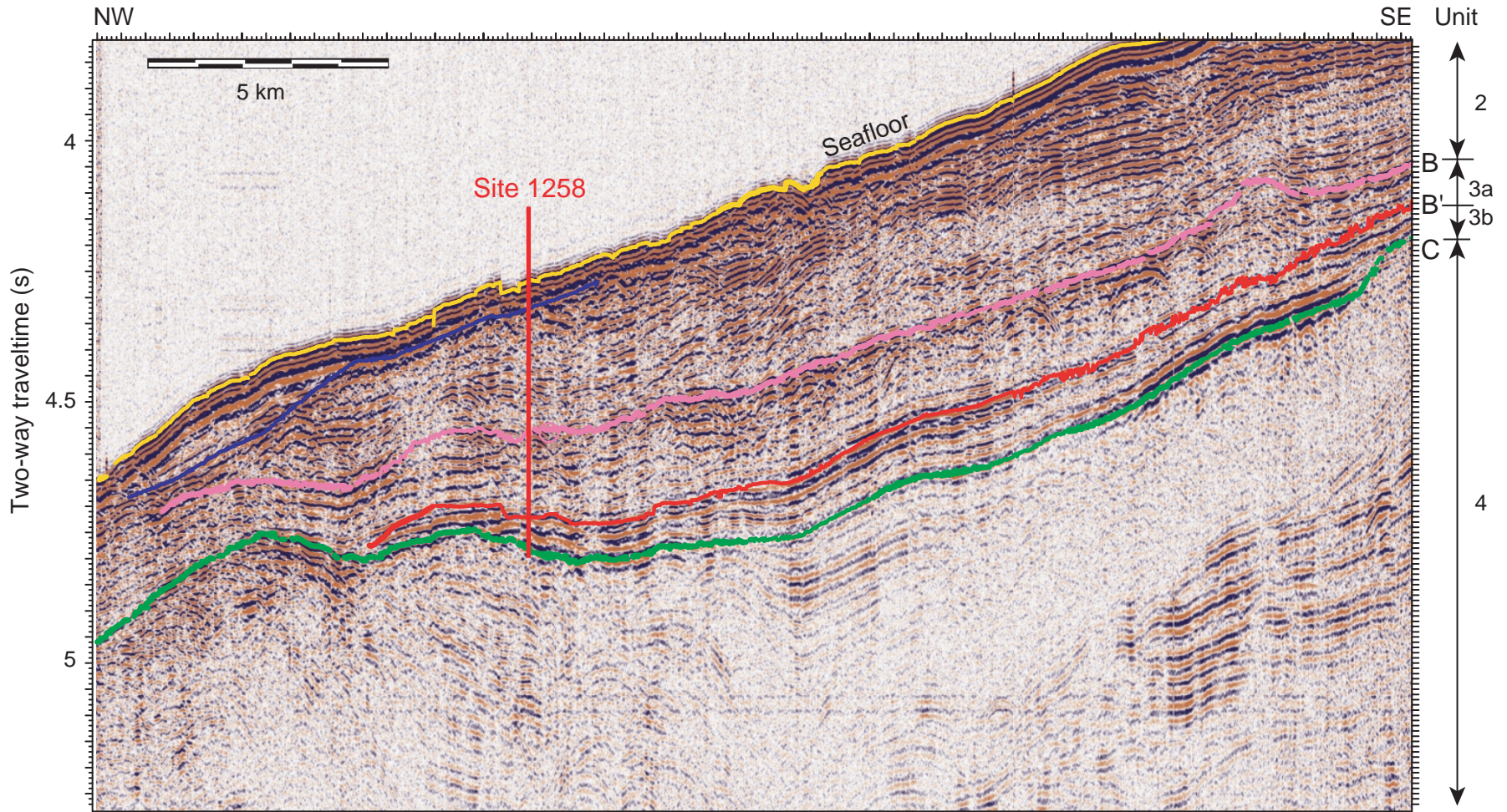
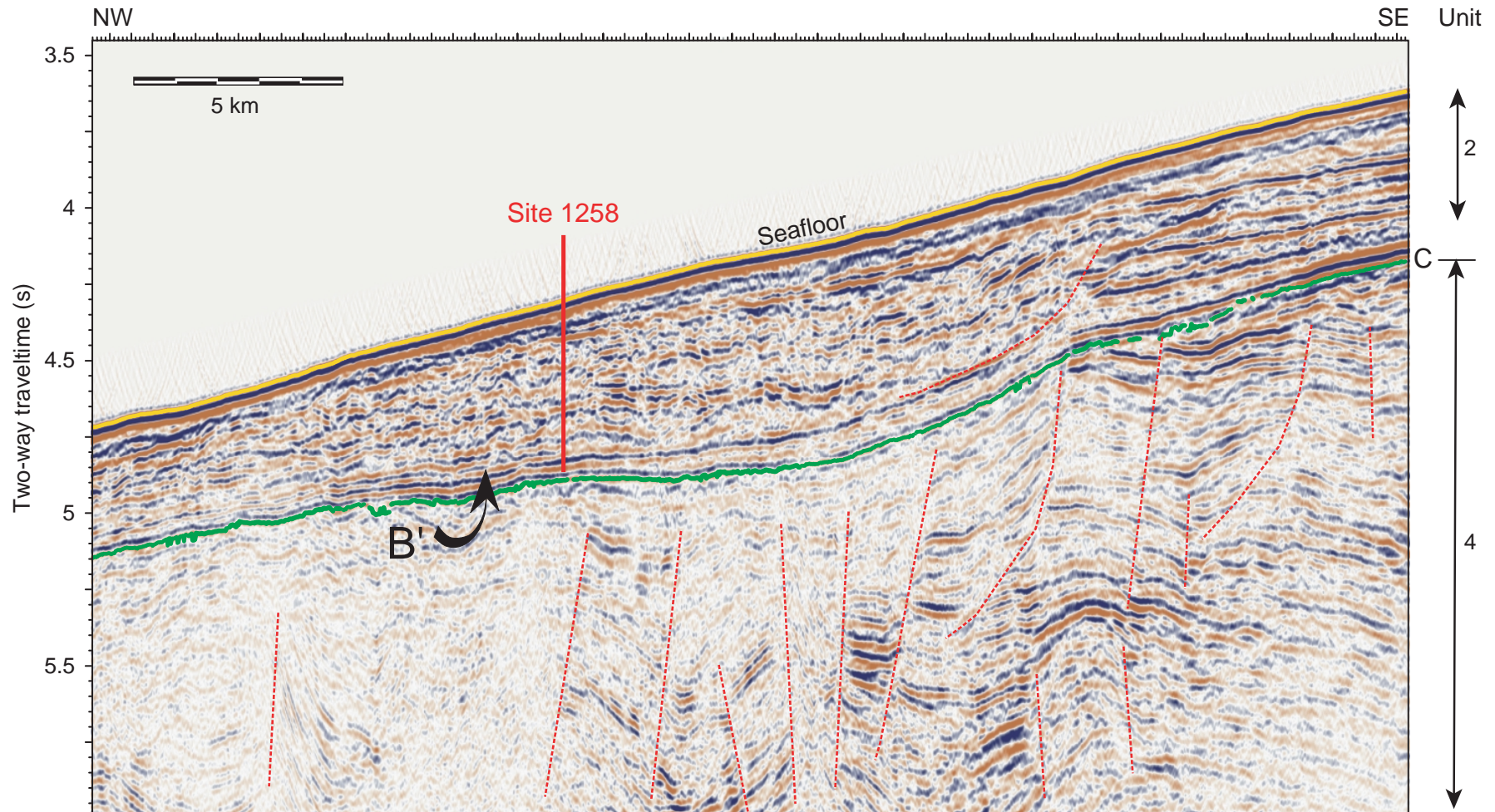


Figure F2. Seismic line 207-L1S at Site 1258. See Figure F1, p. 5, in Shipboard Scientific Party ("Site Survey and Underway Geophysics"), this volume, for a location map for this line.



**Figure F3.** Industry multichannel seismic reflection line passing 5.5 km east of Site 1258. See Figure F1, p. 5, in Shipboard Scientific Party (“Site Survey and Underway Geophysics”), this volume, for a location map for this line. The site location is projected onto the line at the point of closest passing. Note the coherent nature of seismic Unit 2 to the right of the figure, which terminates abruptly at the upper red dashed line then becomes incoherent in the central portion of the figure. Unit 3 is represented by the two reflection cycles above the Horizon C and is barely resolved with this seismic system. The sediment package underlying Horizon C is part of the synrift sequence and is heavily faulted and folded.



**Figure F4.** Lithostratigraphy, biostratigraphy, carbonate content, and total organic carbon (TOC) at Site 1258. Note that due to faulting, a 20-m-thick stratigraphic interval is missing in Hole 1258A. Boundaries of different lithostratigraphic units are based on the mbsf depth scale of Holes 1258B and 1258C. K/T = Cretaceous/Tertiary.

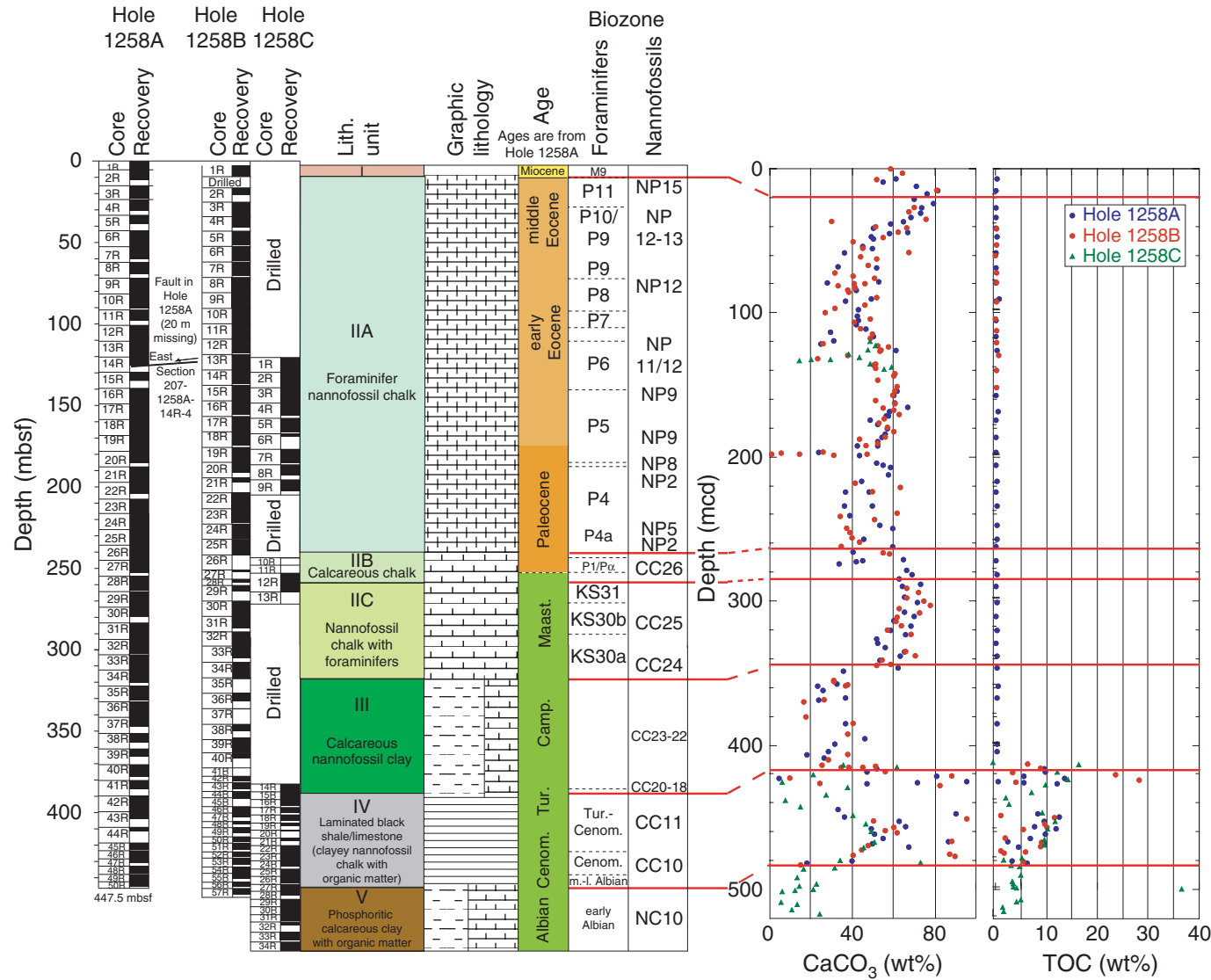


**Figure F5.** Close-up photographs of representative lithologies from lithostratigraphic Unit II at Site 1258. **A.** Foraminifer nannofossil chalk from Subunit IIA, with the Paleocene/Eocene Thermal Maximum interval and Paleocene/Eocene (P/E) boundary (interval 207-1258A-19R-5, 105–125 cm). **B.** Bioturbated calcareous chalk followed by clay, the ejecta layer, and the topmost Maastrichtian nannofossil-rich chalk of Subunit IIB (Cretaceous/Tertiary [K/T] boundary interval [48.5–50 cm]) (interval 207-1258B-27R-1, 40–60 cm). (Continued on next page.)

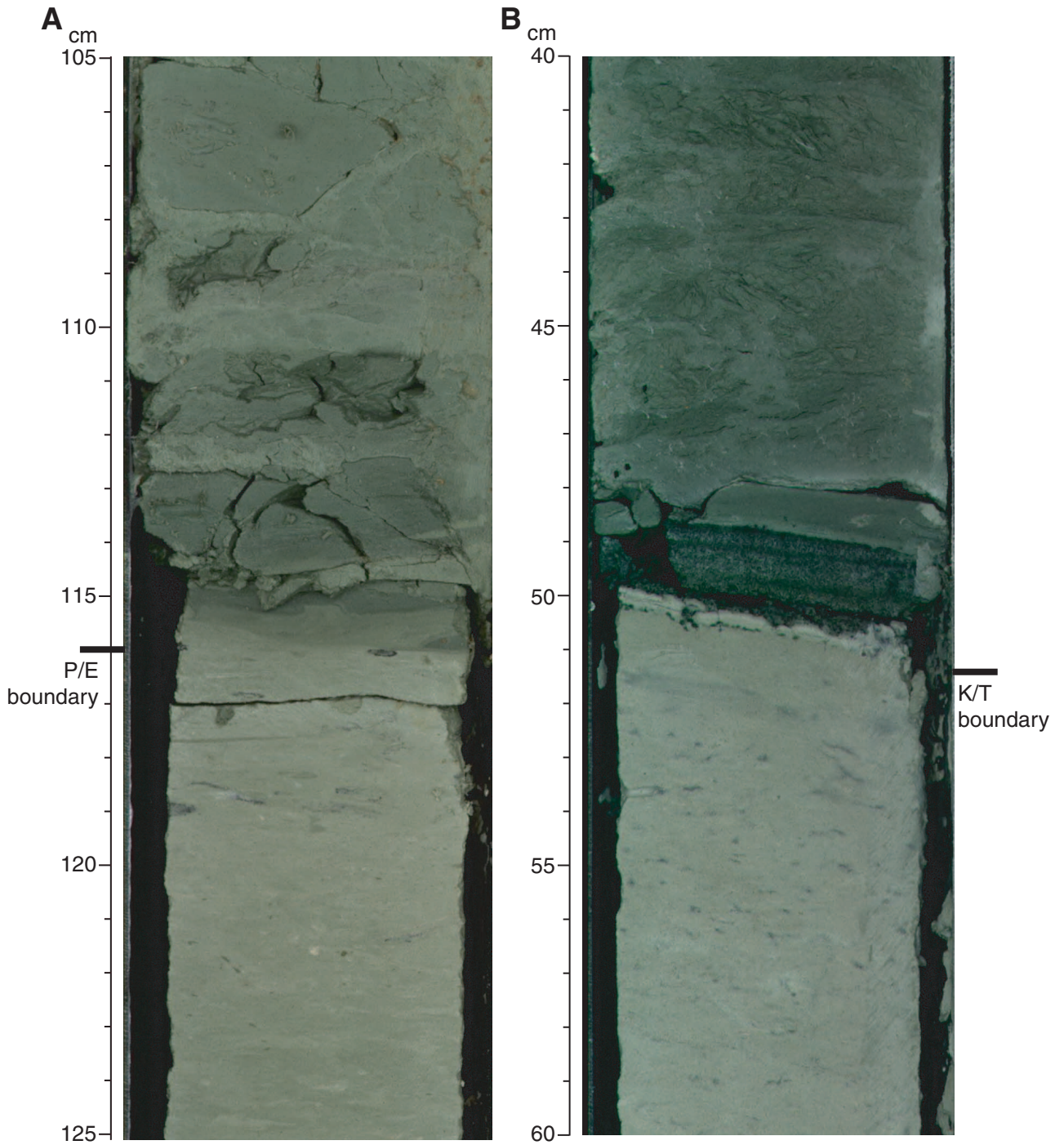
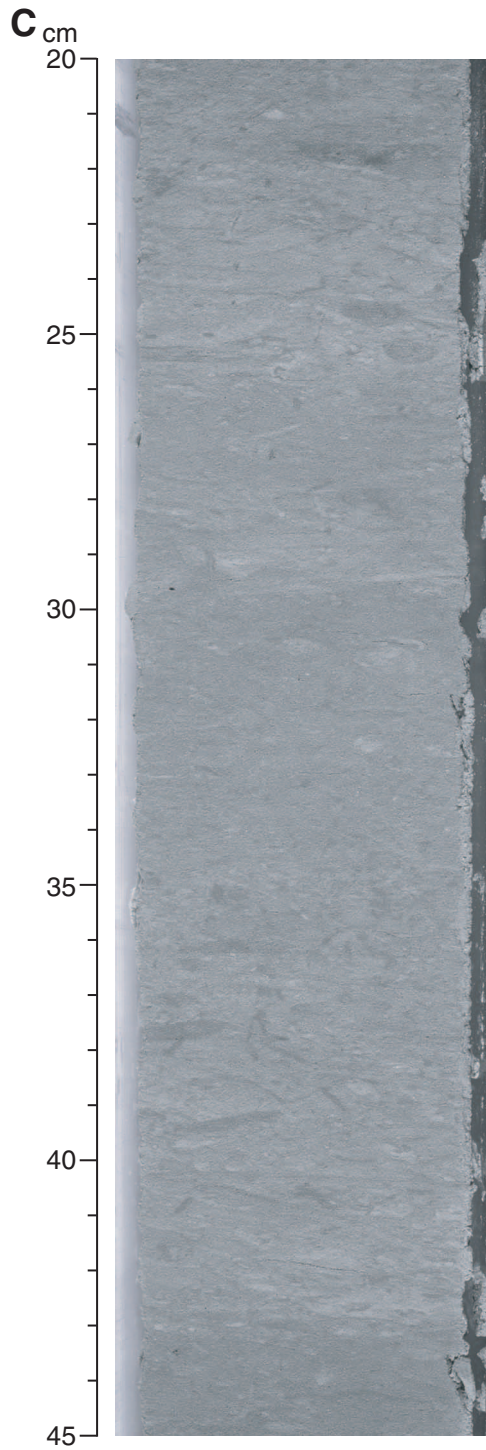
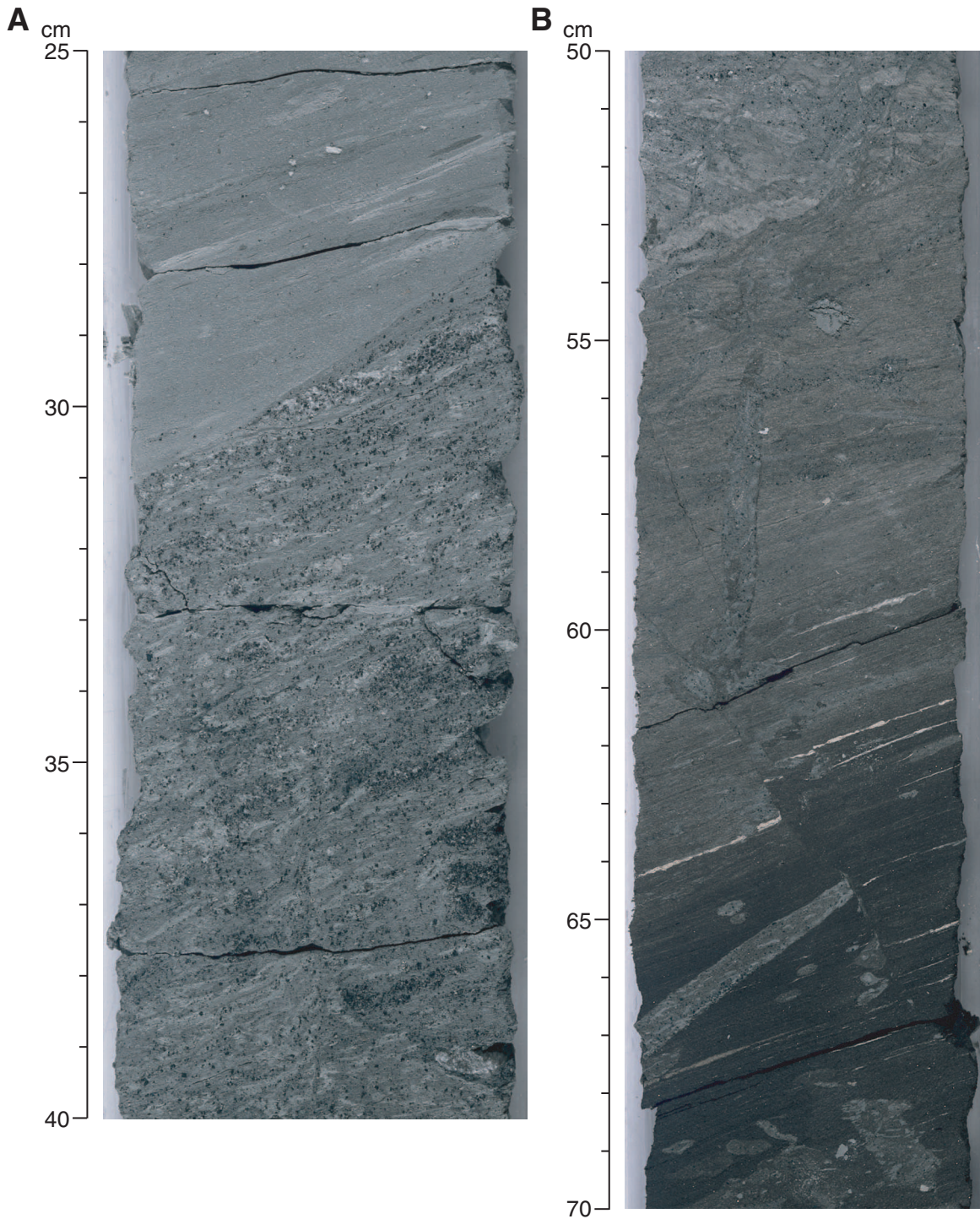


Figure F5 (continued). C. Cyclic dark–light alternations characteristic of the chalk of Subunit IIC (interval 207-1258A-32R-5, 20–45 cm).



**Figure F6.** Close-up photographs of representative lithologies for the transition from calcareous nannofossil clay in lithostratigraphic Unit III to black shale in lithostratigraphic Unit IV. **A.** The transition from calcareous nannofossil clay of Unit III (25–31 cm) (note the distinct burrows) into the basal glauconitic interval of Unit III (31–40 cm) (interval 207-1258B-44R-2, 25–40 cm). **B.** The transition from glauconitic interval via leached brownish laminated sediments (Unit III) into black shale (Unit IV; note burrows with glauconite in laminated black shale) (interval 207-1258B-44R-2, 50–70 cm). (Continued on next page.)



**Figure F6 (continued).** C. Gravity flow deposit without obvious internal fabric in the uppermost part of Unit IV (interval 207-1258B-44R-3, 78–98 cm). The sediment contains phosphatic nodules, a clast of laminated black shale, and shell fragments. D. Sharp contact (96 cm) between calcareous nannofossil clay of Unit III and laminated black shale of Unit IV (interval 207-1258C-15R-3, 85–100 cm). The basal sediment of Unit III contains poorly preserved radiolarians, glauconite, quartz, and feldspar. The fabric of the black shale in the topmost few centimeters is strongly disturbed.

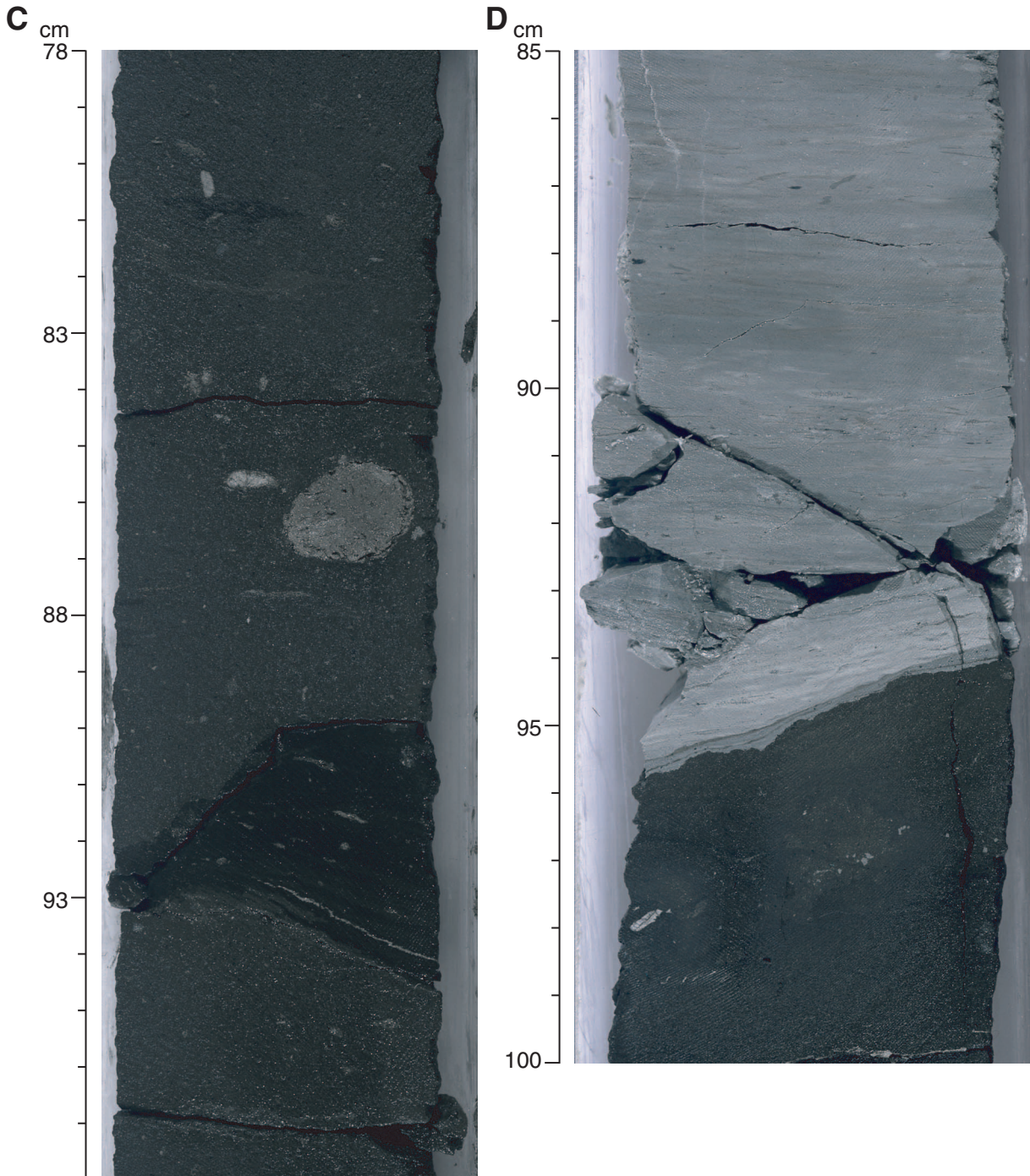
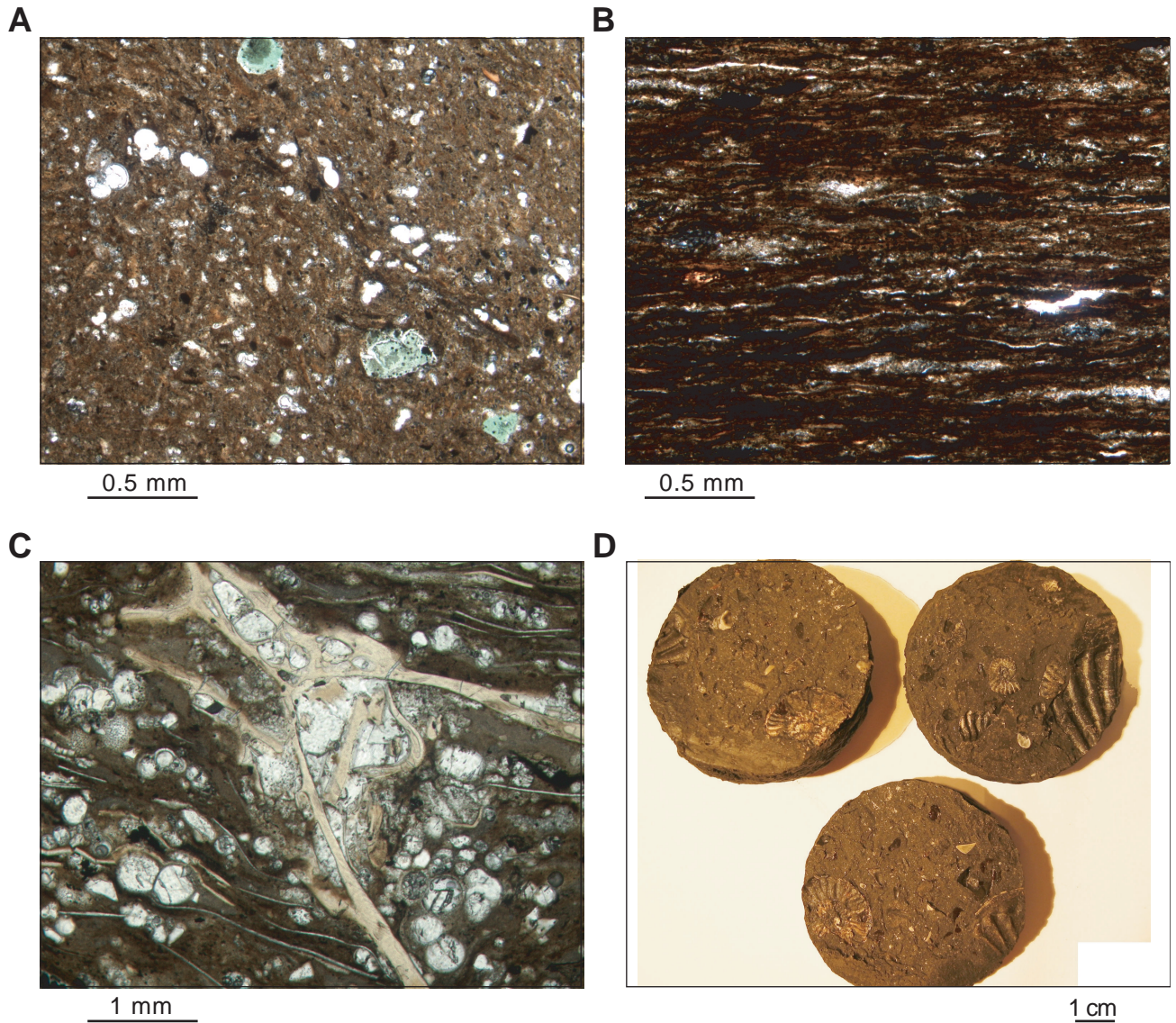


Figure F7. A. Photomicrograph of glauconite and quartz-rich sediments at the base of Unit III (Sample 207-1258C-15R-3, 93–97 cm; TS 72; polarized light). B. Photomicrograph of thinly laminated black shale of Unit IV with abundant organic matter (TOC = 28 wt%), rare nannofossil-rich fecal pellets (bright streaks), and abundant clay (Sample 207-1258B-45R-4, 114–117 cm; TS 59; parallel light). Note the absence of foraminifers. C. Photomicrograph of sediments enriched in fish fragments (vertebra), pelecypod fragments, and planktonic foraminifers (Sample 207-1258A-49R-3, 97–100 cm; TS 45; parallel light). D. Photograph of bedding plane surface of black shales of Unit V showing abundant ammonites, bivalves, and fish fragments (Section 207-1258C-31R-CC).



**Figure F8.** Close-up photographs of representative lithologies from the black shale of Unit IV. **A.** Typical cyclicity developed in the upper part of the unit (interval 207-1258A-43R-3, 10–60 cm). Clay/organic matter-rich intervals (dark) alternate with foraminifer-rich intervals (light). Note phosphoritic stringers and phosphatic nodules in the dark parts of a cycle (top and bottom of photograph). **B.** Concentrations of fish debris and phosphatic nodules (coproliths) in distinct intervals, which are interpreted as tempestites (interval 207-1258B-53R-1, 8–28 cm). (Continued on next page.)

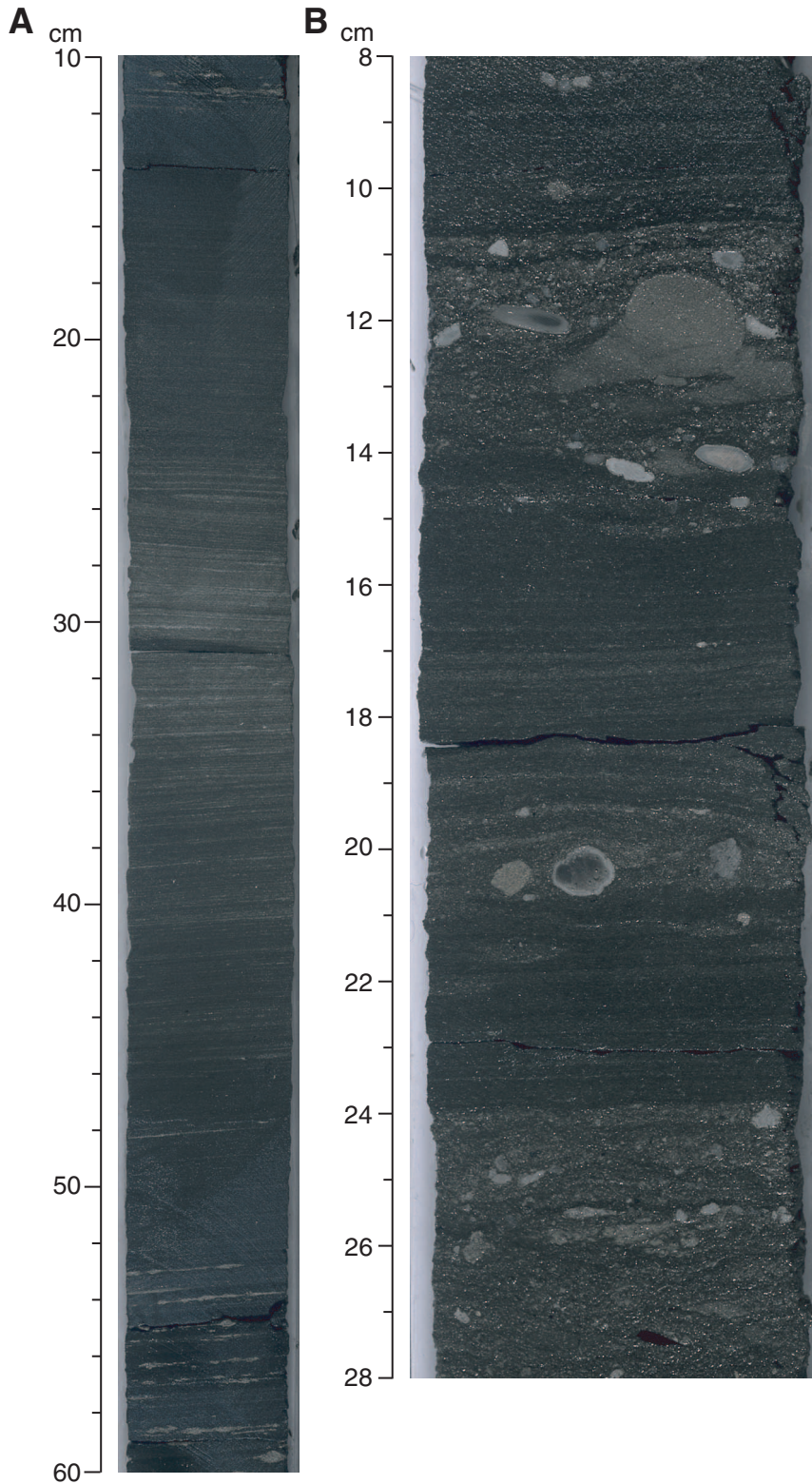
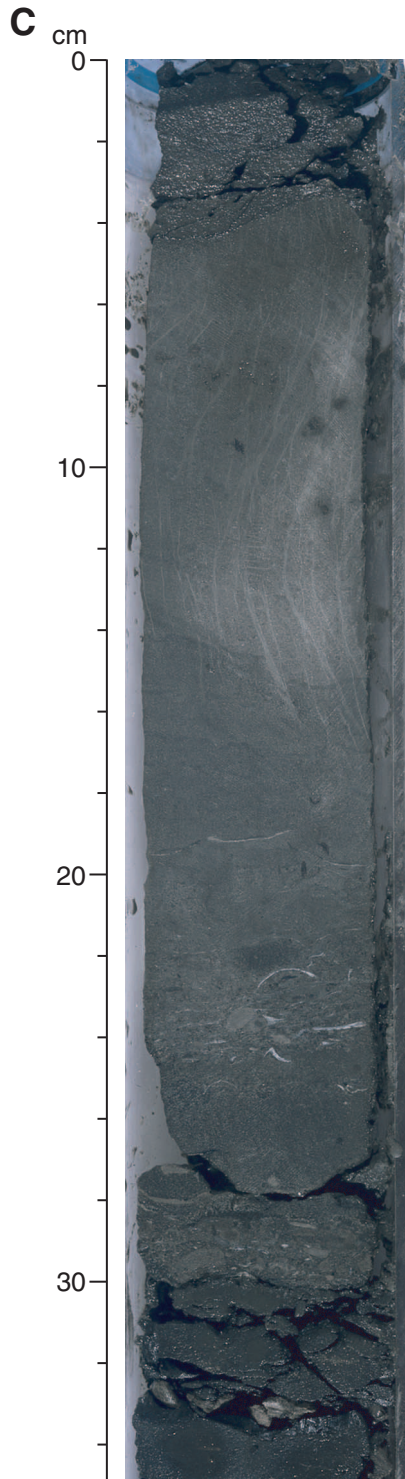


Figure F8 (continued). C. Graded interval typical for the basal part of Unit IV (interval 207-1258A-50R-2, 0-35 cm). Note the large shell fragments 3 cm above the base of the graded interval.



**Figure F9.** Close-up photographs of minor lithologies in the black shale of Unit IV. **A.** Correlative bluish layer (present in all three holes at this site) of coarse-grained diagenetic calcite (interval 207-1258B-54R-1, 5–15 cm). Calcite growing from top and bottom shows pinnacle-like crystal structure. **B.** Concentration of fish debris with the coarser but less dense skeletal elements concentrated in the upper part of the interval (interval 207-1258B-56R-2, 29–39 cm). This structure is frequently observed in tempestites. (Continued on next page.)

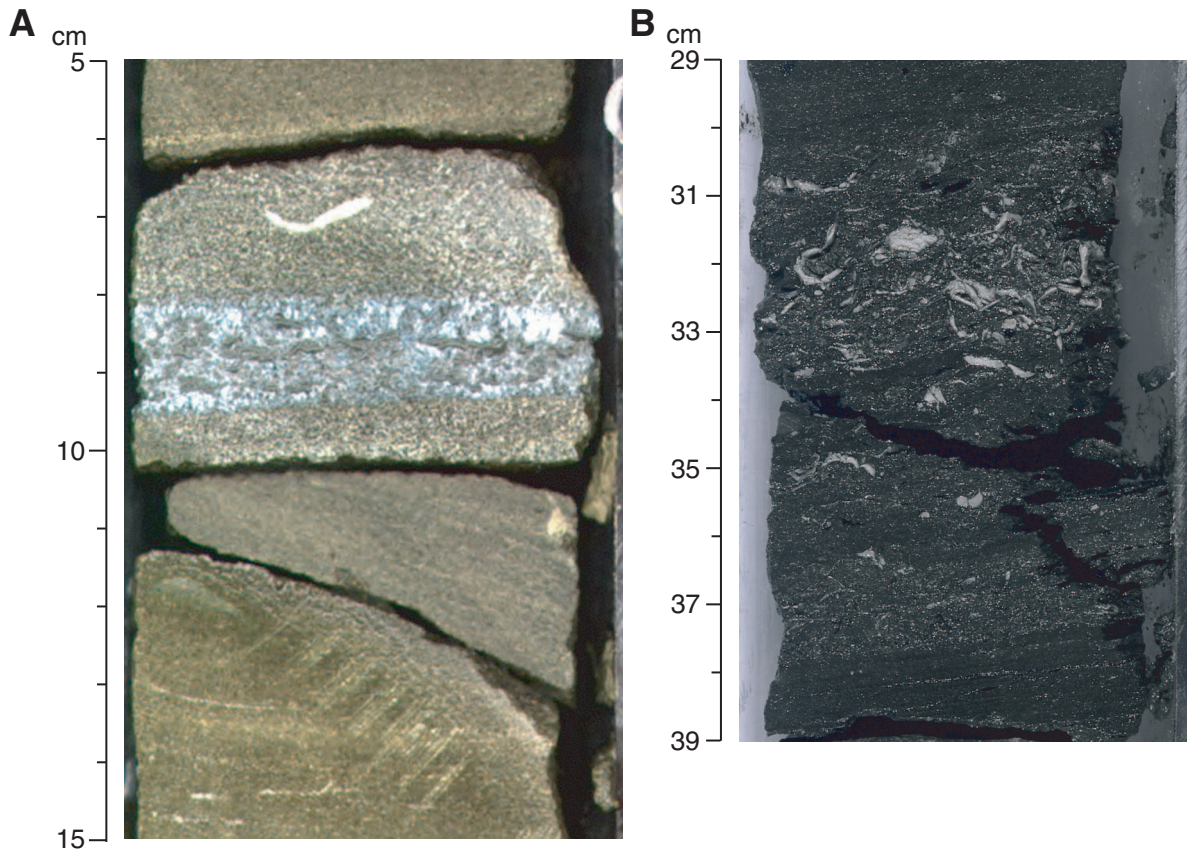


Figure F9 (continued). C. Sequence of shell lags in graded limestone intervals (interval 207-1258A-49R-3, 90–115 cm). D. Parts of a fish skeleton, with the backbone displaying four vertebrae oriented from upper middle-left middle of the image (Section 207-1258B-45R-4, 75 cm).

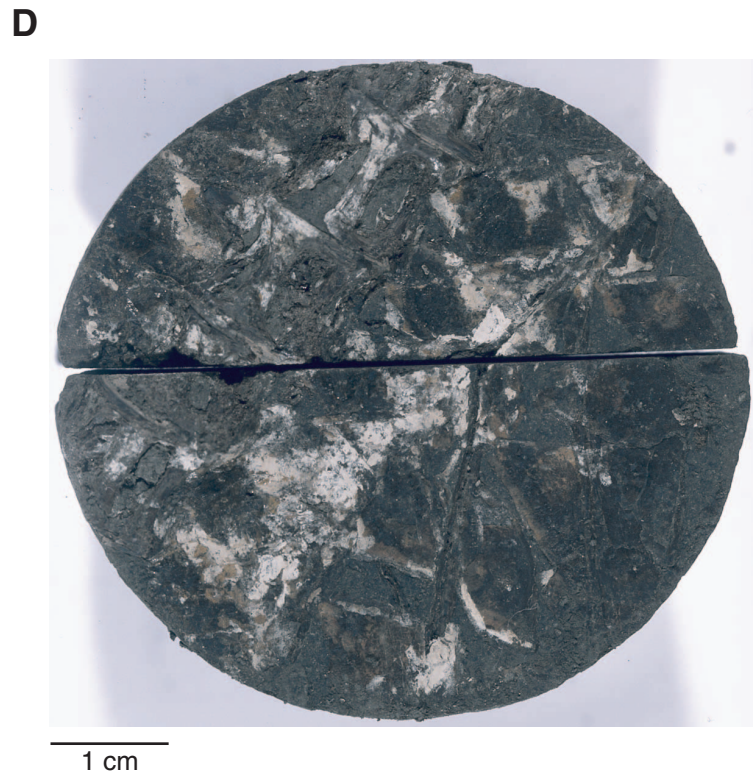
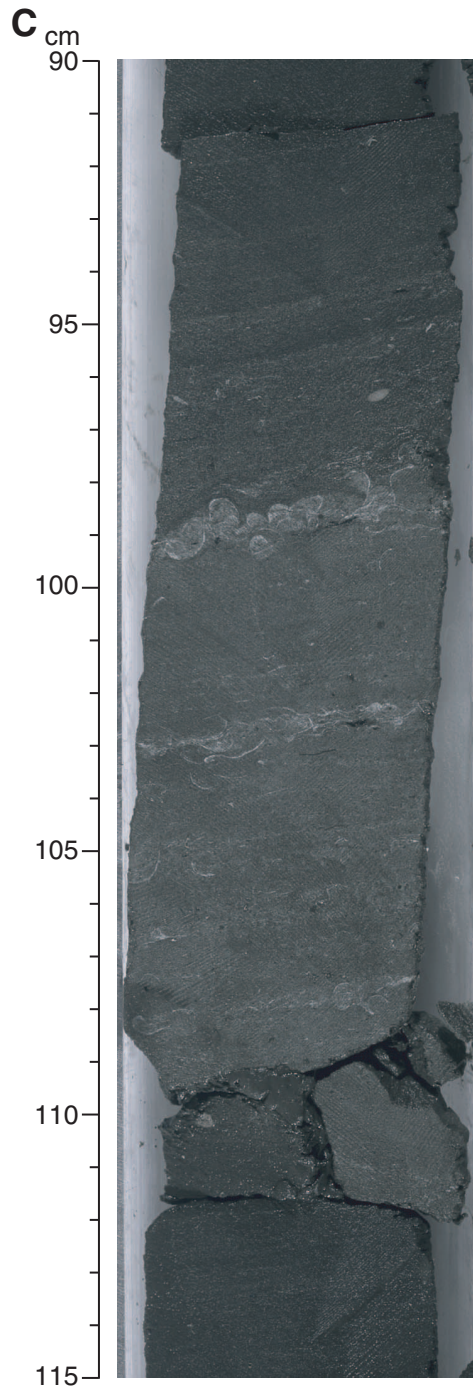
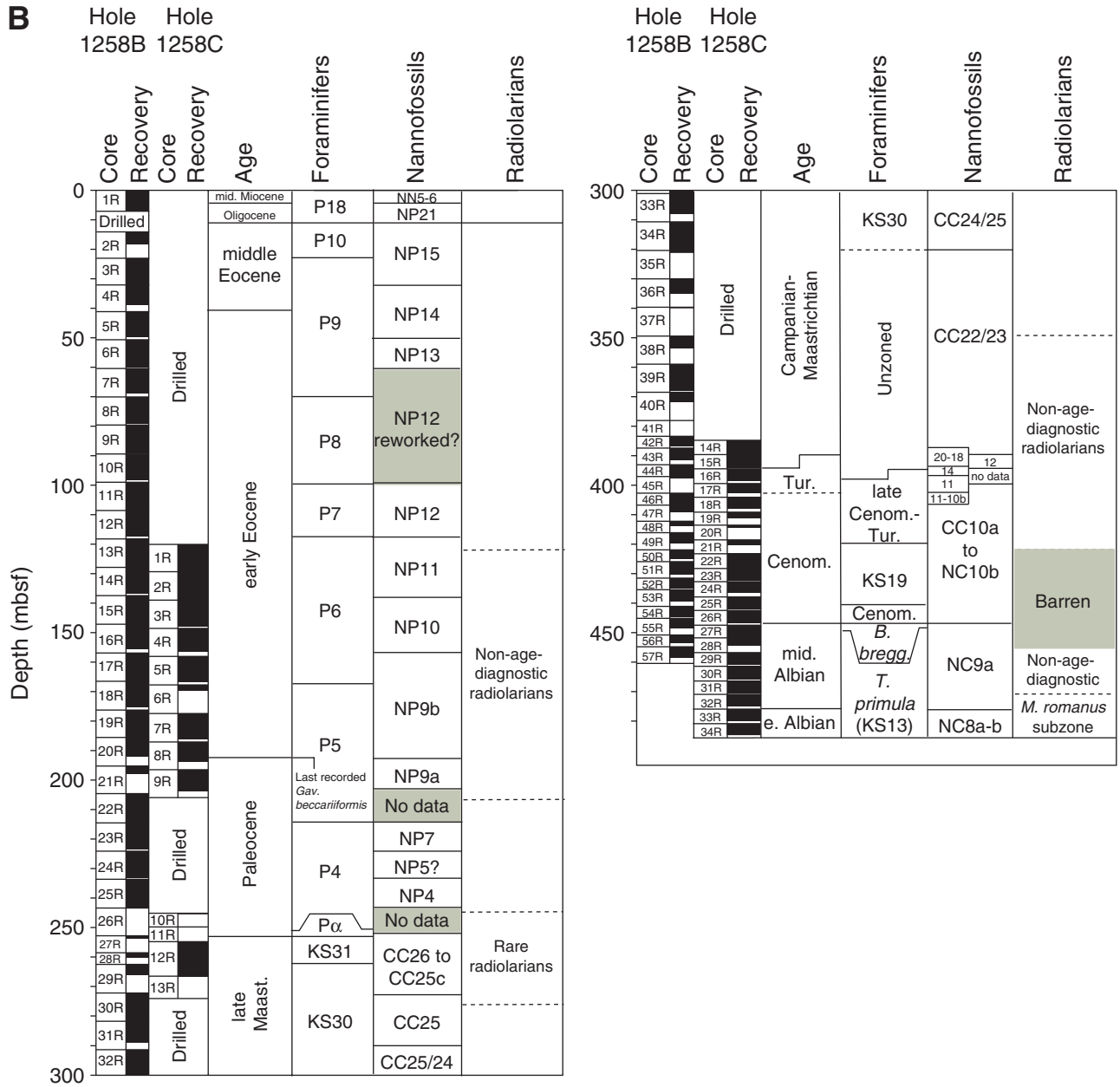




Figure F10 (continued). B. Planktonic foraminifer, calcareous nannofossil, and radiolarian biozonation of Holes 1258A and 1258B.



**Figure F11.** Shipboard paleomagnetic data and initial interpretations of inclination clusters of the Eocene–Cretaceous of Holes 1258A, 1258B, and 1258C. The paleomagnetic data from the holes have been compared using the composite depth offsets, and these adjustments are shown schematically for each hole (rightmost columns). Magnetic inclinations are from intact blocks (excluding measurements in 5 cm of the end of each blocks) after 15-mT demagnetization. The inclination data exclude measurements near the background noise limit of the cryogenic magnetometer ( $<3 \times 10^{-5}$  A/m); therefore, measurements with intensities  $<5 \times 10^{-5}$  A/m are not considered reliable. In addition, the upper 20 cm of each core that commonly displays spurious high-intensity magnetization or downhole contamination, and the upper 5 cm of each section that is influenced by magnetization carried by the blue-colored end cap are excluded. The displayed inclinations are either 3-point running means (solid circles), 2-point means (open circles), or single-level data (open triangles, from the central portion of blocks between 10 and 15 cm long, or from isolated levels in a larger block in which the adjacent measurements were  $<5 \times 10^{-5}$  A/m). The magnetic intensity column is from Hole 1258A and includes NRM (small orange dots, are a 21-point running mean) and after 15-mT demagnetization (small black dots; with the large blue dots being a 101-point logging-mean average). Magnetic susceptibility of Hole 1258A, obtained using a magnetic susceptibility core logger (MSCL), is shown by green dots in the rightmost column. Shipboard assignment of polarity zones was based on clusters of magnetic inclinations from intact blocks (to right of polarity zone column), as delimited by the thin lines. Zones of positive inclinations (originally considered to be normal polarity zones) = black or medium gray, if reliability is less certain; negative or mixed inclinations (originally considered to be reversed polarity zones) = white or light gray, if reliability is less certain. Uncertain inclination characteristics or gaps in data coverage = cross hatched. The shipboard interpretations of polarity zones were not always supported by analyses of magnetic characteristics during progressive thermal demagnetization of minicores (Fig. F12, p. 58). F = foraminifer, N = nannofossil. (This figure is available in an **oversized format**.)

**Figure F12.** Magnetostratigraphy and characteristic directions of Eocene–Cretaceous of Holes 1258A and 1258B based on shore-based analysis of minicores. The minicore data from the two holes have been merged using composite depth scales from each hole, and these adjustments are shown schematically by offset mbsf columns for each hole (rightmost columns). Polarity ratings are graded according to reliability and number of vectors utilized in the characteristic direction. R = reliable reversed polarity, INT = indeterminate, N = reliable normal polarity) (and relative placement of other points indicates degree of precision or uncertainty). Methods of polarity interpretation, polarity ratings, and derivation of characteristic inclinations and intensities are in *“Paleomagnetism,”* p. 16, in the “Explanatory Notes” chapter. Polarity zones are assigned according to clusters of individual polarity interpretations. Normal polarity zones = dark gray; reversed polarity zones = white; uncertain polarity or gaps in data coverage = cross hatched. Assignments of polarity chrons are based on the polarity zone pattern and the constraints from microfossil biostratigraphy. F = foraminifer, N = nannofossil. **(Figure shown on next page.)**

Figure F12 (continued). (Caption shown on previous page.)

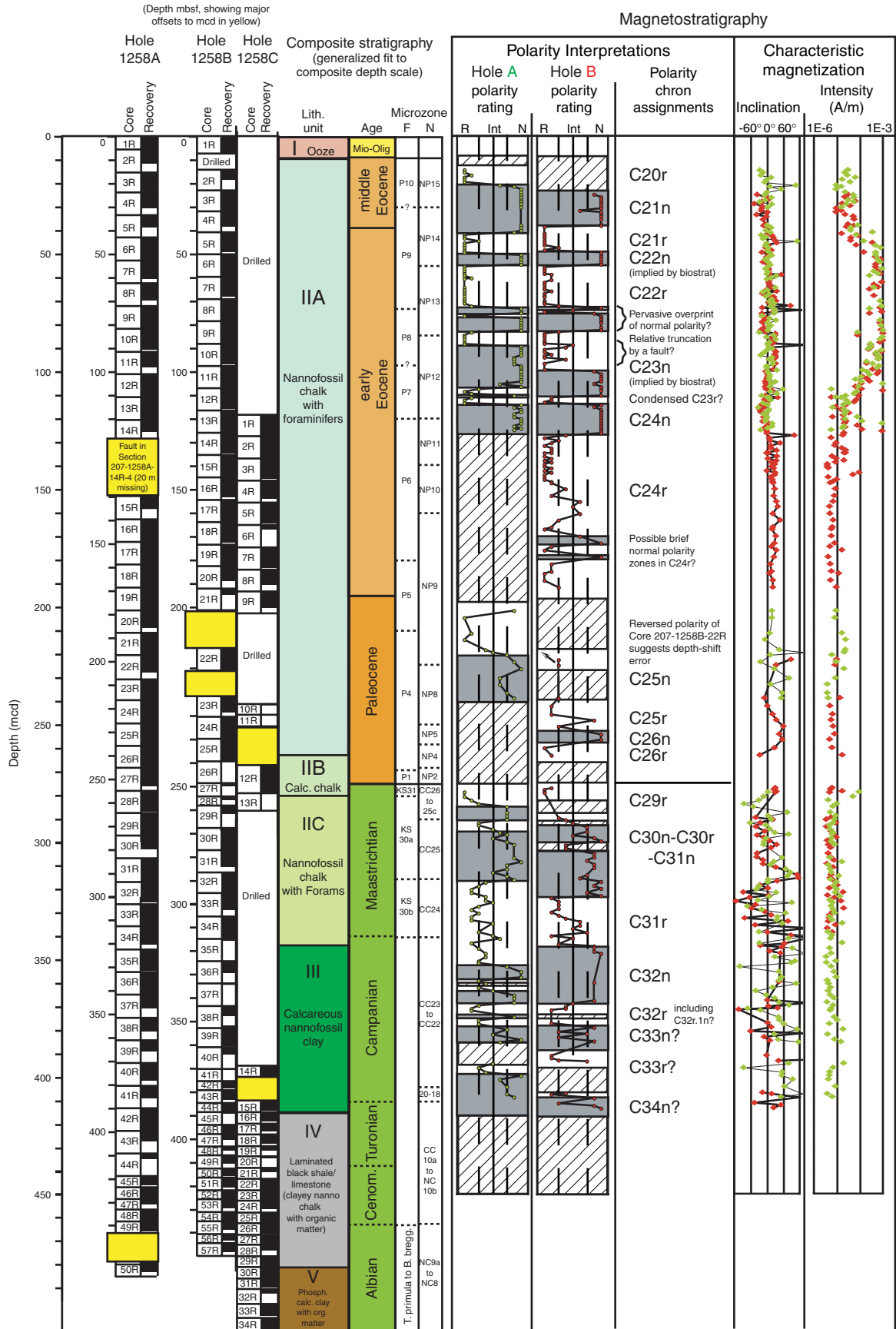


Figure F13. Composite and spliced magnetic susceptibility for the lower Eocene section of Holes 1257A (black), 1258B (blue), and 1258C (green). The composite data from Holes 1258B and 1258C are offset by a constant (10 and 20 units, respectively) for illustration purposes. All data sets are smoothed with a nine-point Gaussian filter.

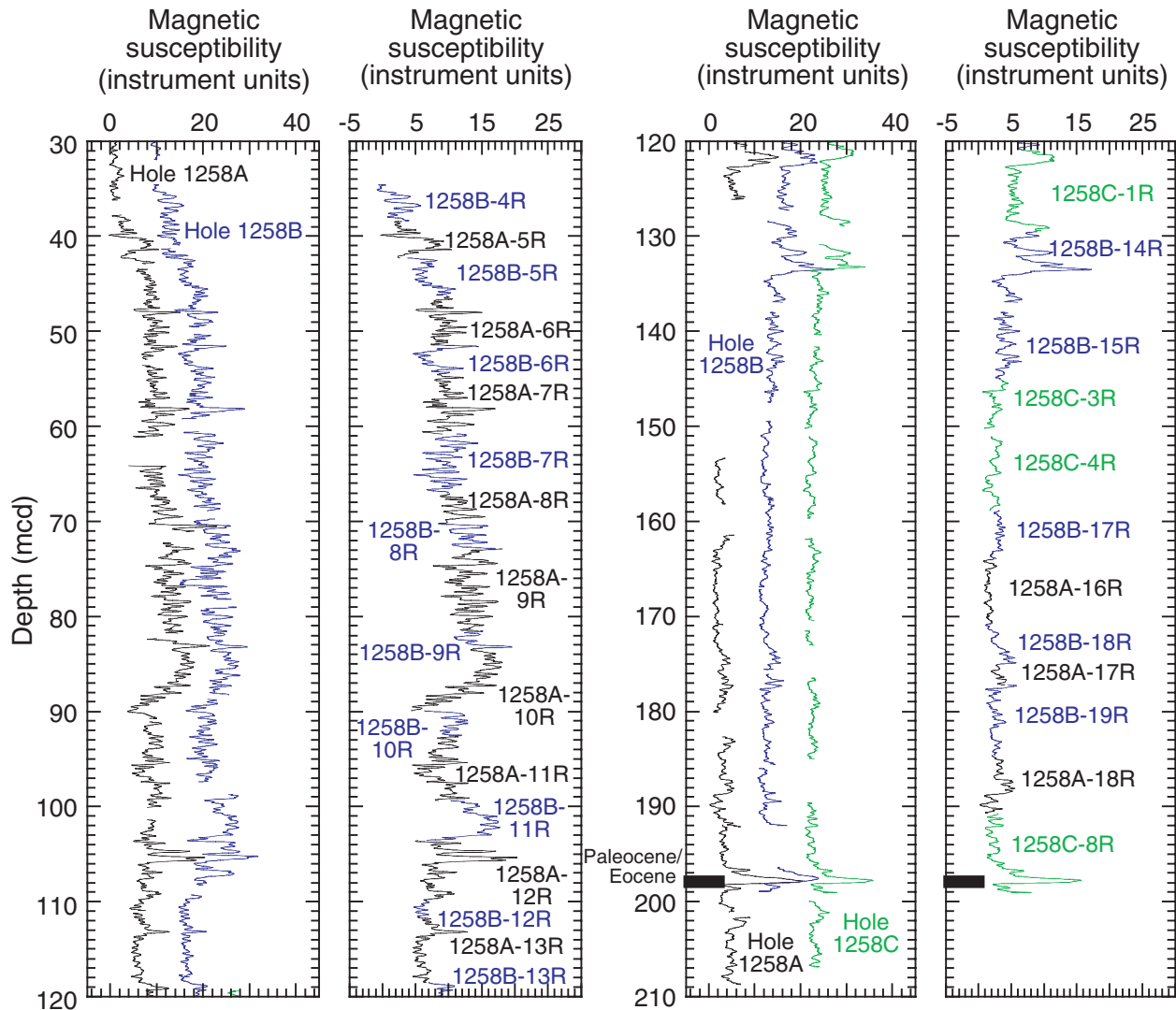
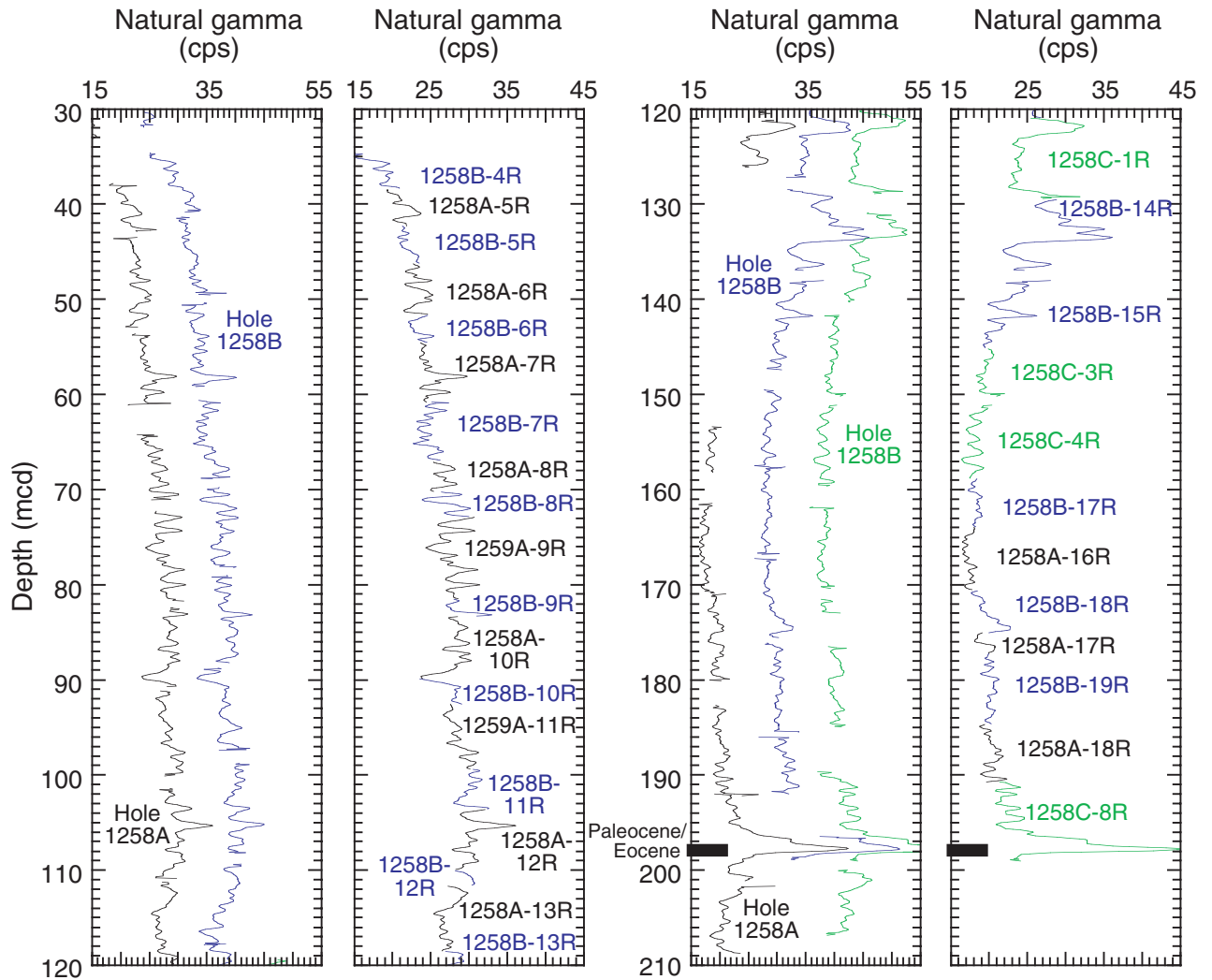


Figure F14. Composite and spliced NGR data for the lower Eocene section of Holes 1257A (black), 1258B (blue), and 1258C (green). The composite data from Holes 1258B and 1258C are offset by a constant (10 and 20 units, respectively) for illustration purposes. All data sets are smoothed with a nine-point Gaussian filter.



**Figure F15.** Magnetic susceptibility data vs. composite depth plotted along with a qualitative estimate of the confidence of the core-to-core correlations among holes at Site 1258. **A.** Data from Holes 1257A (black), 1258B (blue), and 1258C (green). The composite data from Holes 1258B and 1258C are offset by a constant (10 and 20 units, respectively) for illustration purposes. **B.** Green indicates intervals with definitive hole-to-hole correlations and good depth control resulting from core gaps being spanned. Yellow indicates intervals where good core-to-core correlations could be made (i.e., a one-to-one match of signals between holes) but definitive depth positions could not be established because coring gaps could not be spanned. Gray indicates intervals where correlations were made using similarities in trends of MST signals. The diagonal line pattern indicates intervals where hole-to-hole correlations could not be made (primarily the result of only one hole or core in that interval). P/E = Paleocene/Eocene boundary, K/T = Cretaceous/Tertiary boundary.

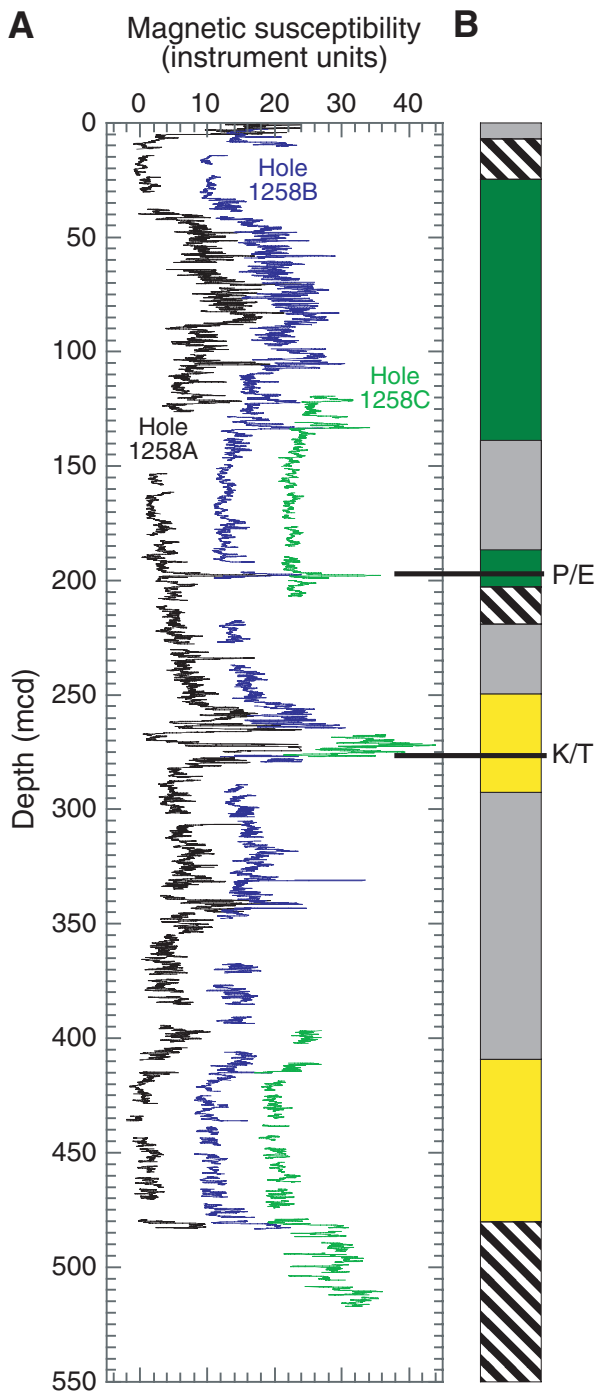


Figure F16. NGR data from Holes 1257A (black), 1258B (blue), and 1258C (green) for two intervals in the Cretaceous black shales. The composite data from Holes 1258B and 1258C are offset by a constant (60 and 120 units, respectively) for illustration purposes. Although the core-to-core correlations between holes are easily established, the core gaps could rarely be spanned in these black shale sections.

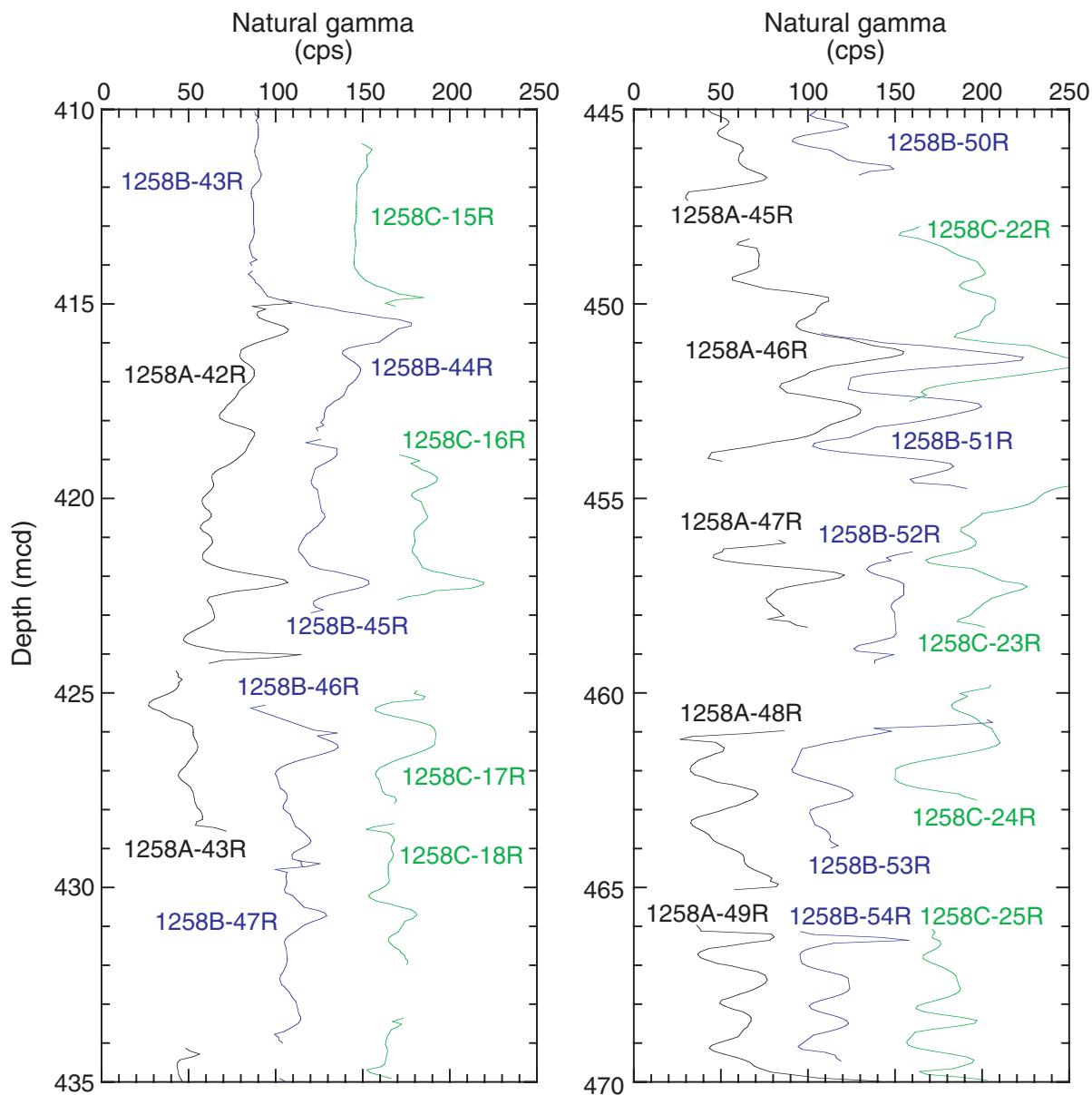


Figure F17. Age-depth plot combining available biostratigraphic and magnetostratigraphic datums from Hole 1258A. Letters A–E indicate five distinct hiatuses in between those intervals. See “Hiatuses,” p. 23, in “Age-Depth Model” in “Sedimentation Rates” for more details.

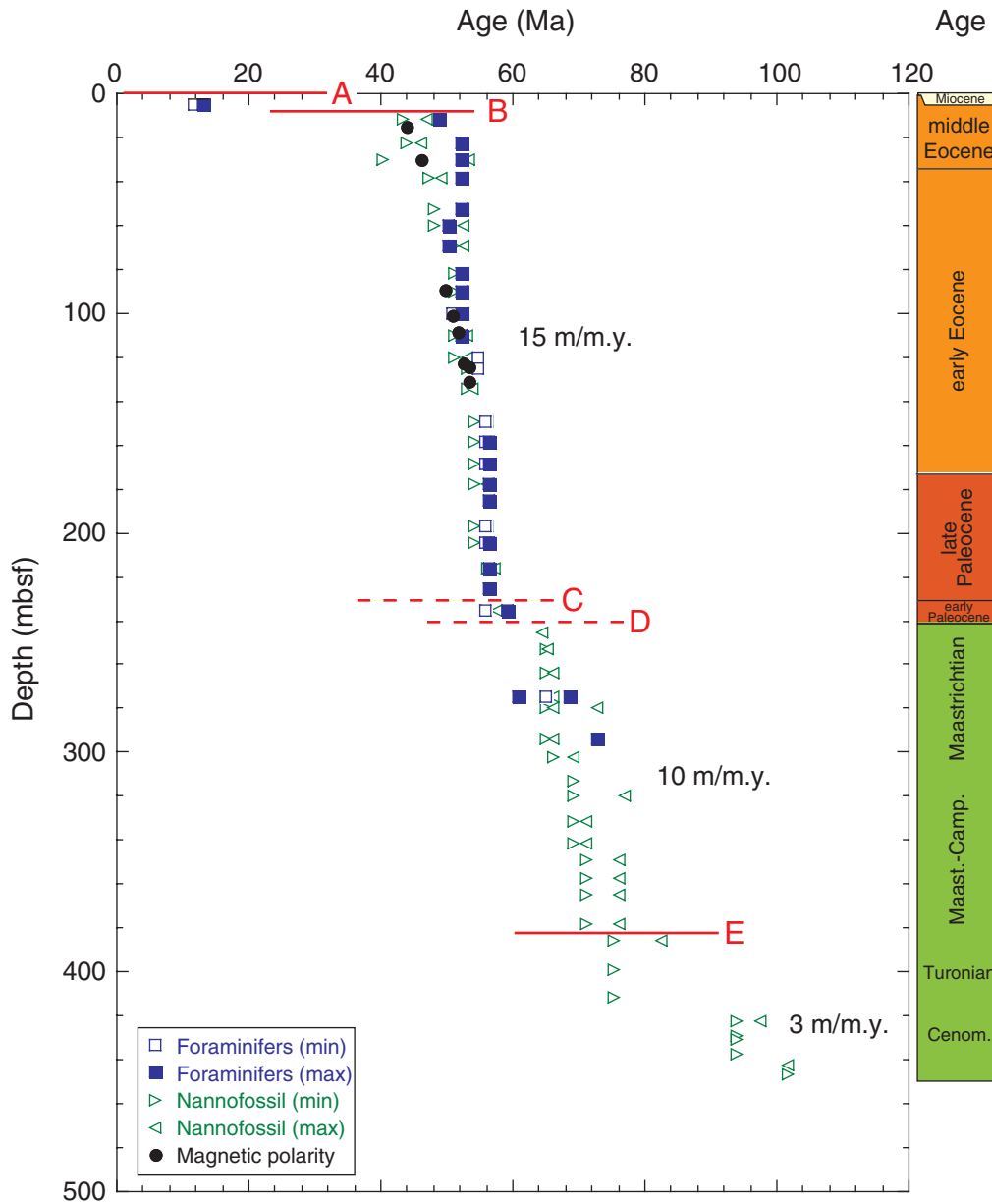


Figure F18. Rock-Eval van Krevelen-type diagram of sediment samples from Holes 1258A, 1258B, and 1258C. Organic matter appears to be predominantly Type II algal material for Unit IV and represents a mixture of Types II and III for Unit V (gray shaded area).

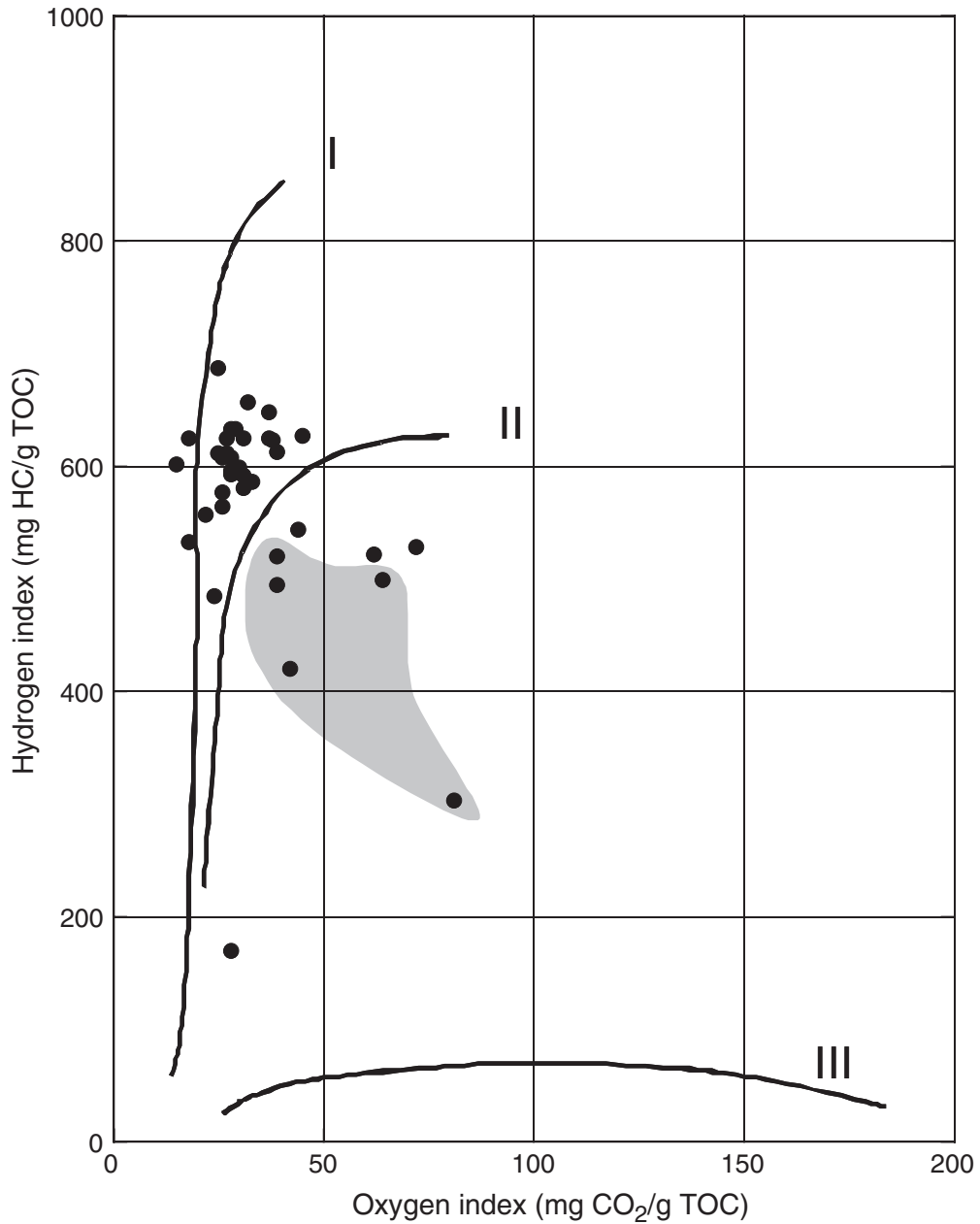


Figure F19. Comparison of concentrations of routine headspace gas (HS) and microbial methane analyses at Site 1258.

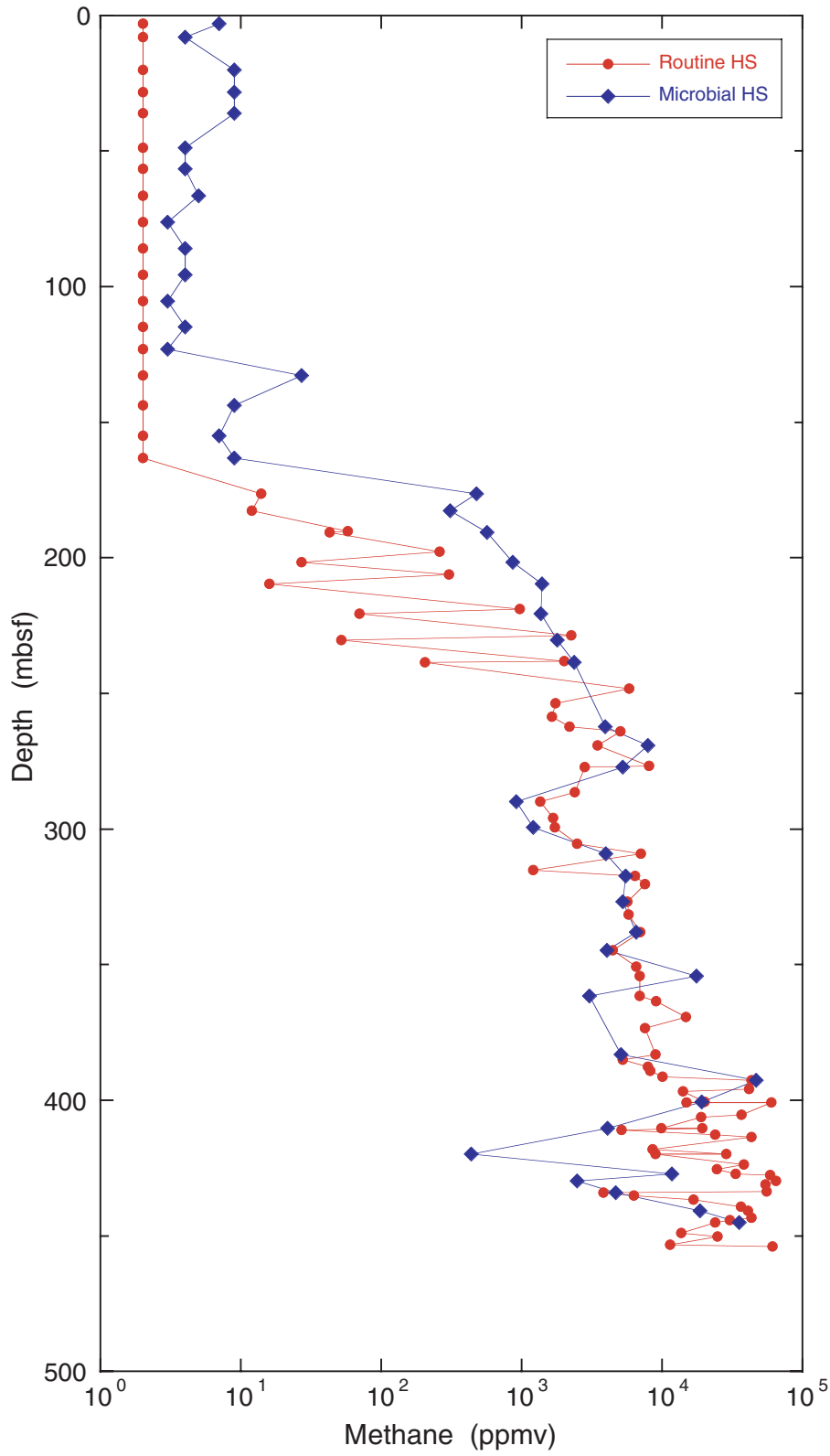


Figure F20. Profiles of chemical constituents in interstitial water at Site 1258. A. Salinity. B. Chloride. C. Sodium. D. Potassium. E. Alkalinity. F. Sulfate. G. Ammonium. H. Barium. ICP-AES = inductively coupled plasma-atomic emission spectroscopy. "?" = a questionable data point. Shaded bar = the black shale sequence (Unit IV). (Continued on next page.)

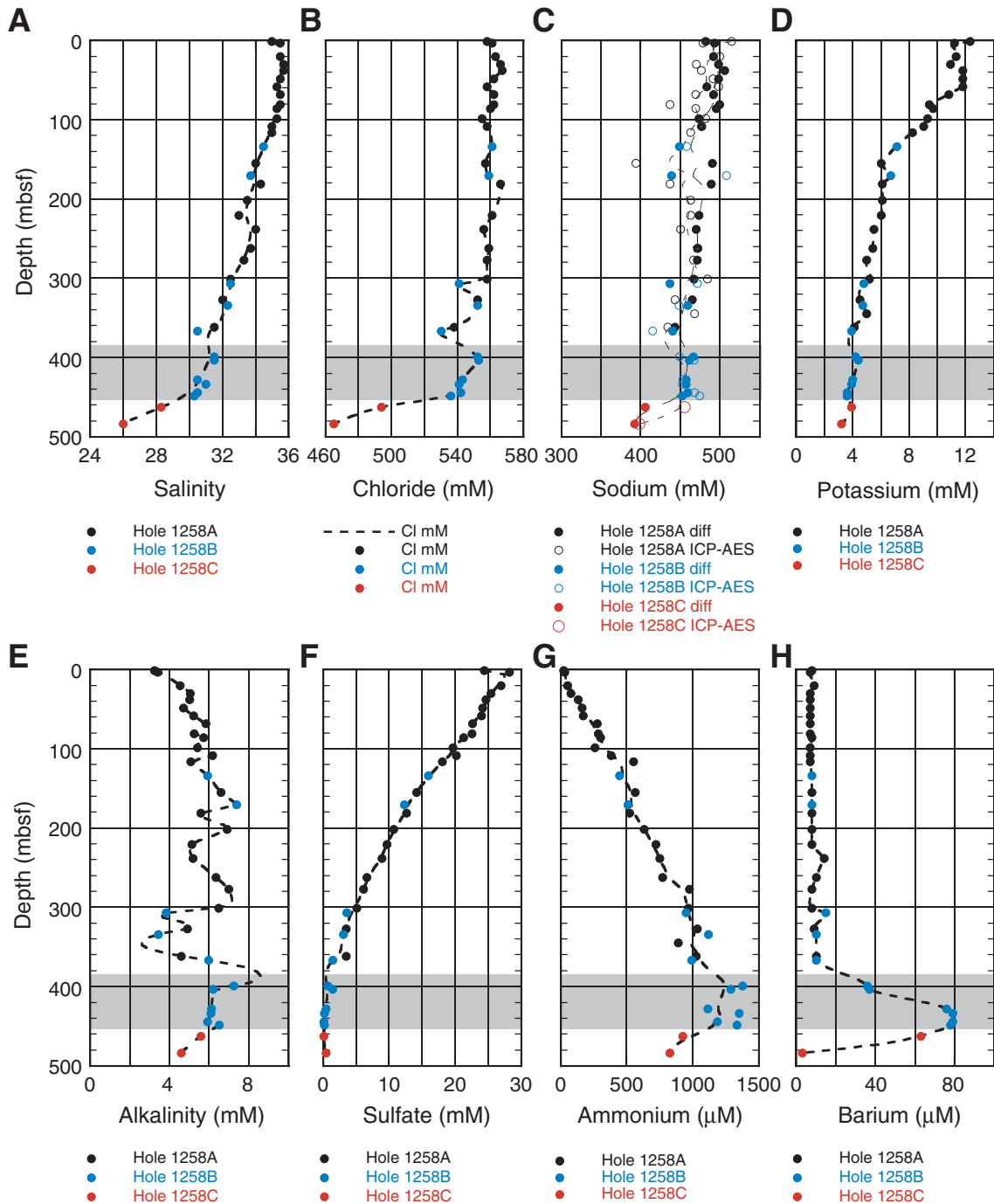


Figure F20 (continued). I. Calcium. J. Strontium. K. Magnesium. L. Lithium. M. Boron. N. Silica. O. Iron. P. Manganese.

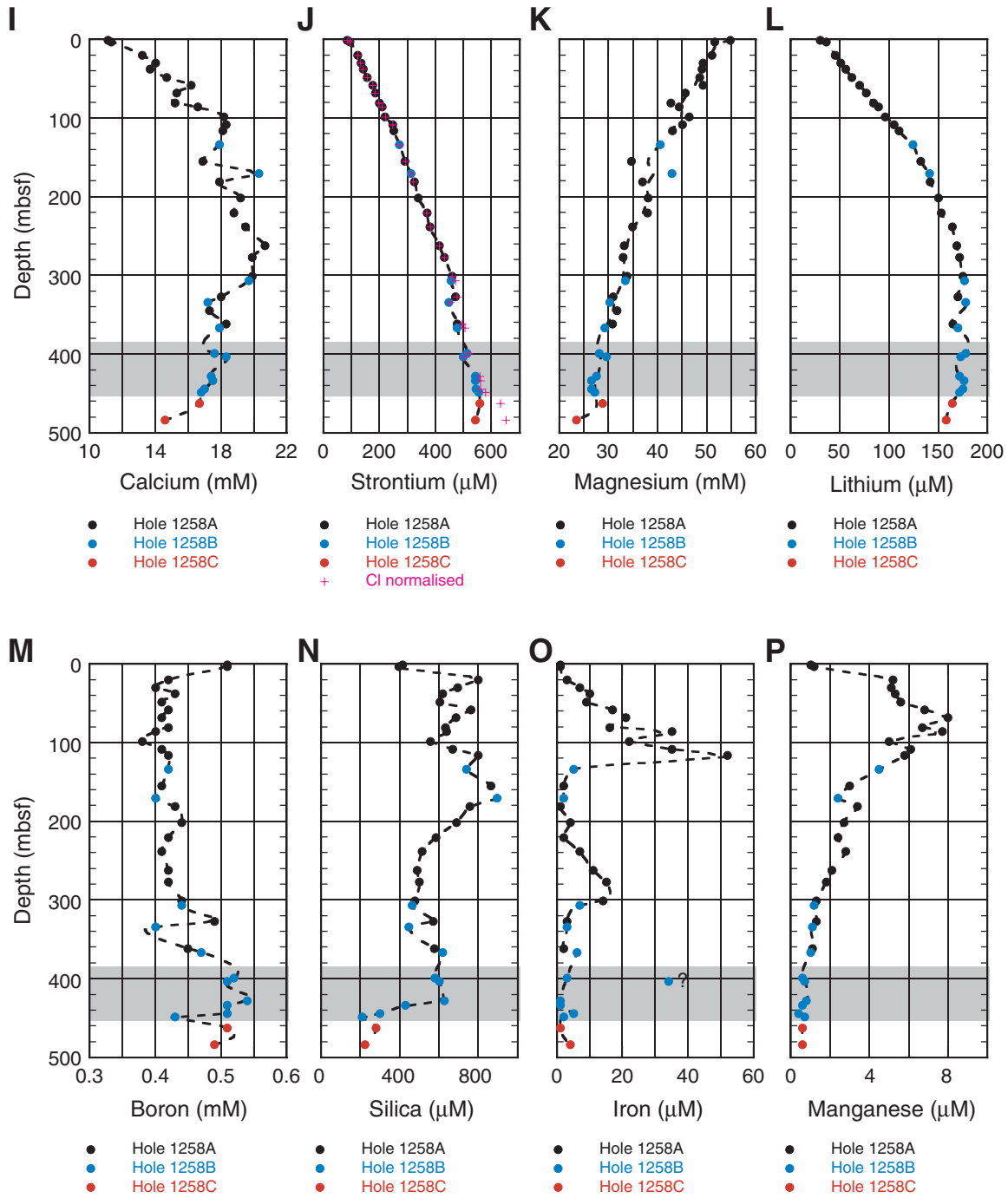


Figure F21. Sample bulk density vs. MST gamma ray attenuation (GRA) bulk density at Site 1258. Red = Hole 1258A, blue = Hole 1258B.

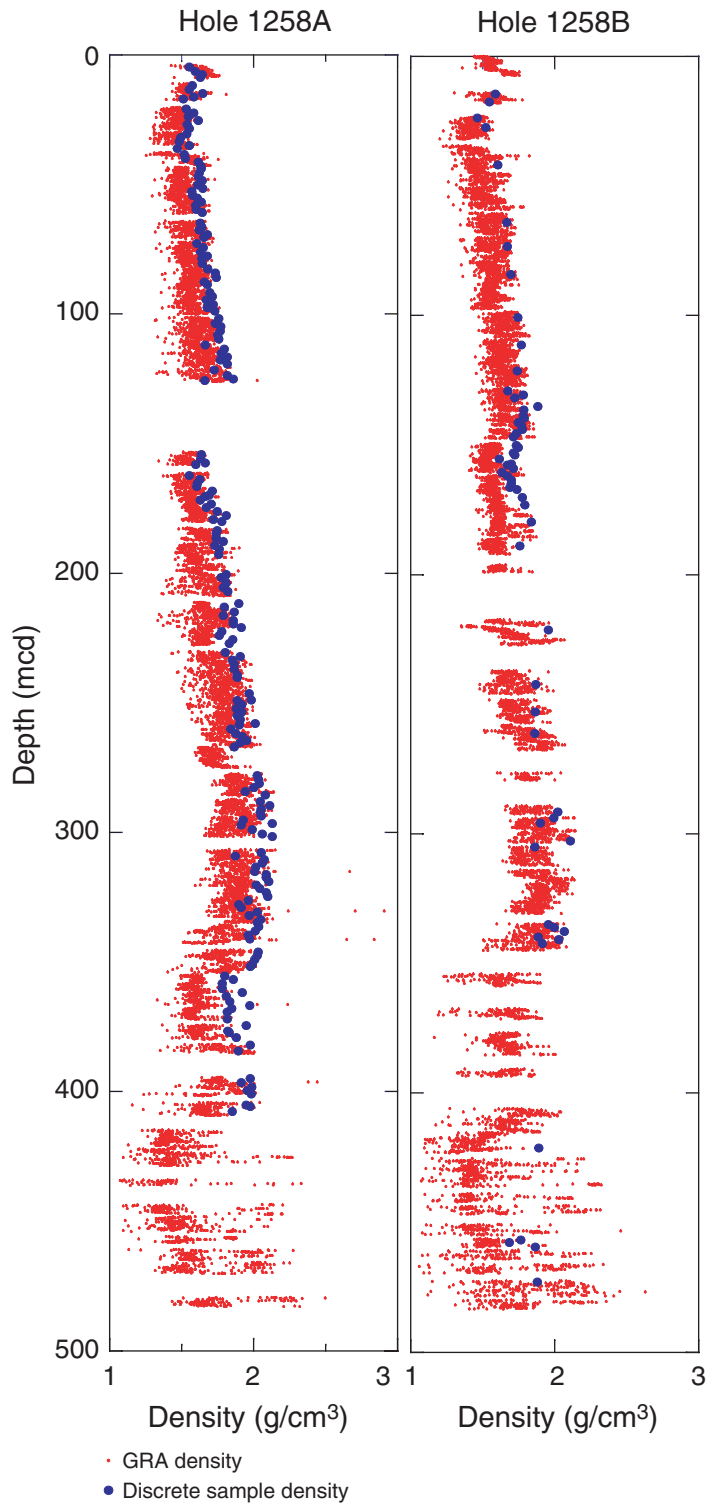


Figure F22. Bulk density, *P*-wave velocity, grain density, and porosity of discrete samples at Site 1258. Red = Hole 1258A, blue = Hole 1258B.

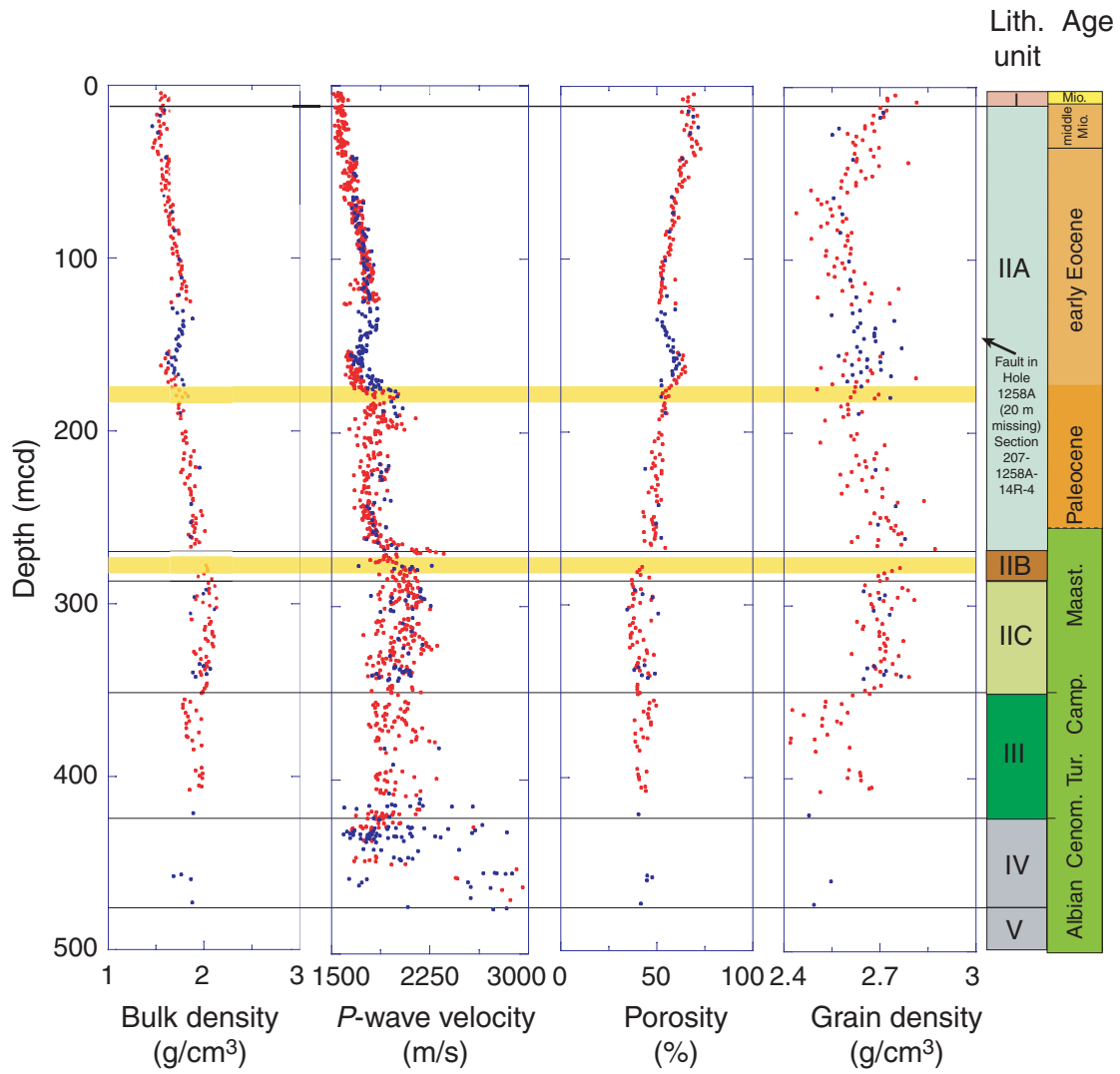


Figure F23. *P*-wave velocity measurements from split cores at Site 1258 and *P*-wave anisotropy measured on 8-cm<sup>3</sup> cube samples from Hole 1258B. For anisotropy calculations, see “Compressional Wave Velocity,” p. 37, in “Physical Properties” in the “Explanatory Notes” chapter. Red = Hole 1258A, blue = Hole 1258B.

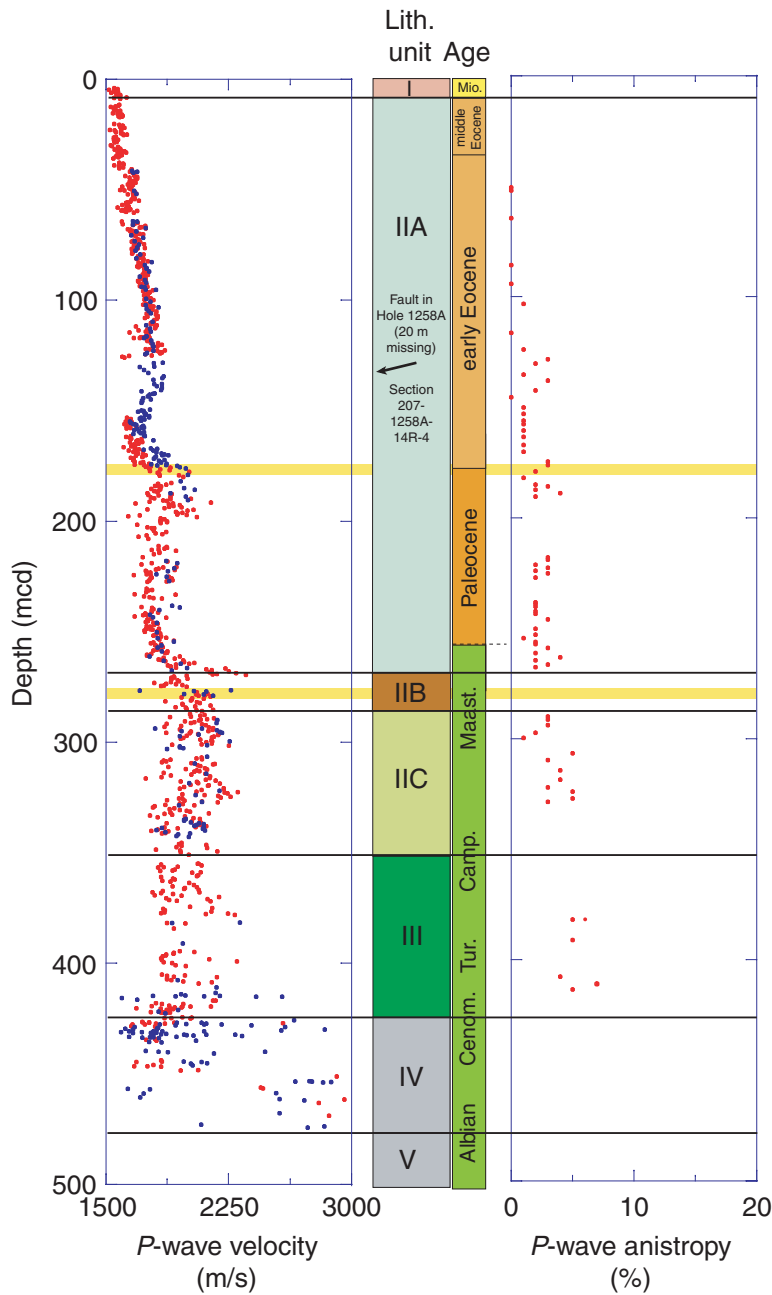


Figure F24. MST data vs. lithostratigraphic units and discrete carbonate measurements (see “Organic Geochemistry,” p. 24) from A. Hole 1258A. NGR = natural gamma radiation. (Continued on next two pages.)

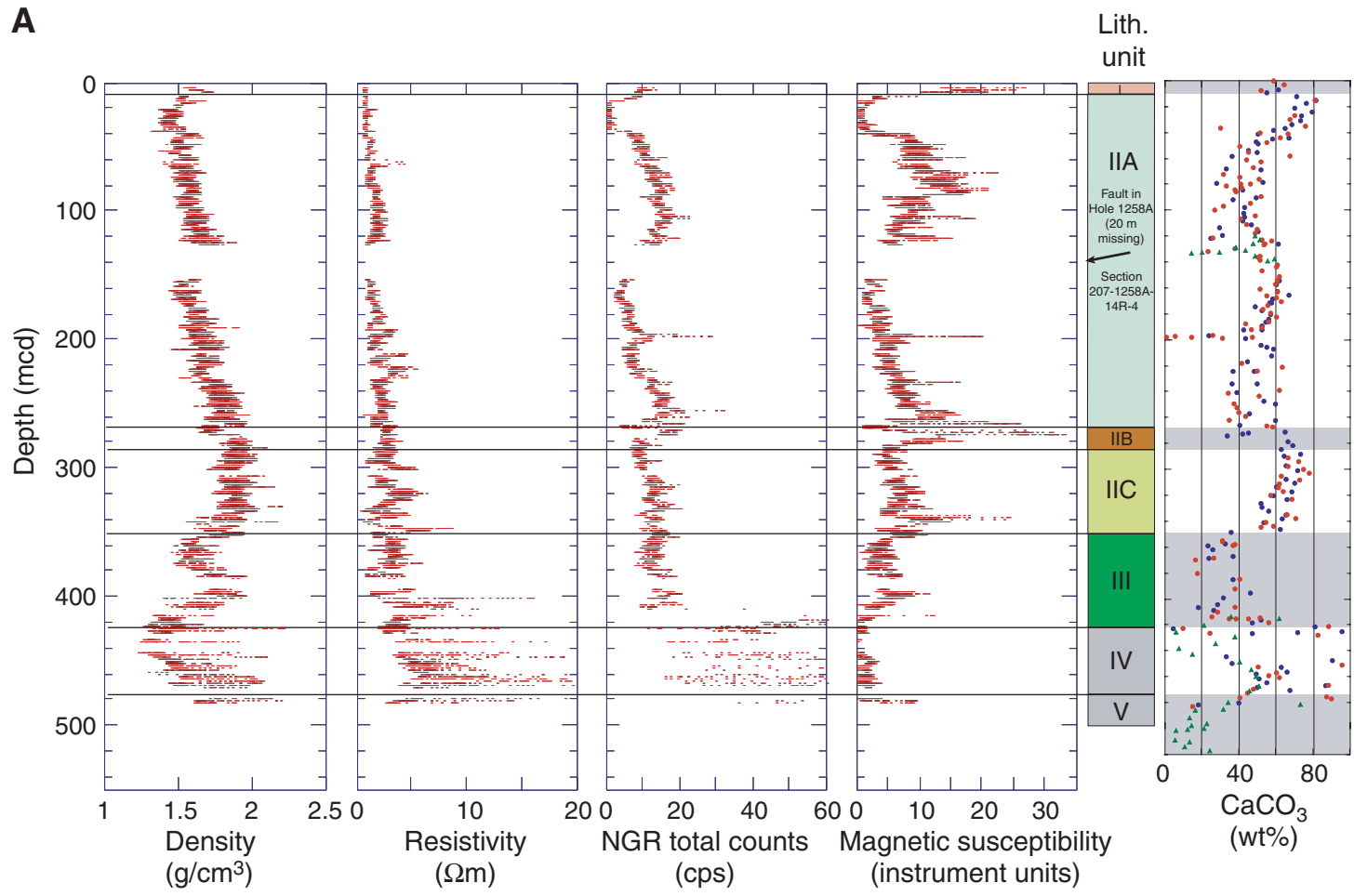


Figure F24 (continued). B. Hole 1258B.

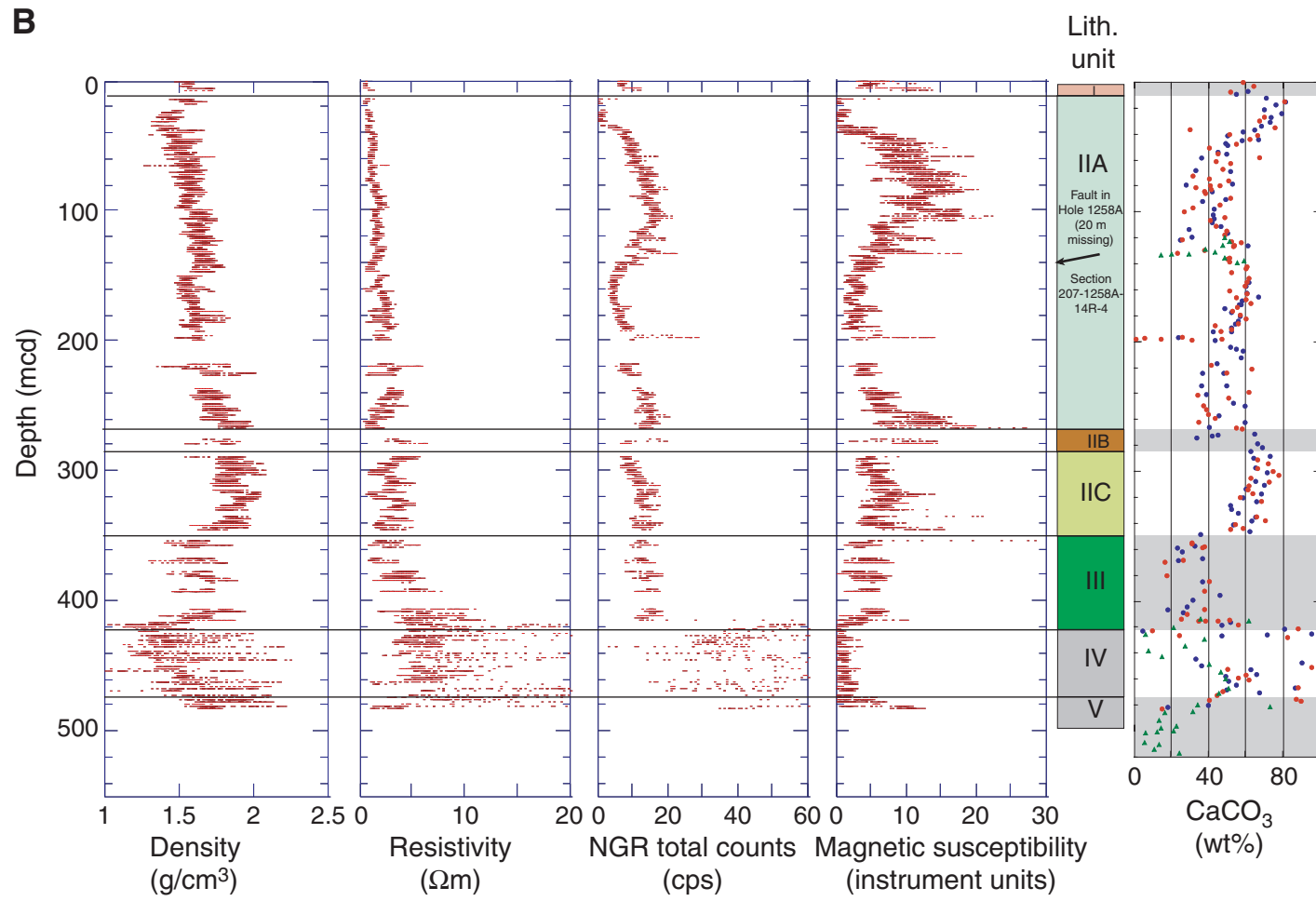


Figure F24 (continued). C. Hole 1258C.

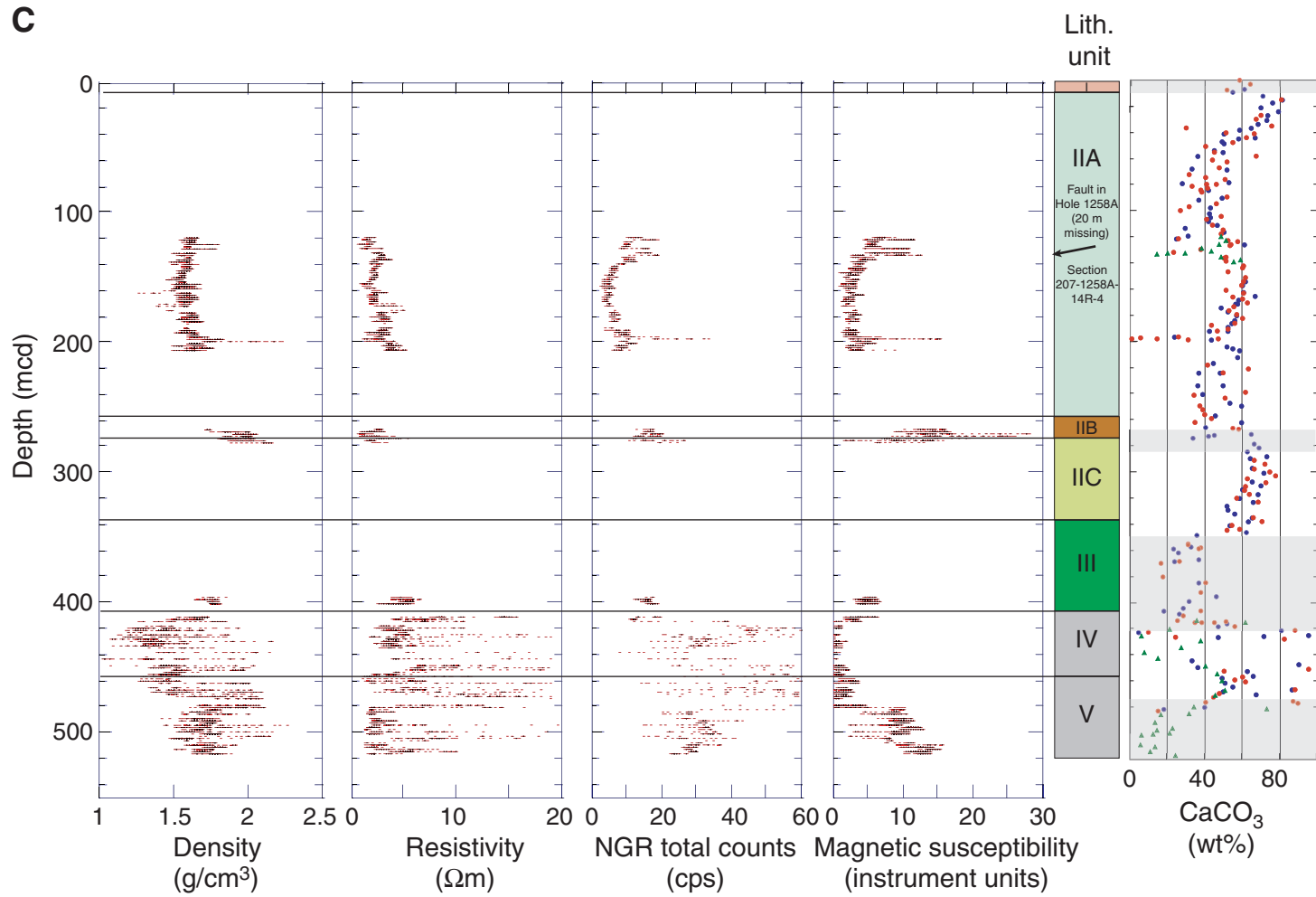


Figure F25. High-resolution MGT gamma ray logs from Hole 1258C. CGR = computed gamma ray.

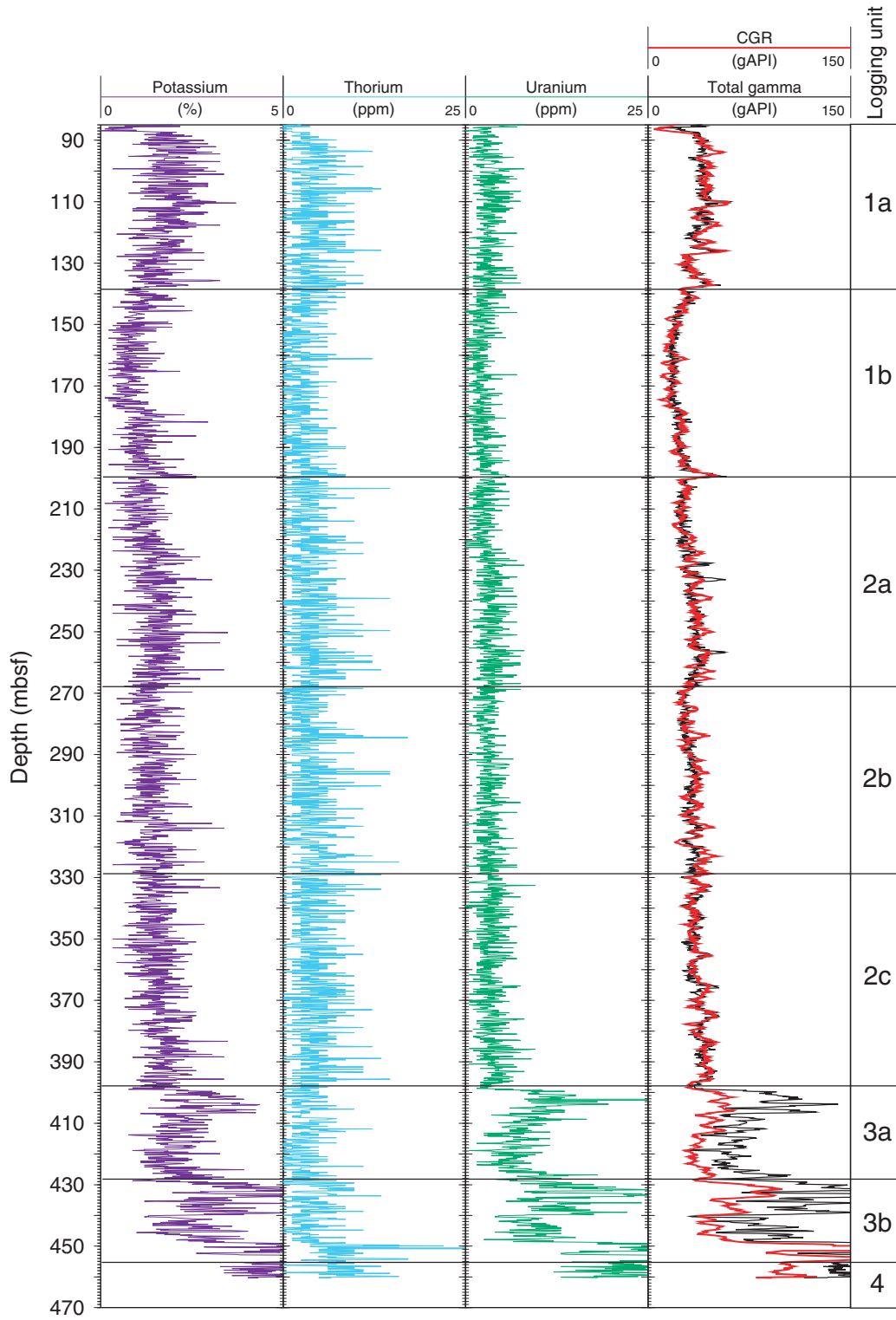


Figure F26. Summary of the logging runs undertaken in Hole 1258C. MGT = Multi-Sensor Spectral Gamma Ray tool, FMS = Formation MicroScanner.

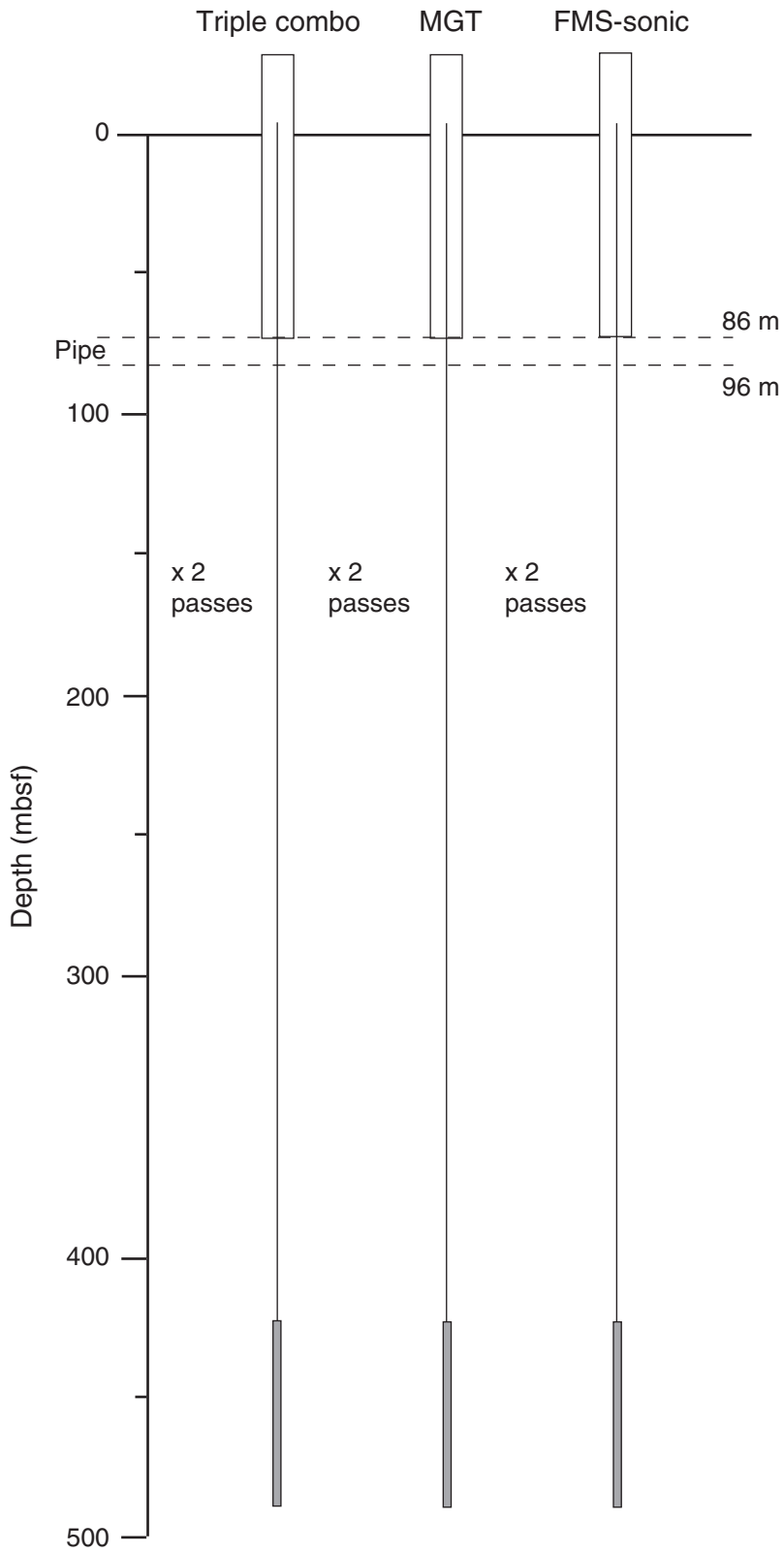
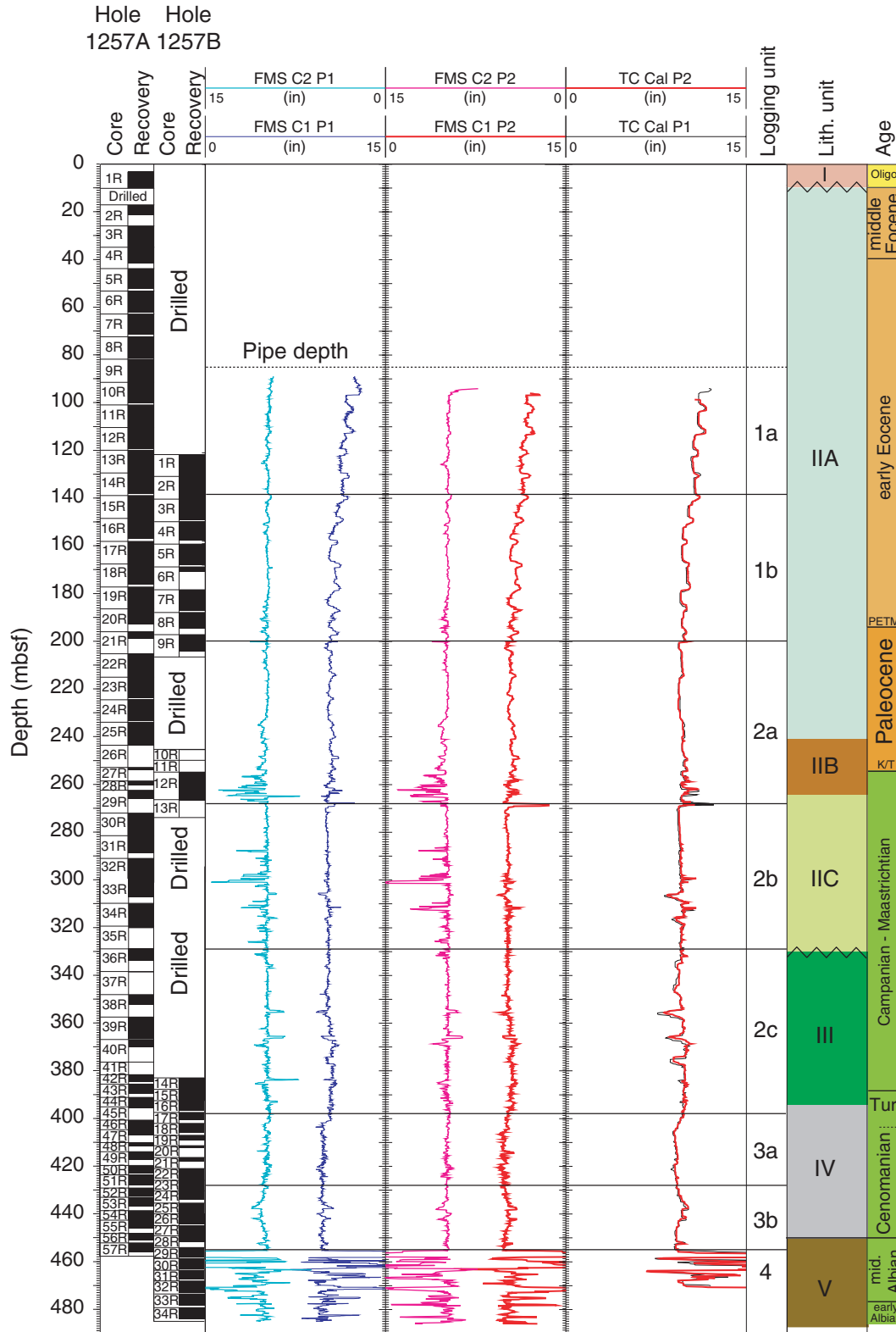
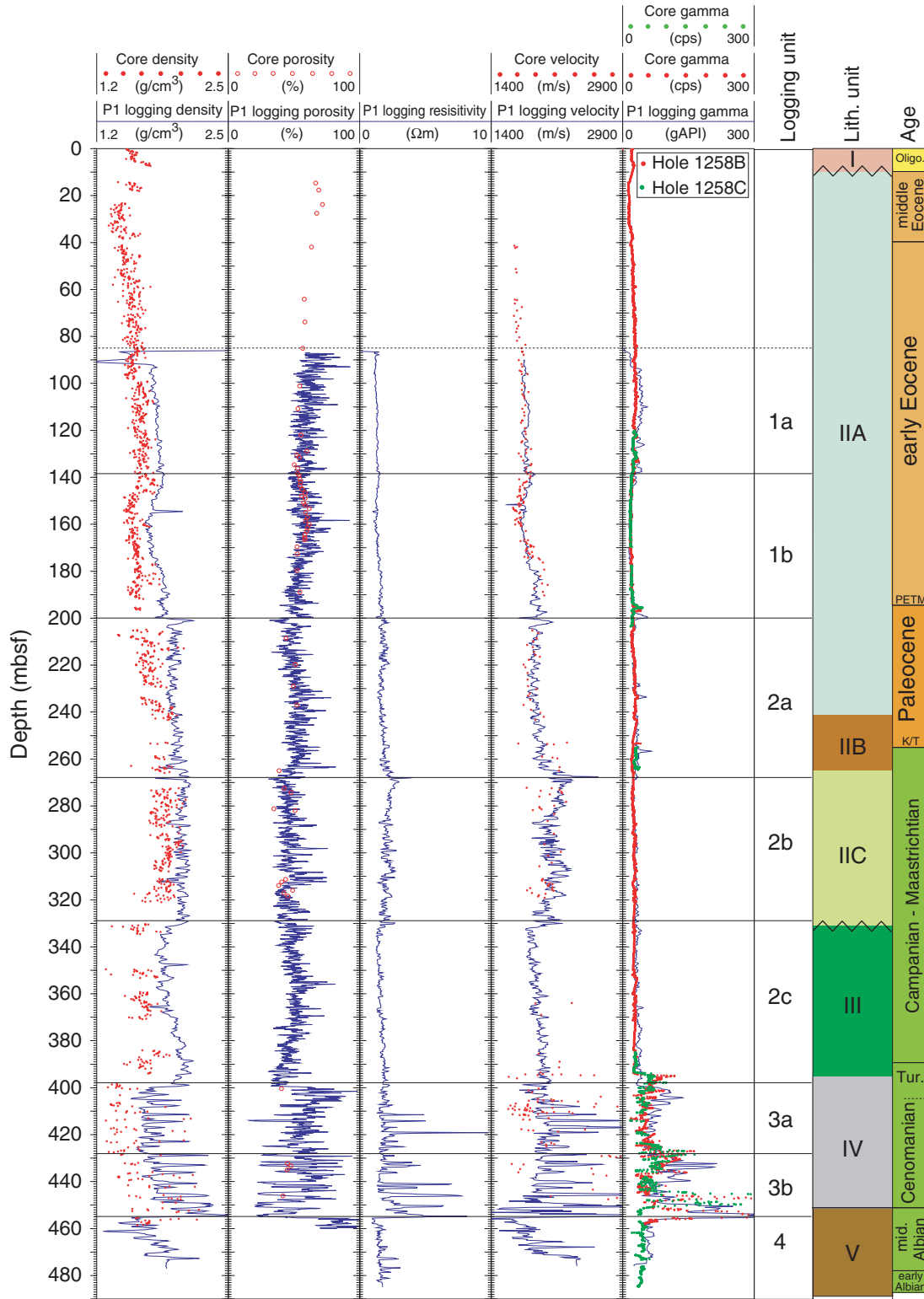


Figure F27. Borehole caliper logs from two passes of the triple combination (TC) and Formation MicroScanner (FMS)-sonic tool strings. PETM = Paleocene/Eocene Thermal Maximum, K/T = Cretaceous/Tertiary boundary.



**Figure F28.** Geophysical logs from Hole 1258C and equivalent core physical properties (MST and MAD) from Holes 1258B and 1258C. PETM = Paleocene/Eocene Thermal Maximum, K/T = Cretaceous/Tertiary boundary.





**Figure F30.** Correlation of wireline physical property variations with Formation MicroScanner (FMS) imagery from an interval through logging Subunit 2a from Hole 1258C. These data show cyclic variability. TC = triple combination, MGT = Multi-Sensor Spectral Gamma Ray tool, HSGR = HNGS Standard (total) Gamma Ray, PEF = photoelectric effect.

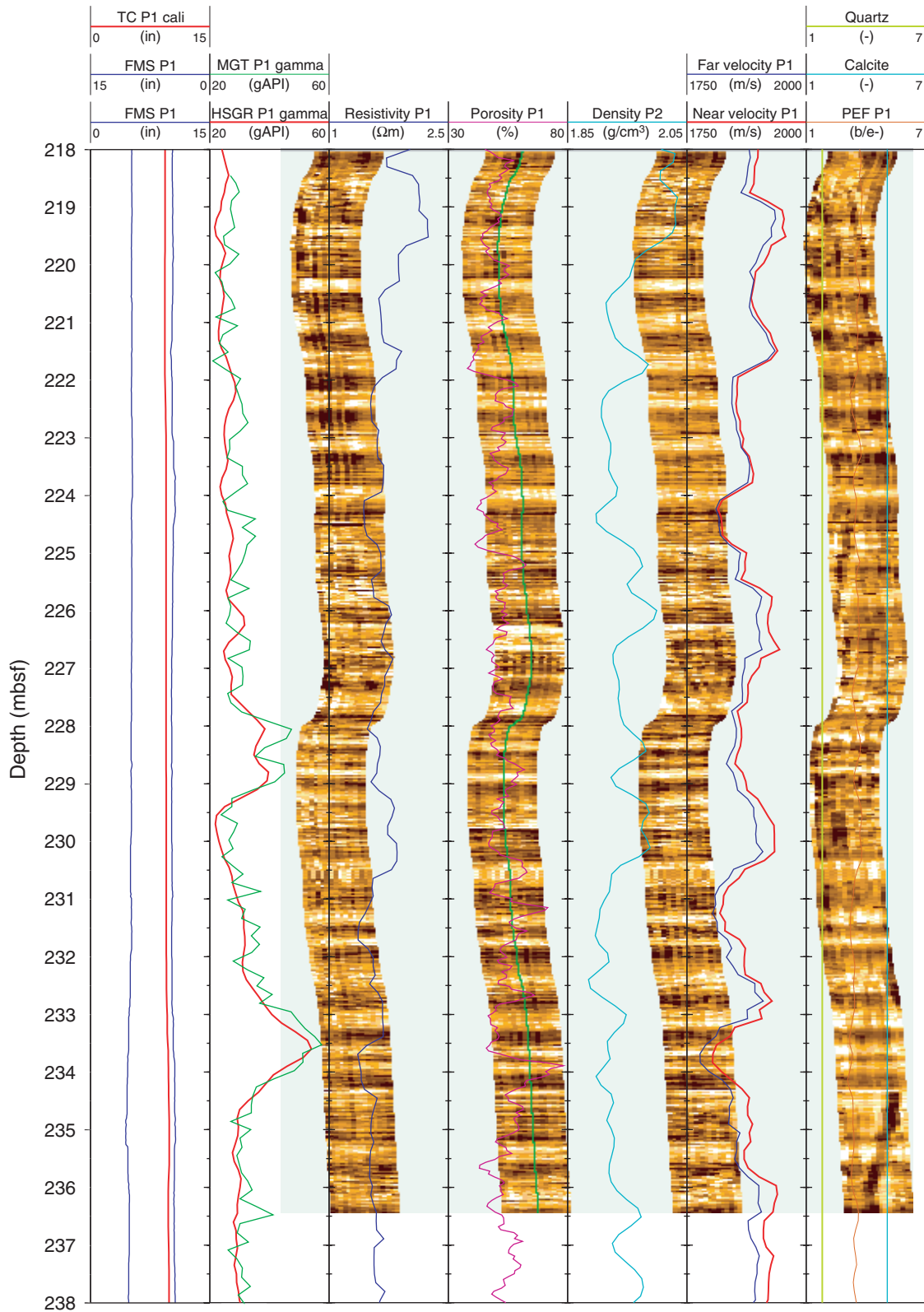




Figure F32. Comparison of core-measured total organic carbon (TOC) in Holes 1258B and 1258C and log-calculated TOC values through the black shale interval in Hole 1258C.

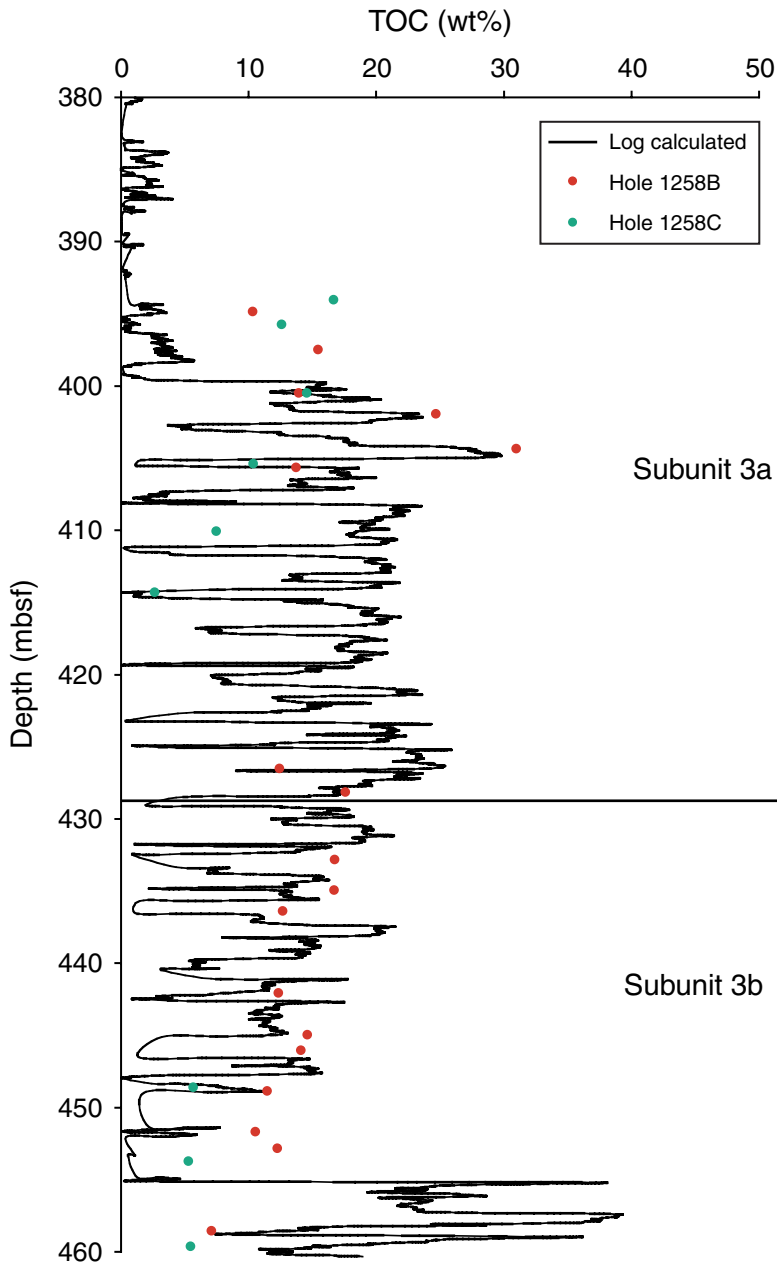


Figure F33. Photoelectric effect (PEF) log from triple combination (TC) pass 1 in Hole 1258C and core-measured  $\text{CaCO}_3$  percentages in Holes 1258B and 1258C.

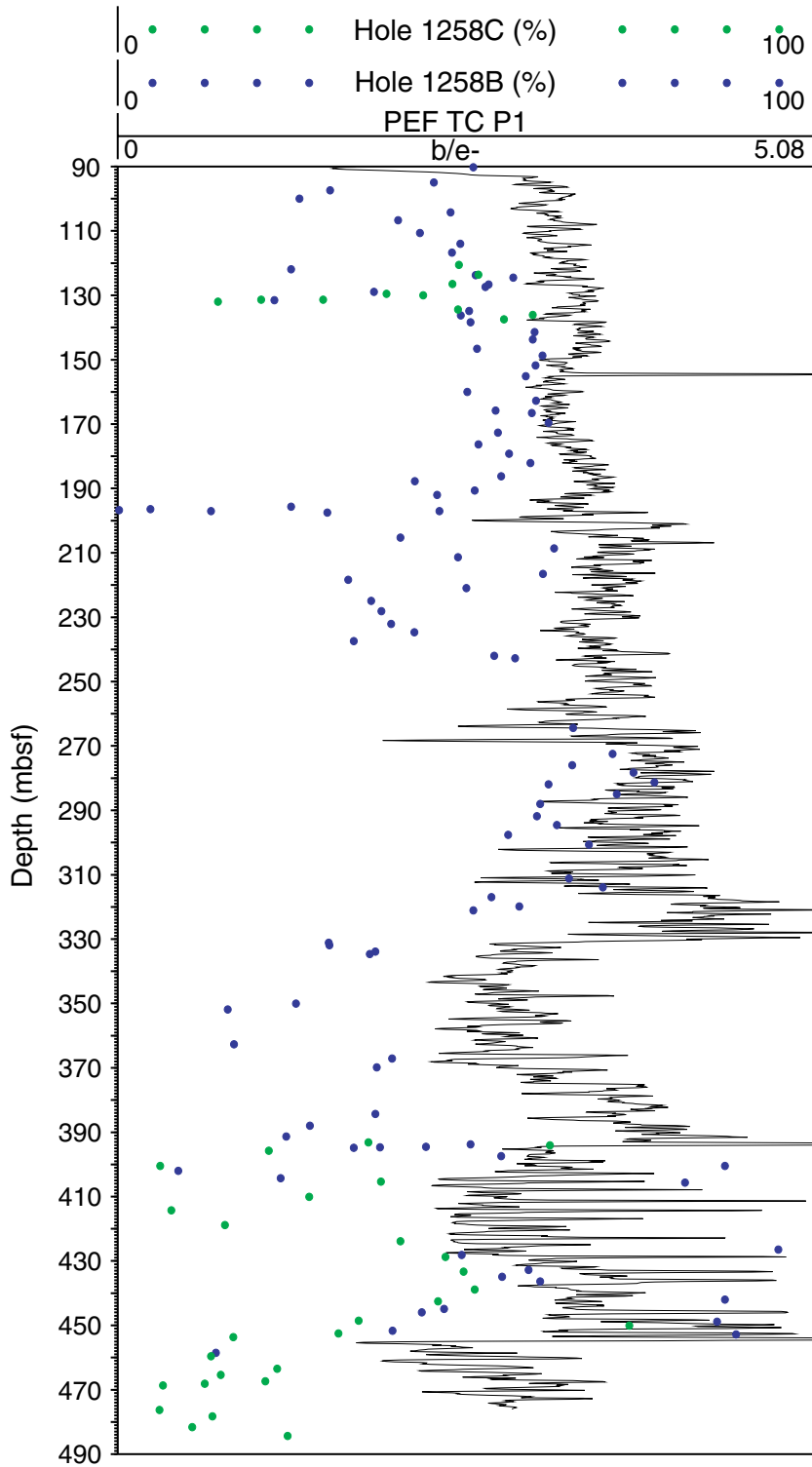


Figure F34. Formation density, velocity, impedance, and reflection coefficient series profiles obtained from downhole logging and core physical property measurements from Hole 1258C.

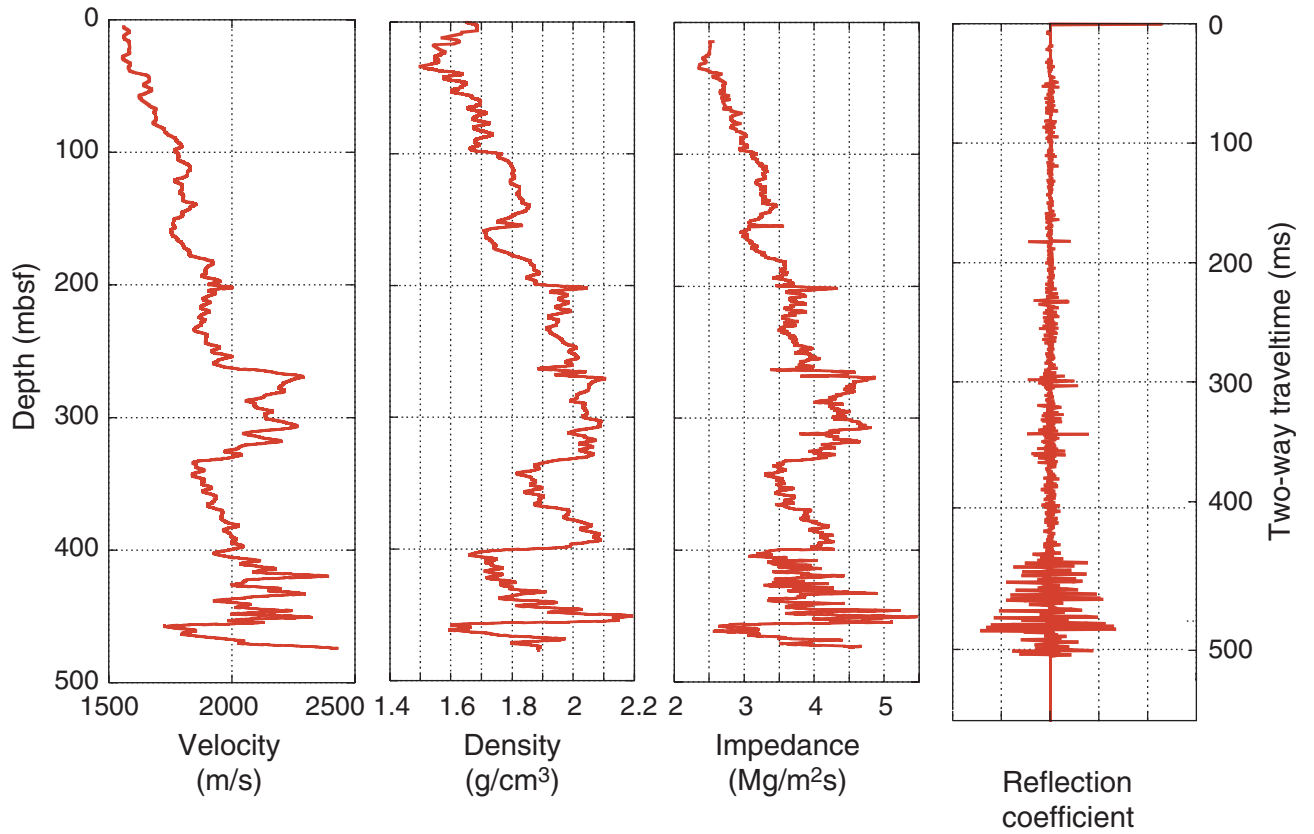


Figure F35. Part of seismic line GeoB221, the calculated synthetic seismogram (plotted at the Hole 1258C position on the seismic line), and the associated impedance profile (from which the synthetic was derived) plotted in mbsf.

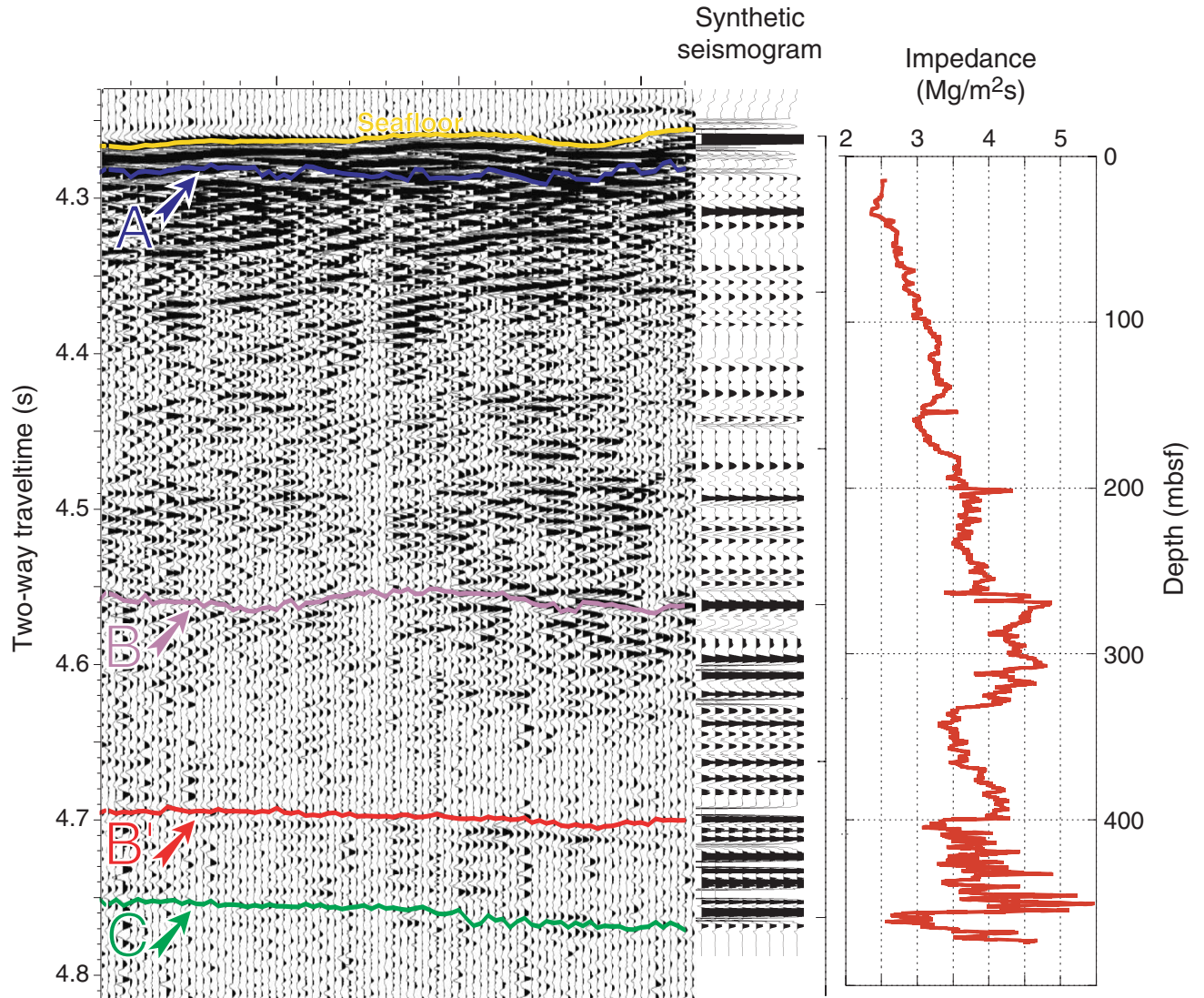


Table T1. Coring summary, Site 1258. (See table note. Continued on next two pages.)

**Hole 1258A**

Latitude: 9°26.0003'N  
 Longitude: 54°43.9994'W  
 Time on site: 229.75 (1815 hr, 22 Jan–0750 hr, 1 Feb 2003)  
 Time on hole: 63.92 (1815 hr, 22 Jan–1010 hr, 25 Jan 2003)  
 Seafloor (drill pipe measurement from rig floor, mbrf): 3203.2  
 Distance between rig floor and sea level (m): 11.0  
 Water depth (drill pipe measurement from sea level, m): 3192.2  
 Total depth (drill pipe measurement from rig floor, mbrf): 3650.7  
 Total penetration (meters below seafloor, mbsf): 447.5  
 Total length of cored section (m): 447.5  
 Total core recovered (m): 375.46  
 Core recovery (%): 83.9  
 Total number of cores: 50  
 Total number of drilled intervals: 0

**Hole 1258B**

Latitude: 9°26.0003'N  
 Longitude: 54°43.9825'W  
 Time on hole: 72.0 (1010 hr, 25 Jan–1010 hr, 28 Jan 2003)  
 Seafloor (drill pipe measurement from rig floor, mbrf): 3203.2  
 Distance between rig floor and sea level (m): 11.0  
 Water depth (drill pipe measurement from sea level, m): 3192.2  
 Total depth (drill pipe measurement from rig floor, mbrf): 3664.1  
 Total penetration (meters below seafloor, mbsf): 460.9  
 Total length of cored section (m): 453.9  
 Total length of drilled intervals (m): 7.0  
 Total core recovered (m): 346.13  
 Core recovery (%): 76.3  
 Total number of cores: 57  
 Total number of drilled intervals: 1

**Hole 1258C**

Latitude: 9°25.9999'N  
 Longitude: 54°43.9662'W  
 Time on hole: 93.83 (1010 hr, 28 Jan–0750 hr, 1 Feb 2003)  
 Seafloor (drill pipe measurement from rig floor, mbrf): 3203.2  
 Distance between rig floor and sea level (m): 11.00  
 Water depth (drill pipe measurement from sea level, m): 3192.2  
 Total depth (drill pipe measurement from rig floor, mbrf): 3688.2  
 Total penetration (meters below seafloor, mbsf): 485.0  
 Total length of cored section (m): 215.2  
 Total length of drilled intervals (m): 269.8  
 Total core recovered (m): 161.08  
 Core recovery (%): 74.9  
 Total number of cores: 34  
 Total number of drilled intervals: 3

Core	Date (Jan 2003)	Local time (hr)	Depth (mbsf)		Length (m)		Recovery (%)	Remarks
			Top	Bottom	Cored	Recovered		
207-1258A-								
1R	23	0050	0.0	5.1	5.1	5.09	99.8	
2R	23	0150	5.1	14.2	9.1	6.44	70.8	
3R	23	0235	14.2	23.8	9.6	8.79	91.6	
4R	23	0315	23.8	33.2	9.4	6.58	70.0	
5R	23	0405	33.2	42.8	9.6	5.44	56.7	AHC on
6R	23	0445	42.8	52.5	9.7	9.76	100.6	AHC on
7R	23	0525	52.5	62.2	9.7	7.89	81.3	AHC on
8R	23	0610	62.2	71.9	9.7	7.23	74.5	AHC on
9R	23	0655	71.9	81.6	9.7	9.93	102.4	AHC on
10R	23	0740	81.6	91.3	9.7	8.68	89.5	AHC on
11R	23	0830	91.3	100.9	9.6	9.29	96.8	AHC on
12R	23	0920	100.9	110.5	9.6	9.84	102.5	AHC on
13R	23	1015	110.5	120.1	9.6	9.58	99.8	AHC on
14R	23	1105	120.1	129.7	9.6	5.34	55.6	AHC on
15R	23	1155	129.7	139.4	9.7	5.03	51.9	AHC on
16R	23	1245	139.4	149.0	9.6	9.81	102.2	AHC on
17R	23	1330	149.0	158.7	9.7	9.49	97.8	AHC on
18R	23	1415	158.7	168.4	9.7	9.67	99.7	AHC on
19R	23	1505	168.4	178.1	9.7	9.65	99.5	AHC on
20R	23	1600	178.1	187.7	9.6	7.52	78.3	AHC on

Table T1 (continued).

Core	Date (Jan 2003)	Local time (hr)	Depth (mbsf)		Length (m)		Recovery (%)		Remarks	
			Top	Bottom	Cored	Recovered				
21R	23	1655	187.7	197.1	9.4	9.84	104.7	AHC on		
22R	23	1800	197.1	206.7	9.6	7.28	75.8	AHC on		
23R	23	1855	206.7	216.3	9.6	9.49	98.9	AHC on		
24R	23	1945	216.3	226.0	9.7	9.48	97.7	AHC on		
25R	23	2030	226.0	235.6	9.6	9.93	103.4	AHC on		
26R	23	2115	235.6	245.3	9.7	9.93	102.4	AHC on		
27R	23	2200	245.3	254.9	9.6	7.33	76.4	AHC on		
28R	23	2245	254.9	264.6	9.7	8.74	90.1	AHC on		
29R	23	2330	264.6	274.2	9.6	9.97	103.9	AHC on		
30R	24	0015	274.2	283.9	9.7	5.16	53.2	AHC on		
31R	24	0105	283.9	293.5	9.6	10.01	104.3	AHC on		
32R	24	0150	293.5	303.1	9.6	8.66	90.2	AHC on		
33R	24	0240	303.1	312.8	9.7	9.76	100.6	AHC on		
34R	24	0715	312.8	322.4	9.6	7.49	78.0	AHC on;	wireline parted; core sat in hole for over 4 hr until retrieved	
35R	24	0845	322.4	332.0	9.6	8.96	93.3	AHC on		
36R	24	1010	332.0	341.7	9.7	9.84	101.4	AHC on		
37R	24	1215	341.7	351.3	9.6	7.64	79.6	AHC on		
38R	24	1335	351.3	360.9	9.6	5.91	61.6	AHC on		
39R	24	1520	360.9	370.5	9.6	3.98	41.5	AHC on		
40R	24	1720	370.5	380.2	9.7	7.49	77.2	AHC on		
41R	24	1935	380.2	389.8	9.6	5.54	57.7	AHC on		
42R	24	2100	389.8	399.4	9.6	9.73	101.4	AHC on		
43R	24	2240	399.4	409.1	9.7	4.51	46.5	AHC on		
44R	25	0035	409.1	418.7	9.6	2.29	23.9	AHC on		
45R	25	0155	418.7	423.3	4.6	3.98	86.5	AHC on		
46R	25	0250	423.3	428.3	5.0	6.15	123.0	AHC on		
47R	25	0340	428.3	432.9	4.6	2.50	54.4	AHC on		
48R	25	0445	432.9	437.9	5.0	4.42	88.4	AHC on		
49R	25	0615	437.9	442.5	4.6	4.65	101.1	AHC on		
50R	25	0800	442.5	447.5	5.0	3.75	75.0	AHC on		
			Cored totals:		447.5	375.46	83.9			
207-1258B-										
1R	25	1325	0.0	7.1	7.1	7.70	108.5	AHC on		
			*****Drilled from 7.1 to 14.1 mbsf*****							
2R	25	1525	14.1	23.1	9.0	4.16	46.2	AHC on		
3R	25	1610	23.1	32.1	9.0	9.01	100.1	AHC on		
4R	25	1655	32.1	41.1	9.0	6.73	74.8	AHC on		
5R	25	1740	41.1	50.8	9.7	8.57	88.4	AHC on		
6R	25	1825	50.8	60.5	9.7	9.15	94.3	AHC on		
7R	25	1910	60.5	70.1	9.6	8.58	89.4	AHC on		
8R	25	1950	70.1	79.7	9.6	8.91	92.8	AHC on		
9R	25	2030	79.7	89.3	9.6	9.52	99.2	AHC on		
10R	25	2115	89.3	99.0	9.7	8.91	91.9	AHC on		
11R	25	2155	99.0	108.6	9.6	9.82	102.3	AHC on		
12R	25	2235	108.6	118.2	9.6	8.85	92.2	AHC on		
13R	25	2320	118.2	127.9	9.7	9.88	101.9	AHC on		
14R	26	0010	127.9	137.5	9.6	8.93	93.0	AHC on		
15R	26	0055	137.5	147.2	9.7	9.79	100.9	AHC on		
16R	26	0140	147.2	156.9	9.7	8.58	88.5	AHC on		
17R	26	0220	156.9	166.5	9.6	9.54	99.4	AHC on		
18R	26	0305	166.5	176.1	9.6	8.69	90.5	AHC on		
19R	26	0355	176.1	185.7	9.6	9.88	102.9	AHC on		
20R	26	0450	185.7	195.2	9.5	6.34	66.7	AHC on		
21R	26	0550	195.2	204.7	9.5	2.79	29.4	AHC on		
22R	26	0705	204.7	214.4	9.7	9.99	103.0	AHC on		
23R	26	0800	214.4	224.1	9.7	9.17	94.5	AHC on		
24R	26	0850	224.1	233.7	9.6	9.02	94.0	AHC on		
25R	26	0935	233.7	243.3	9.6	9.90	103.1	AHC on		
26R	26	1020	243.3	252.9	9.6	0.00	0.0	No recovery; AHC on		
27R	26	1105	252.9	258.6	5.7	1.07	18.8	AHC on		
28R	26	1200	258.6	262.6	4.0	1.66	41.5	AHC on		
29R	26	1245	262.6	272.2	9.6	3.46	36.0	AHC on		
30R	26	1330	272.2	281.9	9.7	9.96	102.7	AHC on		
31R	26	1415	281.9	291.5	9.6	7.30	76.0	AHC on		
32R	26	1500	291.5	301.1	9.6	9.94	103.5	AHC on		
33R	26	1545	301.1	310.8	9.7	6.93	71.4	AHC on		
34R	26	1640	310.8	320.4	9.6	9.95	103.7	AHC on		
35R	26	1740	320.4	330.1	9.7	0.88	9.1	AHC on		

Table T1 (continued).

Core	Date (Jan 2003)	Local time (hr)	Depth (mbsf)		Length (m)		Recovery (%)	Remarks	
			Top	Bottom	Cored	Recovered			
36R	26	1910	330.1	339.7	9.6	5.02	52.3	AHC on	
37R	26	2115	339.7	349.3	9.6	0.11	1.2	AHC on	
38R	27	0100	349.3	359.0	9.7	4.34	44.7	AHC on	
39R	27	0255	359.0	368.6	9.6	8.82	91.9	AHC on	
40R	27	0455	368.6	378.2	9.6	3.16	32.9	AHC on	
41R	27	0635	378.2	383.8	5.6	0.00	0.0	No recovery; AHC on	
42R	27	1030	383.8	387.8	4.0	3.35	83.8		
43R	27	1205	387.8	393.5	5.7	4.23	74.2		
44R	27	1320	393.5	397.5	4.0	4.56	114.0		
45R	27	1445	397.5	403.1	5.6	4.83	86.3		
46R	27	1610	403.1	407.1	4.0	4.49	112.3		
47R	27	1725	407.1	412.7	5.6	5.15	92.0		
48R	27	1915	412.7	416.7	4.0	1.69	42.3		
49R	27	2040	416.7	422.3	5.6	3.50	62.5		
50R	27	2200	422.3	426.3	4.0	3.35	83.8		
51R	27	2320	426.3	431.9	5.6	4.51	80.5		
52R	28	0030	431.9	435.9	4.0	3.52	88.0		
53R	28	0135	435.9	441.5	5.6	3.78	67.5		
54R	28	0300	441.5	445.5	4.0	3.80	95.0		
55R	28	0435	445.5	451.2	5.7	3.72	65.3		
56R	28	0635	451.2	455.2	4.0	2.89	72.3		
57R	28	0815	455.2	460.9	5.7	3.75	65.8		
			Cored totals:		453.9	346.13	76.3		
			Drilled total:		7.0				
			Total:		460.9				
207-1258C-									
			*****Drilled from 0.0 to 120.0 mbsf*****						AHC on
1R	28	1710	120.0	129.4	9.4	9.89	105.2		
2R	28	1815	129.4	139.0	9.6	9.86	102.7		
3R	28	1900	139.0	148.6	9.6	8.95	93.2		
4R	28	1945	148.6	158.2	9.6	8.96	93.3		
5R	28	2020	158.2	167.9	9.7	8.87	91.4		
6R	28	2110	167.9	177.5	9.6	1.83	19.1		
7R	28	2210	177.5	187.2	9.7	8.75	90.2		
8R	28	2255	187.2	196.5	9.3	9.87	106.1		
9R	28	2350	196.5	206.1	9.6	7.15	74.5		
			*****Drilled from 206.1 to 245.3 mbsf*****						Drill with center bit; AHC on
10R	29	0340	245.3	249.9	4.6	0.06	1.3		
11R	29	0430	249.9	254.9	5.0	0.00	0.0	No recovery	
12R	29	0615	254.9	264.6	9.7	9.95	102.6		
13R	29	0730	264.6	274.2	9.6	0.02	0.2		
			*****Drilled from 274.2 to 384.8 mbsf*****						
14R	29	1805	384.8	389.8	5.0	5.64	112.8		
15R	29	1905	389.8	394.4	4.6	4.53	98.5		
16R	29	2000	394.4	399.4	5.0	4.21	84.2		
17R	29	2050	399.4	404.1	4.7	3.38	71.9		
18R	29	2145	404.1	409.1	5.0	4.13	82.6		
19R	29	2230	409.1	413.7	4.6	2.00	43.5		
20R	29	2325	413.7	418.7	5.0	0.91	18.2		
21R	30	0010	418.7	423.3	4.6	1.84	40.0		
22R	30	0110	423.3	428.3	5.0	4.96	99.2		
23R	30	0150	428.3	432.9	4.6	4.41	95.9		
24R	30	0245	432.9	437.9	5.0	3.37	67.4		
25R	30	0350	437.9	442.5	4.6	4.33	94.1		
26R	30	0505	442.5	447.5	5.0	3.47	69.4		
27R	30	0655	447.5	451.8	4.3	4.28	99.5		
28R	30	0810	451.8	456.8	5.0	2.61	52.2		
29R	30	0925	456.8	461.4	4.6	4.06	88.3		
30R	30	1100	461.4	466.4	5.0	4.36	87.2		
31R	30	1220	466.4	471.0	4.6	3.67	79.8		
32R	30	1340	471.0	476.0	5.0	2.55	51.0		
33R	30	1500	476.0	480.7	4.7	3.98	84.7		
34R	30	1615	480.7	485.0	4.3	4.23	98.4		
			Cored totals:		215.2	161.08	74.9		
			Drilled total:		269.8				
			Total:		485.0				

Note: AHC = active heave compensator.

**Table T2.** Lithostratigraphic unit boundaries, Site 1258.

Unit/ subunit	Core, section, interval (cm)	Depth (mbsf)	Core, section, interval (cm)	Depth (mbsf)	Core, section, interval (cm)	Depth (mbsf)
	207-1258A-		207-1258B-		207-1258C-	
I-IIA	2R-3, 42	8.52	1R-4, 111	5.61	Drilled, boundaries not cored	—
IIA-IIIB	26R-4, 15	240.15	25R-6, 12	241.32	Drilled, boundaries not cored	—
IIB-IIC	28R-3, 20	258.10	28-CC, base	260.26	12R-7, 45	263.58
IIC-III	34R-4, 128	318.58	36R-1, 55	330.65	Drilled, boundaries not cored	—
III-IV	42R-1, 0	389.80	44R-2, 51	394.67	15R-3, 96	393.73
IV-V	50R-2, 30	444.06	56R-CC, base	454.09	27R-2, 65	449.56
base of V	50R-3, 103	446.22	57R-CC, 15	458.90	34R-3, 117	484.87

Notes: I = nannofossil ooze with foraminifers, IIA = nannofossil chalk with foraminifers, IIB = calcareous chalk with foraminifers, IIC = nannofossil chalk with foraminifers, III = calcareous nannofossil clay (clayey nannofossil chalk with organic matter), IV = laminated shale/limestone, V = phosphoric calcareous clay with organic matter. — = not applicable.

**Table T3.** Datum levels for calcareous nannofossils, Site 1258.

Core, section, interval (cm)	Depth (mbsf)		Depth (mcd)		Datum	Species	Zone	Age	Age (Ma)
	Top	Bottom	Top	Bottom					
207-1258A-									
1R-CC, 6-11	5.04	11.49	5.04	11.49	B	<i>Discoaster kugleri</i>	NN7	middle Miocene	11.6-11.9
2R-CC, 6-11	11.49	22.93	11.49	22.93	B	<i>Nannotetrina fulgens</i>	NP15	middle Eocene	43.4-47.0
5R-CC, 14-20	30.33	38.58	30.33	43.08	T	<i>Discoaster sublodoensis</i>	NP14	middle Eocene	47.2
6R-CC, 0-6	38.58	52.50	43.08	53.02	T	<i>Discoaster lodoensis</i>	NP14	middle Eocene	48.0
9R-CC, 24	69.38	81.83	71.23	82.08	T	<i>Tribrachiatius orthostylus</i>	NP12	early Eocene	51.0
10R-CC, 6-12	90.22	100.52	90.85	100.22	B	<i>Discoaster lodoensis</i>	NP12	early Eocene	52.4
11R-CC, 6-13	90.22	100.52	90.85	100.22	T	<i>Sphenolithus conspicuus</i>	NP12	early Eocene	51.0
11R-CC, 6-13	100.52	110.69	100.22	111.08	B	<i>Sphenolithus radians</i>	NP12	early Eocene	53.3
12R-CC, 9-14	110.69	120.03	111.08	120.64	B	<i>Sphenolithus radians</i>	NP12	early Eocene	53.3
13R-CC, 0-5	120.03	125.39	120.64	126.30	B	<i>Tribrachiatius orthostylus</i>	NP12	early Eocene	53.4
13R-CC, 0-5	120.03	125.39	120.64	126.30	B	<i>Sphenolithus conspicuus</i>	NP12	early Eocene	53.3
15R-4, 51-53	134.71	149.16	158.25	171.10	B	<i>Discoaster diastypus</i>	NP10	early Eocene	53.9
15R-4, 51-53	125.39	134.71	126.30	158.25	T	<i>Discoaster multiradiatus</i>	NP10	early Eocene	53.0
19R-CC, 24-29	168.35	178.00	192.21	201.43	T	<i>Fasciculithus</i> spp.	NP9	late Paleocene	54.1
23R-CC, 17-22	216.14	225.73	239.57	249.16	B	<i>Discoaster mohleri</i>	NP8	late Paleocene	57.5
25R-CC, 12-17	235.88	245.47	258.33	267.92	B	<i>Heliolithus riedeli</i>	NP7	late Paleocene	57.3
27R-1, 3	245.33	252.60	267.78	275.05	B	<i>Cruciplacolithus tenuis</i>	NP2	early Paleocene	64.5
27R-CC, 0-5	245.33	252.60	267.78	275.05	T	<i>Micula murus</i>	CC25/CC26	late Maastrichtian	65.0
31R-CC, 21-26	293.86	302.09	316.60	325.30	B	<i>Micula murus</i>	CC25	late Maastrichtian	66.2
33R-CC, 0-5	302.09	312.81	325.30	334.92	T	<i>Reinhardtites levis</i>	CC24	early Maastrichtian/late Campanian	69.2
35R-CC, 0-2	320.24	331.34	345.13	354.21	T	<i>Reinhardtites levis</i>	CC23	late Campanian	69.2
35R-CC, 0-2	320.24	331.34	345.13	354.21	T	<i>Uniplanarius sissinghi</i>	CC23	late Campanian	69.6
35R-CC, 0-2	320.24	331.34	345.13	354.21	T	<i>Uniplanarius trifidum</i>	CC23	late Campanian	69.6
40R-CC, 0-5	377.77	385.69	401.70	409.62	B	<i>Uniplanarius trifidum</i>	CC23	late Campanian	76.0
41R-CC, 24-29	385.69	399.47	409.62	424.42	B	<i>Broinsonia parca constricta</i>	CC20	early Campanian	82.5
45R-CC, 0-1	411.38	422.58	436.26	447.46	T	<i>Corollithion kennedyi</i>	CC10	Cenomanian	94.0
46R-CC, 16-19	422.58	429.42	447.46	454.30	T	<i>Axopodorhabdus albianus</i>	CC10	Cenomanian	94.0
207-1258B-									
2R-CC, 7-12	7.65	18.16	10.55	18.16	T	<i>Chiasmolithus gigas</i>	NP15	middle Eocene	46.1
5R-CC, 9-14	38.64	49.62	38.64	49.72	T	<i>Discoaster lodoensis</i>	NP14	middle Eocene	48.0
8R-CC, 22-27	69.02	78.96	69.01	78.49	T	<i>Tribrachiatius orthostylus</i>	NP12	early Eocene	51.0
17R-CC, 0-7	155.72	166.37	157.86	166.96	T	<i>Discoaster multiradiatus</i>	NP9	early Eocene	53.0
27R-CC, 20-23	243.57	253.94	264.82	277.37	T	<i>Micula murus</i>	CC25/CC26	late Maastrichtian	65.0
29R-CC, 0-4	266.02	282.11	292.50	303.61	B	<i>Micula murus</i>	CC25	late Maastrichtian	66.2
36R-CC, 11-16	321.22	334.93	341.61	347.74	T	<i>Uniplanarius trifidum</i>	CC23	late Campanian~	71.3
42R-CC, 0-4	387.11	392.00	409.22	414.11	B	<i>Uniplanarius trifidum</i>	CC23	late Campanian~	76.0
47R-CC, 8-13	407.54	412.20	429.60	434.26	T	<i>Axopodorhabdus albianus</i>	CC10	Cenomanian	94.0
57R-CC, 15-20	458.90		483.47		B	<i>Eiffelithus turriseiffelii</i>	CC9	Albian	101.7
207-1258C-									
1R-CC, 9-14	129.84	139.21	129.11	140.58	B	<i>Discoaster diastypus</i>	NP11	early Eocene	53.9
22R-CC, 14-17	420.37	428.26	444.48	452.82	T	<i>Corollithion kennedyi</i>	CC10	Cenomanian	94.0
27R-CC, 19-23	451.74	454.38	483.12	486.88	B	<i>Eiffelithus turriseiffelii</i>	NC9a	Albian	101.7

Note: T = top, B = bottom.

Table T4. Distribution of planktonic foraminifers, Hole 1258A. (This table is available in an [oversized format](#).)

Table T5. Datum levels for planktonic foraminifers, Site 1258.

Core, section, interval (cm)	Depth (mbsf)		Depth (mcd)		Datum	Species	Zone	Age	Age (Ma)
	Top	Bottom	Top	Bottom					
207-1258A-									
1R-CC, 6–11	5.04	5.60	5.04	5.60	B	<i>Globorotalia fohsi robusta*</i>	M9	middle Miocene	13.2
2R-2, 50–53	5.60	7.10	5.60	7.10	T	<i>Chiloguembelina</i> spp.	P21b	late Oligocene	27.1
2R-3, 50–53	8.60	10.10	8.60	10.10	B	<i>Globigerina angulisurealis*</i>	P21a and P12 mix	early Oligocene	29.4
3R-5, 50–54	20.70	22.20	20.70	22.20	B	<i>Guembeltrioides nuttali</i>	P10	middle Eocene	49.0
9R-2, 49–51	73.89	75.35	74.14	75.60	B	<i>Planorotalites palmerae</i>	P9	early Eocene	50.4
11R-3, 50–53	93.30	94.80	93.00	94.50	T	<i>Morozovella formosa</i>	P7	early Eocene	50.8
13R-7, 49–53	119.99	120.03	120.60	120.64	B	<i>Morozovella aragonensis</i>	P7	early Eocene	52.3
21R-CC, 16–21	185.57	197.49	209.00	220.92	T	<i>Globanomalina pseudomenardii</i>	P4	late Paleocene	55.9
26R-7, 50–54	244.50	245.47	266.95	267.92	B	<i>Globanomalina pseudomenardii</i>	P4	late Paleocene	59.2
27R-3, 0–2	248.30	249.80	270.75	272.25	B	<i>Subbotina triloculinoides</i>	P1b	early Paleocene	64.5
27R-4, 0–2	248.30	249.80	270.75	272.25	T	<i>Parvulorogoglobigerina eugubina</i>	Pa	early Paleocene	64.5
28R-1, 5–6	252.60	254.95	275.05	277.40	T	<i>Abathomphalus mayaroensis</i>	KS31	late Maastrichtian	65.0
29R-CC, 13–18	274.52	279.31	296.97	301.68	B	<i>Abathomphalus mayaroensis</i>	KS31	late Maastrichtian	68.6
33R-CC, 0–5	312.81	320.24	334.92	345.13	B	<i>Globotruncana aegyptiaca*</i>	KS29–KS30	early Maastrichtian–late Campanian	73.8
47R-CC, 0–5	429.42	430.75	454.30	458.37	T	<i>Rotalipora</i> spp.*	Not defined	Cenomanian	96.6
50R-CC, 0–3	446.22	447.50	483.01	484.29	B	<i>Biticinella breggiensis</i>	KS14	Albian	105.0
207-1258B-									
1R-CC, 18–23	0	7.65	2.90	10.55	T	<i>Pseudohastigerina micra*</i>	P18	early Oligocene	32.0
2R-CC, 7–12	18.16	32.04	18.16	32.04	B	<i>Guembeltrioides nuttali</i>	P10	middle Eocene	49.0
8R-CC, 22–27	78.74	78.96	78.27	78.49	B	<i>Planorotalites palmerae</i>	P9	early Eocene	50.4
11R-CC, 6–12	98.14	108.76	97.47	108.39	T	<i>Morozovella formosa</i>	P7	early Eocene	50.8
12R-CC, 0–5	117.40	128.03	118.00	127.42	B	<i>Morozovella aragonensis</i>	P7	early Eocene	52.3
18R-CC, 6–11	166.37	175.14	166.96	175.73	T	<i>Morozovella velascoensis</i> group	P5	early Eocene	54.7
23R-CC, 14–19	223.52	243.57	246.15	264.82	B	<i>Globanomalina pseudomenardii</i>	P4	late Paleocene	59.2
27R-CC, 20–23	243.57	253.94	264.82	277.37	T	<i>Abathomphalus mayaroensis</i>	KS31	late Maastrichtian	65.0
34R-CC, 20–25	320.70	321.22	340.89	341.61	B	<i>Gansserina gansseri</i>	KS30	early Maastrichtian–late Campanian	72.8
52R-CC, 31–37	433.25	435.36	457.57	459.68	T	<i>Rotalipora cushmani</i>	KS19	late Cenomanian	94.0
56R-1, 61–64	451.81	453.36	476.38	477.93	B	<i>Biticinella breggiensis</i>	KS14	Albian	105.0
207-1258C-									
8R-CC, 18–23	186.20	197.02	185.09	199.31	T	<i>Morozovella velascoensis</i> group	P5	late Paleocene	54.7
12R-CC, 19–22	254.90	264.82	267.33	277.25	T	Cretaceous species	KS30–KS31	Maastrichtian	65.0
27R-1, 85–89	448.35	449.78	479.73	481.16	B	<i>Biticinella breggiensis</i>	KS14	Albian	105.0

Notes: Top and bottom depth values refer to the range of possible depths in the core within which the datum is believed to fall. B = bottom, T = top. \* = probably reflect incomplete ranges of the foraminiferal marker species.

Table T6. Datum levels, ages, and preservation of samples for calcareous nannofossils, Site 1258. (See table notes. Continued on next page.)

Core, section, interval (cm)	Depth (mbsf)	Zone	Age	Preservation	Group abundance	Core, section, interval (cm)	Depth (mbsf)	Zone	Age	Preservation	Group abundance
207-1258A-						12R-CC, 0-5	117.40	NP12	early Eocene	M	C
1R-CC, 6-11	5.04	NN5	middle Miocene	M	C	13R-CC, 12-17	128.03	NP11	early Eocene	M	C
2R-CC, 6-11	11.49	NP15	middle Eocene	G	C	14R-CC, 19-25	136.77	NP11	early Eocene	M	C
3R-CC, 10-16	22.93	NP15	middle Eocene	G	C	15R-CC, 11-16	147.24	NP10	early Eocene	G	C
4R-CC, 7-12	30.33	NP15	middle Eocene	G	C	16R-CC, 0-6	155.72	NP10	early Eocene	G	C
5R-CC, 14-20	38.58	NP14	early Eocene	G	C	17R-CC, 0-7	166.37	NP9	early Eocene	G	C
6R-CC, 0-6	52.50	NP14	early Eocene	G	C	18R-CC, 6-11	175.14	NP9	early Eocene	G	C
7R-CC, 14-19	60.34	NP13	early Eocene	G	C	19R-CC, 19-24	185.93	NP9	early Eocene	G	C
8R-CC, 8-13	69.38	NP13	early Eocene	G	C	20R-CC, 14-17	192.01	NP9	early Eocene	G	C
9R-CC, 0-4	81.59	NP12	early Eocene	G	C	21R-CC, 0-6	197.93	NP9	Paleocene	G	C
10R-CC, 6-12	90.22	NP12	early Eocene	G	C	22R-CC, 20-24	214.65				
11R-CC, 6-13	100.52	NP12	early Eocene	G	C	23R-CC, 14-19	223.52	NP7	Paleocene	M	C
12R-CC, 9-14	110.69	NP12	early Eocene	G	C	24R-CC, 0-3	233.09	NP5	Paleocene	M	C
13R-CC, 0-5	120.03	NP12	early Eocene	G	C	25R-CC, 18-21	243.57	NP4	Paleocene	G	C
14R-CC, 8-13	125.39	NP10	early Eocene	G	C	27R-CC, 20-23	253.94	CC26	Maastrichtian	G	C
15R-4, 51-53	134.71	NP10	early Eocene	G	C	28R-CC, 9-14	260.21	CC26	Maastrichtian	G	C
16R-CC, 15-20	149.16	NP9	early Eocene	G	C	29R-CC, 0-4	266.02	CC25	Maastrichtian	M	C
17R-CC, 12-17	158.44	NP9	early Eocene	G	C	30R-CC, 23-28	282.11	CC25	Maastrichtian	M	C
18R-CC, 0-2	168.35	NP9	early Eocene	G	C	31R-CC, 7-13	289.14	CC25	Maastrichtian	M	C
19R-CC, 24-29	178.00	NP9	Paleocene	G	C	32R-CC, 13-18	301.39	CC25	Maastrichtian	M	C
20R-CC, 18-23	185.57	NP9	Paleocene	G	C	33R-CC, 0-5	307.98	CC25	Maastrichtian	M	C
21R-CC, 16-21	197.49	NP9	Paleocene	G	C	34R-CC, 20-25	320.70	CC25	Maastrichtian	M	C
22R-CC, 0-7	204.31	NP9	Paleocene	G	C	35R-CC, 0-6	321.22	CC23	Maastrichtian	G	C
23R-CC, 17-22	216.14	NP8	Paleocene	G	C	36R-CC, 11-16	334.93	CC23	Campanian	G	C
24R-CC, 12-17	225.73	NP7	Paleocene	G	C	38R-CC, 30-38	353.56	CC23	Campanian	M	F
25R-CC, 12-17	235.88	NP7	Paleocene	G	C	39R-CC, 20-27	367.75	CC23	Campanian	G	C
26R-CC, 15-21	245.47	NP5	Paleocene	P-M	R	40R-CC, 22-28	371.70	CC23	Campanian	G	C
27R-CC, 0-5	252.60	NP2	Paleocene	P-M	R	42R-CC, 0-4	387.11	CC23	Campanian	G	C
28R-6, 119-124	263.59	CC25	Maastrichtian	G	C	43R-3, 130-133	392.00	CC20	Campanian	G	C
29R-CC, 13-18	274.52	CC25	Maastrichtian	M	C	44R-2, 0-2	394.16				
30R-CC, 0-5	279.31	CC25	Maastrichtian	M	C	44R-CC, 0-5	397.90	CC11	Turonian	G	M
31R-CC, 21-26	293.86	CC25	Maastrichtian	M	C	45R-CC, 0-5	402.28	CC11	Turonian	G	M
32R-CC, 0-7	302.09	CC25	Maastrichtian	M	C	46R-CC, 0-5	407.54	CC11	Turonian	G	M
33R-CC, 0-5	312.81	CC24	Maastrichtian	M	C	47R-CC, 8-13	412.20	CC10	Cenomanian	M	M
34R-CC, 13-18	320.24	CC23	Campanian	M	C	48R-CC, 13-17	414.26	CC10	Cenomanian	VG	C
35R-CC, 0-2	331.34	CC23	Campanian	M	C	49R-CC, 3-8	419.99	CC10	Cenomanian	VG	C
36R-CC, 21-26	341.79	CC23	Campanian	M	C	50R-CC, 0-6	425.59	CC10	Cenomanian	G	C
37R-6, 0-2	348.70	CC23	Campanian	M	C	51R-CC, 0-5	430.58	CC10	Cenomanian	G	C
38R-CC, 15-20	357.16	CC23	Campanian	M	C	52R-CC, 31-37	435.36	CC10	Cenomanian	G	C
39R-CC, 23-28	364.79	CC23	Campanian	M	C	53R-CC, 13-19	439.62	CC10	Cenomanian	G	C
40R-CC, 0-5	377.77	CC23	Campanian	M	C	54R-CC, 15-20	445.25	CC10	Cenomanian	G	C
41R-CC, 24-29	385.69	CC20	Campanian	M	C	55R-CC, 0-4	449.10	NC9a	Albian	G	C
42R-CC, 12-18	399.47	CC11	Turonian	VG	C	56R-CC, 10-14	454.05	NC9a	Albian	M	C
43R-CC, 9-14	403.86	CC11	Turonian	M	C	57R-CC, 15-20	458.90	NC9a	Albian	G	
44R-CC, 12-13	411.38	CC11	Turonian	G	C	207-1258C-					
45R-CC, 0-1	422.58	CC10	Cenomanian	G	C	1R-CC, 9-14	129.84	NP11	early Eocene	M	C
46R-CC, 16-19	429.42	CC10	Cenomanian	M	C	2R-CC, 13-18	139.21	NP11	early Eocene	P	C
47R-CC, 0-5	430.75	NC10a	Cenomanian	M	C	3R-6, 128-133	147.78	NP10	early Eocene	M	C
48R-3, 137-138	437.16	NC10a	Cenomanian	G	C	4R-CC, 19-24	157.51	NP10	early Eocene	M	C
49R-CC, 0-3	442.35	NC10a	Cenomanian	G	C	5R-CC, 0-6	167.01	NP9	early Eocene	M	C
50R-CC, 0-3	446.22		Albian	G	C	6R-CC, 8-13	169.68	NP9	early Eocene	M	C
207-1258B-						7R-CC, 5-10	186.20	NP9	early Eocene	M	C
1R-CC, 18-23	7.65	NP21	early Oligocene	VG	C	8R-CC, 18-23	197.02	NP9	Paleocene	G	C
2R-CC, 7-12	18.16	NP15	middle Eocene	VG	C	9R-CC, 0-8	203.57	NP9	Paleocene	G	C
3R-CC, 0-7	32.04	NP15	middle Eocene	VG	C	10R-CC, 0-6	245.30				
4R-CC, 0-5	38.64	NP14	middle Eocene	VG	C	12R-1, 0-1	254.90				
5R-CC, 9-14	49.62	NP14	middle Eocene	VG	C	12R-CC, 19-22	264.82	CC26	Maastrichtian	M	C
6R-CC, 6-12	59.89	CC13	early Eocene	M	C	13R-CC, 0-2	264.60				
7R-CC, 4-10	69.02	NP12	early Eocene	M	C	14R-CC, 15-20	390.39	CC23	Campanian	M	C
8R-CC, 22-27	78.96	NP12	early Eocene	M	C	15R-CC, 6-9	394.30	CC12	Turonian	G	C
9R-CC, 0-8	89.14	NP12	early Eocene	M	C	16R-CC, 11-16	398.53				
10R-CC, 0-7	98.14	NP12	early Eocene	M	C	17R-CC, 18-21	402.75	CC10	Cenomanian	G	C
11R-CC, 6-12	108.76	NP12	early Eocene	M	C	18R-3, 112-117	408.01	CC10	Cenomanian	G	C
						19R-CC, 4-12	410.96	CC10	Cenomanian	G	C

**Table T6 (continued).**

Core, section, interval (cm)	Depth (mbsf)	Zone	Age	Preservation	Group abundance
20R-CC, 0-3	414.50	CC10	Cenomanian	G	C
21R-CC, 0-3	420.37	CC10	Cenomanian	M	C
22R-CC, 14-17	428.26	CC10	Cenomanian	G	C
23R-CC, 16-21	432.66	CC10	Cenomanian	G	C
24R-CC, 16-17	436.26	CC10	Cenomanian	G	C
25R-CC, 8-14	442.17	CC10	Cenomanian	G	C
26R-CC, 0-1	445.77				
26R-CC, 10-12	445.87	CC10	Cenomanian	G	C
27R-CC, 19-23	451.74	NC9a	Albian	M	C
28R-CC, 20-23	454.38	NC9a	Albian	M	F
29R-CC, 14-19	460.81	NC9a	Albian	M	C
30R-CC, 26-31	465.71	NC9a	Albian	M	F
31R-3, 53-55	469.93				
31R-CC, 7-12	470.02	NC9a	Albian	M	C
32R-CC, 12-17	473.50	NC9a	Albian	M	C
33R-CC, 17-22	479.93	NC8a	Albian	M	F
34R-CC, 0-5	484.88	NC8a	Albian	M	F

Notes: Preservation: VG = very good, G = good, M = moderate, P = poor. Abundance: C = common, M = moderate, F = few, R = rare.

Table T7. Distribution of planktonic foraminifers, Hole 1258B. (This table is available in an [oversized format](#).)

Table T8. Distribution of planktonic foraminifers, Hole 1258C. (Continued on next page.)

Core, section, interval (cm)	Depth (mbsf)	Zone	Age	Preservation	Group abundance	<i>Clavohedbergella subretacea</i>	<i>Ticinella primula</i>	<i>Ticinella raynaudi</i>	<i>Ticinella roberti</i>	<i>Clavohedbergella moremani</i>	<i>Globigerinelloides benitonensis</i>	<i>Ticinella madecassiana</i>	<i>Clavohedbergella simplex</i>	<i>Hedbergella planispira</i>	<i>Biticinella breggiensis</i>	<i>Costellagerina lybica</i>	<i>Heterohelix moremani</i>	<i>Guembeltria cenomana</i>	<i>Hedbergella delrioensis</i>	<i>Globigerinelloides caseyi</i>	<i>Whiteinella baltica</i>	<i>Rotalipora bratzeri</i>	<i>Rotalipora gandolfii</i>	<i>Schackoina cenomana</i>	<i>Heterohelix globulosa</i>	<i>Heterohelix reussi</i>	<i>Whiteinella archaeocretacea</i>	<i>Whiteinella inornata</i>	<i>Whiteinella brittonensis</i>	<i>Marginotruncana pseudolinmeliana</i>	<i>Gansserina gansseri</i>	<i>Globigerinelloides prairiehillensis</i>	<i>Rugoglobigerina rugosa</i>	<i>Acarinina nitida</i>	<i>Acarinina soldadoensis</i>		
207-1258C-																																					
1R-CC, 9-14	129.84	P6	early Eocene	M	A																															X	
2R-CC, 13-18	139.21	P6	early Eocene	P	C																														X		
3R-6, 128-133	147.78	P6	early Eocene	M	C																														X		
4R-CC, 19-24	157.51	P6	early Eocene	P	C																														X		
5R-CC, 0-6	167.01	P6	early Eocene	P	C																														X		
6R-CC, 8-13	169.68	P6	early Eocene	M	C																														X		
7R-CC, 5-10	186.20	Not defined	No age assignment	P	R																																
8R-CC, 18-23	197.02	P5	late Paleocene	P	C																																
9R-CC, 0-8	203.57	P5	late Paleocene	P	C																														X		
10R-CC, 0-6	245.30	P5	late Paleocene	P	F																														X		
12R-1, 0-1	254.90	P5	late Paleocene	M	C																													X	X		
12R-CC, 19-22	264.82	KS30-KS31	Maastrichtian	P	C																				X							X	X	X			
14R-CC, 15-20	390.39	Not defined	No age assignment	B																																	
15R-CC, 6-9	394.30	Not defined	Turonian	M	C																	X															
16R-CC, 11-16	398.53	Not defined	No age assignment	B																							X	X	X		X						
17R-CC, 18-21	402.75	Not defined	late Cenomanian-Turonian	P	C																	X	X				X	X		X							
18R-3, 112-117	408.01	Not defined	late Cenomanian-Turonian	P	F								X									X	X				X	X		X							
19R-CC, 4-12	410.96	Not defined	late Cenomanian-Turonian	M	C								X									X	X				X	X									
20R-CC, 0-3	414.50	Not defined	No age assignment	P	F												X	X	X																		
21R-1, 120-125	419.82	Not defined	No age assignment	G	F												X	X	X																		
21R-CC, 0-3	420.37	Not defined	late Cenomanian	G	C								X				X	X				X	X														
22R-CC, 14-17	428.26	Not defined	late Cenomanian	M	C								X	X			X	X	X			X	X														
23R-CC, 16-21	432.66	Not defined	late Cenomanian	M	C												X	X	X			X	X	X													
24R-CC, 16-17	436.26	Not defined	Cenomanian	M	C														X	X	X	X															
25R-CC, 8-14	442.17	Not defined	Cenomanian	G	F									X					X	X	X																
26R-CC, 10-12	445.87	Not defined	Cenomanian	M	C								X	X	X				X	X																	
27R-1, 8-11	447.58	Not defined	Albian	M	F		X	X				X	X			X	X																				
27R-1, 85-89	448.35	KS14	Albian	M	R		X	X				X	X	X		X	X																				
27R-2, 87-92	449.78	KS13	Albian	G	C		X					X	X																								
27R-CC, 19-23	451.74	KS13	Albian	G	F		X					X	X	X																							
28R-CC, 20-23	454.38	KS13	Albian	M	F		X	X				X	X	X																							
29R-CC, 14-19	460.81	KS13	Albian	M	F		X	X				X	X																								
30R-CC, 26-31	465.71	KS13	Albian	M	C		X	X					X																								
31R-3, 53-55	469.93	KS13	Albian	G	A		X	X	X	X		X																									
32R-CC, 12-17	473.50	KS13	Albian	G	C		X	X	X	X	X																										
33R-CC, 17-22	479.93	KS13	Albian	G	F		X		X																												
34R-CC, 0-5	484.88	KS13	Albian	G	A		X	X	X	X																											

Notes: Preservation: G = good, M = moderate, P = poor. Abundance: A = abundant, C = common, F = few, R = rare, B = barren.

Table T8 (continued).

Core, section, interval (cm)	Depth (mbsf)	Zone	Age	Preservation	Group abundance	<i>Morozovella acuta</i>	<i>Morozovella aequa</i>	<i>Morozovella occlusa</i>	<i>Subbotina velascoensis</i>	<i>Igorina albeari</i>	<i>Morozovella velascoensis</i>	<i>Subbotina triangularis</i>	<i>Acarina coalingensis</i>	<i>Morozovella subbotinae</i>	<i>Subbotina trilobuloides</i>	<i>Subbotina patagonica</i>	<i>Chiloguembelina wilcoxensis</i>	<i>Morozovella gracilis</i>	<i>Morozovella marginodentata</i>	<i>Pseudohastigerina wilcoxensis</i>	<i>Acarina wilcoxensis</i>	<i>Igorina broedermanni</i>	<i>Turborotalia praecentralis</i>	<i>Chiloguembelina midwayensis</i>	<i>Globigerina lozanoi</i>	<i>Morozovella formosa</i>	<i>Pseudohastigerina micra</i>
207-1258C-																											
1R-CC, 9-14	129.84	P6	early Eocene	M	A							X	X			X	X				X	X	X	X	X	X	X
2R-CC, 13-18	139.21	P6	early Eocene	P	C							X					X	X	X		X	X					
3R-6, 128-133	147.78	P6	early Eocene	M	C							X									X	X					
4R-CC, 19-24	157.51	P6	early Eocene	P	C							X				X	X	X			X	X	X				
5R-CC, 0-6	167.01	P6	early Eocene	P	C							X	X			X	X		X		X	X					
6R-CC, 8-13	169.68	P6	early Eocene	M	C						X		X			X	X	X	X	X	X	X					
7R-CC, 5-10	186.20	Not defined	No age assignment	P	R							X		X		X	X	X	X	X							
8R-CC, 18-23	197.02	P5	late Paleocene	P	C	X					X	X	X			X											
9R-CC, 0-8	203.57	P5	late Paleocene	P	C		X				X	X	X	X													
10R-CC, 0-6	245.30	P5	late Paleocene	P	F	X	X	X	X	X	X	X															
12R-1, 0-1	254.90	P5	late Paleocene	M	C	X	X	X	X		X	X															
12R-CC, 19-22	264.82	KS30-KS31	Maastrichtian	P	C																						
14R-CC, 15-20	390.39	Not defined	No age assignment		B																						
15R-CC, 6-9	394.30	Not defined	Turonian	M	C																						
16R-CC, 11-16	398.53	Not defined	No age assignment		B																						
17R-CC, 18-21	402.75	Not defined	late Cenomanian-Turonian	P	C																						
18R-3, 112-117	408.01	Not defined	late Cenomanian-Turonian	P	F																						
19R-CC, 4-12	410.96	Not defined	late Cenomanian-Turonian	M	C																						
20R-CC, 0-3	414.50	Not defined	No age assignment	P	F																						
21R-1, 120-125	419.82	Not defined	No age assignment	G	F																						
21R-CC, 0-3	420.37	Not defined	late Cenomanian	G	C																						
22R-CC, 14-17	428.26	Not defined	late Cenomanian	M	C																						
23R-CC, 16-21	432.66	Not defined	late Cenomanian	M	C																						
24R-CC, 16-17	436.26	Not defined	Cenomanian	M	C																						
25R-CC, 8-14	442.17	Not defined	Cenomanian	G	F																						
26R-CC, 10-12	445.87	Not defined	Cenomanian	M	C																						
27R-1, 8-11	447.58	Not defined	Albian	M	F																						
27R-1, 85-89	448.35	KS14	Albian	M	R																						
27R-2, 87-92	449.78	KS13	Albian	G	C																						
27R-CC, 19-23	451.74	KS13	Albian	G	F																						
28R-CC, 20-23	454.38	KS13	Albian	M	F																						
29R-CC, 14-19	460.81	KS13	Albian	M	F																						
30R-CC, 26-31	465.71	KS13	Albian	M	C																						
31R-3, 53-55	469.93	KS13	Albian	G	A																						
32R-CC, 12-17	473.50	KS13	Albian	G	C																						
33R-CC, 17-22	479.93	KS13	Albian	G	F																						
34R-CC, 0-5	484.88	KS13	Albian	G	A																						

**Table T9.** Shipboard cryogenic magnetometer analyses, Site 1258.

Core interval	Approximate age range	NRM demagnetization
207-1258A- 2R-4R	middle Eocene	10 and 15 mT
5R-8R	lower-middle Eocene transition interval (reddish tinted facies)	10, 15, and 20 mT
9R-41R	lower Eocene-Campanian	10 and 15 mT
49R-51R	Albian	10 and 15 mT
207-1258B- 3R-44R	Eocene-Turonian	10 and 15 mT
207-1258C- 3R-15R	Eocene-Turonian	10 and 15 mT

Note: NRM = natural remanent magnetization.

Table T10. Characteristic directions of minicores, Holes 1258A and 1258B. (This table is available in an [oversized format](#).)

**Table T11. Composite depths, Site 1258.**

Core	Depth (mbsf)	Offset (m)	Depth (mcd)	Depth shifted	Core	Depth (mbsf)	Offset (m)	Depth (mcd)	Depth shifted	Core	Depth (mbsf)	Offset (m)	Depth (mcd)	Depth shifted
207-1258A-					47R	428.3	27.62	455.92	Y	45R	397.5	20.83	418.33	Y
1R	0.0	0.00	0.00	N	48R	432.9	27.92	460.82	Y	46R	403.1	22.06	425.16	Y
2R	5.1	0.00	5.10	N	49R	437.9	27.92	465.82	N	47R	407.1	22.06	429.16	N
3R	14.2	0.00	14.20	N	50R	442.5	36.79	479.29	Y	48R	412.7	22.06	434.76	N
4R	23.8	0.00	23.80	N	207-1258B-					49R	416.7	22.06	438.76	N
5R	33.2	4.50	37.70	Y	1R	0.0	2.90	2.90	Y	50R	422.3	21.18	443.48	Y
6R	42.8	0.52	43.32	Y	2R	14.1	0.00	14.10	N	51R	426.3	24.32	450.62	Y
7R	52.5	0.99	53.49	Y	3R	23.1	0.00	23.10	N	52R	431.9	24.32	456.22	N
8R	62.2	1.85	64.05	Y	4R	32.1	0.00	32.10	N	53R	435.9	24.64	460.54	Y
9R	71.9	0.25	72.15	Y	5R	41.1	0.10	41.20	Y	54R	441.5	24.48	465.98	Y
10R	81.6	0.63	82.23	Y	6R	50.8	-0.57	50.23	Y	55R	445.5	26.86	472.36	Y
11R	91.3	-0.30	91.00	Y	7R	60.5	-0.01	60.49	Y	56R	451.2	24.57	475.77	Y
12R	100.9	0.39	101.29	Y	8R	70.1	-0.47	69.63	Y	57R	455.2	24.57	479.77	N
13R	110.5	0.61	111.11	Y	9R	79.7	-0.83	78.87	Y	207-1258C-				
14R	120.1	0.91	121.01	Y	10R	89.3	-0.67	88.63	Y	1R	120.0	-0.73	119.27	Y
15R	129.7	23.54	153.24	Y	11R	99.0	-0.37	98.63	Y	2R	129.4	1.37	130.77	Y
16R	139.4	21.94	161.34	Y	12R	108.6	0.60	109.20	Y	3R	139.0	2.52	141.52	Y
17R	149.0	21.84	170.84	Y	13R	118.2	-0.61	117.59	Y	4R	148.6	2.39	150.99	Y
18R	158.7	23.86	182.56	Y	14R	127.9	0.42	128.32	Y	5R	158.2	3.48	161.68	N
19R	168.4	23.43	191.83	N	15R	137.5	0.42	137.92	N	6R	167.9	3.48	171.38	N
20R	178.1	23.43	201.53	N	16R	147.2	2.14	149.34	Y	7R	177.5	-1.11	176.39	Y
21R	187.7	23.43	211.13	N	17R	156.9	0.59	157.49	Y	8R	187.2	2.29	189.49	Y
22R	197.1	23.43	220.53	N	18R	166.5	0.59	167.09	Y	9R	196.5	3.35	199.85	Y
23R	206.7	23.43	230.13	N	19R	176.1	-0.14	175.96	Y	12R	254.9	12.43	267.33	Y
24R	216.3	23.43	239.73	N	20R	185.7	0.19	185.89	Y	14R	384.8	11.89	396.69	N
25R	226.0	22.45	248.45	N	21R	195.2	1.08	196.28	Y	15R	389.8	20.93	410.73	Y
26R	235.6	22.45	258.05	N	22R	204.7	12.73	217.43	Y	16R	394.4	24.33	418.73	Y
27R	245.3	22.45	267.75	N	23R	214.4	22.63	237.03	Y	17R	399.4	25.39	424.79	Y
28R	254.9	22.45	277.35	N	24R	224.1	22.23	246.33	Y	18R	404.1	24.11	428.21	Y
29R	264.6	22.45	287.05	N	25R	233.7	21.25	254.95	Y	19R	409.1	24.11	433.21	N
30R	274.2	22.37	296.57	Y	27R	252.9	23.43	276.33	N	20R	413.7	24.11	437.81	N
31R	283.9	22.74	306.64	N	28R	258.6	19.28	277.88	Y	21R	418.7	24.11	442.81	N
32R	293.5	23.21	316.71	Y	29R	262.6	26.48	289.08	Y	22R	423.3	24.56	447.86	Y
33R	303.1	22.11	325.21	Y	30R	272.2	21.50	293.70	Y	23R	428.3	25.96	454.26	Y
34R	312.8	24.89	337.69	Y	31R	281.9	23.14	305.04	Y	24R	432.9	26.74	459.64	Y
35R	322.4	22.87	345.27	N	32R	291.5	22.41	313.91	Y	25R	437.9	28.02	465.92	Y
36R	332.0	22.87	354.87	N	33R	301.1	22.81	323.91	Y	26R	442.5	28.43	470.93	N
37R	341.7	22.87	364.57	N	34R	310.8	20.19	330.99	Y	27R	447.5	31.38	478.88	Y
38R	351.3	22.87	374.17	N	35R	320.4	20.39	340.79	Y	28R	451.8	32.50	484.30	Y
39R	360.9	20.74	381.64	Y	36R	330.1	12.81	342.91	Y	29R	456.8	32.50	489.30	N
40R	370.5	23.93	394.43	N	38R	349.3	18.09	367.39	Y	30R	461.4	32.50	493.90	N
41R	380.2	23.93	404.13	N	39R	359.0	17.75	376.75	Y	31R	466.4	32.50	498.90	N
42R	389.8	24.95	414.75	Y	40R	368.6	22.11	390.71	N	32R	471.0	32.50	503.50	N
43R	399.4	24.88	424.28	N	42R	383.8	22.11	405.91	N	33R	476.0	32.50	508.50	N
44R	409.1	24.88	433.98	N	43R	387.8	22.11	409.91	N	34R	480.7	32.50	513.20	N
45R	418.7	24.88	443.58	N	44R	393.5	20.50	414.00	Y					
46R	423.3	24.88	448.18	N										

Note: N = no, Y = yes.

**Table T12.** Splice tie points, Site 1258.

Hole, core, section, interval (cm)	Depth			Hole, core, section, interval (cm)	Depth	
	(mbsf)	(mcd)			(mbsf)	(mcd)
207-				207-		
1258B-4R-5, 5	38.15	38.15	Tie to	1258A-5R-1, 45	33.65	38.15
1258A-5R-4, 7.5	37.78	42.28	Tie to	1258B-5R-1, 107.5	42.18	42.28
1258B-5R-4, 52.5	46.13	46.23	Tie to	1258A-6R-2, 139.5	45.71	46.23
1258A-6R-6, 80	51.10	51.62	Tie to	1258B-6R-1, 138.5	52.19	51.62
1258B-6R-3, 127.5	55.08	54.51	Tie to	1258A-7R-1, 101	53.52	54.51
1258A-7R-6, 7.5	59.78	60.77	Tie to	1258B-7R-1, 27.5	60.78	60.77
1258B-7R-5, 50	67.00	66.99	Tie to	1258A-8R-2, 147	65.14	66.99
1258A-8R-5, 20	68.37	70.22	Tie to	1258B-8R-1, 58.5	70.69	70.22
1258B-8R-3, 25	73.35	72.88	Tie to	1258A-9R-1, 72.5	72.63	72.88
1258A-9R-7, 35	81.25	81.50	Tie to	1258B-9R-2, 112.5	82.33	81.50
1258B-9R-3, 145	84.15	83.32	Tie to	1258A-10R-1, 108.5	82.69	83.32
1258A-10R-6, 15	89.25	89.88	Tie to	1258B-10R-1, 125	90.55	89.88
1258B-10R-3, 95	93.25	92.58	Tie to	1258A-11R-2, 7.5	92.88	92.58
1258A-11R-6, 90	99.65	99.35	Tie to	1258B-11R-1, 71	99.72	99.35
1258B-11R-4, 45	103.95	103.58	Tie to	1258A-12R-2, 78.5	103.19	103.58
1258A-12R-6, 117.5	109.58	109.97	Tie to	1258B-12R-1, 76	109.37	109.97
1258B-12R-2, 95	111.05	111.65	Tie to	1258A-13R-1, 53.5	111.04	111.65
1258A-13R-5, 140	117.90	118.51	Tie to	1258B-13R-1, 91	119.12	118.51
1258B-13R-3, 30	121.50	120.89	Tie to	1258C-1R-1, 105	121.05	120.89
1258C-1R-7, 62.5	129.63	129.47	Tie to	1258B-14R-1, 115	129.05	129.47
1258B-14R-6, 115	136.55	136.97	Append to	1258B-15R-1, 0	137.50	137.92
1258B-15R-5, 120	144.70	145.12	Tie to	1258C-3R-3, 60	142.60	145.12
1258C-3R-6, 132.5	147.83	150.35	Append to	1258C-4R-1, 0	148.60	150.99
1258C-4R-6, 32.5	156.43	158.82	Tie to	1258B-17R-1, 132.5	158.23	158.82
1258B-17R-5, 65	163.35	163.94	Tie to	1258A-16R-2, 110	142.00	163.94
1258A-16R-7, 25	148.60	170.54	Tie to	1258B-18R-3, 43	169.95	170.54
1258B-18R-6, 47.5	174.48	175.07	Tie to	1258A-17R-3, 117.5	153.23	175.07
1258A-17R-5, 30	155.35	177.19	Tie to	1258B-19R-1, 122	177.33	177.19
1258B-19R-6, 112.5	184.73	184.59	Tie to	1258A-18R-2, 52	160.73	184.59
1258A-18R-6, 70	166.90	190.76	Tie to	1258C-8R-1, 126	188.47	190.76
1258C-8R-5, 80	194.00	196.29	Tie to	1258A-19R-3, 146	172.86	196.29
1258A-19R-7, 30	176.86	200.29	Tie to	1258C-9R-1, 43.5	196.94	200.29
1258C-9R-5, 102.5	203.53	206.88				

**Table T13.** Calcareous nannofossil and planktonic foraminifer datums used in the preliminary age-depth model, Hole 1258A. (Continued on next page.)

Core, section, interval (cm)	Depth (mbsf) Top	Age (Ma)		Foraminifer zone	Nannofossil zone	Epoch
		Minimum	Maximum			
207-1258A-						
1R-CC	4.98	11.6	11.9		NN7	middle Miocene
1R-CC	4.98	11.68	13.18	M9		middle Miocene
2R-CC	11.43	43.4	47		NP15	middle Eocene
2R-CC	11.43		49	P10		middle Eocene
3R-CC	22.83	44	46.1		NP15	middle Eocene
3R-CC	22.83		52.3	P9		early Eocene
4R-CC	30.26	40.4	53.3		NP14	early Eocene
4R-CC	30.26		52.3	P9		early Eocene
5R-CC	38.44	47.2	49.3		NP14	early Eocene
5R-CC	38.44		52.3	P9		early Eocene
6R-CC	52.50	48	52.4		NP14	early Eocene
6R-CC	52.50		52.3	P9		early Eocene
7R-CC	60.20	48	52.4		NP14	early Eocene
7R-CC	60.20		50.4	P9		early Eocene
8R-CC	69.30	51	52.4		NP13	early Eocene
8R-CC	69.30		50.4	P9		early Eocene
9R-CC	81.59	51	52.4		NP13	early Eocene
9R-CC	81.59		52.3	P8		early Eocene
10R-CC	90.16	51	52.4		NP13	early Eocene
10R-CC	90.16		52.3	P8		early Eocene
11R-CC	100.46	51	52.4		NP13	early Eocene
11R-CC	100.46	50.8	52.3	P7		early Eocene
12R-CC	110.60	51	53		NP12	early Eocene
12R-CC	110.60		52.3	P7		early Eocene
13R-CC	120.03	51	53		NP12	early Eocene
13R-CC	120.03	54.7		P6		early Eocene
14R-CC	125.31	53	53.9		NP10	early Eocene
14R-CC	125.31	54.7		P6a		earliest Eocene
15R-4, 53	134.73	53	53.9		NP9	earliest Eocene
16R-CC	149.01	54.1	56.2		NP9	earliest Eocene
16R-CC	149.01	55.9			P6	earliest Eocene
17R-CC	158.32	54.1	56.2		NP9	earliest Eocene
17R-CC	158.32	55.9	56.5	P5		earliest Eocene
18R-CC	168.35	54.1	56.2		NP9	earliest Eocene
18R-CC	168.35	55.9	56.5	P5		earliest Eocene
19R-CC	177.76	54.1	56.2		NP9	latest Paleocene
19R-CC	177.76		56.5	P5		latest Paleocene
20R-CC	185.39		56.5	P5		latest Paleocene
21R-CC	197.33	54.1	56.2		NP9	latest Paleocene
21R-CC	197.33	55.9		P4		latest Paleocene
22R-CC	204.31	54.1	56.2		NP9	latest Paleocene
22R-CC	204.31	55.9	56.5	P4		late Paleocene
23R-CC	215.97	56.2	57.3		NP8	late Paleocene
23R-CC	215.97		56.5	P4		late Paleocene
24R-CC	225.61		56.5	P4		late Paleocene
25R-CC	235.76	56.2	57.5		NP7	late Paleocene
25R-CC	235.76	55.9	59.2	P4a		late Paleocene
26R-CC	245.32		60.9	P3a		late Paleocene
27R-1, 0	245.30		64.5		NP2	early Paleocene
27R-CC	252.58	65	65.4		CC26	latest Maastrichtian
28R-6, 124	263.64	65	66.2		CC25	latest Maastrichtian
29R-CC	274.39	65	66.2		CC25	latest Maastrichtian
29R-CC	274.39	65	68.6	KS31		latest Maastrichtian
30R-CC	279.31	65	66.2		CC25	latest Maastrichtian
30R-CC	279.31		72.8			latest Maastrichtian
31R-CC	293.65	65	66.2		CC25	latest Maastrichtian
31R-CC	293.65		72.8			latest Maastrichtian
32R-CC	302.09	66.2	69.2		CC25	late Maastrichtian
33R-CC	312.81	69.2			CC24	latest Maastrichtian
34R-CC	320.11	69.2	77		CC23	Maastrichtian–Campanian
35R-CC	331.34	69.2	71		CC23	Maastrichtian–Campanian
36R-CC	341.58	69.2	71		CC23	Maastrichtian–Campanian
37R-6, 64	348.70	71	76		CC23	Maastrichtian–Campanian
38R-CC	357.01	71	76		CC23	Maastrichtian–Campanian
39R-CC	364.56	71	76		CC23	Maastrichtian–Campanian
40R-CC	377.77	71	76		CC23	Maastrichtian–Campanian

**Table T13 (continued).**

Core, section, interval (cm)	Depth (mbsf)	Age (Ma)		Foraminifer zone	Nannofossil zone	Epoch
	Top	Minimum	Maximum			
41R-CC	385.45	75.2	82.5		CC23	Maastrichtian–Campanian
42R-CC	399.35	75.3				Turonian
43R-CC	403.77	75.3				Turonian
44R-CC	411.26	75.3				Turonian
45R-CC	422.58	94	97.6		CC10	Cenomanian
46R-CC	429.26	94			CC10	Cenomanian
47R-CC	430.75	94				Cenomanian
48R-CC	437.17	94				Cenomanian
49R-CC	442.35	40.4	101.7		CC9	Cenomanian
50R-CC	446.22	40.4	101.7		CC9	Cenomanian

**Table T14.** Magnetostratigraphic datums used in the preliminary age-depth model, Hole 1258A.

Core, section	Depth (mbsf)	Age (Ma)	Polarity chron	Epoch
207-1258A-				
3R-1	15.2	43.8	C20r (top)	middle Eocene
4R-5	29.9	46.2	C21n (top)	middle Eocene
10R-5	88.9	49.7	C22r (top)	early Eocene
12R-1	101.15	50.8	C22r (base)	early Eocene
12R-1	101.35	50.8	C23n (top)	early Eocene
12R-5	108.3	51.8	C23n (base)	early Eocene
12R-6	108.45	51.8	C23r (top)	early Eocene
14R-2	122.6	52.4	C23r (base)	early Eocene
14R-2	122.65	52.4	C24n (top)	early Eocene
14R-3	124.3	53.4	C24n (base)	early Eocene
15R-2	131.25	53.4	C24r (top)	early Eocene
21R-3	190.9	55.9	C24r (base)	late Paleocene
21R-4	192.85	55.9	C25n (top)	late Paleocene
23R-3	210.25	56.4	C25n (base)	late Paleocene
23R-3	210.65	56.4	C25r (top)	late Paleocene
24R-4	222.25	57.6	C25r (base)	late Paleocene
24R-5	222.5	57.6	C26n? (top)	late Paleocene
24R-5	222.9	58	C26n? (base)	late Paleocene
24R-5	223.55	58	C26r (top)	late Paleocene

**Table T15.** Linear sedimentation rates and mass accumulation rates, Hole 1258A.

Epoch	Core, section, interval (cm)	Top		Bottom		Thickness (m)	Duration (m.y.)	LSR		DBD (g/cm <sup>3</sup> )	MAR (g/cm <sup>2</sup> /k.y.)	Main lithology
		Depth (mbsf)	Age (Ma)	Depth (mbsf)	Age (Ma)			(m/m.y.)	(cm/k.y.)			
	207-1258A-											
Neogene	1R-1, 0, to 1R-CC, 0	0	—	4.98	11.7	4.98	—	—	—	0.92	—	Nannofossil ooze
middle Eocene–late Paleocene	2R-CC, 0, to 26R-CC, 0	11.43	45.2	245.32	60.9	233.89	15.7	15	1.5	1.14	1.7	Nannofossil chalk
early Paleocene	27R-1, 0, to 27R-CC, 0	245.30	64.5	252.58	65.2	7.28	0.7	10	1.0	1.45	1.5	Nannofossil chalk
Maastrichtian–Campanian	27R-CC, 0, to 41R-CC, 0	252.58	65.2	385.45	79	132.87	13.8	10	1.0	1.55	1.6	Nannofossil chalk
Turonian–Albian	42R-CC, 0, to 50R-CC, 0	399.35	83	446.22	101.7	46.87	18.7	3	0.3	None	—	Organic-rich limestone

Notes: Averaged dry bulk densities (DBD) of major lithologies per studied interval were used (see “Physical Properties,” p. 30) to calculate mass accumulation rate (MAR) values. LSR = linear sedimentation rate. — = not assigned.

**Table T16.** Total carbon, inorganic carbon, carbonate, total organic carbon, and total nitrogen concentrations and carbon/nitrogen ratios, Site 1258. (See table notes. Continued on next four pages.)

Hole, core, section, interval (cm)	Depth (mbsf)	TC (wt%)	IC (wt%)	CaCO <sub>3</sub> (wt%)	TOC (wt%)	N (wt%)	C/N (atomic)
207-							
Unit I (nannofossil ooze):							
1258B-1R-1, 38-39	0.38		6.96	58.0			
1258A-1R-2, 120-121	2.70	7.47	7.35	61.2	0.12	0.02	8.5
1258B-1R-3, 38-39	3.38		7.59	63.2			
1258A-1R-4, 40-41	4.90		6.59	54.9			
1258A-2R-1, 90-91	6.00		8.49	70.7			
Unit II (nannofossil chalk):							
1258B-1R-5, 134-135	7.34		6.11	50.9			
1258A-2R-3, 90-91	9.00	9.70	9.75	81.2		0.01	
1258A-2R-5, 45-46	11.25		9.15	76.2			
1258A-3R-1, 36-37	14.56		8.37	69.7			
1258B-2R-1, 52-53	14.62		9.63	80.2			
1258A-3R-3, 35-36	17.55		9.52	79.3			
1258A-3R-5, 35-36	20.55	8.77	8.84	73.7		0.01	
1258A-4R-1, 80-81	24.60		8.73	72.7			
1258B-3R-3, 73-74	26.83		8.32	69.3			
1258A-4R-3, 79-81	27.59	8.15	8.20	68.3			
1258B-3R-5, 73-74	29.83		8.01	66.7			
1258A-4R-5, 44-45	30.24		7.75	64.5			
1258B-4R-1, 80-81	32.90		8.98	74.8			
1258A-5R-1, 30-32	33.50		7.00	58.3			
1258B-4R-2, 80-81	34.40		3.52	29.3			
1258A-5R-3, 30-32	36.50	6.03	6.04	50.3		0.02	
1258B-4R-4, 128-129	37.88		6.08	50.6			
1258B-5R-1, 15-16	41.25		7.88	65.6			
1258A-6R-1, 34-35	43.14		7.98	66.5			
1258A-6R-1, 122-124	44.02		6.93	57.7			
1258B-5R-3, 16-17	44.26	7.49	7.40	61.6	0.09		
1258A-6R-3, 28-29	46.08	5.91	5.86	48.9	0.05	0.01	4.6
1258B-5R-5, 26-27	47.36		6.48	53.9			
1258A-6R-4, 84-85	48.14		6.02	50.2			
1258B-6R-1, 34-35	51.14		4.74	39.5			
1258A-7R-1, 28-29	52.78		5.40	45.0			
1258A-7R-2, 26-27	53.96		5.93	49.4			
1258B-6R-4, 12-13	55.42	5.43	5.32	44.3	0.11	0.13	1.0
1258A-7R-4, 37-39	57.07	4.29	4.31	35.9		0.01	
1258B-6R-6, 32-33	58.62		7.98	66.4			
1258B-7R-1, 32-33	60.82		5.20	43.3			
1258B-7R-2, 32-33	62.32	5.83	6.13	51.0	0.00	0.01	
1258A-8R-3, 110-111	66.27		3.96	33.0			
1258A-8R-3, 129-130	66.46	6.14	6.21	51.7		0.03	
1258B-7R-5, 32-33	66.82		5.64	47.0			
1258B-8R-2, 75-76	72.35		3.72	31.0			
1258B-8R-4, 60-61	75.20	4.78	4.73	39.4	0.05	0.01	6.4
1258B-8R-5, 23-24	76.33		5.98	49.8			
1258A-9R-4, 126-127	77.66		6.35	52.9			
1258A-9R-5, 43-44	78.33	3.26	3.32	27.7	0.00	0.04	
1258B-9R-1, 66-67	80.36		4.83	40.2			
1258B-9R-1, 89-90	80.59		5.45	45.4			
1258B-9R-2, 66-67	81.86	4.04	3.90	32.5	0.14	0.01	12.6
1258A-10R-2, 37-38	83.47		4.98	41.5			
1258B-9R-3, 89-90	83.59		4.90	40.8			
1258B-9R-4, 66-67	84.86		4.43	36.9			
1258B-9R-5, 99-100	86.69		4.51	37.6			
1258A-10R-6, 24-25	89.34	6.38	5.90	49.2	0.48	0.03	19.0
1258B-10R-1, 90-91	90.20		6.14	51.1			
1258A-11R-1, 89-90	92.19	4.35	4.36	36.3		0.03	
1258B-10R-4, 108-109	94.88	5.62	5.45	45.4	0.17	0.01	14.8
1258B-10R-6, 58-59	97.38		3.66	30.5			
1258A-11R-5, 71-72	98.01		5.14	42.8			
1258B-11R-1, 96-97	99.96		3.14	26.1			
1258A-12R-1, 40-41	101.30		5.09	42.4			
1258B-11R-4, 76-77	104.26		5.73	47.8			
1258A-12R-3, 40-41	104.30	5.13	5.11	42.6	0.02	0.02	1.7

**Table T16 (continued).**

Hole, core, section, interval (cm)	Depth (mbsf)	TC (wt%)	IC (wt%)	CaCO <sub>3</sub> (wt%)	TOC (wt%)	N (wt%)	C/N (atomic)
1258B-11R-6, 10-11	106.60	4.87	4.84	40.3	0.03	0.02	1.9
1258A-12R-5, 40-41	107.30		5.03	41.9			
1258A-12R-7, 40-41	110.30		5.56	46.3			
1258B-12R-2, 53-54	110.63		5.21	43.4			
1258A-13R-2, 57-59	112.57		3.50	29.1			
1258B-12R-4, 84-85	113.94	5.97	5.90	49.2	0.07	0.01	8.6
1258A-13R-4, 57-59	115.57	6.02	6.03	50.2		0.03	
1258B-12R-6, 57-58	116.67		5.76	48.0			
1258A-13R-6, 57-59	118.57		3.69	30.8			
1258B-13R-1, 69-70	118.89						
1258C-1R-1, 50-51	120.50		5.88	49.0			
1258A-14R-1, 48-49	120.58		2.94	24.5			
1258B-13R-3, 76-77	121.96		2.99	24.9			
1258C-1R-3, 50-52	123.50		6.21	51.8			
1258B-13R-4, 95-96	123.65	6.25	6.16	51.4	0.09	0.01	7.4
1258B-13R-5, 30-31	124.50		6.82	56.8			
1258A-14R-4, 48-49	125.08	7.36	7.29	60.7	0.07	0.03	2.6
1258C-1R-5, 50-52	126.50		5.77	48.1			
1258B-13R-6, 96-97	126.66		6.40	53.3			
1258B-13R-7, 14-15	127.34		6.33	52.8			
1258B-14R-1, 94-95	128.84		4.42	36.8			
1258C-1R-7, 50-52	129.50		4.64	38.6			
1258C-2R-1, 50-51	129.90		5.27	43.9			
1258A-15R-1, 95-96	130.65		7.36	61.3			
1258C-2R-2, 40-41	131.30		2.47	20.6			
1258C-2R-2, 50-51	131.40		3.54	29.5			
1258B-14R-3, 58-59	131.48	3.36	2.70	22.5	0.66	0.01	64.1
1258C-2R-2, 102-103	131.92		1.73	14.4			
1258A-15R-3, 95-96	133.65	7.17	7.19	59.9	0.00	0.04	
1258C-2R-4, 50-51	134.40		5.87	48.9			
1258B-14R-5, 93-94	134.83		6.06	50.5			
1258C-2R-5, 60-61	136.00		7.16	59.6			
1258B-14R-6, 74-75	136.14		5.92	49.3			
1258C-2R-6, 50-51	137.40		6.67	55.5			
1258B-15R-1, 88-88	138.38		6.09	50.7			
1258A-16R-1, 77-78	140.17		7.26	60.5			
1258B-15R-3, 96-96	141.46	7.43	7.18	59.9	0.25		
1258A-16R-3, 77-78	143.17		8.04	66.9			
1258B-15R-5, 12-12	143.62		7.15	59.6			
1258A-16R-5, 77-78	146.17	7.29	6.93	57.7	0.36	0.02	17.0
1258B-15R-7, 5-5	146.55		6.20	51.6			
1258B-16R-2, 8-9	148.78		7.33	61.0			
1258A-16R-7, 60-61	148.95		6.87	57.2			
1258A-17R-1, 49-50	149.49		6.73	56.1			
1258B-16R-4, 8-9	151.78	7.44	7.20	60.0	0.24	0.02	18.3
1258A-17R-3, 49-50	152.54	5.72	5.80	48.3		0.07	
1258B-16R-6, 37-38	155.07		7.03	58.6			
1258A-17R-5, 49-50	155.54		6.27	52.2			
1258A-17R-7, 49-50	158.04		6.81	56.7			
1258A-18R-1, 94-96	159.64		6.70	55.8			
1258B-17R-3, 10-11	160.00		6.03	50.2			
1258A-18R-3, 89-90	162.59	6.53	6.53	54.4		0.04	
1258B-17R-5, 6-7	162.76		7.21	60.1			
1258A-18R-5, 63-64	165.33		6.27	52.2			
1258B-17R-7, 6-7	165.76		6.52	54.3			
1258B-18R-1, 7-8	166.57		7.14	59.5			
1258A-18R-7, 29-30	167.99		5.08	42.4			
1258A-19R-1, 55-56	168.95		6.23	51.9			
1258B-18R-3, 7-8	169.57		7.42	61.9			
1258B-18R-5, 7-8	172.57		6.56	54.6			
1258A-19R-4, 50-51	173.40	2.84	2.84	23.6		0.06	
1258A-19R-6, 4-5	175.10		5.19	43.2			
1258A-19R-6, 56-57	175.62						
1258B-19R-1, 24-26	176.34		6.22	51.8			
1258A-19R-6, 147-148	176.53						
1258B-19R-3, 10-12	179.20		6.74	56.2			
1258A-20R-2, 70-71	180.30		6.20	51.7			
1258B-19R-5, 4-5	182.14		7.11	59.3			
1258A-20R-3, 110-111	182.20	6.56	6.55	54.5	0.01	0.04	0.2

**Table T16 (continued).**

Hole, core, section, interval (cm)	Depth (mbsf)	TC (wt%)	IC (wt%)	CaCO <sub>3</sub> (wt%)	TOC (wt%)	N (wt%)	C/N (atomic)
1258A-20R-4, 111-112	183.71		7.00	58.3			
1258B-20R-1, 49-50	186.19		6.61	55.1			
1258B-20R-2, 49-50	187.69		5.12	42.7			
1258A-21R-1, 107-108	188.77		6.87	57.2			
1258B-20R-4, 48-49	190.68		6.16	51.3			
1258B-20R-CC, 9-10	191.96		5.52	45.9			
1258A-21R-4, 65-66	192.85	5.40	5.33	44.4	0.07	0.02	4.5
1258B-21R-1, 40-41	195.60		2.99	24.9			
1258B-21R-1, 123-124	196.43		0.56	4.7			
1258B-21R-2, 20-21	196.66		0.03	0.2			
1258B-21R-2, 51-52	196.97		1.60	13.4			
1258B-21R-2, 53-54	196.99		5.55	46.2			
1258B-21R-2, 98-99	197.44		3.61	30.1			
1258A-22R-3, 42-42	200.52		5.75	47.9			
1258A-22R-3, 70-71	200.80	4.42	4.41	36.7	0.01	0.03	0.5
1258B-22R-1, 53-54	205.23		4.87	40.6			
1258B-22R-3, 82-84	208.52		7.52	62.7			
1258A-23R-3, 53-54	210.23		5.96	49.6			
1258A-23R-3, 79-80	210.49	4.56	4.32	36.0	0.24	0.03	9.0
1258B-22R-5, 61-62	211.31		5.87	48.9			
1258B-23R-2, 54-55	216.44		7.33	61.1			
1258A-24R-1, 42-43	216.72		4.66	38.8			
1258B-23R-3, 90-91	218.30		3.98	33.1			
1258B-23R-5, 55-56	220.95		6.02	50.1			
1258A-24R-5, 117-118	223.47	6.47	6.40	53.3	0.07	0.03	2.7
1258B-24R-1, 76-77	224.86		4.37	36.4			
1258A-25R-1, 88-89	226.88		7.11	59.2			
1258B-24R-3, 98-99	228.08		4.55	37.9			
1258B-24R-6, 100-101	232.09		4.71	39.3			
1258A-25R-6, 109-110	234.59	5.56	5.47	45.6	0.09	0.04	3.0
1258B-25R-1, 96-97	234.66		5.11	42.6			
1258B-25R-1, 96-97	234.66						
1258B-25R-3, 73-74	237.43		4.07	33.9			
1258B-25R-3, 73-74	237.43						
1258A-26R-3, 80-81	239.40	7.18	7.14	59.5	0.04	0.03	1.5
1258B-25R-6, 80-81	242.00		6.49	54.1			
1258B-25R-6, 80-81	242.00						
1258B-25R-7, 1-2	242.71		6.86	57.1			
1258B-25R-7, 1-2	242.71						
1258A-26R-6, 60-61	243.10		4.80	40.0			
1258A-27R-3, 32-32	248.62		7.74	64.5			
1258A-27R-3, 88-88	249.18	5.43	5.40	45.0	0.03	0.03	1.1
1258A-27R-4, 29-29	250.09		5.01	41.7			
1258A-27R-4, 142-142	251.22		3.99	33.2			
1258A-28R-1, 67-69	255.57		7.92	66.0			
1258A-28R-3, 81-83	258.71	8.29	8.23	68.6	0.06	0.02	3.7
1258A-28R-5, 79-80	261.69		7.54	62.8			
1258B-29R-2, 22-23	264.32		7.85	65.4			
1258B-29R-2, 22-23	264.32						
1258A-29R-1, 93-94	265.53		8.74	72.8			
1258A-29R-2, 94-95	267.04	7.74	7.71	64.2	0.03	0.02	1.6
1258A-29R-4, 96-97	270.06						
1258B-30R-1, 18-19	272.38		8.53	71.1			
1258A-29R-6, 92-93	272.84						
1258A-30R-1, 59-60	274.79		7.84	65.3			
1258B-30R-3, 72-73	275.92		7.84	65.3			
1258B-30R-5, 5-6	278.25		8.89	74.1			
1258A-30R-3, 108-109	278.28	8.64	8.54	71.2	0.10	0.03	4.1
1258B-30R-7, 5-6	281.25		9.26	77.1			
1258B-31R-1, 6-6	281.96		7.43	61.9			
1258A-31R-1, 97-98	284.87		7.81	65.0			
1258B-31R-3, 5-5	284.95		8.60	71.7			
1258A-31R-3, 93-94	287.83	8.41	8.41	70.1		0.02	
1258B-31R-5, 9-9	287.99		7.29	60.7			
1258A-31R-5, 67-68	290.57		7.22	60.1			
1258B-32R-1, 31-32	291.81		7.23	60.2			
1258A-32R-1, 57-57.5	294.07		8.21	68.4			
1258B-32R-3, 4-5	294.54		7.58	63.1			
1258A-32R-3, 57-57.5	297.07	7.06	6.98	58.2	0.08	0.02	4.3

**Table T16 (continued).**

Hole, core, section, interval (cm)	Depth (mbsf)	TC (wt%)	IC (wt%)	CaCO <sub>3</sub> (wt%)	TOC (wt%)	N (wt%)	C/N (atomic)
1258B-32R-5, 5-6	297.55		6.74	56.1			
1258A-32R-5, 57-57.5	300.07		7.90	65.8			
1258B-32R-7, 12-13	300.62		8.12	67.7			
1258A-33R-1, 95-96	304.05		6.18	51.5			
1258A-33R-3, 78-79	306.88	6.27	6.27	52.2		0.02	
1258A-33R-5, 58-59	309.68		6.69	55.7			
1258B-34R-1, 41-42	311.21		7.78	64.8			
1258A-33R-7, 58-59	312.68		7.84	65.3			
1258B-34R-3, 5-6	313.85		8.37	69.7			
1258A-34R-2, 91-92	315.21	7.63	7.54	62.8	0.09	0.02	4.6
1258B-34R-5, 14-15	316.94		6.45	53.7			
1258A-34R-4, 95-96	318.25		6.40	53.3			
1258B-34R-7, 7-8	319.87		6.93	57.7			
1258B-35R-1, 70-71	321.10		6.13	51.1			
Unit III (clayey nannofossil chalk):							
1258A-35R-1, 114-115	323.54	7.68	7.45	62.1	0.23	0.02	16.5
1258A-35R-3, 12-13	325.52		4.26	35.5			
1258B-36R-1, 100-101	331.10		3.64	30.3			
1258B-36R-2, 25-26	331.85		3.65	30.4			
1258B-36R-3, 70-71	333.80		4.44	37.0			
1258A-36R-2, 95-96	334.45		3.87	32.2			
1258B-36R-4, 37-38	334.67		4.34	36.2			
1258A-36R-3, 88-89	335.88	3.10	2.76	23.0	0.34	0.02	16.6
1258A-36R-5, 95-96	338.95		3.10	25.8			
1258A-37R-2, 80-83	344.00	4.43	4.37	36.4	0.06	0.01	11.2
1258A-37R-3, 82-83	345.52		2.84	23.6			
1258B-38R-1, 69-70	349.99		3.08	25.6			
1258B-38R-2, 109-110	351.89		1.90	15.8			
1258B-39R-3, 60-61	362.60		2.00	16.7			
1258A-39R-3, 81-82	363.94	4.50	4.36	36.3	0.14	0.02	7.1
1258B-39R-6, 60-61	367.10		4.73	39.4			
1258B-40R-2, 17-18	369.77		4.46	37.2			
1258A-40R-1, 80-81	371.30		5.51	45.9			
1258A-40R-3, 140-141	374.90	3.92	3.76	31.4	0.16	0.03	7.5
1258A-41R-1, 32-33	380.52	3.50	3.38	28.2	0.12	0.01	13.1
1258A-41R-2, 72-73	382.42		2.14	17.8			
1258B-42R-1, 54-55	384.34		4.44	37.0			
1258A-41R-4, 15-16	384.70		3.15	26.3			
1258B-43R-1, 21-22	388.01		3.31	27.6			
Unit IV (laminated black shale):							
1258A-42R-1, 134-135	391.14	15.57	6.18	51.5	9.39	0.32	34.3
1258B-43R-3, 64-65	391.34		2.91	24.2			
1258A-42R-3, 23-24	392.92	15.25	5.66	47.1	9.59	0.34	32.8
1258C-15R-3, 34-35	393.11	4.44	4.32	36.0	0.12		
1258B-44R-1, 21-22	393.71		6.09	50.7			
1258C-15R-3, 121-122	393.98	13.68	7.45	62.1	6.23	0.23	31.0
1258B-44R-2, 32-33	394.48		5.32	44.3			
1258B-44R-2, 53-54	394.69		4.52	37.7			
1258B-44R-2, 66-67	394.82	10.27	4.07	33.9	6.20	0.22	32.9
1258C-16R-1, 130-132	395.70	15.16	2.60	21.7	12.56	0.49	30.1
1258A-42R-5, 94-95	396.16	15.08	9.69	80.7	5.39	0.17	38.1
1258B-44R-4, 75-76	397.46	15.40	6.62	55.1	8.78	0.33	31.0
1258A-42R-6, 108-109	397.62	13.95	0.49	4.1	13.46	0.47	33.3
1258A-43R-1, 95-96	400.35	11.85	11.47	95.6	0.38	0.02	24.2
1258B-45R-3, 109-110	400.44	13.88	10.47	87.2	3.41	0.12	33.1
1258C-17R-1, 107-108	400.47	15.24	0.73	6.1	14.51	0.41	41.5
1258A-43R-2, 9-10	400.77	14.08	8.57	71.4	5.51	0.22	29.7
1258A-43R-2, 64-65	401.32	17.53	5.64	46.9	11.89	0.45	30.7
1258B-45R-4, 116-117	401.92	24.64	1.05	8.7	23.59	0.70	39.4
1258B-46R-2, 56-57	404.30	30.93	2.80	23.4	28.13	0.89	37.0
1258C-18R-1, 124-125	405.34	14.85	4.54	37.8	10.31	0.37	32.5
1258B-46R-3, 38-39	405.61	13.70	9.79	81.5	3.91	0.13	35.1
1258C-19R-1, 95-96	410.05	10.72	3.30	27.5	7.42	0.26	33.6
1258C-20R-1, 58-59	414.28	3.55	0.93	7.7	2.62	0.11	28.0
1258C-21R-1, 15-16	418.85	4.90	1.85	15.4	3.05	0.13	26.8
1258A-45R-1, 45-45	419.15	18.82	3.97	33.1	14.85	0.61	28.1
1258A-45R-3, 122-122	422.56	12.60	10.81	90.1	1.79	0.10	21.7
1258C-22R-1, 58-59	423.88	14.48	4.88	40.6	9.60	0.37	30.7

**Table T16 (continued).**

Hole, core, section, interval (cm)	Depth (mbsf)	TC (wt%)	IC (wt%)	CaCO <sub>3</sub> (wt%)	TOC (wt%)	N (wt%)	C/N (atomic)
1258A-46R-1, 103-104	424.33	16.67	4.31	35.9	12.36	0.44	32.8
1258B-51R-1, 18-19	426.48	12.38	11.39	94.9	0.99	0.05	22.5
1258A-46R-4, 28-29	427.60	17.01	7.49	62.4	9.52	0.31	35.4
1258B-51R-2, 40-41	428.12	17.55	5.92	49.4	11.63	0.41	32.9
1258A-47R-1, 32-33	428.62	15.39	7.88	65.6	7.51	0.27	32.5
1258C-23R-1, 41-43	428.71	17.80	5.66	47.1	12.14	0.41	34.4
1258A-47R-2, 36-37	430.16	17.68	5.90	49.2	11.78	0.40	34.5
1258B-52R-1, 89-90	432.79	16.73	7.09	59.0	9.64	0.35	31.7
1258C-24R-1, 41-43	433.31	16.68	5.96	49.7	10.72	0.36	34.8
1258A-48R-1, 48-48	433.38	15.67	6.05	50.4	9.62	0.37	30.2
1258B-52R-3, 90-91	434.91	16.68	6.63	55.2	10.05	0.39	30.4
1258A-48R-3, 42-42	436.21	13.38	6.59	54.9	6.79	0.24	32.4
1258B-53R-1, 45-46	436.35	12.65	7.28	60.7	5.37	0.21	30.1
1258C-25R-1, 96-97	438.86	16.17	6.16	51.3	10.01	0.33	35.1
1258A-49R-1, 109-110	438.99	12.62	10.39	86.5	2.23	0.14	18.6
1258A-49R-2, 108-109	440.46	15.40	5.92	49.3	9.48	0.35	31.4
1258B-54R-1, 53-54	442.03	12.31	10.47	87.2	1.84	0.07	30.0
1258A-49R-3, 126-127	442.10	12.40	8.07	67.2	4.33	0.16	31.5
1258C-26R-1, 2-3	442.52	15.51	5.52	46.0	9.99	0.33	35.1
1258A-50R-1, 79-79	443.29	7.93	4.73	39.4	3.20	0.13	28.9
1258A-50R-2, 79-79	444.55	8.10	2.12	17.7	5.98	0.26	26.9
1258B-54R-3, 54-55	444.92	14.56	5.63	46.9	8.93	0.33	31.7
1258B-55R-1, 49-50	445.99	14.05	5.25	43.7	8.80	0.32	32.6
1258C-27R-1, 108-109	448.58	9.80	4.16	34.6	5.64	0.19	35.2
1258B-55R-4, 25-26	448.82	11.42	10.34	86.1	1.08	0.05	27.9
1258C-27R-2, 117-118	450.08	11.03	8.83	73.5	2.20	0.12	21.4
1258B-56R-1, 44-45	451.64	10.51	4.74	39.5	5.77	0.23	29.7
1258C-28R-1, 75-76	452.55	7.43	3.81	31.7	3.62	0.13	31.9
1258B-56R-2, 54-55	452.81	12.23	10.66	88.8	1.57	0.06	29.3
Unit V (clayey chalk with organic matter):							
1258C-28R-2, 39-40	453.69	7.25	1.99	16.6	5.26	0.20	30.1
1258B-57R-3, 30-31	458.50	7.06	1.69	14.1	5.37	0.24	26.0
1258C-29R-2, 130-131	459.60	7.03	1.61	13.4	5.42	0.21	30.1
1258C-30R-2, 87-88	463.49	6.54	2.74	22.9	3.80	0.18	24.3
1258C-30R-3, 128-130	465.40	5.70	1.77	14.8	3.93	0.17	27.7
1258C-31R-1, 100-101	467.40	6.52	2.54	21.2	3.98	0.18	26.5
1258C-31R-2, 26-27	468.16	6.04	1.50	12.5	4.54	0.20	26.9
1258C-31R-2, 74-75	468.64	37.41	0.78	6.5	36.63	0.94	45.3
1258C-33R-1, 31-32	476.31	6.23	0.72	6.0	5.51	0.23	28.5
1258C-33R-2, 76-77	478.26	6.31	1.64	13.6	4.67	0.22	25.1
1258C-34R-1, 91-92	481.61	3.17	1.29	10.7	1.88	0.12	18.2
1258C-34R-3, 63-64	484.33	5.11	2.92	24.4	2.19	0.13	20.2

Notes: TC = total carbon, IC = inorganic carbon, TOC = total organic carbon.  
 Atomic C/N ratios are calculated from concentrations of organic carbon and total nitrogen.

Table T17. Rock-Eval pyrolysis analyses of sediment samples, Site 1258.

Hole, core, section, interval (cm)	Depth (mbsf)	TOC (wt%)	$T_{max}$ (°C)	$S_1$	$S_2$	$S_3$	HI (mg $S_2$ /g TOC)	OI (mg $S_3$ /g TOC)
207-								
Unit IV (laminated black shale):								
1258A-42R-1, 134-135	391.14	9.39	396	1.80	57.49	2.61	612	27
1258A-42R-3, 23-24	392.92	9.59	398	2.02	58.38	2.55	608	26
1258C-15R-3, 121-122	393.98	6.23	401	1.06	38.96	2.12	625	18
1258C-16R-1, 130-132	395.70	12.56	401	1.61	70.04	2.79	557	22
1258A-42R-5, 94-95	396.16	5.39	384	1.29	37.07	1.37	687	25
1258A-42R-6, 108-109	397.62	13.46	390	3.93	81.03	2.07	602	15
1258C-17R-1, 107-108	400.47	14.51	394	2.84	90.72	4.04	625	27
1258A-43R-2, 9-10	400.77	5.51	399	1.01	34.92	1.64	633	29
1258A-43R-2, 64-65	401.32	11.89	401	1.88	68.95	3.18	577	26
1258B-45R-4, 116-117	401.92	23.59	398	4.33	125.77	4.30	533	18
1258B-46R-2, 56-57	404.30	28.13	398	5.14	136.46	6.86	485	24
1258C-18R-1, 124-125	405.34	10.31	397	1.90	61.15	2.96	593	28
1258C-19R-1, 95-96	410.05	7.42	405	1.63	44.00	2.31	592	31
1258C-20R-1, 58-59	414.28	2.62	402	0.57	17.00	0.98	648	37
1258A-45R-1, 45-45	419.15	14.85	403	2.18	83.76	3.81	564	26
1258A-45R-3, 122-122	422.56	1.79	403	0.23	11.80	0.64	657	32
1258A-46R-1, 103-104	424.33	12.36	403	1.94	75.22	3.52	608	28
1258A-46R-4, 28-29	427.60	9.52	404	1.22	57.05	2.90	599	30
1258A-47R-1, 32-33	428.62	7.51	401	1.21	47.00	2.79	625	37
1258A-47R-2, 36-37	430.16	11.78	399	1.96	73.70	3.74	625	31
1258A-48R-1, 48-48	433.38	9.62	397	1.23	56.46	3.27	586	33
1258B-52R-3, 90-91	434.91	10.05	404	1.62	59.90	2.90	596	28
1258A-48R-3, 42-42	436.21	6.79	397	0.88	41.63	2.67	613	39
1258A-49R-1, 109-110	438.99	2.23	400	0.26	11.76	1.62	528	72
1258A-49R-2, 108-109	440.46	9.48	398	1.42	59.07	3.66	623	38
1258A-49R-3, 126-127	442.10	4.33	403	0.61	27.15	1.99	627	45
1258A-50R-1, 79-79	443.29	3.20	402	0.38	16.73	1.99	522	62
1258A-50R-2, 79-79	444.55	5.98	406	0.73	32.58	2.65	544	44
1258B-55R-1, 49-50	445.99	8.80	402	1.35	53.70	2.39	610	27
1258C-27R-1, 108-109	448.58	5.64	404	0.52	35.75	1.61	633	28
1258B-56R-1, 44-45	451.64	5.77	400	0.77	33.54	1.61	581	31
Unit V (clayey chalk with organic matter):								
1258C-28R-2, 39-40	453.69	5.26	414	0.45	27.38	2.06	520	39
1258C-29R-2, 130-131	459.60	5.42	415	0.38	26.87	2.16	495	39
1258C-31R-2, 26-27	468.16	4.54	415	0.30	22.68	2.91	499	64
1258C-31R-2, 74-75	468.64	36.63	394	0.49	62.53	10.38	170	28
1258C-33R-2, 76-77	478.26	4.67	417	0.27	19.66	1.97	420	42
1258C-34R-3, 63-64	484.33	2.19	427	0.18	6.65	1.79	303	81

Note: TOC = total organic carbon. HI = hydrogen index, OI = oxygen index. See "Organic Matter Characterization and Maturity Determination," p. 29, in "Organic Geochemistry" in the "Explanatory Notes" chapter for definitions of  $T_{max}$ ,  $S_1$ ,  $S_2$ , and  $S_3$ .

Table T18. Headspace analyses of interstitial and microbial gases, Site 1258. (See table note. Continued on next page.)

Hole, core, section, interval (cm)	Depth (mbsf)	Routine safety monitoring					Microbial study				
		C <sub>1</sub> (ppmv)	C <sub>2</sub> (ppmv)	C <sub>2=</sub> (ppmv)	C <sub>3</sub> (ppmv)	C <sub>1/C<sub>2</sub></sub>	C <sub>1</sub> (ppmv)	C <sub>2</sub> (ppmv)	C <sub>2=</sub> (ppmv)	C <sub>3</sub> (ppmv)	C <sub>1/C<sub>2</sub></sub>
207-											
Unit I (nannofossil ooze):											
1258A-1R-3, 0-5	3.0	2	0	0	0		7	0	0	0	
Unit II (nannofossil chalk):											
1258A-2R-3, 0-5	8.1	2	0	0	0		4	0	0	0	
1258A-3R-5, 0-5	20.2	2	0	0	0		9	2	0	0	5
1258A-4R-4, 0-5	28.3	2	0	0	0		9	1	0	0	10
1258A-5R-3, 0-5	36.2	2	0	0	0		9	0	0	0	
1258A-6R-5, 0-5	48.8	2	0	0	0		4	0	0	0	
1258A-7R-4, 0-5	56.7	2	0	0	0		4	0	0	0	
1258A-8R-4, 0-5	66.7	2	0	0	0		5	0	0	0	
1258A-9R-4, 0-5	76.4	2	0	0	0		3	0	0	0	
1258A-10R-4, 0-5	86.1	2	0	0	0		4	0	0	0	
1258A-11R-4, 0-5	95.8	2	0	0	0		4	0	0	0	
1258A-12R-4, 0-5	105.4	2	0	0	0		3	0	0	0	
1258A-13R-4, 0-5	115.0	2	0	0	0		4	0	0	0	
1258A-14R-3, 0-5	123.1	2	0	0	0		3	0	0	0	
1258A-15R-3, 0-5	132.7	2	0	0	0		27	2	0	0	11
1258A-16R-4, 0-5	143.9	2	0	0	0		9	1	0	0	7
1258A-17R-5, 0-5	155.1	2	0	0	0		7	0	0	0	
1258A-18R-4, 0-5	163.2	2	0	0	0		9	0	0	0	
1258A-19R-6, 145-150	176.5	14	0	0	0		476	1	0	0	512
1258A-20R-4, 0-5	182.6	12	0	0	0		309	1	0	0	573
1258B-20R-3, 145-150	190.2	58	0	0	0						
1258A-21R-3, 0-5	190.7	43	0	0	0		566	1	0	0	682
1258B-21R-2, 142-147	197.9	260	0	0	0						
1258A-22R-4, 0-5	201.6	27	0	0	0		865	1	0	0	848
1258B-22R-2, 0-5	206.2	305	0	0	0						
1258A-23R-3, 0-5	209.7	16	0	0	0		1,395	1	0	0	1,018
1258B-23R-4, 0-5	218.9	969	1	0	0	969					
1258A-24R-4, 0-5	220.8	70	0	0	0		1,367	1	0	0	1,059
1258B-24R-4, 0-5	228.6	2,257	2	0	0	1,026					
1258A-25R-4, 0-5	230.5	52	0	0	0		1,802	2	0	0	969
1258B-25R-4, 0-4	238.2	2,016	2	0	0	1,120					
1258A-26R-3, 0-5	238.6	205	0	0	0		2,375	2	0	0	1,011
1258A-27R-3, 0-5	248.3	5,843	4	0	0	1,328					
1258B-27R-1, 79-84	253.7	1,747	2	0	0	1,165					
1258B-28R-1, 0-5	258.6	1,642	2	0	0	966					
1258A-28R-6, 0-5	262.4	2,187	2	0	0	1,151	3,940	4	0	0	978
1258B-29R-2, 0-5	264.1	5,063	4	0	0	1,235					
1258A-29R-4, 0-5	269.1	3,468	3	0	0	1,196	7,920	7	0	0	1,120
1258B-30R-4, 0-5	276.7	8,102	6	0	0	1,350					
1258A-30R-3, 0-5	277.2	2,800	2	0	0	1,167	5,255	5	0	0	1,095
1258B-31R-4, 0-5	286.4	2,376	2			1,212					
1258A-31R-5, 0-5	289.9	1,354	1	0	0	1,042	913	1	0	0	748
1258B-32R-4, 0-5	296.0	1,687	1	0	0	1,205					
1258A-32R-5, 0-5	299.5	1,733	2	0	0	1,083	1,205	1	0	0	874
1258B-33R-4, 0-5	305.6	2,473	3	0	0	989					
1258A-33R-5, 0-5	309.1	7,075	6	0	0	1,160	3,972	4	0	0	937
1258B-34R-4, 0-5	315.3	1,212	1	0	0	1,212					
1258A-34R-4, 0-5	317.3	6,428	5	0	0	1,312	5,521	5	0	0	1,148
1258B-35R-1, 0-5	320.4	7,541	6	0	0	1,236					
Unit III (clayey nannofossil chalk):											
1258A-35R-4, 0-5	326.9	5,656	5	0	0	1,257	5,257	4	0	0	1,173
1258B-36R-2, 0-5	331.6	5,792	5	0	0	1,158					
1258A-36R-5, 0-5	338.0	6,975	5	0	0	1,316	6,546	6	0	0	1,068
1258A-37R-3, 0-5	344.7	4,481	4	0	0	1,179	4,056	4	0	0	1,136
1258B-38R-2, 0-5	350.8	6,548	5	0	0	1,423					
1258A-38R-3, 0-5	354.3	6,928	5	0	0	1,307	17,652	14	0	0	1,227
1258A-39R-2, 0-5	361.6	6,938	10	0	0	680	3,048	4	0	0	826
1258B-39R-4, 0-5	363.5	9,047	8	0	0	1,190					
1258B-40R-1, 75-80	369.4	14,787	11	0	0	1,309					
1258A-40R-3, 0-5	373.5	7,569	6	0	0	1,261					
1258A-41R-3, 0-5	383.2	8,987	7	0	0	1,302	5,094	4	0	0	1,396
1258B-42R-2, 0-5	385.1	5,275	5	0	0	1,147					
1258C-14R-3, 0-5	387.7	7,925	7	0	0	1,116					

**Table T18 (continued).**

Hole, core, section, interval (cm)	Depth (mbsf)	Routine safety monitoring					Microbial study				
		C <sub>1</sub> (ppmv)	C <sub>2</sub> (ppmv)	C <sub>2=</sub> (ppmv)	C <sub>3</sub> (ppmv)	C <sub>1</sub> /C <sub>2</sub>	C <sub>1</sub> (ppmv)	C <sub>2</sub> (ppmv)	C <sub>2=</sub> (ppmv)	C <sub>3</sub> (ppmv)	C <sub>1</sub> /C <sub>2</sub>
1258B-43R-2, 0-5	389.3	8,208	6	0	0	1,391					
1258C-15R-2, 0-5	391.3	10,113	8	0	0	1,331					
Unit IV (laminated black shale):											
1258A-42R-3, 0-5	392.7	43,309	133	0	7	326	46,956	131	1	8	358
1258C-16R-1, 145-150	395.9	41,727	137	0	4	305					
1258B-44R-3, 132-138	396.7	14,136	33	0	0	425					
1258A-43R-1, 123-128	400.6	20,135	57	0	0	353	19,077	48	0	0	399
1258B-45R-4, 0-5	400.8	14,961	57	0	0	262					
1258C-17R-2, 0-5	400.8	60,245	253	0	4	238					
1258C-18R-2, 0-5	405.4	36,958	130	0	0	284					
1258B-46R-4, 0-5	406.2	19,010	75	0	0	253					
1258A-44R-1, 115-120	410.3	9,882	22	0	0	443	4,077	10	0	0	392
1258C-19R-2, 0-5	410.3	19,409	88	0	0	221					
1258B-47R-3, 139-144	411.0	5,162	10	0	0	501					
1258B-48R-1, 0-5	412.7	23,859	81	0	0	296					
1258C-20R-1, 0-5	413.7	43,245	179	0	0	242					
1258B-49R-2, 0-5	418.2	8,556	21	0	0	411					
1258C-21R-1, 120-125	419.9	28,587	122	0	0	235					
1258A-45R-1, 123-128	419.9	9,004	34	0	0	267	436	4	0	0	120
1258B-50R-2, 0-5	423.7	38,317	130	0	0	294					
1258C-22R-2, 100-103	425.4	24,661	158	0	12	156					
1258A-46R-4, 0-5	427.3	33,531	180	0	19	187	11,716	107	1	13	109
1258B-51R-1, 140-142	427.7	58,740	190	0	11	310					
1258A-47R-1, 145-150	429.8	64,888	254	1	28	256	2,478	23	0	0	110
1258C-23R-2, 142-144	431.0	54,662	248	0	19	221					
1258B-52R-2, 65-70	433.7	55,707	231	0	25	241					
1258A-48R-1, 134-139	434.2	3,821	37	0	5	103	4,698	41	0	6	116
1258C-24R-2, 100-101	435.3	6,310	35	0	3	181					
1258B-53R-1, 85-90	436.8	16,844	62	0	6	272					
1258C-25R-1, 144-145	439.3	36,627	237	0	26	155					
1258A-49R-2, 141-146	440.8	41,050	230	1	35	179	18,643	124	1	17	151
1258C-26R-2, 0-5	443.5	43,237	246	0	31	176					
1258B-54R-2, 137-142	444.3	30,365	224	0	40	136					
1258A-50R-2, 138-143	445.1	23,895	110	0	13	218	35,519	194	1	28	183
1258B-55R-4, 48-53	449.1	13,783	97	0	12	142					
1258C-27R-2, 145-150	450.4	24,694	125	0	12	197					
1258C-28R-1, 145-150	453.3	11,454	64	0	6	179					
1258B-56R-3, 80-84	453.9	61,530	513	1	96	120					
1258B-57R-2, 0-5	456.7	30,292	219	0	38	138					
Unit V (clayey chalk with organic matter):											
1258C-29R-2, 0-5	458.3	41,833	233	0	24	180					
1258C-30R-2, 145-150	464.1	34,310	316	0	44	109					
1258C-31R-2, 0-5	467.9	44,261	283	0	27	156					
1258C-32R-2, 0-5	472.4	26,691	192	0	13	139					
1258C-33R-2, 0-5	477.5	10,206	125	0	10	81					
1258C-34R-2, 0-5	482.2	30,537	189	0	11	161					

Note: C<sub>1</sub> = methane, C<sub>2</sub> = ethane, C<sub>2=</sub> = ethylene, C<sub>3</sub> = propane.

**Table T19.** Natural gas analyzer results of headspace analyses, Site 1258.

Hole, core, section, interval (cm)	Depth (mbsf)	C <sub>1</sub> (ppmv)	C <sub>2</sub> + C <sub>2=</sub> (ppmv)	C <sub>3</sub> + C <sub>3=</sub> (ppmv)	<i>i</i> -C <sub>4</sub> (ppmv)	<i>n</i> -C <sub>4</sub> (ppmv)	<i>i</i> -C <sub>5</sub> (ppmv)	<i>n</i> -C <sub>5</sub> (ppmv)	<i>i</i> -C <sub>6</sub> (ppmv)	<i>n</i> -C <sub>6</sub> (ppmv)	CO <sub>2</sub> (ppmv)
207-											
Unit III (clayey nannofossil chalk):											
1258C-14R-3, 0-5	387.7	5,648	0	0	0	0	0	0	0	0	6,315
1258C-15R-2, 0-5	391.3	6,926	0	0	0	1	0	0	0	0	9,925
Unit IV (laminated black shale):											
1258C-16R-1, 145-150	395.9	39,721	339	17	1	3	1	0	0	0	16,011
1258C-17R-2, 0-5	400.8	47,683	425	21	2	2	1	0	0	0	22,896
1258C-18R-2, 0-5	405.4	39,084	337	13	0	0	0	0	0	0	16,867
1258C-19R-2, 0-5	410.3	11,007	180	5	0	1	0	0	0	0	16,674
1258C-20R-1, 0-5	413.7	37,523	368	15	1	3	1	0	0	0	25,113
1258C-21R-1, 120-125	419.9	24,583	282	11	1	1	0	0	0	0	20,620
1258C-22R-2, 100-103	425.4	41,851	475	41	5	10	7	5	3	1	27,270
1258A-47R-1, 145-150	429.8	8,593	116	7	1	3	2	2	1	0	5,524
1258C-23R-2, 142-144	431.0	30,587	352	28	3	8	4	3	2	1	13,974
1258B-52R-2, 65-70	433.7	9,752	148	9	1	3	2	1	1	0	4,480
1258A-48R-1, 134-139	434.2	2,679	56	5	1	3	2	2	1	0	4,607
1258C-24R-2, 100-101	435.3	2,943	42	2	0	1	1	1	0	0	3,893
1258B-53R-1, 85-90	436.8	8,123	67	4	1	3	1	1	1	0	5,909
1258C-25R-1, 144-145	439.3	25,057	349	33	4	11	5	5	3	2	22,644
1258A-49R-2, 141-146	440.8	18,987	263	28	4	12	7	8	5	4	11,688
1258C-26R-2, 0-5	443.5	32,880	405	47	6	17	9	11	5	5	13,605
1258B-54R-2, 137-142	444.3	13,259	234	25	4	13	7	9	5	4	12,378
1258A-50R-2, 138-143	445.1	16,307	218	18	3	7	4	5	2	2	6,571
1258B-55R-4, 48-53	449.1	7,746	114	9	2	4	2	2	1	1	6,413
1258C-27R-2, 145-150	450.4	22,341	256	19	2	5	2	3	1	1	6,970
1258C-28R-1, 145-150	453.3	29,613	329	29	3	8	4	4	2	1	8,388
1258B-56R-3, 80-84	453.9	30,278	461	67	11	32	15	20	9	7	16,184
1258B-57R-2, 0-5	456.7	16,130	266	30	5	14	7	9	4	3	6,198
Unit V (clayey chalk with organic matter):											
1258C-29R-2, 0-5	458.3	27,697	322	27	3	7	3	3	1	1	8,350
1258C-30R-2, 145-150	464.1	30,645	438	49	7	17	11	10	5	3	5,684
1258C-31R-2, 0-5	467.9	33,926	450	40	5	11	7	6	4	2	11,273
1258C-32R-2, 0-5	472.4	12,716	225	12	1	3	2	2	1	0	4,859
1258C-33R-2, 0-5	477.5	8,912	210	12	2	4	2	2	1	1	9,756
1258C-34R-2, 0-5	482.2	34,155	413	29	2	6	3	3	2	1	5,077

Notes: C<sub>1</sub> = methane, C<sub>2</sub> = ethane, C<sub>2=</sub> = ethylene, C<sub>3</sub> = propane, C<sub>3=</sub> = propylene, *i*-C<sub>4</sub> = isobutane, *n*-C<sub>4</sub> = normal butane, *i*-C<sub>5</sub> = isopentane, *n*-C<sub>5</sub> = normal pentane, *i*-C<sub>6</sub> = isohexane, *n*-C<sub>6</sub> = normal hexane, CO<sub>2</sub> = carbon dioxide.

**Table T20.** Interstitial water analyses, Site 1258.

Core, section, interval (cm)	Depth		Salinity	Alkalinity (mM)	pH	Cl <sup>-</sup> (mM)	*SO <sub>4</sub> <sup>2-</sup> (mM)	NH <sub>4</sub> <sup>+</sup> (μM)	*H <sub>4</sub> SiO <sub>4</sub> (μM)	B (mM)	Li <sup>+</sup> (μM)	Sr <sup>2+</sup> (μM)	Ca <sup>2+</sup> (mM)	K <sup>+</sup> (mM)	Mg <sup>2+</sup> (mM)	Ba <sup>2+</sup> (μM)	Fe <sup>2+</sup> (μM)	Mn <sup>2+</sup> (μM)	Na <sup>+</sup> (mM)	Na <sup>+</sup> diff
	(mbsf)	(mcd)																		
207-1258A-																				
1R-1, 145-150	1.45	1.45	35.0	3.23	7.55	558	24.4	20	414	0.51	30	86	11.1	12.3	54.8	8	1	1.0	514	485
1R-2, 145-150	2.95	2.95	35.5	3.41	7.48	561	28.2	30	396	0.51	36	95	11.3	11.2	51.6	7	1	1.2	478	495
3R-4, 145-150	20.15	20.15	35.5	4.55	7.24	563	26.9	50	800	0.42	45	123	13.2	11.3	51.1	9	3	5.2	499	492
4R-4, 145-150	29.75	29.75	35.7	5.03	7.26	566	25.4	75	696	0.40	51	134	14.0	10.9	49.2	7	7	5.1	470	495
5R-3, 145-150	37.65	42.15	35.7	5.02	7.25	567	24.7	130	618	0.43	56	141	13.7	11.8	49.0	7	10	5.3	476	495
6R-4, 145-150	48.75	49.27	35.5	4.71	7.35	562	24.1	160	603	0.41	62	157	14.7	11.8	48.6	7	9	5.6	491	488
7R-4, 145-150	58.15	59.14	35.3	5.20	7.31	558	24.0	170	762	0.42	70	175	16.2	11.8	49.2	7	17	6.8	498	479
8R-4, 140-150	68.07	69.92	35.5	5.82	7.13	562	22.6	275	686	0.41	77	185	15.3	10.8	45.6	7	21	8.0	469	491
9R-6, 140-150	80.80	81.05	35.5	5.25	7.12	562	22.5	285	633	0.42	84	199	15.2	9.4	42.7	7	16	6.7	437	496
10R-3, 140-150	86.00	86.63	35.3	5.72	7.13	560	21.3	300	639	0.40	89	209	16.6	9.7	44.4	8	35	7.7	469	485
11R-5, 135-145	98.65	98.35	35.3	5.40	7.29	555	19.6	260	556	0.38	96	219	18.2	9.3	46.4	7	22	5.0	482	470
12R-5, 140-150	108.30	108.69	35.0	6.17	7.13	558	20.2	380	670	0.41	105	246	18.3	9.0	45.1	7	35	6.1	476	477
13R-4, 140-150	116.40	117.01	35.0	5.06	7.19	ND	18.0	550	800	0.42	110	251	18.1	8.2	43.1	7	52	5.8	463	ND
17R-4, 140-150	154.95	176.79	34.0	6.60	7.10	557	14.1	565	863	0.41	132	291	16.9	6.0	34.7	8	2	3.0	394	488
20R-2, 140-150	181.00	204.43	34.3	5.58	7.19	566	12.6	520	758	0.43	142	325	17.9	6.1	37.0	8	1	3.4	437	486
22R-3, 140-150	201.50	224.93	33.5	6.90	7.07	ND	10.7	630	690	0.44	150	338	19.2	6.1	38.1	8	4	2.7	463	ND
24R-3, 139-150	220.69	244.12	33.0	5.13	7.20	561	9.7	720	584	0.42	153	369	18.8	6.0	38.0	8	2	2.4	463	470
26R-2, 140-150	238.50	260.95	34.0	5.19	7.21	556	8.9	750	514	0.41	164	379	19.5	5.5	34.9	14	7	2.8	450	469
28R-5, 140-150	262.30	284.75	33.7	6.35	7.18	559	6.6	770	489	0.42	169	413	20.7	5.4	33.2	10	11	2.1	471	470
30R-2, 140-150	277.10	299.47	33.3	7.00	7.08	558	6.1	975	500	0.42	172	431	19.9	5.0	33.0	8	15	1.8	466	469
32R-5, 140-150	300.90	324.11	32.5	6.48	7.08	558	5.1	965	478	0.44	175	458	19.9	5.2	33.8	8	14	1.3	484	465
35R-3, 140-150	326.80	349.67	32.0	4.89	7.16	552	3.5	1035	572	0.49	170	471	18.0	4.5	31.0	9	3	1.3	443	464
37R-2, 140-150	344.60	367.47	ND	ND	ND	ND	ND	890	ND	ND	ND	ND	17.3	5.0	31.8	ND	ND	ND	468	ND
39R-1, 63-73	361.53	382.27	31.5	4.59	7.22	538	3.5	1025	576	0.45	165	477	18.3	4.1	30.9	10	2	1.1	434	450
207-1258B-																				
14R-4, 140-150	133.80	134.22	34.5	5.93	7.11	561	15.9	445	738	0.42	124	272	17.9	7.1	40.6	8	5	4.5	458	481
18R-3, 140-150	170.90	171.49	33.7	7.38	7.13	559	12.3	510	894	0.40	141	313	20.3	6.7	42.9	8	2	2.4	508	464
33R-4, 140-150	307.00	329.81	32.5	3.83	7.26	541	3.6	950	463	0.44	177	455	19.7	4.8	33.5	15	7	1.2	471	444
36R-3, 90-100	334.00	346.81	32.3	3.43	7.41	552	3.1	1120	447	0.40	178	447	17.2	4.7	30.3	10	3	1.1	448	465
39R-5, 135-150	366.35	384.10	30.5	5.97	7.24	530	1.4	990	618	0.47	170	477	17.9	3.9	29.2	10	6	1.0	415	443
43R-2, 110-120	390.40	412.51	ND	ND	ND	ND	ND	ND	ND	ND	ND	ND	ND	ND	ND	ND	ND	ND	ND	ND
45R-2, 75-85	399.25	420.08	31.5	7.24	7.08	552	0.7	1375	578	0.52	178	511	17.6	4.2	28.1	36	3	0.6	449	467
46R-1, 31-44	403.41	425.47	31.5	6.19	7.12	553	1.4	1290	602	0.51	173	498	18.3	4.4	29.6	37	34	0.7	467	464
51R-2, 20-29	427.92	452.24	30.5	6.13	7.33	543	0.4	1115	627	0.54	172	541	17.4	4.0	27.6	76	1	0.8	453	458
52R-2, 70-80	433.71	458.03	31.0	6.10	7.23	541	0.2	1350	429	0.51	176	542	17.5	3.9	26.5	79	1	0.6	452	457
54R-3, 0-10	444.38	468.86	30.5	5.93	7.22	542	0.1	1185	299	0.51	175	543	17.0	3.6	26.5	79	5	0.4	468	459
55R-3, 58-68	448.27	475.13	30.3	6.50	7.22	536	0.2	1335	209	0.43	172	554	16.8	3.6	27.2	78	2	0.7	474	453
207-1258C-																				
30R-1, 112-122	462.52	495.02	28.3	5.58	7.57	494	0.1	925	280	0.51	164	557	16.7	3.9	28.8	63	1	0.6	455	406
34R-2, 135-150	483.55	516.05	26.0	4.60	7.45	465	0.4	825	222	0.49	158	541	14.6	3.2	23.5	48	4	0.6	398	392

Notes: \* = ICP-AES. ND = not determined.

**Table T21.** Index properties of discrete samples, Holes 1258A and 1258B.

Core, section, interval (cm)	Depth		Water content (%)		Density (g/cm <sup>3</sup> )			Porosity	Void ratio
	(mbsf)	(mcd)	Wet	Dry	Wet bulk	Dry bulk	Grain		
207-1258A-									
1R-1, 70-72	0.70	0.70	45.8	84.6	1.55	0.84	2.75	69.4	2.27
1R-2, 88-90	2.38	2.38	42.6	74.3	1.60	0.92	2.72	66.4	1.98
1R-3, 70-72	3.70	3.70	39.7	65.8	1.64	0.99	2.72	63.6	1.75
1R-4, 27-29	4.77	4.77	41.6	71.1	1.63	0.95	2.82	66.2	1.96
2R-1, 68-70	5.78	5.78	43.7	77.7	1.57	0.89	2.70	67.2	2.05
2R-2, 68-70	7.28	7.28	45.4	83.2	1.55	0.85	2.72	68.9	2.21
2R-3, 70-72	8.80	8.80	39.3	64.6	1.65	1.00	2.71	63.1	1.71
2R-4, 69-71	10.29	10.29	42.8	74.9	1.58	0.91	2.68	66.2	1.96
2R-5, 28-30	11.08	11.08	48.2	93.0	1.51	0.78	2.71	71.1	2.46
3R-1, 70-72	14.90	14.90	46.1	85.6	1.53	0.83	2.68	69.1	2.24
3R-2, 70-72	16.40	16.40	42.4	73.7	1.58	0.91	2.65	65.6	1.91
3R-3, 70-72	17.90	17.90	44.9	81.4	1.55	0.85	2.65	67.9	2.11
3R-4, 70-72	19.40	19.40	40.8	68.9	1.62	0.96	2.68	64.3	1.80
3R-5, 70-72	20.90	20.90	44.9	81.5	1.54	0.85	2.60	67.4	2.07
3R-6, 70-72	22.40	22.40	44.1	78.8	1.55	0.87	2.63	66.9	2.02
4R-1, 70-72	24.50	24.50	45.6	83.9	1.54	0.84	2.65	68.4	2.17
4R-2, 70-72	26.00	26.00	48.3	93.4	1.49	0.77	2.62	70.5	2.39
4R-3, 68-70	27.48	27.48	49.0	96.0	1.49	0.76	2.62	71.1	2.46
4R-4, 70-72	29.00	29.00	45.0	81.7	1.56	0.86	2.70	68.3	2.15
4R-5, 25-27	30.05	30.05	50.8	103.4	1.47	0.72	2.67	72.9	2.70
5R-1, 80-82	34.00	38.50	46.7	87.6	1.52	0.81	2.62	69.2	2.24
5R-2, 70-72	35.40	39.90	46.8	88.1	1.53	0.81	2.68	69.8	2.31
5R-3, 70-72	36.90	41.40	39.9	66.3	1.62	0.97	2.63	63.0	1.70
5R-4, 70-72	38.40	42.90	38.9	63.8	1.63	1.00	2.63	62.1	1.64
6R-1, 57-59	43.37	43.89	40.9	69.1	1.64	0.97	2.79	65.3	1.88
6R-2, 80-82	45.10	45.62	40.5	68.2	1.62	0.96	2.70	64.2	1.80
6R-3, 58-60	46.38	46.90	39.5	65.4	1.62	0.98	2.60	62.4	1.66
6R-4, 54-56	47.84	48.36	38.3	62.1	1.65	1.02	2.64	61.6	1.60
6R-5, 88-90	49.68	50.20	39.7	65.9	1.61	0.97	2.59	62.5	1.67
6R-6, 70-72	51.00	51.52	38.7	63.2	1.65	1.01	2.68	62.3	1.65
6R-7, 45-47	52.25	52.77	43.4	76.8	1.57	0.89	2.66	66.6	1.99
7R-1, 68-70	53.18	54.17	41.8	71.9	1.58	0.92	2.58	64.4	1.81
7R-2, 60-62	54.30	55.29	40.4	67.7	1.61	0.96	2.63	63.4	1.74
7R-3, 54-56	55.74	56.73	38.5	62.7	1.64	1.01	2.63	61.7	1.61
7R-4, 52-54	57.22	58.21	40.4	67.7	1.60	0.95	2.58	63.0	1.71
7R-5, 50-52	58.70	59.69	38.5	62.6	1.60	0.99	2.49	60.3	1.52
7R-6, 24-26	59.94	60.93	37.9	60.9	1.64	1.02	2.60	60.7	1.55
8R-1, 78-80	62.98	64.83	37.1	58.9	1.63	1.03	2.51	59.0	1.44
8R-2, 84-86	64.54	66.39	37.0	58.6	1.64	1.03	2.54	59.2	1.45
8R-3, 60-62	65.77	67.62	37.9	61.1	1.62	1.01	2.52	60.0	1.50
8R-4, 91-93	67.58	69.43	35.2	54.2	1.68	1.09	2.57	57.7	1.36
8R-5, 55-57	68.72	70.57	36.3	56.9	1.65	1.05	2.55	58.6	1.42
9R-1, 55-57	72.45	72.70	37.6	60.3	1.61	1.00	2.44	59.0	1.44
9R-2, 63-65	74.03	74.28	36.6	57.6	1.65	1.05	2.55	59.0	1.44
9R-3, 88-90	75.78	76.03	38.4	62.4	1.63	1.01	2.60	61.3	1.58
9R-4, 98-100	77.38	77.63	35.5	54.9	1.68	1.08	2.58	58.1	1.39
9R-5, 34-36	78.24	78.49	37.0	58.7	1.64	1.03	2.54	59.2	1.45
9R-6, 95-97	80.35	80.60	36.5	57.4	1.64	1.04	2.52	58.5	1.41
10R-1, 43-45	82.03	82.66	35.0	53.9	1.68	1.09	2.57	57.4	1.35
10R-2, 50-52	83.60	84.23	32.7	48.5	1.73	1.17	2.61	55.3	1.24
10R-3, 63-65	85.23	85.86	32.1	47.3	1.74	1.18	2.60	54.6	1.20
10R-4, 87-89	86.97	87.60	35.0	53.9	1.66	1.08	2.49	56.7	1.31
10R-5, 50-52	88.10	88.73	35.7	55.5	1.68	1.08	2.60	58.5	1.41
11R-1, 73-75	92.03	91.73	34.5	52.7	1.70	1.11	2.59	57.2	1.34
11R-2, 61-63	93.41	93.11	33.9	51.3	1.71	1.13	2.61	56.6	1.31
11R-3, 61-63	94.91	94.61	35.1	54.1	1.67	1.08	2.53	57.2	1.34
11R-4, 80-82	96.60	96.30	33.3	50.0	1.72	1.15	2.61	56.0	1.27
11R-5, 44-46	97.74	97.44	34.6	53.0	1.68	1.10	2.53	56.7	1.31
11R-6, 42-44	99.17	98.87	32.1	47.3	1.73	1.17	2.57	54.2	1.19
12R-1, 45-47	101.35	101.74	30.8	44.4	1.76	1.22	2.58	52.8	1.12
12R-2, 94-96	103.34	103.73	31.6	46.1	1.74	1.19	2.56	53.5	1.15
12R-3, 53-55	104.43	104.82	30.1	43.1	1.77	1.24	2.59	52.1	1.09
12R-4, 80-82	106.20	106.59	31.0	44.8	1.77	1.22	2.62	53.4	1.15
12R-5, 83-85	107.73	108.12	30.5	43.9	1.75	1.22	2.54	52.1	1.09
12R-6, 80-82	109.20	109.59	30.4	43.6	1.76	1.22	2.56	52.2	1.09

Note: Only a portion of this table appears here. The complete table is available in [ASCII](#).

Table T22. Discrete measurements of *P*-wave velocity, Site 1258.

Core, section, interval (cm)	Depth		Velocity (m/s)			Core, section, interval (cm)	Depth		Velocity (m/s)		
	(mbsf)	(mcd)	x	y	z		(mbsf)	(mcd)	x	y	z
207-1258A-						4R-4, 42	28.72	28.72	1594.9		
1R-1, 16	0.16	0.16	1557.2			4R-4, 72.7	29.03	29.03	1568.7		
1R-1, 54.3	0.54	0.54	1577.1			4R-4, 110.1	29.40	29.40	1585.1		
1R-1, 86.7	0.87	0.87	1524.3			4R-5, 17.9	29.98	29.98	1552.5		
1R-1, 119.5	1.20	1.20	1573.8			5R-1, 21.3	33.41	37.91	1589.1		
1R-2, 7.3	1.57	1.57	1556.4			5R-1, 54.4	33.74	38.24	1612.1		
1R-2, 34.8	1.85	1.85	1578.6			5R-1, 95.7	34.16	38.66	1614.0		
1R-2, 79.2	2.29	2.29	1537.9			5R-1, 128.5	34.49	38.99	1558.9		
1R-2, 122.7	2.73	2.73	1568.6			5R-2, 18.1	34.88	39.38	1587.4		
1R-3, 24.2	3.24	3.24	1593.4			5R-2, 39.5	35.10	39.60	1590.1		
1R-3, 56.5	3.57	3.57	1595.2			5R-2, 86.4	35.56	40.06	1612.1		
1R-3, 82	3.82	3.82	1585.5			5R-2, 125.4	35.95	40.45	1590.7		
1R-3, 124.2	4.24	4.24	1634.0			5R-3, 17.7	36.38	40.88	1664.9		
1R-4, 8.4	4.58	4.58	1560.0			5R-3, 52.1	36.72	41.22	1665.2		
1R-4, 40.1	4.90	4.90	1595.3			5R-3, 96.8	37.17	41.67	1655.5		
2R-1, 11.4	5.21	5.21	1418.8			5R-3, 128	37.48	41.98	1654.2		
2R-1, 49.4	5.59	5.59	1588.4			5R-4, 24.8	37.95	42.45	1672.7		
2R-1, 96.1	6.06	6.06	1583.9			5R-4, 58.2	38.28	42.78	1680.5		
2R-1, 135.3	6.45	6.45	1564.4			6R-1, 27.6	43.08	43.60	1681.3		
2R-2, 9	6.69	6.69	1536.4			6R-1, 57.1	43.37	43.89	1625.4		
2R-2, 52.2	7.12	7.12	1558.1			6R-1, 86.4	43.66	44.18	1699.1		
2R-2, 95.3	7.55	7.55	1549.9			6R-1, 136.9	44.17	44.69	1651.1		
2R-2, 135.7	7.96	7.96	1560.6			6R-2, 30.9	44.61	45.13	1700.7		
2R-3, 20.6	8.31	8.31	1593.4			6R-2, 81.4	45.11	45.63	1689.0		
2R-3, 47.1	8.57	8.57	1582.7			6R-2, 131.5	45.62	46.13	1668.1		
2R-3, 88.9	8.99	8.99	1575.8			6R-3, 14.2	45.94	46.46	1651.6		
2R-3, 140.5	9.51	9.51	1547.7			6R-3, 58	46.38	46.90	1690.7		
2R-4, 17.7	9.78	9.78	1575.4			6R-3, 102.5	46.83	47.35	1666.7		
2R-4, 42.9	10.03	10.03	1601.1			6R-3, 134.8	47.15	47.67	1640.8		
2R-4, 70	10.30	10.30	1583.7			6R-4, 9.4	47.39	47.91	1673.9		
2R-4, 107.7	10.68	10.68	1607.8			6R-4, 54.8	47.85	48.37	1664.9		
2R-5, 12.3	10.92	10.92	1581.1			6R-4, 90.3	48.20	48.72	1607.7		
2R-5, 22.9	11.03	11.03	1600.9			6R-4, 120.8	48.51	49.03	1650.7		
2R-5, 51.1	11.31	11.31	1589.3			6R-5, 11.4	48.91	49.43	1654.0		
3R-1, 22	14.42	14.42	1560.0			6R-5, 50.1	49.30	49.82	1661.5		
3R-1, 47.5	14.68	14.68	1590.1			6R-5, 90.1	49.70	50.22	1595.9		
3R-1, 80.3	15.00	15.00	1608.7			6R-5, 119.1	49.99	50.51	1621.3		
3R-1, 132	15.52	15.52	1595.2			6R-6, 16.5	50.47	50.99	1683.0		
3R-2, 20	15.90	15.90	1599.5			6R-6, 71	51.01	51.53	1672.5		
3R-2, 32.6	16.03	16.03	1621.9			6R-6, 103.6	51.34	51.86	1693.5		
3R-2, 103.9	16.74	16.74	1604.2			6R-6, 130.7	51.61	52.13	1643.0		
3R-2, 135.5	17.06	17.06	1535.5			6R-7, 10.6	51.91	52.43	1681.4		
3R-3, 7.2	17.27	17.27	1563.6			6R-7, 45.2	52.25	52.77	1675.5		
3R-3, 37.7	17.58	17.58	1603.2			7R-1, 31.5	52.81	53.81	1682.8		
3R-3, 71.7	17.92	17.92	1570.6			7R-1, 68.4	53.18	54.17	1682.3		
3R-3, 130.4	18.50	18.50	1601.0			7R-1, 102.4	53.52	54.51	1663.8		
3R-4, 10.7	18.81	18.81	1612.5			7R-2, 27.5	53.97	54.97	1707.4		
3R-4, 43.8	19.14	19.14	1637.5			7R-2, 61.7	54.32	55.31	1656.7		
3R-4, 74.5	19.44	19.44	1619.4			7R-2, 100.8	54.71	55.70	1637.6		
3R-4, 128.1	19.98	19.98	1572.0			7R-2, 133.7	55.04	56.03	1632.0		
3R-5, 35.3	20.55	20.55	1558.1			7R-3, 12.8	55.33	56.32	1633.2		
3R-5, 66.9	20.87	20.87	1559.3			7R-3, 54.6	55.75	56.74	1632.3		
3R-5, 100.8	21.21	21.21	1557.9			7R-3, 85.8	56.06	57.05	1607.5		
3R-5, 125.9	21.46	21.46	1583.6			7R-3, 132.5	56.53	57.51	1647.7		
3R-6, 24.9	21.95	21.95	1557.7			7R-4, 21.6	56.92	57.91	1632.5		
3R-6, 66.8	22.37	22.37	1574.5			7R-4, 53.4	57.23	58.22	1578.5		
3R-6, 97.5	22.67	22.67	1560.3			7R-4, 99.6	57.70	58.69	1629.6		
4R-1, 17.1	23.97	23.97	1537.6			7R-4, 117.9	57.88	58.87	1654.7		
4R-1, 45.9	24.26	24.26	1546.0			7R-5, 18.5	58.38	59.38	1648.4		
4R-1, 88.7	24.69	24.69	1581.6			7R-5, 51.2	58.71	59.70	1621.4		
4R-2, 10.8	25.41	25.41	1593.8			7R-5, 97.1	59.17	60.16	1631.4		
4R-2, 51.7	25.82	25.82	1560.8			7R-5, 133.8	59.54	60.53	1677.8		
4R-2, 97.4	26.27	26.27	1600.3								
4R-2, 132.8	26.63	26.63	1620.8								
4R-3, 22.6	27.03	27.03	1582.5								
4R-3, 50.2	27.30	27.30	1630.1								
4R-3, 84.4	27.64	27.64	1578.9								
4R-3, 118.7	27.99	27.99	1602.5								
4R-4, 11.5	28.42	28.42	1605.1								

Notes: Multiple axis measurements were performed on 2-cm<sup>3</sup> samples. X-direction is perpendicular to the surface of a split core, y-direction is parallel to the surface of a split core, and z-direction is perpendicular to the top of the core. Only a portion of this table appears here. The complete table is available in [ASCII](#).